

Deposit & Copying of Dissertation Declaration



UNIVERSITY OF
CAMBRIDGE

Board of Graduate Studies

Please note that you will also need to bind a copy of this Declaration into your final, hardbound copy of thesis - this has to be the very first page of the hardbound thesis.

1	Surname (Family Name)	Forenames(s)	Title
	Goedel	Karl Christoph	Mr.
2	Title of Dissertation as approved by the Degree Committee		
	Optoelectronic applications of solution-processable sulfide semiconductors		

In accordance with the University Regulations in *Statutes and Ordinances* for the PhD, MSc and MLitt Degrees, I agree to deposit one print copy of my dissertation entitled above and one print copy of the summary with the Secretary of the Board of Graduate Studies who shall deposit the dissertation and summary in the University Library under the following terms and conditions:

1. Dissertation Author Declaration

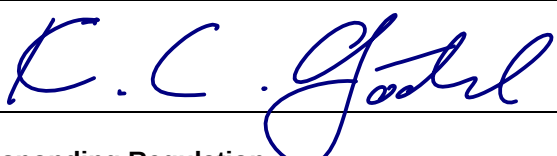
I am the author of this dissertation and hereby give the University the right to make my dissertation available in print form as described in 2. below.

My dissertation is my original work and a product of my own research endeavours and includes nothing which is the outcome of work done in collaboration with others except as declared in the Preface and specified in the text. I hereby assert my moral right to be identified as the author of the dissertation.

The deposit and dissemination of my dissertation by the University does not constitute a breach of any other agreement, publishing or otherwise, including any confidentiality or publication restriction provisions in sponsorship or collaboration agreements governing my research or work at the University or elsewhere.


2. Access to Dissertation

I understand that one print copy of my dissertation will be deposited in the University Library for archival and preservation purposes, and that, unless upon my application restricted access to my dissertation for a specified period of time has been granted by the Board of Graduate Studies prior to this deposit, the dissertation will be made available by the University Library for consultation by readers in accordance with University Library Regulations and copies of my dissertation may be provided to readers in accordance with applicable legislation.

3	Signature	Date
		12/03/2017

Corresponding Regulation

Before being admitted to a degree, a student shall deposit with the Secretary of the Board one copy of his or her hard-bound dissertation and one copy of the summary (bearing student's name and thesis title), both the dissertation and the summary in a form approved by the Board. The Secretary shall deposit the copy of the dissertation together with the copy of the summary in the University Library where, subject to restricted access to the dissertation for a specified period of time having been granted by the Board of Graduate Studies, they shall be made available for consultation by readers in accordance with University Library Regulations and copies of the dissertation provided to readers in accordance with applicable legislation.

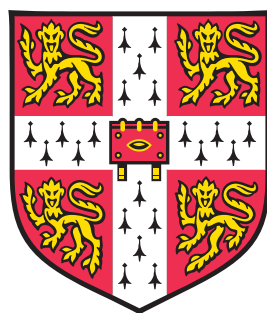


Optoelectronic applications of solution-processable sulfide semiconductors

Karl Christoph Gödel

This dissertation is submitted
for the degree of
Doctor of Philosophy

December 2016



Cavendish Laboratory
University of Cambridge
Corpus Christi College



Abstract

Optoelectronic applications of solution-processable sulfide semiconductors

Karl Christoph Gödel

Solar cells and photodetectors rely on similar physical principles based on the interaction of light and matter. Both types of optoelectronic devices are indispensable in a wide range of technological applications, from large-scale renewable power conversion to everyday consumer items. In this thesis, the use of facile solution-processable semiconductors in solar cells and light sensors is studied with a focus on antimony sulfide (Sb_2S_3) and antimony sulfoiodide (SbSI). The improvement of the photovoltaic performance in Sb_2S_3 sensitized solar cells upon the controlled partial oxidation of the absorber layer is investigated. A reduction in charge carrier recombination is the reason for the improved efficiency, caused by the oxidation process. Further, a new chemical bath deposition method for antimony sulfide is developed. Carried out at room temperature, this technique eliminates the necessity of cooling equipment during the deposition process. The antimony sulfide from this method decreases the density of trap states compared to the conventional deposition. Power-conversion efficiencies of up to $\eta = 5.1\%$ are achieved in antimony sulfide sensitised solar cells using the new room temperature deposition method. Finally, antimony sulfide is used as a precursor to form films of antimony sulfoiodide (SbSI) micro-crystals in a facile physical vapour process. These films are then used to fabricate photodetectors. With PMMA as an insulating spacer layer, the devices are built in a sandwich-type architecture. Optoelectronic characterisation shows that these devices have the shortest response and recovery times reported for SbSI photodetectors to date.

Overview

The first four chapters provide the background for this thesis. In **Chapter 1**, a brief introduction into the basic physical principles underlying the interaction of light with matter is given. Starting from the classification of matter into the categories metals, semiconductors and insulators, the elementary question how electronic bands in semiconductors form is addressed. Building on this concept, the photoelectric and photovoltaic effects are briefly introduced. This helps to gain a better understanding of the interaction of photons from the visible part of the electromagnetic spectrum with semiconductors in optoelectronic devices.

Chapter 2 then provides a more profound introduction into two kinds of optoelectronic devices, namely photodetectors and solar cells. Their key performance metrics are discussed. In the solar cell section, the focus is laid on the class of “sensitised solar cells”, as these types of photovoltaic devices are at the centre of two of the results chapters.

In **Chapter 3** solution processable sulfide semiconductors are described, in particular antimony sulfide (Sb_2S_3) and antimony sulfoiodide (SbSI). A summary of their physical properties is given and different deposition techniques are discussed. To be able to evaluate and assess the results of the thesis, a literature overview of antimony sulfide solar cells and antimony sulfoiodide sensors concludes this chapter.

Chapter 4 completes the introductory part of the thesis. It presents details of the experimental techniques used in this work, including the characterisation of materials, the fabrication of devices and the optoelectronic measurements.

In the first results chapter, **Chapter 5**, the effect of a partial oxidation of the antimony

sulfide layer in sensitised solar cells is investigated. On a phenomenological level, it was reported before that Sb_2S_3 solar cells show increased efficiencies, when the absorber film is cooled in air after the annealing step in an inert atmosphere. Here, the improvement of the photovoltaic parameters by oxidising antimony sulfide in a post heat treatment in air is systematically studied. For short oxidation times of one minute at 200°C , the device efficiency is improved from $\eta = 1.4\%$ to $\eta = 2.4\%$. Intensity modulated photovoltage spectroscopy gives a physical explanation of the origin of this effect: Charge carrier recombination is reduced fourfold in solar cells with an oxidised absorber film.

The necessity for low temperature equipment complicates the deposition of antimony sulfide films. This motivated the development of a room temperature deposition for Sb_2S_3 , which is presented in **Chapter 6**. The method is based on the hydrolysis of SbCl_3 to complex antimony ions to decelerate the reaction at ambient conditions. This method greatly simplifies the deposition of antimony sulfide films. Sensitised solar cells using the new room temperature deposition are compared with the conventional low temperature method. Photothermal deflection spectroscopy confirms that a decrease in the electronic trap state density leads to improved short-circuit currents and open-circuit voltages. Further optimisation of the solar cells enable power conversion efficiencies of up to $\eta = 5.1\%$.

In **Chapter 7** antimony sulfide films are used as a precursor for a thin layer of antimony sulfoiodide micro-crystals. Sb_2S_3 is converted to SbSI using antimony iodide (SbI_3) via a simple and fast physical vapour method. The SbSI films are then used to build photodetectors in a sandwich-type architecture. When using different materials for the top and bottom electrode (FTO and gold), the device can be operated in a self-powered mode. All figures-of-merit are improved, compared to previously published SbSI light detectors. Especially raise and fall times are reduced by more than one order of magnitude, making the devices presented here the fastest SbSI photodetector reported to date.

Declaration

This dissertation is the result of my own work and includes nothing which is the outcome of work done in collaboration except as specified in the text. It is not substantially the same as any that I have submitted, or, is being concurrently submitted for a degree or diploma or other qualification at the University of Cambridge or any other University or similar institution except as specified in the text. I further state that no substantial part of my dissertation has already been submitted, or, is being concurrently submitted for any such degree, diploma or other qualification at the University of Cambridge or any other University of similar institution except as specified in the text. This thesis does not exceed the word limit of 60000 words set by the Physics and Chemistry Degree Committee, including abstract, tables, footnotes and appendices.

Cambridge, 9th December 2016

A handwritten signature in blue ink, appearing to read 'K. C. Gödel', written in a cursive style.

Karl Christoph Gödel

Contents

Acknowledgements	13
List of publications	15
List of abbreviations	19
1 Interaction of light and matter	21
1.1 Band theory of semiconductors	23
1.2 Photoelectric effect	25
Bibliography	28
2 Optoelectronic devices	29
2.1 Photodetectors	30
2.1.1 Mechanisms of detection	30
2.1.2 Performance metrics	31
2.2 Solar cells	35
2.2.1 Basic working mechanism	35
2.2.2 Characterising solar cells	37
2.2.3 Theoretical efficiency limits	43
2.2.4 Sensitised solar cells	46
Bibliography	52
3 Solution-processable sulfide semiconductors	55
3.1 Antimony sulfide	56
3.1.1 Physical properties	56

3.1.2	Synthesis of antimony sulfide	60
3.1.3	Antimony sulfide solar cells	63
3.2	Antimony sulfoiodide	67
3.2.1	Physical properties	68
3.2.2	Synthesis routes of antimony sulfoiodide	71
3.2.3	Antimony sulfoiodide sensors	73
	Bibliography	75
4	Experimental techniques	85
4.1	Material characterisation techniques	86
4.1.1	Electron microscopy	86
4.1.2	X-ray photoelectron spectroscopy	88
4.1.3	X-ray diffraction	89
4.1.4	Absorption measurements	91
4.2	Device fabrication	93
4.2.1	Substrate preparation	94
4.2.2	Porous metal-oxide anodes	95
4.2.3	Hole transport materials	98
4.2.4	Metal electrode deposition	99
4.3	Optoelectronic measurements	100
4.3.1	Current-voltage measurements	100
4.3.2	Spectral response	101
4.3.3	Time response measurements	101
4.3.4	Intensity modulated spectroscopy	102
	Bibliography	104
5	Improving solar cells by the partial oxidation of Sb_2S_3	107
5.1	Introduction	108
5.2	Materials and methods	109
5.2.1	Preparation of photovoltaic cells	109
5.2.2	Material characterisation	110
5.2.3	Optoelectronic characterisation	111

Contents

5.3	Results and discussion	111
5.3.1	Characterisation of oxidised Sb_2S_3	111
5.3.2	Improved photovoltaic devices with oxidised Sb_2S_3	119
5.3.3	Reduced recombination in oxidised Sb_2S_3 solar cells	124
5.4	Conclusion	129
	Bibliography	130
6	Room temperature deposition of antimony sulfide	135
6.1	Introduction	136
6.2	Materials and methods	137
6.2.1	Solar cell preparation	137
6.2.2	Material characterisation	138
6.2.3	Optoelectronic measurements	139
6.3	Results and discussion	139
6.3.1	Synthesis of Sb_2S_3 at room-temperature	139
6.3.2	Characterisation of room-temperature deposited Sb_2S_3	141
6.3.3	Enhanced photovoltaics with room-temperature Sb_2S_3	147
6.3.4	Optimising devices with room-temperature Sb_2S_3	149
6.4	Conclusion	155
	Bibliography	158
7	SbSI micro-crystals for fast response photodetectors	161
7.1	Introduction	162
7.2	Materials and methods	163
7.2.1	Photodetector fabrication	163
7.2.2	Material characterisation	164
7.2.3	Optoelectronic measurements	165
7.3	Conversion of Sb_2S_3 to SbSI in a SbI_3 vapour	165
7.3.1	The conversion process	166
7.3.2	Characterisation of SbSI films	169
7.4	Fabrication process of SbSI photodetectors	172

7.5	Optoelectronic characterisation of SbSI photodetectors	175
7.5.1	Photodetectors under voltage bias	177
7.5.2	Photodetectors in self-powered mode	184
7.5.3	Symmetric photodetectors	187
7.6	Conclusion	188
	Bibliography	191
Conclusion and outlook		195

Acknowledgements

First, I would like to thank my supervisor Ullrich Steiner for giving me the possibility to do the research in his group. I thank Ulli for providing a lot of freedom, for his openness and for his uncomplicated way of getting things sorted. Even after leaving for Switzerland, he made sure that we, the remaining students, could continue our work without any problems and he supported me whenever necessary.

I owe gratitude to Jeremy Baumberg, who took over the official role of being my supervisor after Ullrich Steiner left Cambridge.

Further, I want to acknowledge everyone who directly contributed to the work in this thesis. Sandeep Pathak introduced me to the world of chemistry and pointed me towards antimony sulfide as an interesting material for solar cells when I first arrived in the group. However, I am still not a chemist and I am really grateful that Bart Roose was always there to give advice with his expertise. Further I thank Aditya Sadhanala for his help with PDS measurements, Yana Vaynzof and Adam Brown for the XPS experiments.

I want to express special thanks to the research group of Prof. Sang Il Seok at KRICT in Daejeon, South Korea and in particular to Dr. Yong Chang Choi. I thank them for accommodating me during my research stay in their group and sharing their knowledge and resources. I really had a great time with all members of the group and I am grateful for the many positive experiences I made during the four weeks in beautiful South Korea.

When Ullrich Steiner moved to Switzerland just after the first year of my PhD, the Cambridge branch of the TFI group got continuously smaller. Nevertheless, and perhaps for this very reason, there was a strong cohesion of the remaining group. I thank Jonathan

Acknowledgements

Lim, Tobias Wenzel, Raphael Dehmel, James Dolan and Harry Beeson for making the everyday work in the lab fun and providing support whenever I needed it. I also would like to thank all the “old” group members Bodo, Yuan, Michi, Bart, Maik, Pedro, Sven, Silvia, Gen, Allesandro, Ahu, Stefano, Sarah, Pia and Suzanne.

Further, I thank my office mates, especially Johannes, Jerome, Raphael and Toby for providing a nice atmosphere, discussing interesting physics and making the office an enjoyable place.

The whole group of Optoelectronics provided a good working environment and I am grateful that I met many bright and fascinating people from all over the world. I hope we will keep in touch.

I had a great time with the members of the Swiss part of the group from the Adolphe Merkle Institute, with the Nanophotonics group and the Vignolini group, not only during the annual winterschool! I really had a great time with you during talks, presentations, games and on the slopes.

I owe gratitude to the technical and administrative support staff from Optoelectronics and Nanophotonics. Special thanks to Angela Campbell and Anthony Barnett.

The PhD in Cambridge would have not been possible without the financial support from the scholarships I received. Therefore I would like to thank Corpus Christi College Cambridge, the Mott Fund for the Physics of the Environment and the Cambridge Trust.

But foremost I want to thank my family for their unconditional support. It is good to know that you are always there for me. I know it was not easy, especially for my mother and my sister, to let me go to the UK for such a long time. Words cannot express how grateful I am.

At the end, I would like to express appreciation to Kerstin. Thanks a lot for proof-reading my whole PhD thesis. You always were my support in the moments when I needed it most. I am glad you are there!

List of publications

Core publications

K. C. Gödel, B. Roose, A. Sadhanala, Y. Vaynzof, S. K. Pathak, U. Steiner. “Partial oxidation of the absorber layer reduces charge carrier recombination in antimony sulfide solar cells”. *Physical Chemistry Chemical Physics* (2016). DOI: 10.1039/c6cp07559B.

K. C. Gödel and U. Steiner. “Thin film synthesis of SbSI micro-crystals for self-powered photodetectors with rapid time response”. *Nanoscale* 8 35 (2016), pp. 15920-15925. DOI: 10.1039/c6nr04759A

K. C. Gödel, Y.C. Choi, B. Roose, A. Sadhanala, H. J. Snaith, S. I. Seok, U. Steiner, S. K. Pathak. “Efficient room temperature aqueous Sb_2S_3 synthesis for inorganic–organic sensitized solar cells with 5.1% efficiencies”. *Chemical Communications* 51 41 (2015), pp. 8640-8643. DOI: 10.1039/c5cc01966D

Other publications

B. Zhao, M. Abdi-Jalebi, M. Tabachnyk, H. Glass, V.S. Kamboj, W. Andrew Nie, J. Pearson, Y. Puttisong, K. C. Gödel, H.E. Beere, D.A. Ritchie, A.D. Mohite, S.E. Dutton, R.H. Friend, A. Sadhanala. “High Open-Circuit Voltages in Tin-Rich Low-Bandgap Perovskite-Based Planar Heterojunction Photovoltaics”. *Advanced Materials* (2016).

List of publications

B. Roose, J.-P. Correa Baena, K. C. Gödel, M. Grätzel, A. Hagfeldt, U. Steiner, A. Abate. “Mesoporous SnO₂ electron selective contact enables UV-stable perovskite solar cells”. *Nano Energy* 30 (2016).

B. Roose, K. C. Gödel, S. Pathak, A. Sadhanala, J.P. Correa Baena, B.D. Wilts, H.J. Snaith, U. Wiesner, M. Grätzel, U. Steiner, A. Abate. “Enhanced Efficiency and Stability of Perovskite Solar Cells Through Nd-Doping of Mesostructured TiO₂”. *Advanced Energy Materials* 6 2 (2016).

S. Pathak, A. Sepe, A. Sadhanala, F. Deschler, A. Haghighirad, N. Sakai, K. C. Gödel, S.D. Stranks, N. Noel, M. Price, S. Hüttner, N.A. Hawkins, R.H. Friend, U. Steiner, H.J. Snaith. “Atmospheric Influence upon Crystallization and Electronic Disorder and Its Impact on the Photophysical Properties of Organic–Inorganic Perovskite Solar Cells”. *ACS Nano* 9 3 (2015), pp. 2311-2320.

M.L. Böhm, T.C. Jellicoe, J.P.H. Rivett, A. Sadhanala, N.J.L.K. Davis, F.S.F. Morgenstern, K. C. Gödel, J. Govindasamy, C.G.M. Benson, N.C. Greenham, B. Ehrler. “Size and Energy Level Tuning of Quantum Dot Solids via a Hybrid Ligand Complex”. *The Journal of Physical Chemistry Letters* 6 17 (2015), pp. 3510-3514.

A. Sadhanala, S. Ahmad, B. Zhao, N. Giesbrecht, P.M. Pearce, F. Deschler, R.L.Z. Hoyer, K. C. Gödel, T. Bein, P. Docampo, S.E. Dutton, M.F.L. De Volder, R.H. Friend. “Blue-green color tunable solution processable organolead chloride–bromide mixed halide perovskites for optoelectronic applications”. *Nano Letters* 15 9 (2015), pp. 6095-6101.

A. Sadhanala, F. Deschler, T.H. Thomas, S.E. Dutton, K. C. Gödel, F.C. Hanusch, M.L. Lai, U. Steiner, T. Bein, P. Docampo, D. Cahen, R.H. Friend. “Preparation of single-phase films of CH₃NH₃Pb(I_{1-x}Br_x)₃ with sharp optical band edges”. *The Journal of Physical Chemistry Letters* 5 15 (2014), pp. 2501-2505.

S.K. Pathak, A. Abate, P. Ruckdeschel, B. Roose, K. C. Gödel, Y. Vaynzof, A. Sadhanala, S.-I. Watanabe, D.J. Hollman, N. Noel, A. Sepe, U. Wiesner, R. Friend, H.J. Snaith, U. Steiner. “Performance and Stability Enhancement of Dye-Sensitized and Perovskite Solar Cells by Al Doping of TiO_2 ”. *Advanced Functional Materials* 24 38 (2014), pp. 6046-6055.

A. Ritter, P. Bartl, F. Bayer, K. C. Gödel, W. Haas, T. Michel, G. Pelzer, J. Rieger, T. Weber, A. Zang, G. Anton. “Simulation framework for coherent and incoherent X-ray imaging and its application in Talbot-Lau dark-field imaging”. *Optics Express* 22 19 (2014), pp. 23276-23289.

A. Ritter, G. Anton, F. Bayer, K. C. Gödel, G. Pelzer, J. Rieger, T. Weber, A. Zang, T. Michel. “Simulation of dark-field imaging of micro-calcifications in human breast tissue with X-ray Talbot-Lau interferometry”. *Journal of Instrumentation* 9 5 (2014), C05028.

A. Ritter, F. Bayer, J. Durst, K. C. Gödel, W. Haas, T. Michel, J. Rieger, T. Weber, L. Wucherer, G. Anton. “Simultaneous maximum-likelihood reconstruction for x-ray grating based phase-contrast tomography avoiding intermediate phase retrieval”. *arXiv* (2013), arXiv:1307.7912.

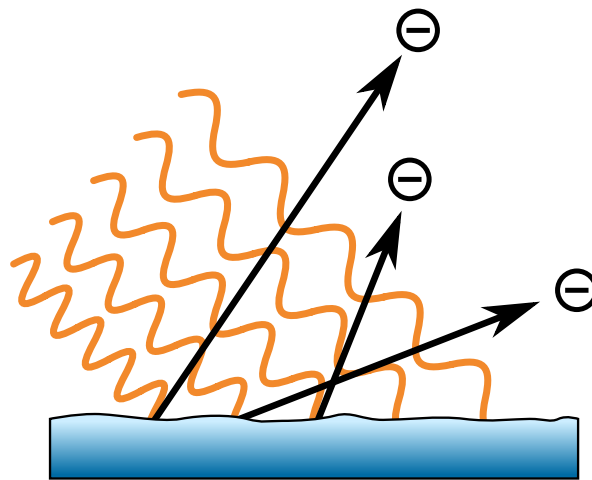
List of abbreviations

ALD	Atomic layer deposition
CBD	Chemical bath deposition
DI	Deionized
DSSC	Dye-sensitised solar cell
EQE	External quantum efficiency
ETA	Extremely thin absorber
FF	Fill factor
FTO	Fluorine-doped tin oxide
FWHM	Full width at half maximum
HTM	Hole transport material
IMPS	Intensity modulated photocurrent spectroscopy
IMVS	Intensity modulated photovoltage spectroscopy
LED	Light emitting diode
P3HT	Poly(3-hexylthiophene-2,5-diyl)
PCBM	Phenyl-C61-butyric acid methyl ester
PCPDTBT	. . .	Poly[2,6-(4,4-bis-(2-ethylhexyl)-4H-cyclopenta[2,1-b;3,4-b']dithiophene)- alt-4,7(2,1,3-benzothiadiazole)]
PDS	Photothermal deflection spectroscopy
RT	Room temperature

List of abbreviations

SEM	Scanning electron microscopy
UHV	Ultra-high vacuum
UV	Ultra-violet
UV-vis	Ultra-violet-visible
XPS	X-ray photoelectron spectroscopy
XRD	X-ray diffraction

Interaction of light and matter



“The new device [...] made of strips of silicon [...] may mark the beginning of a new era, leading to the realisation of one of mankind’s most cherished dreams – the harnessing of the almost limitless energy of the sun for the uses of civilisation.”

New York Times, 26th April 1954

In 1954, a newspaper article titled “Vast Power of the Sun is Tapped by Solar Battery Using Sand Ingredient” appeared in the New York Times, reporting on the first practical optoelectronic device converting sunlight into useful amounts of electricity [1]. This solar cell, developed by G. Pearson, C. Fuller and D. Chapin from the AT&T Bell Laboratories relied on mono-crystalline silicon [2]. Today, more than 60 years later, crystalline silicon still dominates the market of solar cells. More than 90 % of the global annual photovoltaic production are covered by single- and multi-crystalline silicon [3].

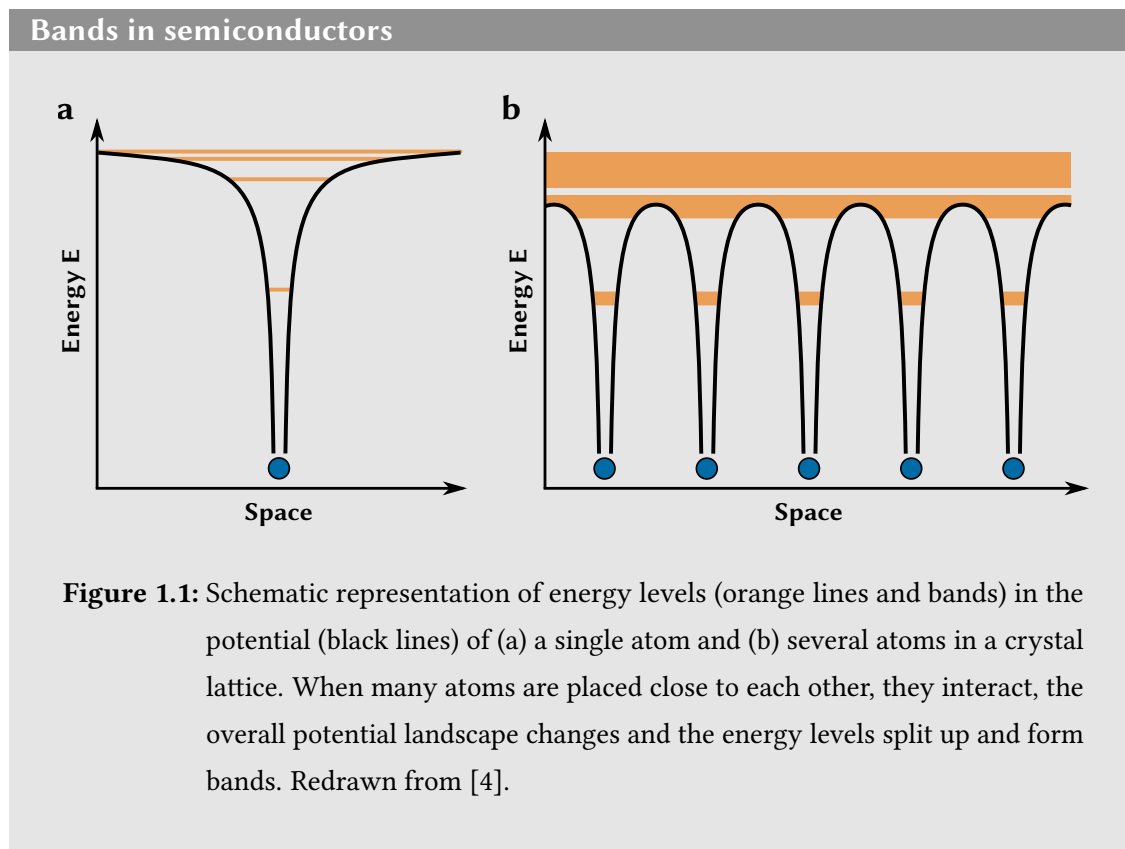
Yet, the interaction of light with matter does not only govern the basic working principle of a solar cell. It also applies to other optoelectronic applications, such as photodetectors. Therefore, crystalline silicon quickly found applications beyond its use in solar cells, marking the beginning of what we now call the “silicon era”. While scientific investigations to optimise and improve the silicon based technologies are still ongoing, new areas of interest emerged in optoelectronic research. Not least because of scientific curiosity, new solution-processable materials with the prospect of cheap and easy manufacturing opened up new ways for the advance of future technologies.

In this thesis such new materials for two distinct optoelectronic applications, solar cells and photodetectors, are explored.

In the following sections of this chapter, the fundamental physical framework for optoelectronic applications is introduced. Briefly, the band theory of matter of semi-conductors is described, including the concepts of energy bands, the band gap and the distribution of electrons within these bands. Then, the photoelectric effect, the dominant interaction of visible light with semiconductors, is introduced.

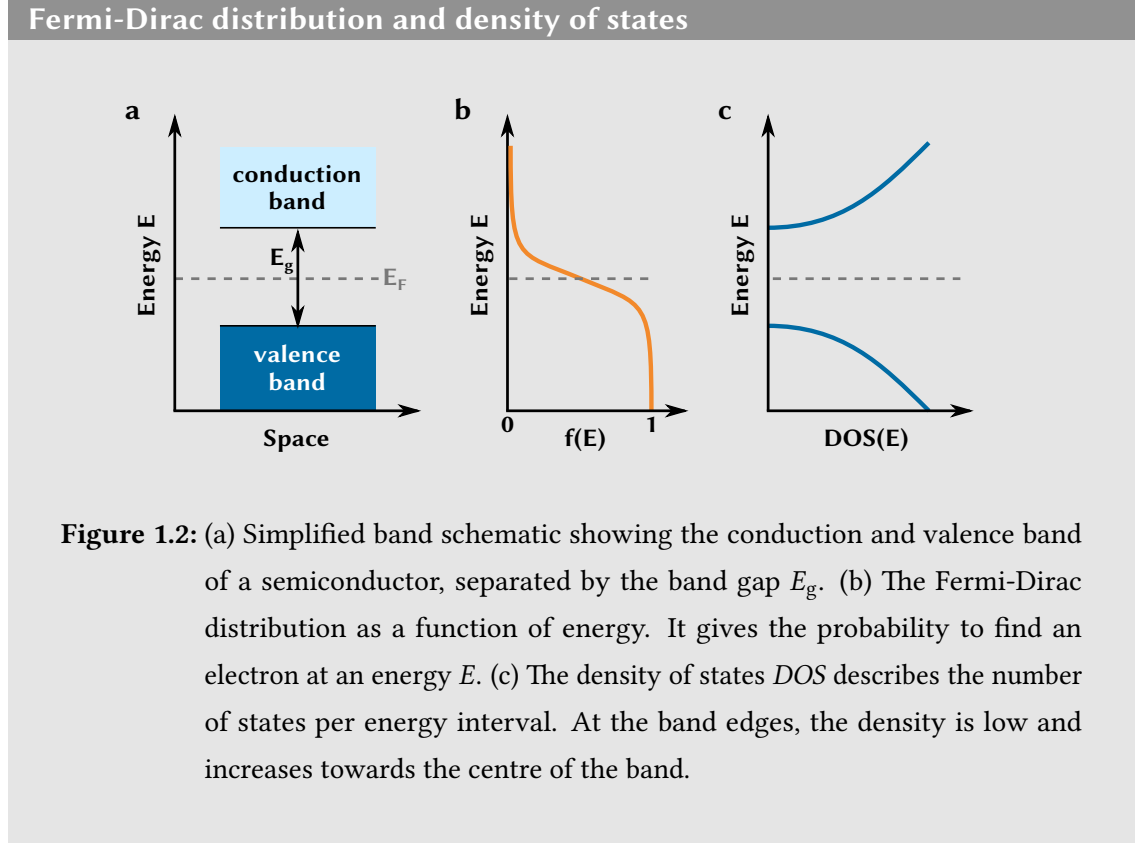
1.1 Band theory of semiconductors

Optoelectronic applications, including those studied in this thesis, combine electronics and optics. On one hand, metals have excellent properties for the conduction of charges, but do not allow light to penetrate. On the other hand, dielectric materials, which are often used for optical applications, cannot carry electric currents [4]. Semiconductors bridge the gap between these two classes of materials and offer favourable electrical and optical properties.



In semiconductors, current is carried either by free electrons in the conduction band or by positive charges in the valence band. These so called holes describe the lack of a bound electron in the atomic lattice of the material. The conduction band and the valence band are separated by an energy gap E_g , the band gap. The band structure of a material results from the periodic assembly of the atoms, which are often arranged in a crystal

lattice. The energy levels of a single atom are quantised with discrete energy values. When there are many atoms, their interaction leads to the splitting of these levels, they become energy bands. The transition from discrete energy levels for single atoms to energy bands in a crystal lattice is schematically illustrated in Figure 1.1.



The energetically highest band filled with electrons is called the valence band, the lowest empty band is named conduction band. Whether a band at a certain energy E is filled or not is given by the Fermi-Dirac probability function

$$f(E) = \frac{1}{\exp\left(\frac{E-E_F}{k_B T}\right) + 1}, \quad (1.1)$$

where E_F , the point of symmetry of the distribution, is called the Fermi level and $k_B T$ is the thermal energy. Depending on where the Fermi-level is located, one describes a material as a metal, as a semiconductor or as an insulator. For a metal, the Fermi-level lies within a band, and thus there are always charge carriers available to conduct electric

current. In insulators and semiconductors, E_F lies within the band gap and the valence band is completely filled, whereas the conduction band is empty at temperatures around room temperature. Semiconductors and insulators are differentiated by the width of the band gap. Semiconductors typically have a band gap of up to $E_g = 3$ eV, the band gap of wide band gap semiconductors and insulators is larger. The Fermi-Dirac distribution is shown in Figure 1.2 b. Quite often, the electronic bands in semiconductors are illustrated in a simplified manner as shown in Figure 1.2 a. However, one needs to keep in mind that the number of possible states do not have a uniform energy distribution. The density of states $DOS(E)$, or rather a section close to the band edges, is shown in Figure 1.2 c

For optoelectronic applications, semiconductors must have band gap values similar to the energy of the light they interact with. In this thesis, photons from the UV, visible and near-infra-red part of the electromagnetic spectrum are of interest. The energy of a photon E_{ph} is dependent on the wavelength λ according to

$$E_{ph} = \frac{hc}{\lambda} \approx \frac{1240 \text{ nm eV}}{\lambda}, \quad (1.2)$$

where c is the speed of light and h the Planck constant. Photons from the for human eyes visible part of the electromagnetic spectrum (390 – 700 nm [5]) thus have energies on the order of $E_{ph} = 1.8 - 3.1$ eV.

1.2 Photoelectric effect

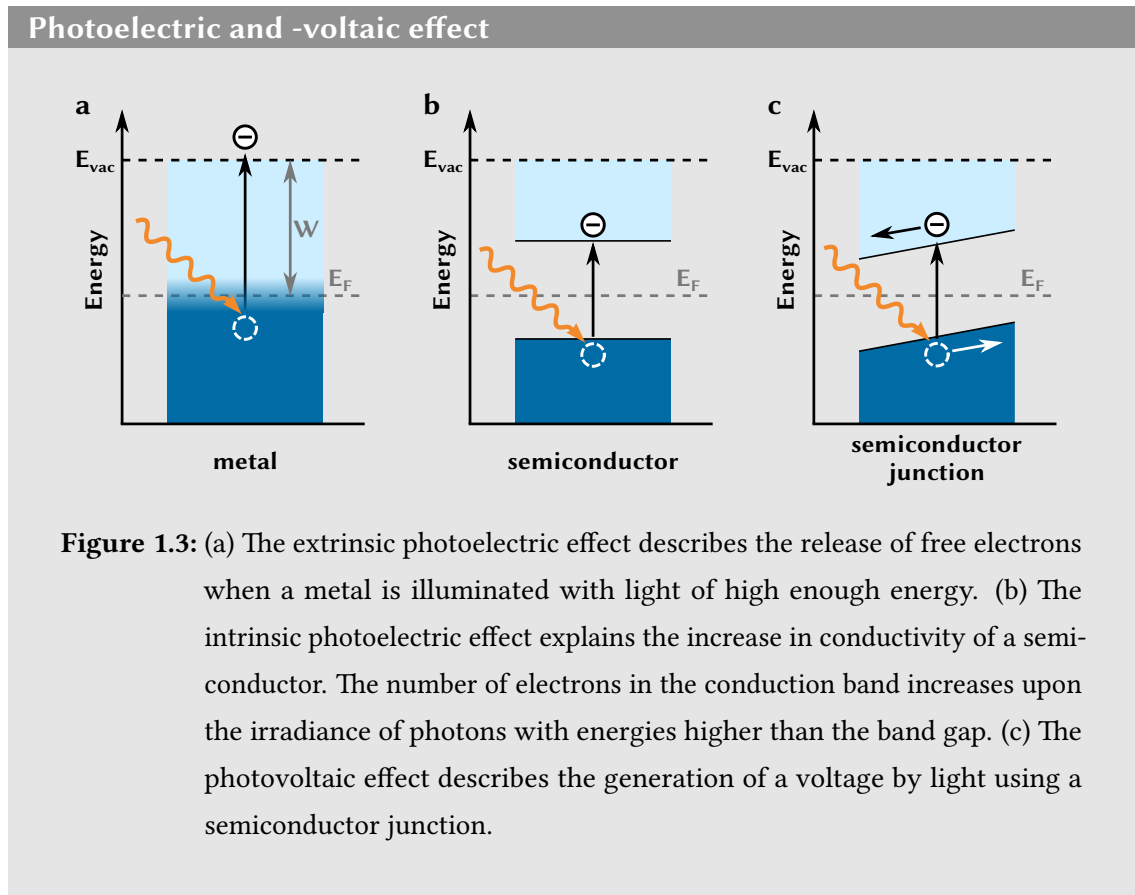
At the energies of visible light, elastic scattering, i.e. Thomson and Rayleigh scattering, and the photoelectric effect are dominant [6]. For work presented here, the photoelectric effect is of particular interest as it forms the basis for the functionality of the optoelectronic applications in this thesis.

Here, only a short introduction to the photoelectric effect is given. The detailed theoretical explanation was presented by Albert Einstein in his famous article from 1905 [7]. The extrinsic photoelectric effect describes the release of electrons from a metallic surface upon irradiation of light. Whether free electrons are produced or not is

dependent on the wavelength of the light, not on its intensity. Thus this effect illustrates the quantum nature of light as it depends on the energy of the individual photons. The kinetic energy E_{kin} of the dislodged electron is given by

$$E_{\text{kin}} = \frac{hc}{\lambda} - W, \quad (1.3)$$

where W is the work function of the metal and $\frac{hc}{\lambda}$ is the energy of the photon with wavelength λ . The extrinsic photoelectric effect is schematically shown in Figure 1.3 a.



The intrinsic photoelectric effect is also called photoconductive effect. It describes the increase of electrical conductivity in a semiconductor upon illumination and it is illustrated in Figure 1.3 b. When photons with energies exceeding the band gap E_g are absorbed by the semiconductor, they can promote electrons from the valence band into the conduction band. These electrons are then available to carry electrical current in the

conduction band (or analogously holes in the valence band) and thus the conductivity of the semiconducting material increases. For most photodetectors, this is the fundamental effect underlying their working principle (see also Chapter 2 and Chapter 7).

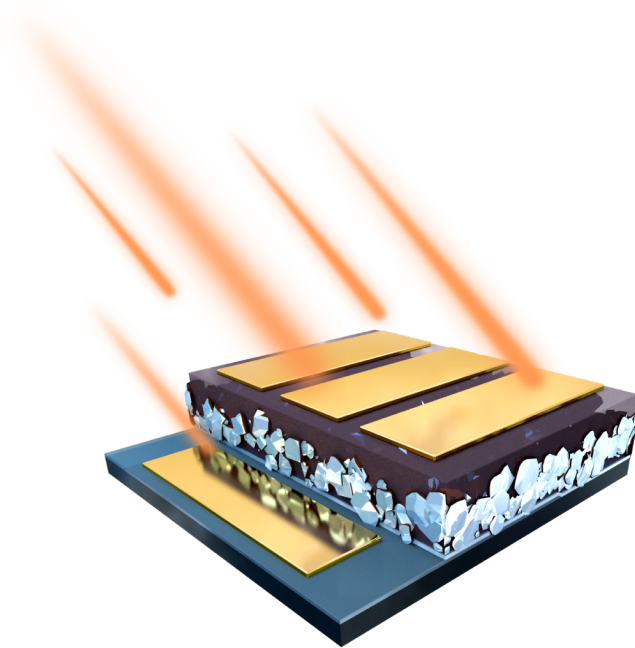
To explain the functional principle of solar cells in Chapter 5 and Chapter 6, one needs to understand the photovoltaic effect. It is closely related to the intrinsic photoelectric effect and it is schematically shown in Figure 1.3 c. Prerequisite for the photovoltaic effect is an asymmetry in the energy band schematic. This can be realised in various ways, for instance via a junction of two semiconductors or a metal and a semiconductor. The most prominent example is the junction of differently doped species of the same semiconductor (p-n junction). When an electron is excited from the valence to the conduction band, the free electron and the hole are separated by the built-in electric field, caused by the asymmetry of the energy bands. Hence, even without an external bias, a non-zero net-current can flow.

Bibliography

- [1] “Vast Power of the Sun is Tapped by Solar Battery Using Sand Ingredient. Special to The New York Times”. *New York Times* (**1954**), pp. 1, 11.
- [2] D. M. Chapin, C. S. Fuller, and G. L. Pearson. “A New Silicon p-n Junction Photocell for Converting Solar Radiation into Electrical Power”. *Journal of Applied Physics* 25.5 (**1954**), pp. 676–677. DOI: <http://dx.doi.org/10.1063/1.1721711>.
- [3] S. Philipps and W. Warmuth. *Photovoltaics Report*. Fraunhofer Institute for Solar Energy Systems and PSE AG, **2016**.
- [4] J. Piprek. *Semiconductor Optoelectronic Devices: Introduction to Physics and Simulation*. Academic Press, **2013**.
- [5] A. Stockman and L. T. Sharpe. “The Spectral Sensitivities of the Middle- and Long-Wavelength-Sensitive Cones Derived from Measurements in Observers of Known Genotype”. *Vision Research* 40.13 (**2000**), pp. 1711–1737. DOI: 10.1016/S0042-6989(00)00021-3.
- [6] H. Bichsel, D. Groom, and S. Klein. “Passage of Particles through Matter, Section 27, Review of Particle Physics”. *Physics Letters B* 592.1-4 (**2004**), pp. 1–1109. DOI: 10.1016/j.physletb.2004.06.001.
- [7] A. Einstein. “Über einen die Erzeugung und Verwandlung des Lichtes betreffenden heuristischen Gesichtspunkt”. *Annalen der Physik* 17 (**1905**), pp. 132–148.

Chapter 2

Optoelectronic devices



The term “optoelectronics” condenses a large field of electronic components which detect, emit or control electromagnetic radiation in or close to the visible spectrum. This chapter describes the basic principles of optoelectronic devices. It builds on the fundamentals laid in the previous chapter and explains the interaction of light and semiconductors particularly with regard to functional devices and their application. For the scope of this thesis, the focus will be put on photodetectors for sensing light signals and solar cells for light to power conversion.

2.1 Photodetectors

Photodetectors are electronic devices which convert light signals into electrical signals. Normally, the electric signal should depend on the light intensity. This section gives a brief overview over the detection mechanism of different types of photodetectors and introduces the performance metrics for light sensing applications, as they become important for the characterisation and evaluation of SbSI micro-crystal photodetectors in Chapter 7.

2.1.1 Mechanisms of detection

Various types of photodetectors exist for diverse purposes and they utilise different physical mechanisms for the detection process. Broadly, photodetectors can be classified into two groups: optoelectronic “quantum” detectors and thermal detectors [1]. Thermal detectors measure the increase in heat, when electromagnetic radiation is absorbed. The rise in temperature can then be converted into an electrical signal using the thermoelectric, pyroelectric or thermoresistive effect. For the scope of this thesis, the other group, optoelectronic detectors, are of greater importance. The photodetector, we humans are most familiar with is our eye. The photoreceptor cells, the rods and cones in the retina, use a photochemical reaction cascade mechanism to convert light signals into electrical signals which can then be processed by the brain. Most photodetectors in

science and technology make use of the photoelectric or the photovoltaic effect to detect light signals. Photomultiplier tubes use the extrinsic photoelectric effect: Electrons are emitted from a metal or semiconductor electrode upon irradiation. This electrical signal is then amplified using secondary emission in a cascade of electrodes. The intrinsic photoelectric effect, also called photoconductivity, can be used in photoresistors. When photons with energies above the band gap of the semiconductor used in the photoresistor are absorbed, electrons are promoted from the valence band into the conduction band. Thus, the carrier concentration of free charges increases and the resistance of the photoresistor decreases, which can directly be measured in an external electrical circuit. Even though the theoretical explanation was not given until Albert Einstein's work in 1905, the photoconductivity of selenium was already studied by Willoughby Smith as early as 1873 [2, 3]. His work can be seen as the foundation of the technological conversion of light signals to electrical signals.

2.1.2 Performance metrics

Depending on the area of application of a photodetector, different properties like a high sensitivity, a rapid time-response or high linearity between input and output signal are important [4]. To determine the performance of photodetectors, a range of figures-of-merit are used to compare different devices. They are described in the following paragraphs.

Responsivity

The responsivity R of a photodetector describes the ratio of the electric output to the optical input. It is sometimes also qualitatively referred to as the sensitivity of the device [5]. The responsivity is defined as

$$R = \frac{I}{\Phi_e}, \quad (2.1)$$

where I is the output current and Φ_e the radiant power of the optical input [4]. The responsivity is thus measured in amperes per watt. If I_{light} is the current signal of the

photodetector illuminated with an irradiance E_e and I_{dark} denotes the dark current of the detector which has an active area A , the responsivity can be written as

$$R = \frac{I_{\text{light}} - I_{\text{dark}}}{E_e A} . \quad (2.2)$$

If there is a regime with a linear relation between the optical input and the output current of a photodetector, the responsivity is constant within that range of input radiant power. The responsivity is a measure of the gain between output and input signals, however it cannot be used to describe the capability of the detector to measure small signals [6].

Noise equivalent power and specific detectivity

For the detectability of small signals the noise equivalent power NEP is a suitable figure-of-merit [1]. The NEP is the input power needed to generate a signal which is equal to the root-mean-square noise of the device [5]. More precisely, the noise equivalent power is defined as the optical input signal which is needed to measure an electric signal with a signal-to-noise ratio of $SNR = 1$ referring to a bandwidth of 1 Hz [7]. The noise equivalent power is measured in units of $\text{W}/\sqrt{\text{Hz}}$. A smaller NEP value is favourable for the detectability of small optical input powers. Thus, the detectivity D is defined as the inverse of the noise equivalent power,

$$D = \frac{1}{NEP} . \quad (2.3)$$

As the noise is often dependent on the square root of the detector area A and the bandwidth Δf [5], the specific detectivity D^* is defined as

$$D^* = D \sqrt{A \Delta f} = \frac{\sqrt{A \Delta f}}{NEP} . \quad (2.4)$$

The specific detectivity is measured in $\text{cm}\sqrt{\text{Hz}}/\text{W}$ or Jones (1 Jones = $1 \frac{\text{cm}\sqrt{\text{Hz}}}{\text{W}}$), named after Robert Clark Jones who introduced the specific detectivity [8]. Depending on the origin of noise, it does not always scale with the square root of A and Δf and one has to be careful with the comparison of photodetector performance using the specific detectivity D^* [1]. D^* can be related to the responsivity by considering the relation

$NEP = \frac{I_n}{R}$, where I_n is the root-mean-square noise current over the full bandwidth [1]. The specific detectivity can then be written as

$$D^* = \frac{R\sqrt{A\Delta f}}{I_n}. \quad (2.5)$$

The expression for the specific detectivity D^* can be simplified under the assumption that the noise is dominated by the shot noise of the dark current I_{dark} of the photodetector. The specific detectivity can then be written as

$$D^* = \frac{R\sqrt{A}}{\sqrt{2e I_{\text{dark}}}}, \quad (2.6)$$

where e is the elementary charge of the electron ($e = 1.60217662 \cdot 10^{-19}$ C) [9].

Time response

For applications where the response speed of a photodetector to variations in the input signal is important, it is necessary to find parameters describing the time characteristics of these changes. A common method to determine the time response of a photodetector is to measure the current output of the device for a square pulse of radiant input power. The rise time τ_r is defined as the time the photocurrent needs to increase from 10 % to 90 % of the final output signal. The fall time τ_f is defined accordingly as the time for a photocurrent to fall from 90 % to 10 % [4]. The definitions of the time response characteristic values τ_r and τ_f are illustrated in Figure 2.1. The time response of a photodetector depends on properties like the device geometry, the used semiconducting materials, the bias voltage, the input radiant power and the external circuit [4]. In general, three different effects contribute to the rise and fall time characteristics [10]: the charge collection or drift time τ_c , the diffusion time τ_d and the RC time constant τ_{RC} . One can connect these time constants to a combined value τ [4]:

$$\tau = \sqrt{\tau_c^2 + \tau_d^2 + \tau_{RC}^2}. \quad (2.7)$$

If the diffusion of charge carriers is not dominant, as e.g. for simple ohmic photoconductors, rise time and fall time are equal $\tau = \tau_r = \tau_f$.

Rise and fall time of a photodetector

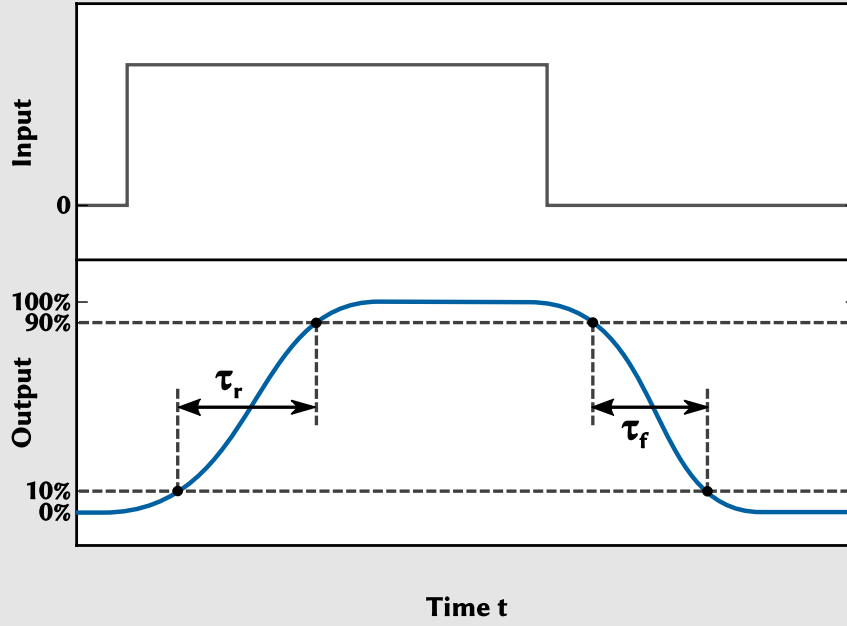


Figure 2.1: The photocurrent output of a photodetector (bottom, blue line) for a square pulse of incident radiant power (top, grey line). The rise time τ_r (fall time τ_f) is the signal increase (decrease) from 10 % (90 %) to 90 % (10 %) of the maximum output signal.

The charge collection time τ_c is dependent on the external bias voltage V_b , the charge carrier mobility μ and the distance d which the charges have to travel. The charge collection time can be expressed as [4]

$$\tau_c = \frac{d^2}{\mu V_b} . \quad (2.8)$$

The RC time constant τ_{RC} is determined by the capacitance C_p and the internal resistance R_p of the photodetector. The higher these two values are, the slower is the charging or discharging process and thus the higher the time response.

As the signal (e.g. the current) of (dis-)charging a RC circuit can be represented using an

exponential function, the RC time constant τ_{RC} can be written as [4]

$$\tau_{RC} = (\ln 90 \% - \ln 10 \%) \cdot R_p C_p \approx 2.2 R_p C_p . \quad (2.9)$$

2.2 Solar cells

From a physicist's point of view the basic principle of a solar cell is not different from a photodetector - both devices convert electromagnetic radiation to electricity. However, the technical requirements are different or rather more specific. A solar cell has to convert as much power as possible from solar radiation to usable electrical power, whereas other properties like the response speed are of less importance.

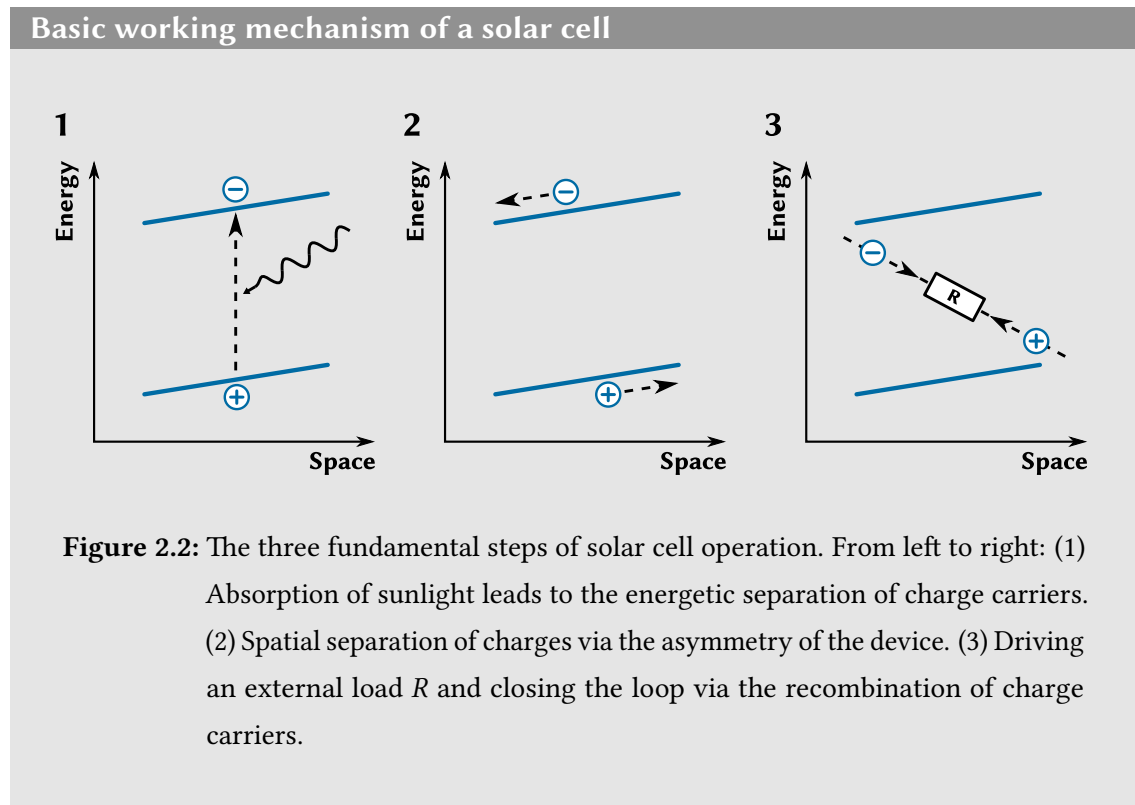
In this section, the basic working mechanism of a solar cell is introduced and the typical parameters which characterise photovoltaic cells are explained. Then, the theoretical efficiency limit are addressed and the physical limits of the conversion process from solar radiation to electricity are deduced. Finally, the concept of sensitised solar cells is discussed, as this type of photovoltaic device is examined in Chapter 5 and Chapter 6.

2.2.1 Basic working mechanism

As discussed earlier in Chapter 1, the photoelectric effect describes the energetic separation of charge carriers when light with sufficient energy to overcome the band gap is absorbed by a semiconducting material. The photovoltaic effect requires a spacial separation of the charge carriers before they recombine. This implies that a photovoltaic device needs to exhibit an asymmetry that enables this spatial separation [11]. This can be achieved in various ways: Using a p-n junction of a contrastingly doped semiconductor, two different semiconductors in a heterojunction or a semiconductor and one or more metals forming Schottky junctions. The asymmetry leads to the formation of a potential difference which can drive a current in an external circuit. Current and voltage are both necessary to provide an electric power which can drive an external load. The basic

working mechanism of a photovoltaic cell can be described as three processes, which are also illustrated in Figure 2.2:

1. Absorption of photons from the solar spectrum in a semiconductor. This leads to the energetic separation of electrons and holes.
2. Spatial separation of the charge carriers via an asymmetry in the device architecture.
3. Release of the energy driving a load in an external circuit. This enables the recombination of the charge carriers to close the electrical circuit.



2.2.2 Characterising solar cells

This section introduces the parameters which are important for the characterisation of photovoltaic devices.

The equivalent circuit of a solar cell

A solar cell can be modelled as a power source in a simple electric circuit, which can be switched on by exposing it to light. More specifically, the solar cell should be treated as a current source, as it delivers a constant current upon illumination, whereas the voltage has a strong dependence on the external load [11]. In the dark, the earlier discussed asymmetry of photovoltaic devices leads to a diode-like behaviour. Thus, the electric properties of a solar cell can be represented by a basic equivalent circuit consisting of a current source and a diode as shown in Figure 2.3 a. With this electronic representation of a solar cell, one can now express the current I of the device as [12]

$$I(V, \Phi_e) = I_{\text{ph}}(\Phi_e) - I_{\text{dark}}(V) . \quad (2.10)$$

Here, $I_{\text{ph}}(\Phi_e)$ is the photocurrent, which is dependent on the radiant power Φ_e of the illumination and $I_{\text{dark}}(V)$, the voltage dependent dark current. At this stage, it is worth to note that the usual sign convention for electronic devices is used in this thesis, such that the power of the solar cell under operation is negative. In the field of solar cell research, both conventions are found and I - V -curves are typically shown in the first rather than the fourth quadrant, i.e. the negative current $-I$ is plotted versus the voltage V , as shown in Figure 2.3 b. Using the Shockley diode equation [13], the current I of the solar cell can be written as

$$I(V, \Phi_e) = I_{\text{ph}}(\Phi_e) - I_0 \left[\exp \left(\frac{eV}{k_B T} \right) - 1 \right] , \quad (2.11)$$

where I_0 is a current constant, e the charge of the electron and $k_B T$ the thermal energy. This function leads to the typical I - V -characteristic, which is shown in Figure 2.3 b. It is discussed in more detail in the following.

The solar cell as a diode and current source

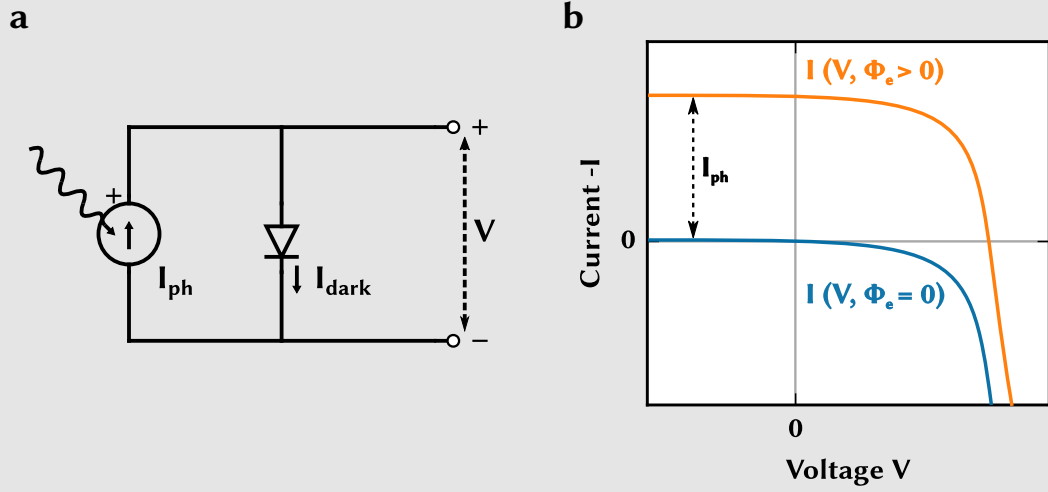


Figure 2.3: (a) The basic equivalent circuit of a photovoltaic cell. An illumination dependent current source (I_{ph}) is connected to a diode which defines the dark current I_{dark} in parallel. (b) The I - V curve of a solar cell with the basic equivalent circuit under illumination (orange line) and in the dark (blue line).

Short circuit current and open circuit voltage

Figure 2.4 shows a plot of the current-voltage characteristic of a solar cell under illumination as described by Equation 2.11. Using this illustration, one can explain the most important parameters of photovoltaic devices. The short circuit current I_{sc} is defined as the photocurrent measured if the two contacts of the solar cell are short circuited, i.e. the current at zero potential ($V = 0$),

$$I_{sc} := I(V = 0) = I_{ph}(\Phi_e). \quad (2.12)$$

The short circuit current normally scales linearly with the radiant power Φ_e of the illumination [11].

When the electrodes are not connected, one can measure the so-called open circuit

Typical I-V characteristic of a solar cell

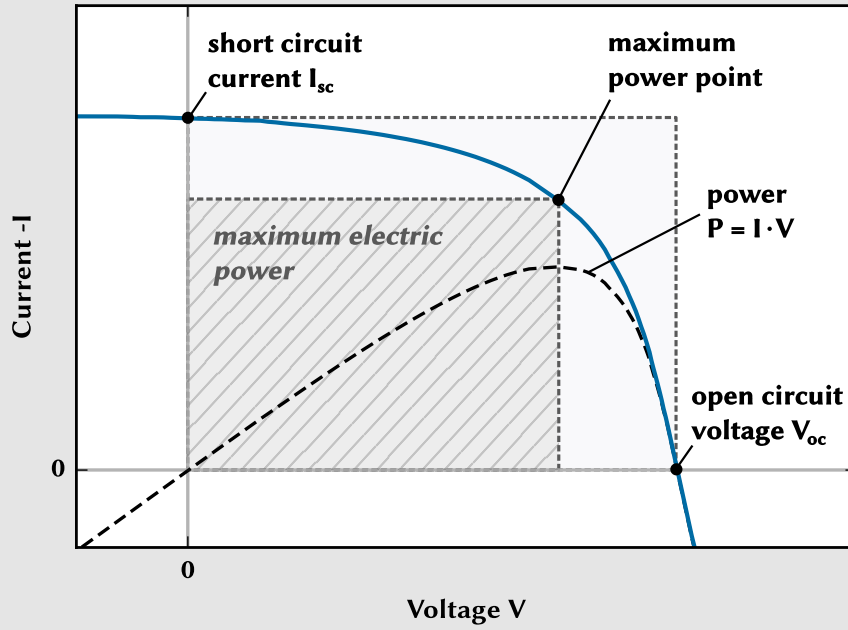


Figure 2.4: Illustration of the current-voltage characteristic of a photovoltaic cell (solid blue line) showing the short circuit current, open circuit voltage and maximum power point. The dashed black line represents the power output $P = I \cdot V$ of the device. The value of the maximum power is the area of the hatched rectangle. The fill factor is the area-ratio of the hatched to the light-shaded rectangle.

voltage V_{oc} . This is the potential when no net current flows ($V(I = 0)$), i.e. the photocurrent and the dark current cancel out ($I = 0 \Rightarrow I_{dark}(V) = I_{ph}(\Phi_e)$). The open circuit voltage V_{oc} can then be written as

$$V_{oc} := V(I = 0) = \frac{k_B T}{e} \ln \left(\frac{I_{ph}(\Phi_e)}{I_0} + 1 \right). \quad (2.13)$$

Thus, V_{oc} depends logarithmically on the radiant power Φ_e of the illumination.

Fill factor

At both points, when the solar cell is operated at short circuit or at open circuit conditions, the power of the device is zero. For voltages $V < 0$ and $V > V_{oc}$, a solar cell consumes electrical power. Hence, the operation regime for a photovoltaic cell as a power source lies between $0 < V < V_{oc}$. The graph of the power curve in Figure 2.4, illustrates that the electrical power $P(V) = I \cdot V$ has a maximum. The current-voltage pair (V_{mp}, I_{mp}) where P has its maximum value $P_{max} = V_{mp}I_{mp}$ is called the maximum power point. The ratio of maximum power and the product of open circuit voltage and short circuit current is called the fill factor FF ,

$$FF := \frac{P_{max}}{V_{oc} \cdot I_{sc}} = \frac{V_{mp} \cdot I_{mp}}{V_{oc} \cdot I_{sc}}. \quad (2.14)$$

The fill factor is a measure for how “rectangular” the I - V curve is. It is dominated by resistive effects.

Power conversion efficiency

The probably most important parameter for the characterisation of solar cells is the power conversion efficiency η . It is the measure for the conversion of the incident radiation power Φ_e to electrical power P . As the solar cell should be operated at its maximum power point, the power conversion efficiency refers to the maximum value P_{max} ,

$$\eta = \frac{P_{max}}{\Phi_e}. \quad (2.15)$$

Using Equation 2.14, the power conversion efficiency can be written as a function of short circuit current, open circuit voltage and fill factor,

$$\eta = \frac{V_{oc} \cdot I_{sc} \cdot FF}{\Phi_e}. \quad (2.16)$$

The parameters in Equation 2.16 are the key parameters for the characterisation of solar cells.

Quantum efficiency

The quantum efficiency of a solar cell is a measure for the contribution of charge carrier pairs to the short circuit current of the solar cell for an incident photon at a given wavelength. Typically, two different types of quantum efficiencies are differentiated: The external quantum efficiency $EQE(\lambda)$ and the internal quantum efficiency $IQE(\lambda)$. The external quantum efficiency, also called incident photon to converted electron ratio ($IPCE$), is defined as the ratio of electrons contributing to the short circuit current I_{sc} and the total number of incident photons with wavelength λ [11]

$$EQE(\lambda) = \frac{I_{sc}(\lambda)}{e \Phi_{e,\lambda}}, \quad (2.17)$$

where e is the elementary charge and $\Phi_{e,\lambda}$ is the spectral flux of the incident light spectrum. The internal quantum efficiency only takes photons into account which are absorbed by the solar cell, hence neglecting optical losses such as reflected $R(\lambda)$ or transmitted photons $T(\lambda)$,

$$IQE(\lambda) = \frac{EQE(\lambda)}{R(\lambda)T(\lambda)}. \quad (2.18)$$

The total short circuit current I_{sc} of a photovoltaic device can be expressed in terms of the EQE as

$$I_{sc} = e \int \Phi_{e,\lambda} EQE(\lambda) d\lambda. \quad (2.19)$$

For an conceptually ideal solar cell, the EQE has a value of one for photons with energies above the band gap energy $E > E_g$ ($\lambda < \lambda_g$) and zero for photons with a smaller energy. Figure 2.5 shows an illustrated EQE spectrum (lower plot). The upper graph of the figure shows the spectral irradiance of sunlight after passing through the earth's atmosphere at a solar zenith angle of 48° . This corresponds to 1.5 air masses (AM1.5) and is chosen to represent the yearly average of mid-latitudes [14]. After multiplying the EQE spectrum with the spectral irradiance, the part of the solar spectrum which contributes to the short circuit current is obtained (blue shaded area in Figure 2.5).

EQE of a photovoltaic device

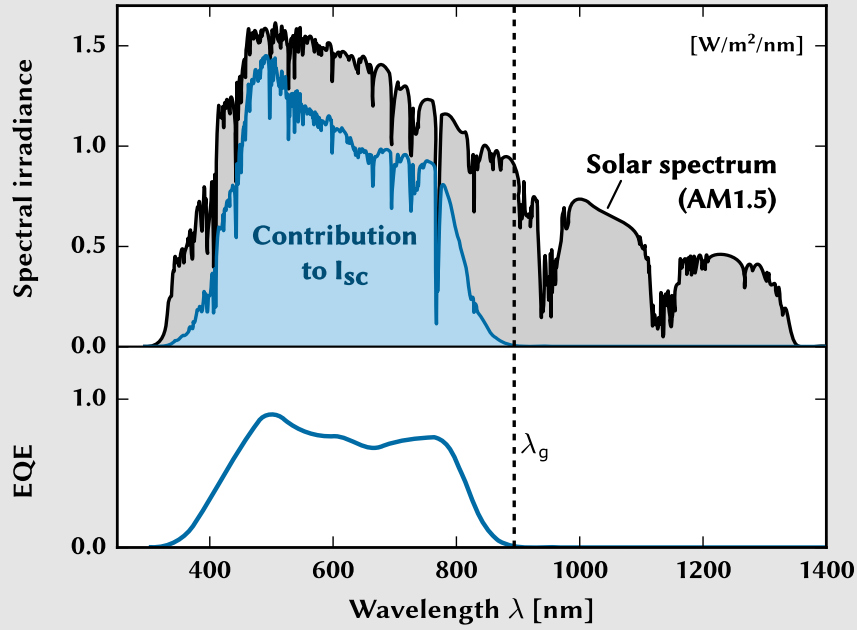


Figure 2.5: Illustration of the external quantum efficiency EQE of a solar cell (bottom graph). The upper plot shows the AM1.5 solar spectrum (grey area) and the part which contributes to the current output of the photovoltaic device (blue area). The spectral irradiance data were taken from [14].

Resistive losses

The diode equation (Equation 2.11) and the equivalent circuit in Figure 2.3 are an idealised representation of a solar cell. In each real photovoltaic device, resistive losses lead to a decay in performance and an alteration of the I - V characteristics. Two loss channels lead to this effect: Contact resistances and the resistivity of the used materials lead to a series resistance R_s , leakage currents lead to an imperfect (finite) shunt resistance R_{sh} [11]. Considering these two resistive loss effects, the equivalent circuit can be redrawn as shown in Figure 2.6. Including R_s and R_{sh} , the diode equation is changed to [11]

$$I(V, \Phi_e) = I_{ph}(\Phi_e) - I_0 \left[\exp \left(\frac{e(V + IR_s)}{k_B T} \right) - 1 \right] - \frac{V + IR_s}{R_{sh}}. \quad (2.20)$$

Equivalent circuit with resistive losses

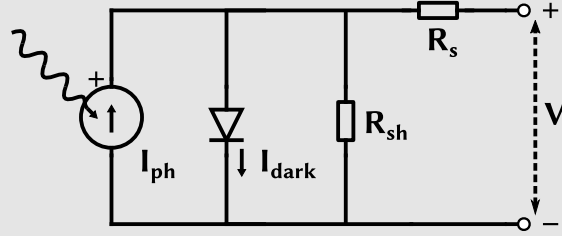


Figure 2.6: The equivalent circuit of a solar cell taking resistive losses into account. Leakage currents are represented by a finite parallel resistance R_{sh} , contact and material resistances via the series resistance R_s .

Both resistive effects lead to a decrease in the fill factor FF . Figure 2.7 schematically shows the change of the I - V curve of a solar cell with increasing series resistance R_s (a) and decreasing shunt resistance R_{sh} (b).

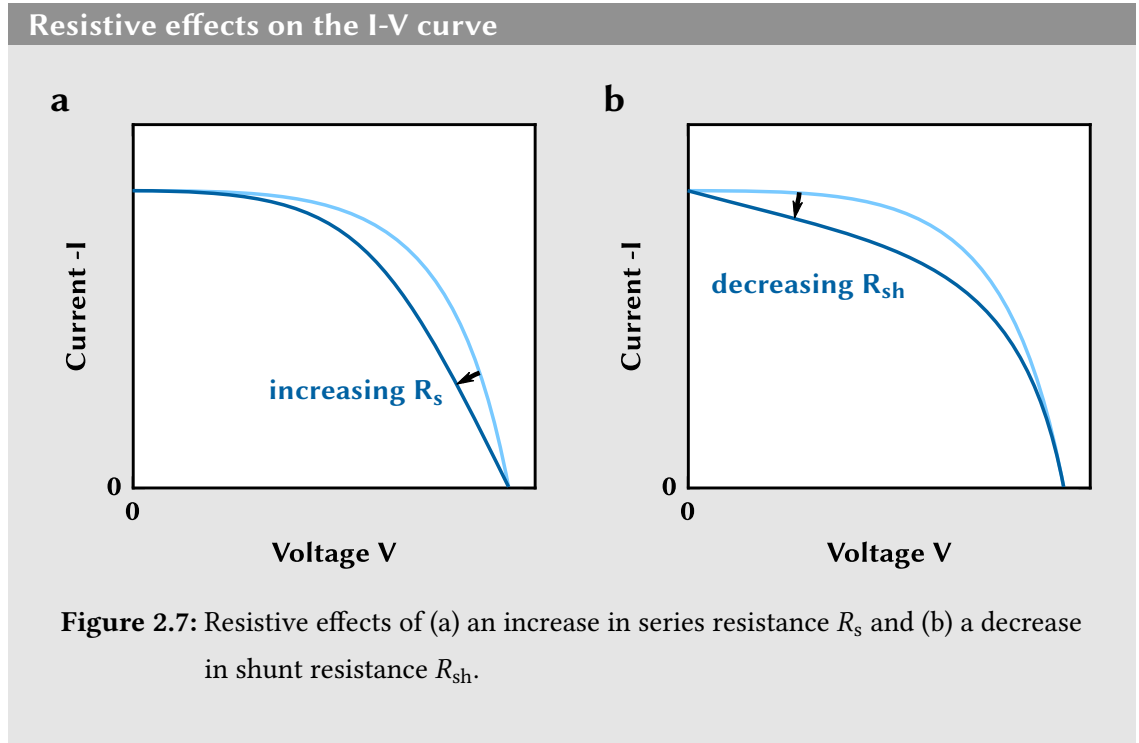
2.2.3 Theoretical efficiency limits

Thermodynamic limit

Thermodynamics set the ultimate upper limit for the conversion efficiency of sunlight to usable power. To estimate the maximum thermodynamic efficiency, the sun as a black body emitter with an temperature of $T_s = 5800$ K can be considered. The solar cell absorbs the light and re-emits radiation as a black body with a temperature T_{sc} . Using Stefan-Boltzmann's law for the emissive power of black bodies, the efficiency of this process is [11]

$$\eta_h = \frac{P_{in}}{P_{out}} = \frac{\sigma_{SB}T_s^4 - \sigma_{SB}T_{sc}^4}{\sigma_{SB}T_s^4} = 1 - \frac{T_{sc}^4}{T_s^4}, \quad (2.21)$$

where σ_{SB} is the Stefan–Boltzmann constant. This approach assumes full concentration of sunlight onto the solar cell. To make use of the solar cell's heat, work needs to be



extracted from it. The most efficient way to do this is the use of a Carnot engine with an efficiency of [15]

$$\eta_C = 1 - \frac{T_0}{T_{sc}}. \quad (2.22)$$

Here, T_0 is the ambient temperature which for a terrestrial solar cell is roughly $T_0 = 300$ K. This leads to a total power conversion efficiency of

$$\eta(T_{sc}) = \eta_h \cdot \eta_C = \left(1 - \frac{T_{sc}^4}{T_s^4}\right) \cdot \left(1 - \frac{T_0}{T_{sc}}\right). \quad (2.23)$$

This function has a maximum value of $\eta_{max} \approx 85\%$ for an optimal solar cell temperature of $T_{sc} \approx 2477$ K. For many applications, lower solar cell temperatures are favourable. Semiconductors are a good choice for solar cells, as they provide reasonably high efficiencies, also at lower temperatures [15].

Shockley-Queisser limit

The efficiency limit for a single semiconductor solar cell was derived in 1961 by William Shockley and Hans Queisser [16]. They used a so called detailed balance calculation, to model the maximum theoretical efficiency for a planar terrestrial solar cell with no light concentration. This approach balances the particle rates (photons or electron-hole pairs). For the calculations, the following assumptions are made:

1. The external quantum efficiency is $EQE(E) = 1$ for energies above the band gap E_g and zero below.
2. The internal and external quantum efficiencies are identical $IQE = EQE$, i.e. no transmission or reflection losses are taken into account.
3. The only recombination mechanism is the radiative recombination of charge-carrier pairs.
4. No resistive losses are considered, all carriers have infinite mobilities.

Here, the calculation of Steven Byrnes is presented [17]. The solar cell with a band gap E_g at a temperature T_{sc} is modelled as a black body above the band gap and as a white body below. The radiative recombination rate RR can then be calculated using Planck's law [17].

$$RR = \exp\left(\frac{eV}{k_B T_{sc}}\right) \cdot \frac{2\pi e}{c^2 h^3} \int_{E_g}^{\infty} \frac{E^2}{\exp\left(\frac{E - eV}{k_B T_{sc}}\right) - 1} dE. \quad (2.24)$$

The current-voltage curve of such an ideal solar cell is then obtained by subtracting the recombination rate from the number of absorbed photons of the solar spectrum.

$$I(V, E_g) = \int_{E_g}^{\infty} \Phi_{e,E} \frac{ehc}{E^3} dE - RR(V, E_g). \quad (2.25)$$

From the I - V characteristic, all important parameters can be derived. In contrast to the original Shockley-Queisser publication, the earlier mentioned AM1.5 solar spectrum [14] is used to evaluate the efficiency limit, the temperature of the solar cell is set to $T_{sc} = 300$ K. Figure 2.8 shows the maximum usable energy (dark blue area). The highest efficiency value of $\eta = 33.7\%$ is achieved for a band gap of $E_g = 1.34$ eV. For larger band

The Shockly-Queisser limit

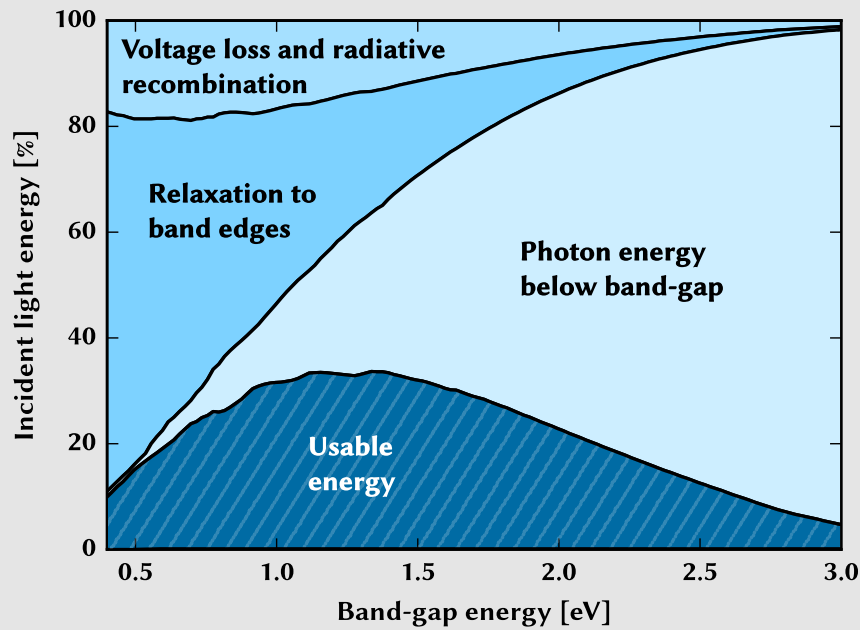


Figure 2.8: The Shockly-Queisser limit of a solar cell. The dark blue shaded area shows the maximum power conversion efficiency as a function of the band gap energy. The other curves show the various percentage losses. All curves were calculated as explained in [17].

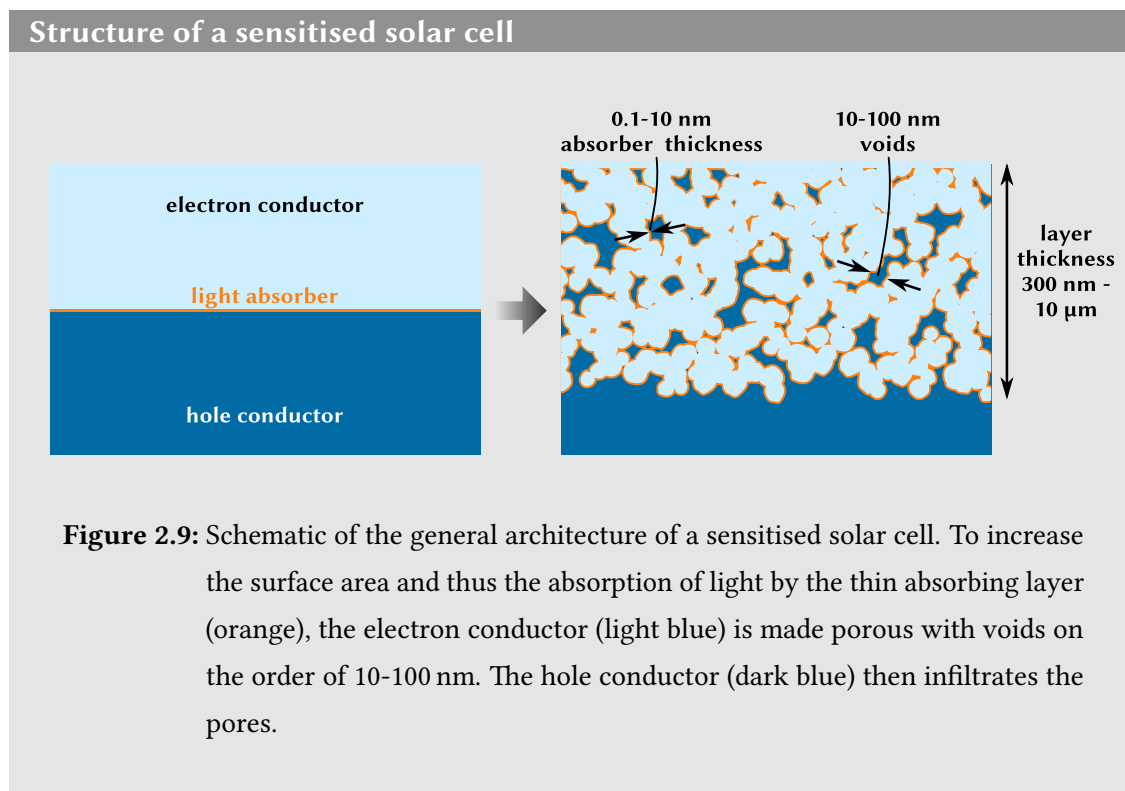
gaps, most energy is lost, because only a small part of the solar spectrum is absorbed (“Photon energy below band gap”). For small band gaps, most of the incident photons have a higher energy than the band gap and the excess energy is wasted (“Relaxation to band-edges”).

2.2.4 Sensitised solar cells

The most wide-spread type of solar cells to date are devices from homojunctions of differently doped crystalline silicon. However, in course of this thesis, so called sensitised solar cells (SSC) were built. In this section, this type of photovoltaic device is introduced.

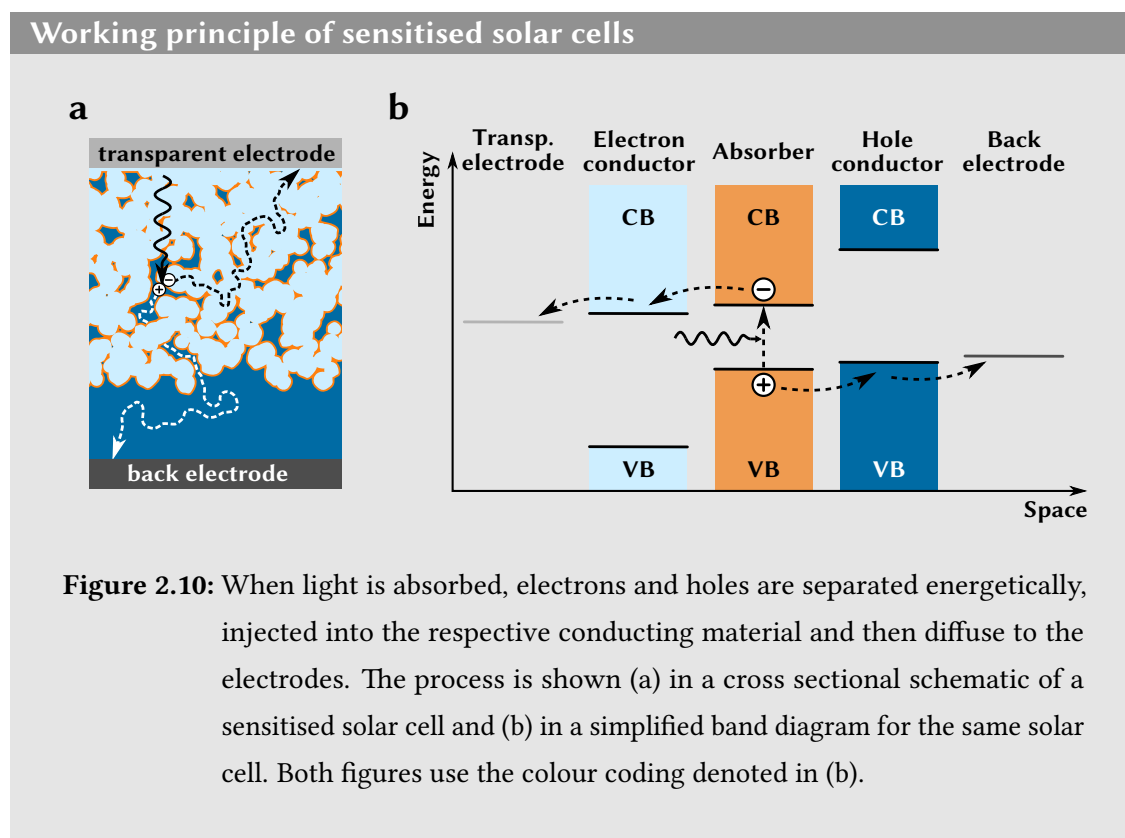
Architecture of sensitised solar cells

In a sensitised solar cell, the function of light absorption, electron transport and hole transport are separated into at least three different material components, in contrast to a p-n homojunction cell. The surface of the electron conductor is covered by a thin layer of light absorbing material with thicknesses varying from mono-molecular layers to a few nanometres. As the electron conductor itself typically does not absorb photons from the visible spectrum, it is “sensitised” to visible light by the addition of the thin absorbing layer [18]. In a planar architecture, the thin layer only absorbs a very small fraction of the incident light and very few charge carrier pairs are generated. This problem can be resolved by using a mesoporous topology for the electron conducting material, as illustrated in Figure 2.9. Voids on the order of tens to hundreds of nanometres increase the surface area, while the connectivity of the material itself is retained for charge transport.

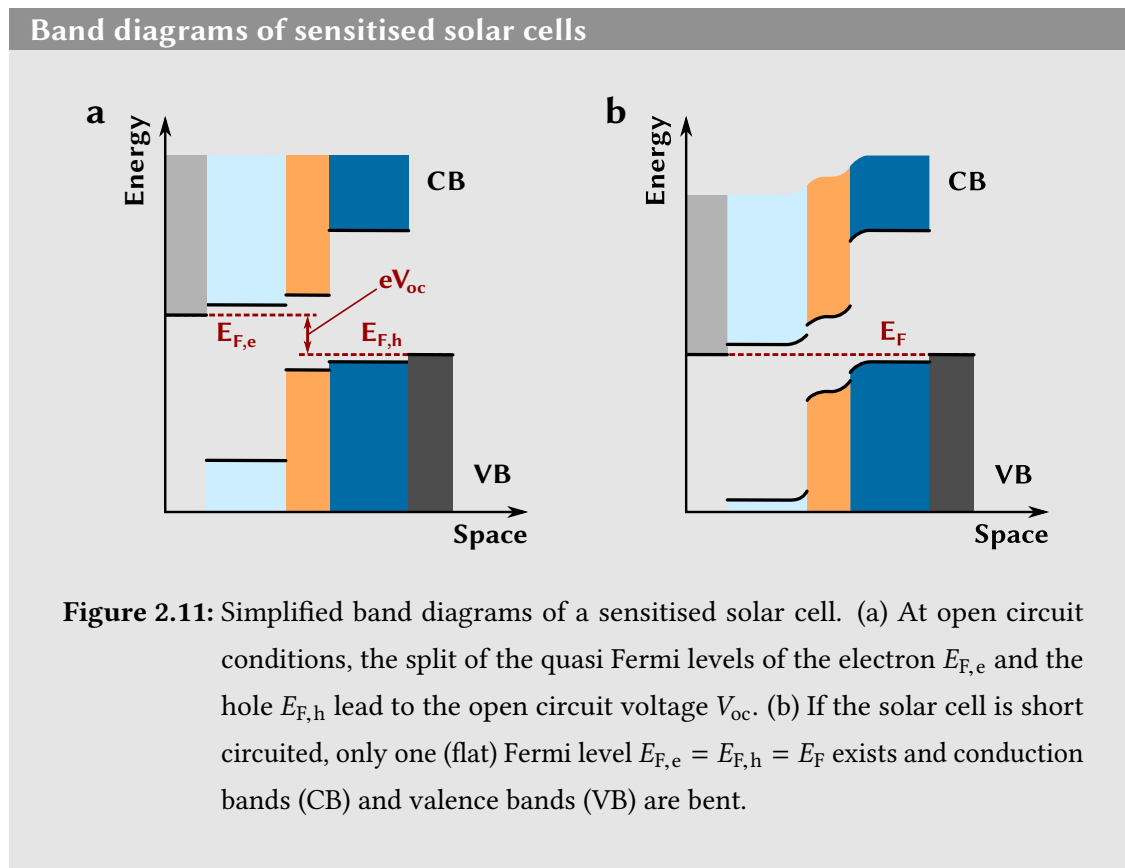


Working principle of sensitised solar cells

Charge carrier pairs are generated in the absorbing semiconductor on the absorption of light as explained in more detail in Chapter 1. Materials with an appropriate band gap have to be chosen so that charge injection for electrons and holes is possible. The conduction band minimum (or lowest unoccupied molecular orbital, LUMO, for organic semiconductors) of the absorber should be slightly higher than the conduction band edge of the electron transport material to ensure electron injection. Accordingly, the position of the valence band maximum (or highest occupied molecular orbital, HOMO, for organic semiconductors) of the hole transport material must lie energetically higher than the valence band maximum of the absorber. Figure 2.10 a depicts a schematic cross section of a sensitised solar cell under operation. Figure 2.10 b shows a simplified band diagram of the same device.



If a solar cell is illuminated, it no longer is in thermal equilibrium and thus the charge distribution introduced in Chapter 1 changes and no well defined Fermi level exists. However, it is possible to resolve this by introducing the concept of quasi-Fermi levels. This concept allows the use of Fermi-Dirac statistics to describe the energetic distribution of electrons in a semiconductor under illumination [19]. The Fermi level is replaced by quasi-Fermi levels $E_{F,e}$ for electrons and $E_{F,h}$ for holes. In light, the quasi-Fermi level for electrons $E_{F,e}$ is shifted towards the conduction band, the one for holes $E_{F,h}$ is shifted towards the valence band [19]. Figure 2.11 presents more detailed, but still simplified, band diagrams for a sensitised solar cell under (a) open circuit and (b) short circuit conditions. The voltage of the device is a result of the splitting of the quasi Fermi levels of the electron $E_{F,e}$ and the hole $E_{F,h}$. In case of a shorted solar cell, the quasi Fermi levels are the same throughout the device and band bending occurs at the junctions of the different materials.



The charge transport mechanism of the electron and hole conductor depends on the choice of material. For the electron transporter, the most widely used material is titanium dioxide (TiO_2) in its crystalline anatase phase [20], amongst others such as ZnO or SnO_2 . All these materials are wide band gap semiconductors and their band gap values of $E_g > 3 \text{ eV}$, provide good transparency in the visible spectrum. The charge transport mechanism in the electron transporting material is due to diffusion, as the band bending is small [21]. The degree of porosity, the size of the individual nanocrystals of the mesoporous layer, and the density of trap states all influence the electron diffusion coefficient and thus the device performance [20].

The hole transport materials used in this thesis are organic semiconductors, such as Poly(3-hexylthiophene-2,5-diyl) (P3HT) or Poly[2,6-(4,4-bis-(2-ethylhexyl)-4H-cyclopenta[2,1-b;3,4-b']dithiophene)-alt-4,7(2,1,3-benzothiadiazole)] (PCPDTBT). The charge transport in these polymers can be described by a hopping mechanism of charge carriers between neighbouring molecules via phonon assisted tunnelling [22].

The working principle of a sensitised solar cell can be summarised in four general steps:

1. Light absorption and generation of a charge carrier pair in the absorbing layer.
2. Injection of charges into electron and hole conducting materials.
3. Charge transport to the two electrodes of the solar cell.
4. Recombination of the charges and release of energy in an external circuit.

From dye sensitised solar cells to inorganic solid-state sensitised solar cells

The concept of dye sensitised solar cells (DSSC) was introduced and demonstrated in 1991 by Michael Grätzel and Brian O'Regan [23]. As an absorber, they used an organic ruthenium complex as a dye, to sensitise nano-crystalline TiO_2 . An iodine based liquid redox electrolyte served as a hole conductor. Their solar cell achieved a power conversion efficiency of more than $\eta = 7 \%$ [23].

The use of a liquid in a photovoltaic device comes with technical challenges such as corrosion and leakage problems [24]. To address these, the use of solid-state hole conductors, such as hole conducting molecules (e.g. spiro-OMeTAD), p-type organic polymers (e.g. P3HT) or solution processable inorganic semiconductors (e.g. CuSCN) were proposed [20].

But also the dye itself gives rise to problems. The organic metal-complexes used for high efficiencies in DSSCs are expensive and prone to degradation. However, the dye can be replaced by an extremely thin layer of inorganic semiconductor (such as Sb_2S_3 , CuInS_2 , In_2S_3 , CdS , CdTe) [25]. These sensitised photovoltaics are sometimes also called extremely thin absorber (ETA) solar cells.

Bibliography

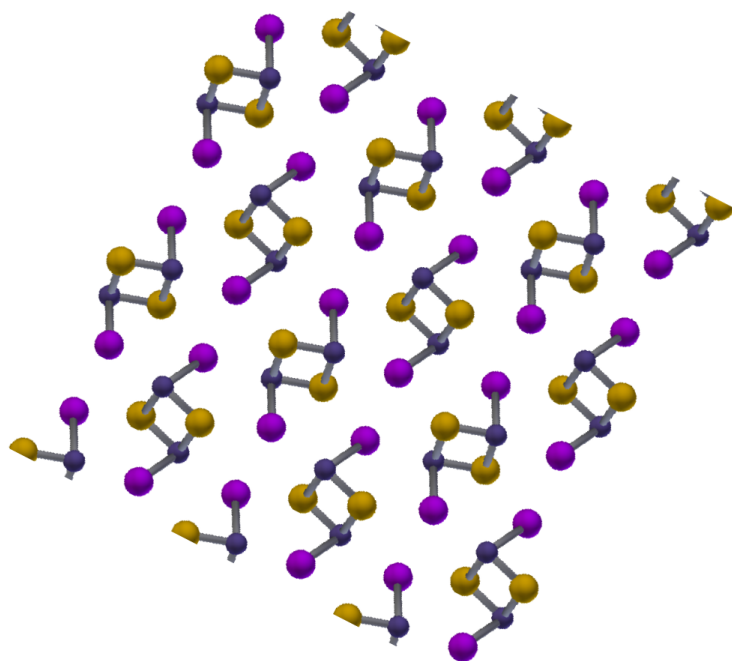
- [1] P. G. Datskos and N. V. Lavrik. “Detectors - Figures of Merit”. *Encyclopedia of Optical Engineering* (2003), pp. 349–357.
- [2] A. Einstein. “Über einen die Erzeugung und Verwandlung des Lichtes betreffenden heuristischen Gesichtspunkt”. *Annalen der Physik* 17 (1905), pp. 132–148.
- [3] W. Smith. “Effect of Light on Selenium During the Passage of An Electric Current”. *Nature* 7.173 (1873), p. 303. DOI: 10.1038/007303e0.
- [4] D. Wood. *Optoelectronic Semiconductor Devices*. International Series in Optoelectronics. UK: Prentice Hall, 1994.
- [5] J. S. Brugler. “Optoelectronic Nomenclature for Solid-State Radiation Detectors and Emitters”. *IEEE Journal of Solid-State Circuits* 5.5 (1970), pp. 276–283. DOI: 10.1109/JSSC.1970.1050127.
- [6] R. C. Jones. “Phenomenological Description of the Response and Detecting Ability of Radiation Detectors”. *Proceedings of the IRE* 47.9 (1959), pp. 1495–1502. DOI: 10.1109/JRPROC.1959.287047.
- [7] P. L. Richards. “Bolometers for Infrared and Millimeter Waves”. *Journal of Applied Physics* 76.1 (1994), pp. 1–24. DOI: 10.1063/1.357128.
- [8] R. C. Jones. “Phenomenological Description of the Response and Detecting Ability of Radiation Detectors”. *Proceedings of the IRE* 47.9 (1959), pp. 1495–1502. DOI: 10.1109/JRPROC.1959.287047.
- [9] L. Dou, Y. (Yang, J. You, Z. Hong, W.-H. Chang, G. Li, and Y. Yang. “Solution-Processed Hybrid Perovskite Photodetectors with High Detectivity”. *Nature Communications* 5 (2014), p. 5404. DOI: 10.1038/ncomms6404.
- [10] M. Razeghi and A. Rogalski. “Semiconductor Ultraviolet Detectors”. *Journal of Applied Physics* 79.10 (1996), pp. 7433–7473. DOI: 10.1063/1.362677.
- [11] J. Nelson. *The Physics of Solar Cells*. London, UK: Imperial College Press, 2003.

-
- [12] S. Fonash. *Solar Cell Device Physics*. Energy Science and Engineering: Resources, Technology, Management. New York, USA: Academic Press, Inc., **1981**.
- [13] W. Shockley. “The Theory of *P-N* Junctions in Semiconductors and *P-N* Junction Transistors”. *Bell System Technical Journal* 28.3 (**1949**), pp. 435–489. DOI: 10.1002/j.1538-7305.1949.tb03645.x.
- [14] ASTM. *American Society for Testing and Materials. Terrestrial Reference Spectra for Photovoltaic Performance Evaluation. Solar Spectral Irradiance: Air Mass 1.5*. <http://rredc.nrel.gov/solar/spectra/am1.5/>. **2016**.
- [15] W. Tress. *Organic Solar Cells: Theory, Experiment, and Device Simulation*. Springer Series in Materials Science 208. Springer, **2014**.
- [16] W. Shockley and H.J. Queisser. “Detailed Balance Limit of Efficiency of *P-n* Junction Solar Cells”. *Journal of Applied Physics* 32.3 (**1961**), pp. 510–519. DOI: 10.1063/1.1736034.
- [17] S. Byrnes. *The Shockley-Queisser Limit*. <http://sjbyrnes.com/sq.html>. **2016**.
- [18] A.J. McEvoy and M. Grätzel. “Sensitisation in Photochemistry and Photovoltaics”. *Solar Energy Materials and Solar Cells* 32.3 (**1994**), pp. 221–227. DOI: 10.1016/0927-0248(94)90260-7.
- [19] J. Giesecke. *Quantitative Recombination and Transport Properties in Silicon from Dynamic Luminescence*. Springer Theses. Springer, **2014**.
- [20] A. Hagfeldt, G. Boschloo, L. Sun, L. Kloo, and H. Pettersson. “Dye-Sensitized Solar Cells.” *Chemical Reviews* 110.11 (**2010**), pp. 6595–663. DOI: 10.1021/cr900356p.
- [21] S. Soedergren, A. Hagfeldt, J. Olsson, and S.-E. Lindquist. “Theoretical Models for the Action Spectrum and the Current-Voltage Characteristics of Microporous Semiconductor Films in Photoelectrochemical Cells”. *The Journal of Physical Chemistry* 98.21 (**1994**), pp. 5552–5556. DOI: 10.1021/j100072a023.
- [22] R.J. Kline and M.D. McGehee. “Morphology and Charge Transport in Conjugated Polymers”. *Journal of Macromolecular Science, Part C* 46.1 (**2006**), pp. 27–45. DOI: 10.1080/15321790500471194.

Bibliography

- [23] B. O'Regan and M. Grätzel. "A Low-Cost, High-Efficiency Solar Cell Based on Dye-Sensitized Colloidal TiO₂ Films". *Nature* 353.6346 (**1991**), pp. 737–740. DOI: 10.1038/353737a0.
- [24] M. Grätzel. "Dye-Sensitized Solar Cells". *Journal of Photochemistry and Photobiology C: Photochemistry Reviews* 4.2 (**2003**), pp. 145–153. DOI: 10.1016/S1389-5567(03)00026-1.
- [25] T. Dittrich, A. Belaidi, and A. Ennaoui. "Concepts of Inorganic Solid-State Nanostructured Solar Cells". *Solar Energy Materials and Solar Cells* 95.6 (**2011**), pp. 1527–1536. DOI: 10.1016/j.solmat.2010.12.034.

Solution-processable sulfide semiconductors



In this chapter antimony sulfide (Sb_2S_3) and antimony sulfoiodide (SbSI), the sulfide semiconductor materials which are used for the optoelectronic devices built in this thesis, are introduced. For both materials, a short overview of the optical and electronic properties is given and a brief literature review of their use in solar cells and photodetectors is provided.

3.1 Antimony sulfide

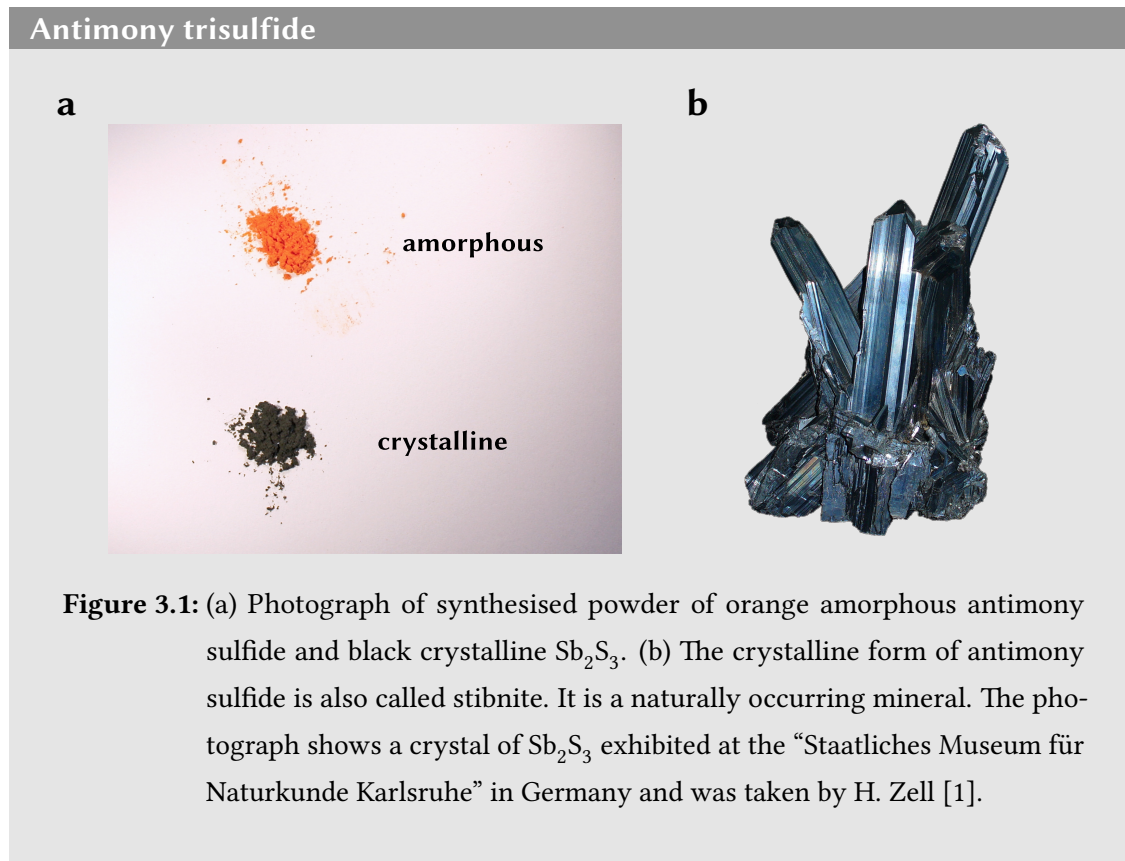
Antimony trisulfide (Sb_2S_3) is a chemical compound which belongs to the group of metal sulfides. It is orange to black in colour, depending on its state of crystallinity. Figure 3.1 a shows amorphous (orange) and crystalline (black) antimony sulfide powder synthesised in the laboratory. Sb_2S_3 also occurs in nature in the crystalline form as a mineral called stibnite. A photograph of a stibnite crystal which is exhibited in the “Staatliches Museum für Naturkunde Karlsruhe” in Germany is shown in Figure 3.1 b.

Due to its low toxicity and its abundant occurrence [2], antimony sulfide was and is used in a wide range of applications. Historically, the black crystalline form of it was used in the Near and Middle East as a cosmetic powder, called “kohl”, to darken eyelids and -lashes [3]. Today, Sb_2S_3 can be found as a pigment in camouflage paints due to its infrared reflection and it is used in safety-matches and for the liners of brakes in the automotive industry [4]. The favourable physical, specifically the optoelectronic properties, which are discussed in the following sections, lead to the use of antimony sulfide as the active material in early video and television cameras (vidicon tubes) [5].

3.1.1 Physical properties

Crystal structure

The crystalline form of antimony sulfide, has an orthorhombic unit cell. Its dimensions are $a = 1.123$ nm, $b = 1.131$ nm and $c = 0.384$ nm and it has a $Pbnm$ space group [6]. The



crystal structure of antimony sulfide forms parallel $(\text{Sb}_4\text{S}_6)_n$ ribbons [7, 8]. The crystal's cleavage is parallel to the c-axis [9]. The ribbons and the crystal structure of crystalline antimony sulfide are illustrated in Figure 3.2. The crystal of antimony sulfide shows perfect cleavage in the $[0\ 1\ 0]$ direction. The cleavage trace is shown as a dashed line in Figure 3.2. Perfect cleavage means that only van der Waals forces, but no covalent bonds (symbolised as sticks in Figure 3.2) have to be broken [9].

Optical properties

Antimony sulfide is especially interesting for optoelectronic applications because of its optical properties. The complex refractive index $n + ik$ of amorphous and crystalline antimony sulfide are plotted in Figure 3.3. Figure 3.3 a shows the real part $n(\lambda)$, Figure 3.3 b the imaginary part $k(\lambda)$, also known as the extinction coefficient. The extinction coeffi-

Crystal structure of antimony sulfide

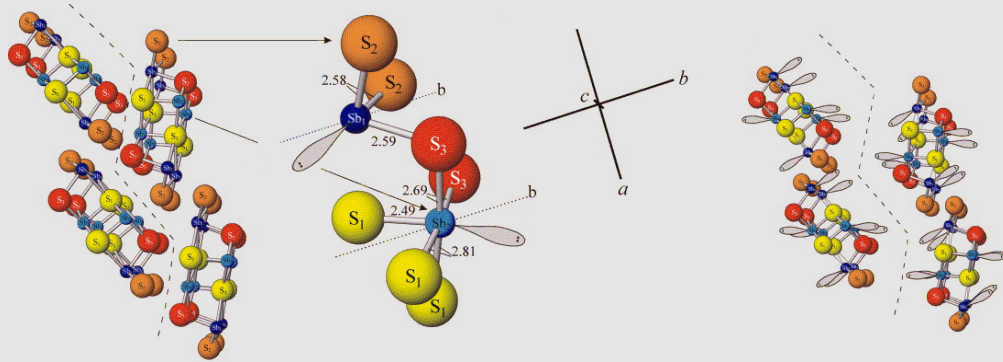


Figure 3.2: The crystal structure of crystalline antimony sulfide looking along the c-axis. Dashed lines indicate the trace of perfect cleavage along the [0 1 0] direction (no covalent bonds, only van der Waals forces have to be overcome). The numbers show the distance between sulfur (S) and antimony (Sb) atoms in units of Angström. Reprinted from [9], with permission from Elsevier.

cient can be converted into the more widely used attenuation coefficient $\alpha(\lambda) = \frac{4\pi k(\lambda)}{\lambda}$. It shows that below a wavelength of $\lambda = 700$ nm, crystalline Sb_2S_3 has a high extinction coefficient of $\alpha > 10^5 \frac{1}{\text{cm}}$. For sensitised solar cells this is beneficial, as already very thin layers are enough to absorb most of the incident light. In fact, optical path lengths of less than 100 nm in Sb_2S_3 are sufficient to absorb more than 90 % of the incident light power of the visible spectrum.

Both, amorphous and crystalline antimony sulfide are semiconductors with a direct band gap of around 2.2 eV and 1.7 eV, respectively [11]. The exact energy of the band gap depends on the method of synthesis, crystallite size and annealing conditions. The amorphous phase of Sb_2S_3 can be turned into a polycrystalline phase by a heat treatment (annealing) in an oxygen free atmosphere. Figure 3.4 shows the band gap value as a function of the annealing temperature. For temperatures above 250 °C, the final crystalline phase is reached and no further change of the band gap energy is observed [12]. A known problem, which reduces the performance of many optoelectronic applications

Complex refractive index of antimony sulfide

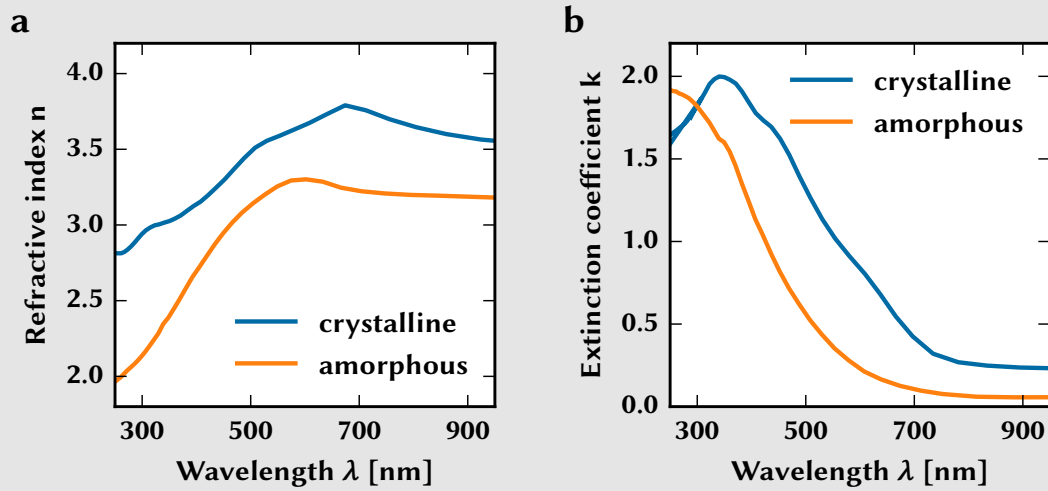


Figure 3.3: The complex refractive index $n + ik$ of antimony sulfide. (a) The real part n of the refractive index lies between 2 and 4 for both, amorphous (orange line) and crystalline (blue line), Sb_2S_3 . (b) The complex part, the extinction coefficient is particularly high for crystalline antimony sulfide. The data for the plots was measured on a 30 nm thick film, extracted from [10].

of antimony sulfide, is a relative high density of trap states. These states lie in the band gap, specifically below the conduction band [13]. In Chapter 6 it will be shown that a reduction of these trap states via a new synthesis method leads to an improved performance of antimony sulfide sensitised solar cells.

Electronic properties

Antimony sulfide is a n-type semiconductor [14], thus it can also be used as an electron transport material. However, its conductivity is relatively low. Amorphous antimony sulfide has a resistivity of $\rho = 3.8 \cdot 10^8 \Omega\text{cm}$ [15]. For crystalline antimony sulfide, the resistivity is reduced by two orders of magnitude to $\rho = 5.3 \cdot 10^6 \Omega\text{cm}$ [15]. However, one should note that the conductivity is illumination dependent and increases sublinearly

Annealing antimony sulfide

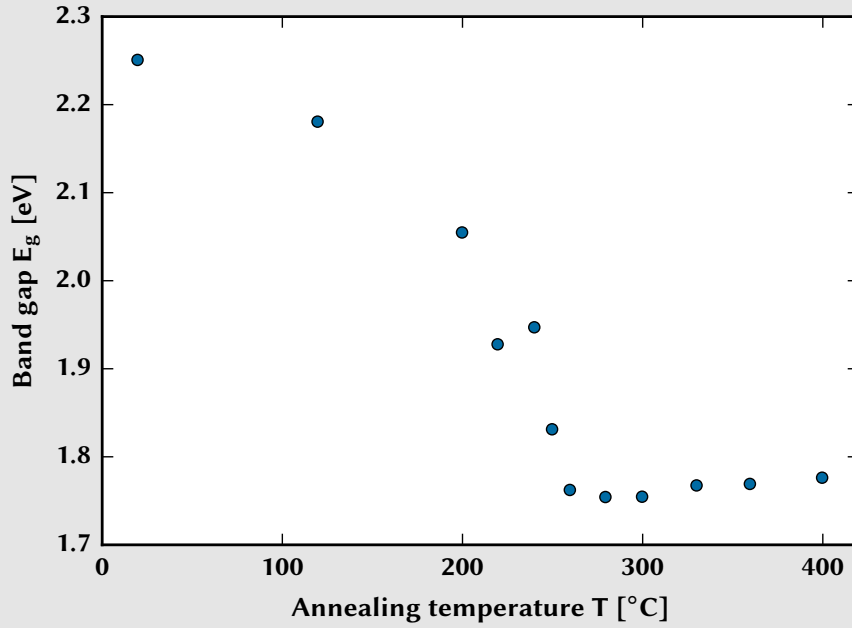


Figure 3.4: Change of the band gap value E_g with annealing temperatures of amorphous Sb_2S_3 . For temperatures $T > 250^\circ\text{C}$, no further change of E_g is observed and antimony sulfide is fully crystalline. Data extracted and replotted from [12].

with the photon flux [16]. The charge carrier concentration is on the order of $N_d = 10^{12} \text{ cm}^{-3}$ and a Sb_2S_3 crystal has an electron mobility of approximately $\mu_n = 10 \frac{\text{cm}^2}{\text{Vs}}$ [15]. Darga *et al.* measured an ambipolar diffusion length on the order of $L_d \approx 100 \text{ nm}$ and an electron diffusion length of approximately $L_{d,e} \approx 1000 \text{ nm}$ [16].

3.1.2 Synthesis of antimony sulfide

Many different routes for the synthesis of antimony sulfide have been reported. For optoelectronic applications and specifically for the scope of this thesis, the deposition of thin films of antimony sulfide (as opposed to free standing structures or particles in sus-

pension) is important. In this section, a brief overview of different ways of synthesising films of antimony sulfide is given.

Evaporation

One of the first reported methods for the deposition of Sb_2S_3 thin films is the thermal evaporation at low pressures [17]. Antimony sulfide powders are often used as a source for the evaporation of thin films [10, 17, 18]. Alternatively, films can be prepared by the co-evaporation of elemental sulfur and antimony [19]. Evaporation is however not suitable when it comes to infiltrating mesoporous materials.

Chemical bath deposition

The most widely used technique for the synthesis of antimony sulfide, especially for sensitised solar cells, is the chemical bath deposition (CBD), also called solution growth. This solution-processable technique can be split into two classes: aqueous and non-aqueous chemical baths.

Non-aqueous CBD for the thin film deposition of antimony sulfide was first proposed by Mane *et al.* [20]. They used antimony chloride (SbCl_3) and thioacetamid ($\text{C}_2\text{H}_5\text{NS}$) dissolved in glacial acetic acid. The same chemical precursor materials (SbCl_3 and $\text{C}_2\text{H}_5\text{NS}$) were also used by Maiti *et al.* for the synthesis of a single precursor ($\text{C}_4\text{H}_{10}\text{Cl}_3\text{N}_2\text{S}_2\text{Sb}$) which decomposes to antimony sulfide in alcoholic baths [21].

For the aqueous CBD, precursors such as antimony potassium tartrate ($\text{K}_2\text{Sb}_2(\text{C}_4\text{H}_2\text{O}_6)_2$) [22] and antimony chloride (SbCl_3) [2, 23, 24] as a antimony source and sodium thiosulfate ($\text{Na}_2\text{S}_2\text{O}_3$) [2], thiourea ($\text{CH}_4\text{N}_2\text{S}$) [23] and thioacetamid ($\text{C}_2\text{H}_5\text{NS}$) [22] as a sulfur source are used.

The by far most widespread CBD method is the synthesis using an aqueous bath of SbCl_3 and $\text{Na}_2\text{S}_2\text{O}_3$ introduced by Nair *et al.* [25]. First, SbCl_3 is dissolved in a small amount of acetone, then an aqueous solution of sodium thiosulfate is added. Finally, the solution is

diluted with water and the substrates are placed vertically into the chemical bath for 1-2 hours for the deposition process. This technique was used unchanged in a wide variety of reports on Sb_2S_3 sensitised solar cells, including the to-date record antimony sulfide solar cell [26]. The method is scalable and has only one drawback: A careful control of the temperature is necessary. The solution needs to be cooled to below 10°C , as the reaction speed is too fast at room temperature. In Chapter 6, the CBD method is altered to eliminate the disadvantage of cooling and allow for a deposition which can be performed at room temperature [27].

Spin coating

More recently, spin-coating of antimony sulfide was reported. Yang *et al.* prepared antimony sulfide from spin-coating a solution of elemental antimony and sulfur in hydrazine [28]. A spin-coating method using a solvent of lower risk was proposed, which uses antimony ethyl xanthate $\text{Sb}(\text{S}_2\text{COEt})_3$ precursors dissolved in chlorobenzene that are thermally decomposed into Sb_2S_3 [14, 29]. In 2015, Choi *et al.* showed highly efficient antimony sulfide sensitised solar cells using a spin-coating method of a SbCl_3 -thiourea complex in N,N-dimethylformamide (DMF) [30]. However, the power conversion efficiencies of antimony sulfide solar cells using this method are still lower than those achieved with chemical bath deposition.

Others

Beside these more widespread deposition routes, single reports exist utilising different methods for the formation of thin films of antimony sulfide. Techniques not mentioned in the earlier sections are electrodeposition [31], spray pyrolysis [32] or atomic layer deposition (ALD) [33].

3.1.3 Antimony sulfide solar cells

In this section, a brief literature overview of solar cells with antimony sulfide as an absorbing material is given.

Early thin film antimony sulfide solar cells

The first antimony sulfide solar cells were presented by Savadogo *et al.* in the early 1990s. In 1992, they presented a Schottky junction solar cell of Sb_2S_3 and gold achieving a power conversion efficiency of $\eta = 3\%$ for an air mass AM 1 spectrum [34]. Just one year later, the same group published a heterojunction solar cell of n-type antimony sulfide on a p-type silicon wafer with $\eta = 5.2\%$ [35]. Another year later, in 1994, they presented the same solar cell principle, but using a p-type germanium wafer as a substrate, which resulted in a further increase in efficiency to $\eta = 7.3\%$ [36]. In the same year, they showed another Schottky junction solar cell using Sb_2S_3 and platinum, which reached an efficiency of $\eta = 5.5\%$ [37]. All four publications report that these high efficiencies of devices with several μm thick flat Sb_2S_3 films are reached by doping the antimony sulfide layer with silicotungstic acid. The work of Savadogo *et al.* is rarely cited in newer publications on Sb_2S_3 solar cells and has not been reproduced so far.

Also in the 1990s, Deshmukh *et al.* and Killedar *et al.* worked on photochemical solar cells using antimony sulfide and liquid electrolytes such as ferrocene-DMSO or potassium iodide [38, 39]. However, these devices did not show efficiencies higher than $\eta = 0.06\%$ [39]. An overview of the early publications about antimony sulfide solar cells is presented in Table 3.1.

Sensitised antimony sulfide solar cells

Antimony sulfide sensitised solar cells were first proposed by Vogel *et al.* in 1994 [40]. They suggested to use Sb_2S_3 quantum dots as the absorber in a dye sensitised solar cell architecture. Unfortunately they did not show any working devices employing antimony

Table 3.1: Overview of early (non-sensitised) antimony sulfide solar cells.

Author [<i>et al.</i>]	Year	Details	η [%]	Ref.
Savadogo	1992	Schottky junction: Sb_2S_3 -Au	3.0	[34]
Savadogo	1993	Sb_2S_3 on p:Si wafer	5.2	[35]
Savadogo	1994	Sb_2S_3 on p:Ge wafer	7.3	[36]
Savadogo	1994	Schottky junction: Sb_2S_3 -Pt	5.5	[37]
Deshmukh	1994	chemical cell: Sb_2S_3 and ferrocyn.	0.008	[38]
Killedar	1998	chemical cell: Sb_2S_3 and KI electrolyte	0.058	[39]

sulfide due to stability problems of the material with the liquid electrolyte.

It took more than 14 years, until the first working Sb_2S_3 sensitised solar cell was demonstrated by Itzhaik *et al.* in 2009. Their device architecture consisted of mesoporous TiO_2 , which was sensitised by CBD antimony sulfide. CuSCN was used as a solid hole transport material achieving an efficiency of $\eta = 3.37\%$ [41]. This publication marks the start of a very active period in research on antimony sulfide solar cells. In 2010, Nezu *et al.* showed efficiencies up to $\eta = 3.7\%$ using the same device structure. Soon after, Chang *et al.* and Moon *et al.* showed that efficiencies of more than $\eta = 5\%$ are achievable with organic hole transport materials such as spiro-OMeTAD and P3HT [42, 43]. Im *et al.* could increase the efficiency to $\eta = 6.57\%$, by using the p-type polymer PCPDTBT [44]. This work held the efficiency record for Sb_2S_3 sensitised solar cells for four years, until Choi *et al.* achieved $\eta = 7.5\%$ by a trap-site reducing post-treatment using thioacetamide in 2014.

In addition to publications which aim to drive the efficiency record higher and higher, there are also a large number of articles explaining mechanisms, presenting new fabrication routes or exploring new device architectures. In 2012 Cardoso *et al.* used rutile TiO_2 nanowires instead of anatase nanoparticles and measured very high current densities, yet the low open-circuit voltage limited the overall device performance [45]. Chang *et al.* showed a relative improvement by adding electron conducting channels of PCBM into the hole transport layer to harvest electrons absorbed in that layer [46]. Tsujimoto *et al.*

improved the charge transfer at the Sb_2S_3 - TiO_2 interface by treating the mesoporous titanium dioxide layer with Mg^{2+} and Ba^{2+} ions [47]. In 2013, Ito *et al.* produced highly efficient solar cells with a power conversion efficiency of $\eta = 5.7\%$ by doping the antimony sulfide sensitisation layer with 5 at. % of titanium [48]. New deposition methods have also been presented: In 2013 Wedemeyer *et al.* introduced the use of atomic layer deposition (ALD) of Sb_2S_3 for sensitised solar cells [33]. And in 2015, we showed that the widely used chemical bath deposition at low temperatures can be altered to a reaction at room temperature, giving high efficiencies with reduced trap states, see Chapter 6 [27]. In the same year, Choi *et al.* presented efficient antimony sulfide sensitised solar cells via spin-coating a SbCl_3 -thiourea complex precursor [30].

Table 3.2 shows an overview of some main publications in the field of Sb_2S_3 sensitised solar cells. It should be noted that this list tries to give an adequate summary and cannot be a complete list of work on antimony sulfide solar cells.

Revival of flat thin film antimony sulfide solar cells

Recently, the work on antimony sulfide has shifted back towards flat film architectures. In 2013, Bansal *et al.* reported on a bulk heterojunction device of antimony sulfide and P3HT with an efficiency of $\eta = 1.29\%$ [14]. Although this was not a flat architecture, the report proved that the antimony sulfide is capable to conduct the electrons itself and no metal oxide was necessary. Muto *et al.* then showed an efficiency of $\eta = 3.6\%$ in the same year for a flat solution-processed antimony sulfide solar cell. Earlier work on thin film solar cells with Sb_2S_3 and CdS by Rodriguez-Lazcano *et al.* and Messina *et al.* showed poor performance with efficiencies not exceeding $\eta = 0.7\%$ [51–53]. In 2014, Kim *et al.* used ALD to fabricate flat oxide-free antimony sulfide photovoltaic devices, reaching a record efficiency of $\eta = 5.77\%$ [54]. Using chemical bath deposition, Zimmermann *et al.* achieved $\eta = 4.1\%$ with a very similar device architecture in 2015 [55].

All of the devices mentioned here rely on a flat, compact layer of TiO_2 . In 2016, different compact layers, such as cadmium sulfide CdS or tin oxide SnO_2 , were examined for flat antimony sulfide solar cells with respectable efficiencies of up to $\eta = 3.5\%$ [56, 57].

Table 3.2: Literature overview of antimony sulfide sensitised solar cells sorted by publication year. All devices use mesoporous titanium dioxide as electron transport material.

Author [<i>et al.</i>]	Year	Details	η [%]	Ref.
Vogel	1994	First TiO_2 sensitised solar cell with Sb_2S_3	—	[40]
Manolache	2008	Sprayed Sb_2S_3 on TiO_2	—	[49]
Itzhaik	2009	TiO_2 - Sb_2S_3 -CuSCN	3.37	[41]
Nezu	2010	TiO_2 - Sb_2S_3 -CuSCN	3.7	[50]
Moon	2010	TiO_2 - Sb_2S_3 -(spiro-OMeTAD)	5.2	[43]
Chang	2010	TiO_2 - Sb_2S_3 -P3HT	5.13	[42]
Im	2011	TiO_2 - Sb_2S_3 -PCPDTBT	6.57	[44]
Cardoso	2012	TiO_2 (rutile nanowires)	4.5	[45]
Chang	2012	Adding PCBM to HTM	6.3	[46]
Maiti	2012	Oxide free Sb_2S_3 (non-aq. Synthesis)	3	[21]
Tsujimoto	2012	Mg^{2+} , Ba^{2+} treatment of TiO_2	4.1	[47]
Wedemeyer	2013	First ALD synthesis of Sb_2S_3 on TiO_2	2.6	[33]
Ito	2013	Doping of Sb_2S_3 with 5 at. % Ti	5.7	[48]
Choi	2014	Extinction of trap states, record efficiency	7.5	[26]
Gödel	2015	Room temperature synthesis of Sb_2S_3	5.1	[27]
Choi	2015	Spin-coating of Sb_2S_3	6.4	[30]

Table 3.3: Recent publications on solution processable solar cells with a flat layer of antimony sulfide as absorber.

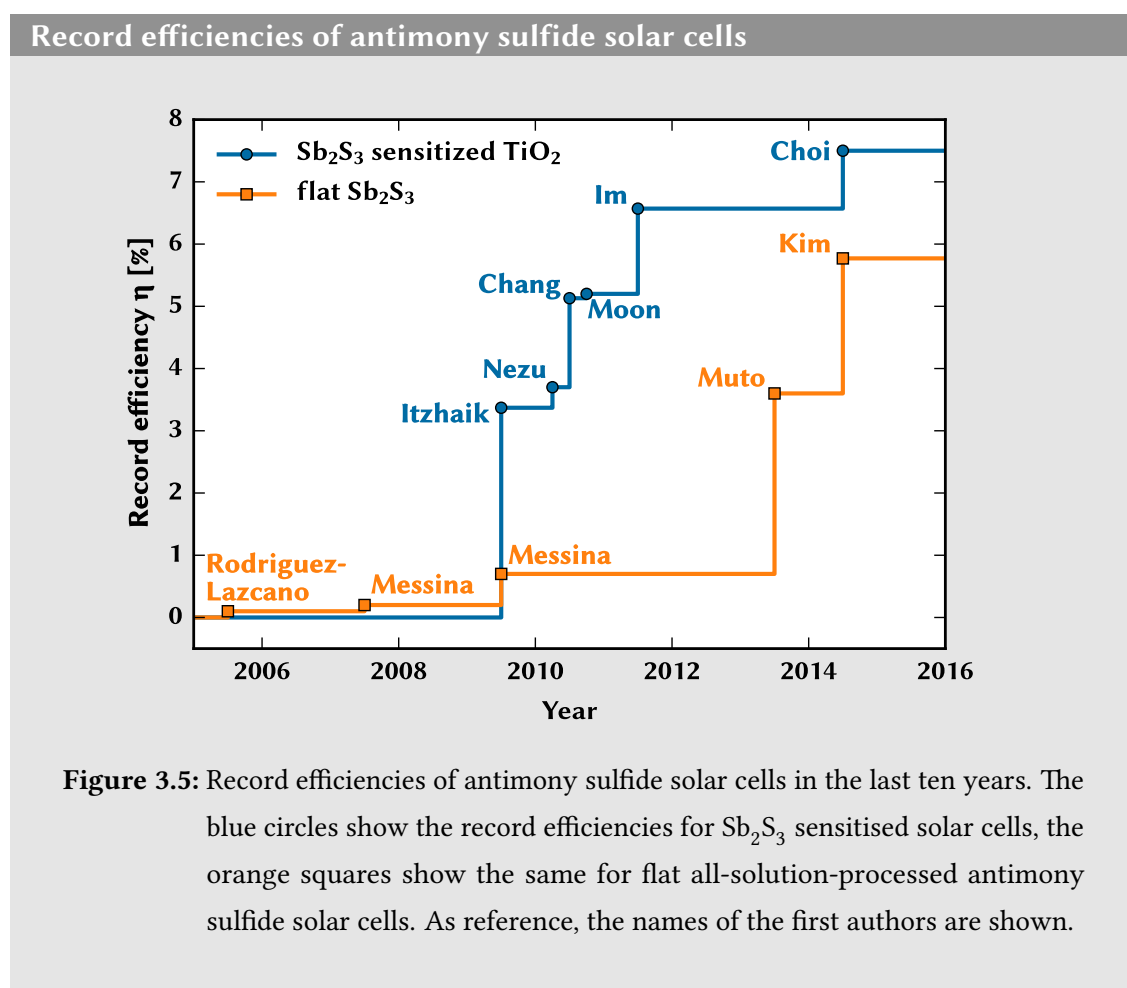
Author [<i>et al.</i>]	Year	Details	η [%]	Ref.
Rodriguez-Lazcano	2005	CdS-Sb ₂ S ₃ -CuSbS ₂	<0.1	[51]
Messina	2007	CdS-Sb ₂ S ₃ -CuS	<0.2	[52]
Messina	2009	CdS-Sb ₂ S ₃ -PbS	0.7	[53]
Bansal	2013	Bulk heterojunction Sb ₂ S ₃ -P3HT	1.29	[14]
Muto	2013	First flat solution processed Sb ₂ S ₃ solar cell	3.6	[58]
Kim	2014	ALD of flat Sb ₂ S ₃	5.77	[54]
Zimmermann	2015	CBD of flat Sb ₂ S ₃	4.1	[55]
Lei	2016	Flat Sb ₂ S ₃ on SnO ₂	2.8	[57]
Yuan	2016	CdS-Sb ₂ S ₃ -Au	3.5	[56]

A literature review of recent flat layer antimony sulfide photovoltaics is shown in Table 3.3. The record efficiencies for both flat and sensitised Sb₂S₃ solar cells are presented in Figure 3.5.

3.2 Antimony sulfoiodide

Antimony sulfoiodide (SbSI) is a compound which belongs to the group of metal thiohalogenides. It appears in the form of long crystalline needles with a red colour. Two photographs of antimony sulfoiodide are presented in Figure 3.6. Figure 3.6 a shows a pile of crystalline SbSI needles and a larger crystal can be seen in detail in Figure 3.6 b.

There are no reports on the natural occurrence of the crystal as a mineral. However, antimony sulfoiodide has been known for a long time, as it was already synthesised at the end of the nineteenth century [61]. Antimony sulfoiodide is not currently produced or used in industrial applications yet. However, the material possesses interesting properties, such as photoconductivity, pyroelectricity and it is well known for its ferroelectric



behaviour. Some important properties of SbSI are discussed in the following sections.

3.2.1 Physical properties

Crystal structure

The crystal structure of antimony sulfoiodide has an orthorhombic symmetry and lattice parameters of $a = 0.84$ nm, $b = 1.01$ nm and $c = 0.41$ nm. The space group is $Pnam$ [61, 62]. SbSI exhibits a ferroelectric and a paraelectric phase. The two phases differ from each other by a slight shift of the antimony atoms with respect to the iodine atoms of

Antimony sulfoiodide

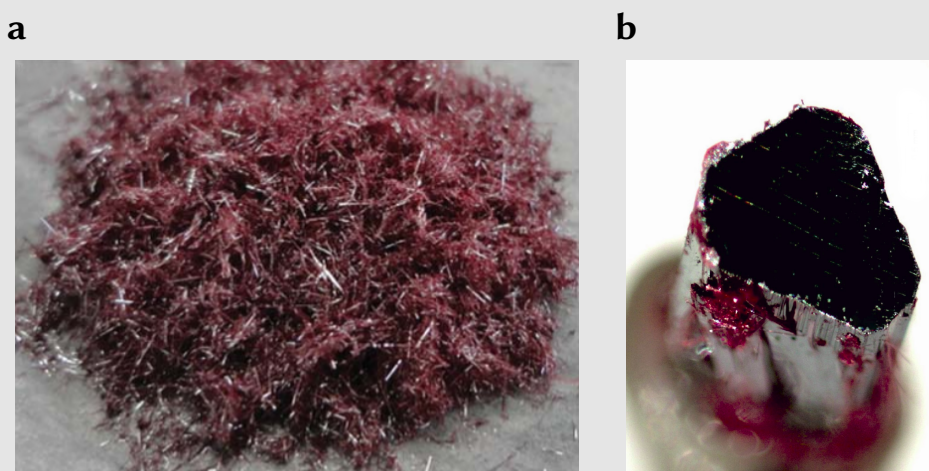


Figure 3.6: (a) Photograph of antimony sulfoiodide single crystals. In part reproduced from [59] with permission of The Royal Society of Chemistry. (b) Detail of an artificial antimony sulfoiodide single crystal. The diameter of the crystal is on the order of 1 mm. The image was reproduced from [60].

about 0.02 nm along the c-axis (0 0 1) [62]. The crystal structure of paraelectric SbSI is illustrated in Figure 3.7 from two perspectives, along the (0 0 1) and along the (0 1 0) axes.

Electronic properties

As result of its ferroelectric properties, antimony sulfoiodide shows spontaneous electric polarisation below its Curie temperature $T_C \approx 20^\circ\text{C}$. Its electric permittivity ε is a function of an applied external electric field [62, 63]. Since all ferroelectric materials are also pyroelectric, which is itself a subclass of piezoelectrics, antimony sulfoiodide also has these properties [64]. A graph for the relative electric permittivity is shown in Figure 3.8 b indicating its pyroelectric properties. The abrupt transition from the ferroelectric to the paraelectric phase at 20°C is clearly visible.

Crystal structure of antimony sulfoiodide

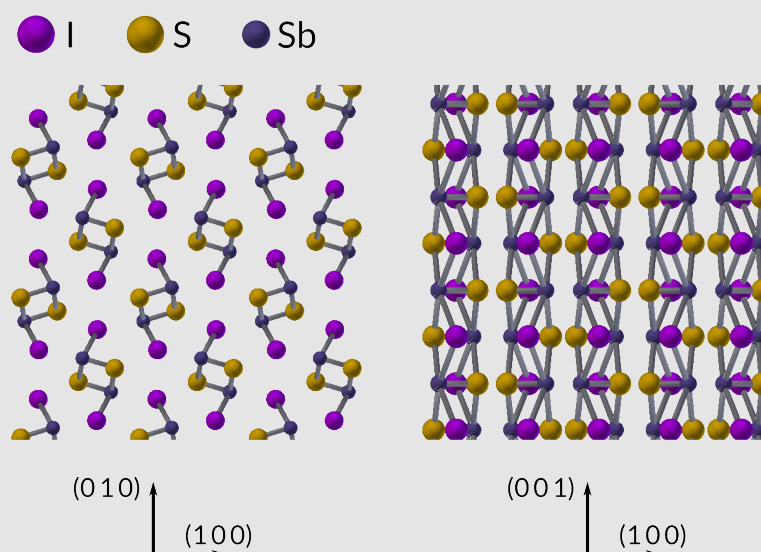


Figure 3.7: The crystal structure of (paraelectric) antimony sulfoiodide. On the left: view along the (0 0 1) axis, on the right: along the (0 1 0) axis. The covalent bonds (grey sticks) form long ribbons along the (0 0 1) axis.

For different synthesis mechanisms of antimony sulfoiodide both conduction types, n-type [65] and p-type [66, 67], were reported.

The conductivity of SbSI is known to be dependent on the incident photon flux. In the dark, the resistivity is on the order of $\rho = 10^{10} \Omega\text{cm}$ and can decrease several orders of magnitude under illumination [68]. In Chapter 7, the photoconductivity of antimony sulfoiodide is exploited to build photodetectors with this material.

Optical properties

The band gap of antimony sulfoiodide is approximately $E_g = 1.95 \text{ eV}$ at room temperature. It is an indirect band gap and its value decreases with increasing temperature. The value of the band gap of SbSI as a function of temperature is shown in Figure 3.8 a [69]. The

Optoelectronic properties of antimony sulfoiodide

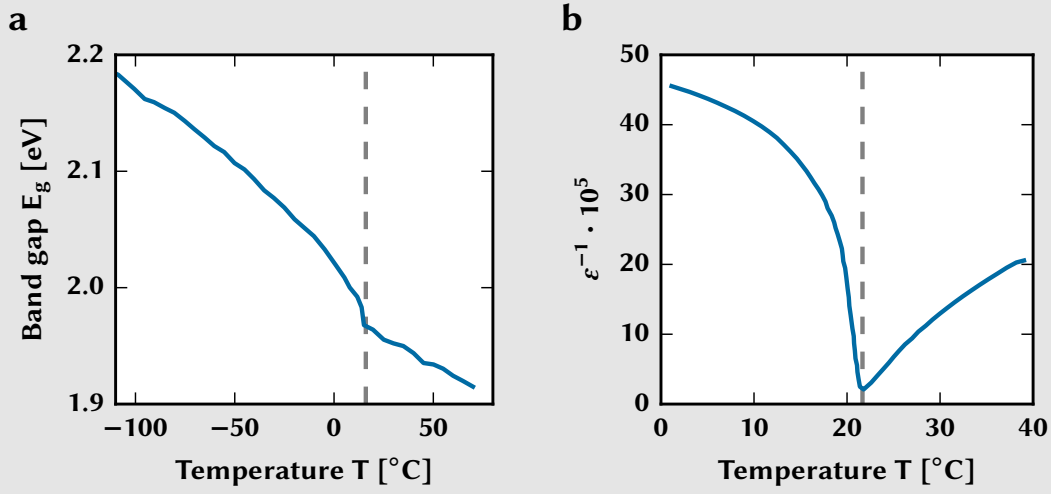


Figure 3.8: Temperature dependent optical properties of antimony sulfoiodide. (a) The band gap of crystalline SbSI as a function of the temperature. (b) The temperature dependent inverse relative permittivity of an antimony sulfoiodide single crystal. In both graphs, the transition from the ferroelectric (below 20 °C) to the paraelectric phase (above 20 °C) is clearly visible. The data was extracted and replotted from [69] and [63].

difference between the direct and the indirect band gap is only on the order of 150 meV, and thus most light absorption is direct [70].

Single crystals of antimony sulfoiodide show birefringence. Hence, there are different refractive indices associated with the three crystal axes, $n_a = 3.1$, $n_b = 3.3$ and $n_c = 4.6$ at a wavelength of $\lambda = 655$ nm [71].

3.2.2 Synthesis routes of antimony sulfoiodide

Different synthesis routes for crystalline antimony sulfoiodide have been reported. Most of the early reports focus on the formation of macroscopic SbSI single crystals. However,

more recently, also synthesis methods forming thin films of polycrystalline SbSI were demonstrated. The different methods are listed in the following paragraphs.

Melting and vacuum evaporation

Stoichiometric amounts of antimony, sulfur and iodine can be heated to high temperatures ($T = 500\text{ }^{\circ}\text{C} - 600\text{ }^{\circ}\text{C}$) in sealed and evacuated glass ampoules to form SbSI single crystals upon cooling [72]. Alternatively, antimony sulfide (Sb_2S_3) and antimony iodide (SbI_3) can be used as precursor materials for the melting process [61, 72].

A very similar method is the co-evaporation of these precursor materials. Different evaporation techniques have been presented for antimony sulfoiodide, such as electron beam evaporation [68], flash evaporation [73] or thermal evaporation [74].

Hydrothermal deposition

An approach, which does not rely on an evacuated environment is the hydrothermal deposition of SbSI [75–77]. Here, SbCl_3 , I_2 and thiourea are mixed in an aqueous solution and then heated in an autoclave for more than 24 hours [77]. Chen *et al.* proposed a hydrothermal deposition using SbCl_3 , $(\text{NH}_2)_2\text{CS}$ and NH_4I in a HCl aqueous solution which produced SbSI crystals at 160°C after 4 hours [59].

Sonochemical deposition

A faster approach was presented by Nowak *et al.* who demonstrated a sonochemical deposition method [78]. They used a powerful ultrasound source to synthesise antimony sulfoiodide from elemental antimony, sulfur and iodine in ethanol in under two hours. A similar approach in an aqueous environment is also possible, as shown by the same research group [79].

Physical vapour deposition

In Chapter 7, a method is proposed, where solution-processed antimony sulfide (Sb_2S_3) is transformed into antimony sulfoiodide via a simple physical vapour evaporation of antimony iodide (SbI_3) at ambient pressure [80]. This is a fast and simple method for the deposition of antimony sulfoiodide needles in a thin film architecture.

3.2.3 Antimony sulfoiodide sensors

Due to its interesting optoelectronic properties, antimony sulfoiodide has been considered for the use in various sensing devices, such as gas sensors, photodetectors and humidity sensors [78].

In 2012, Starczewska *et al.* reported on the influence of humidity on the impedance of sonochemically deposited antimony sulfoiodide gel. They observed a decrease of the electric resistance of the SbSI gel in the dark by up to three orders of magnitude, when increasing the relative humidity from 10% to 85%. Two years later in 2014, these results were reproduced and studied further by Nowak *et al.* [79]. Also the photoconductivity of SbSI gels was studied as a function of humidity [81].

The high photoconductivity of SbSI makes it an interesting material for use in photodetectors. Nowak *et al.* studied the spectral response of aligned antimony sulfoiodide nanowires on a patterned electrode in 2013 [82]. In this work, the SbSI crystals were first synthesised using a sonochemical method and then transferred onto a patterned electrode. A strong electric field was applied to align the SbSI nanowires between the electrode fingers.

A photodetector based on a single antimony sulfoiodide crystal was presented by Chen *et al.* in 2015 [59]. Their photodetector device displayed a response to visible light with a specific detectivity of $D^* = 2.3 \cdot 10^8$ Jones and a response and recovery time of approximately $\tau_r = \tau_f = 0.3$ s.

In Chapter 7, a photodetector based on a thin film of antimony sulfoiodide micro crystals

in a sandwich type architecture is described. Using this approach, a specific detectivity of more than $D^* = 10^9$ Jones and response times of $\tau_r = 7.4$ ms and $\tau_f = 33.8$ ms is achieved in this thesis, see Chapter 7 [80].

Antimony sulfoiodide is theoretically expected to be an interesting material for solar cell applications [70]. However, there are no experimental reports on antimony sulfoiodide solar cells with promising power conversion efficiencies yet.

Bibliography

- [1] H. Zell. “*Stibnite, an Antimony Sulfide Mineral*”. (https://commons.wikimedia.org/wiki/File:Antimonit_02.jpg). The photography is licensed under CC BY-SA 3.0 (<http://creativecommons.org/licenses/by-sa/3.0>). Changes: Made background transparent. **2009**.
- [2] M. T. S. Nair, D. Avellaneda, S. Messina, and P. K. Nair. “Characteristics of Chemically Deposited Thin Film Solar Cells Using SnS and Sb₂S₃ Absorbers”. *Symposium CC –Solar Energy Conversion*. Vol. 974. MRS Online Proceedings Library Archive. **2006**, 0974–CC10–02 (6 pages). DOI: 10.1557/PROC-0974-CC10-02.
- [3] W. D. Blanchard, E. M. Stern, and L. P. Stodulski. “Analysis of Materials Contained in Mid-4th to Early 7th Century A. D. Palestinian Kohl Tubes”. *MRS Proceedings* 267 (**1992**). DOI: 10.1557/PROC-267-239.
- [4] C. G. Anderson. “Hydrometallurgically Treating Antimony-Bearing Industrial Wastes”. *JOM* 53.1 (**2001**), pp. 18–20. DOI: 10.1007/s11837-001-0156-y.
- [5] W. E. Engeler, M. Blumenfeld, and E. A. Taft. “The “Epicon” Array: A New Semiconductor Array-Type Camera Tube Structure”. *Applied Physics Letters* 16.5 (**1970**), pp. 202–205. DOI: 10.1063/1.1653162.
- [6] S. Kuze, D. D. Boulay, N. Ishizawa, A. Saiki, and A. Pring. “X-Ray Diffraction Evidence for a Monoclinic Form of Stibnite, Sb₂S₃, below 290 K”. *American Mineralogist* 89.7 (**2004**), pp. 1022–1025. DOI: 10.2138/am-2004-0712.
- [7] L. F. Lundegaard, R. Miletich, T. Balic-Zunic, and E. Makovicky. “Equation of State and Crystal Structure of Sb₂S₃ between 0 and 10 GPa”. *Physics and Chemistry of Minerals* 30.8 (**2003**), pp. 463–468. DOI: 10.1007/s00269-003-0339-x.
- [8] C.-M. Park, Y. Hwa, N.-E. Sung, and H.-J. Sohn. “Stibnite (Sb₂S₃) and its Amorphous Composite as Dual Electrodes for Rechargeable Lithium Batteries”. *J. Mater. Chem.* 20.6 (**2010**), pp. 1097–1102. DOI: 10.1039/B918220A.

Bibliography

- [9] V. P. Zakaznova-Herzog, S. L. Harmer, H. W. Nesbitt, G. M. Bancroft, R. Flemming, and A. R. Pratt. “High Resolution XPS Study of the Large-Band-Gap Semiconductor Stibnite (Sb₂S₃): Structural Contributions and Surface Reconstruction”. *Surface Science* 600.2 (2006), pp. 348–356. DOI: 10.1016/j.susc.2005.10.034.
- [10] C. Ghosh and B. P. Varma. “Optical Properties of Amorphous and Crystalline Sb₂S₃ Thin Films”. *Thin Solid Films* 60.1 (1979), pp. 61–65. DOI: 10.1016/0040-6090(79)90347-X.
- [11] M. Y. Versavel and J. A. Haber. “Structural and Optical Properties of Amorphous and Crystalline Antimony Sulfide Thin-Films”. *Thin Solid Films* 515.18 (2007), pp. 7171–7176. DOI: 10.1016/j.tsf.2007.03.043.
- [12] F. Perales, G. Lifante, F. Agulló-Rueda, and C. de las Heras. “Optical and Structural Properties in the Amorphous to Polycrystalline Transition in Sb₂S₃ Thin Films”. *Journal of Physics D: Applied Physics* 40.8 (2007), p. 2440. DOI: 10.1088/0022-3727/40/8/005.
- [13] R. H. Bube. “Photoelectronic Analysis of High Resistivity Crystals: (A) GaAs, (B) Sb₂S₃”. *Journal of Applied Physics* 31.2 (1960), pp. 315–322. DOI: 10.1063/1.1735564.
- [14] N. Bansal, F. T. F. O’Mahony, T. Lutz, and S. A. Haque. “Solution Processed Polymer–Inorganic Semiconductor Solar Cells Employing Sb₂S₃ as a Light Harvesting and Electron Transporting Material”. *Advanced Energy Materials* 3.8 (2013), pp. 986–990. DOI: 10.1002/aenm.201300017.
- [15] O. Savadogo and K. C. Mandal. “Studies on New Chemically Deposited Photoconducting Antimony Trisulphide Thin Films”. *Solar Energy Materials and Solar Cells* 26.1 (1992), pp. 117–136. DOI: 10.1016/0927-0248(92)90131-8.
- [16] A. Darga, D. Mencaraglia, C. Longeaud, T. J. Savenije, B. O’Regan, S. Bourdais, T. Muto, B. Delatouche, and G. Dennler. “On Charge Carrier Recombination in Sb₂S₃ and Its Implication for the Performance of Solar Cells”. *The Journal of Physical Chemistry C* 117.40 (2013), pp. 20525–20530. DOI: 10.1021/jp4072394.

-
- [17] B. H. Billings and M. Hyman. "The Infra-Red Refractive Index and Dispersion of Evaporated Stibnite Films". *Journal of the Optical Society of America* 37.2 (1947), p. 119. DOI: 10.1364/JOSA.37.000119.
- [18] Z. S. E. Mandouh and S. N. Salama. "Some Physical Properties of Evaporated Thin Films of Antimony Trisulphide". *Journal of Materials Science* 25.3 (1989), pp. 1715–1718. DOI: 10.1007/BF01045375.
- [19] J. George and M. K. Radhakrishnan. "Electrical Conduction in Coevaporated Antimony Trisulphide Films". *Solid State Communications* 33.9 (1980), pp. 987–989. DOI: 10.1016/0038-1098(80)90296-3.
- [20] R. S. Mane, B. R. Sankapal, and C. D. Lokhande. "Non-Aqueous Chemical Bath Deposition of Sb₂S₃ Thin Films". *Thin Solid Films* 353.1–2 (1999), pp. 29–32. DOI: 10.1016/S0040-6090(99)00362-4.
- [21] N. Maiti, S. H. Im, C.-S. Lim, and S. I. Seok. "A chemical precursor for depositing Sb₂S₃ onto mesoporous TiO₂ layers in nonaqueous media and its application to solar cells." *Dalton Transactions* 41.38 (2012), pp. 11569–72. DOI: 10.1039/c2dt31348k.
- [22] K. C. Mandal and A. Mondal. "A New Chemical Method for Preparing Semiconductor Grade Antimony Tri-Sulphide Thin Films". *Journal of Physics and Chemistry of Solids* 51.11 (1990), pp. 1339–1341. DOI: 10.1016/0022-3697(90)90014-7.
- [23] B. B. Nayak, H. N. Acharya, T. K. Chaudhuri, and G. B. Mitra. "The Dip-Dry Technique for Preparing Photosensitive Sb₂S₃ Films". *Thin Solid Films* 92.4 (1982), pp. 309–314. DOI: 10.1016/0040-6090(82)90153-5.
- [24] I. Grozdanov. "A Simple and Low-Cost Technique for Electroless Deposition of Chalcogenide Thin Films". *Semiconductor Science and Technology* 9.6 (1994), p. 1234. DOI: 10.1088/0268-1242/9/6/013.
- [25] M. T. S. Nair, Y. Pena, J. Campos, V. M. Garcia, and P. K. Nair. "Chemically Deposited Sb₂S₃ and Sb₂S₃-CuS Thin Films". *Journal of The Electrochemical Society* 145.6 (1998), pp. 2113–2120.

- [26] Y. C. Choi, D. U. Lee, J. H. Noh, E. K. Kim, and S. I. Seok. “Highly Improved Sb₂S₃ Sensitized-Inorganic–Organic Heterojunction Solar Cells and Quantification of Traps by Deep-Level Transient Spectroscopy”. *Advanced Functional Materials* 24.23 (2014), pp. 3587–3592. DOI: 10.1002/adfm.201304238.
- [27] K. C. Gödel, Y. C. Choi, B. Roose, A. Sadhanala, H. J. Snaith, S. I. Seok, U. Steiner, and S. K. Pathak. “Efficient room temperature aqueous Sb₂S₃ synthesis for inorganic–organic sensitized solar cells with 5.1% efficiencies”. *Chemical Communications* 51.41 (2015), pp. 8640–8643. DOI: 10.1039/C5CC01966D.
- [28] B. Yang, D.-J. Xue, M. Leng, J. Zhong, L. Wang, H. Song, Y. Zhou, and J. Tang. “Hydrazine Solution Processed Sb₂S₃, Sb₂Se₃ and Sb₂(S_{1-x}Se_x)₃ Film: Molecular Precursor Identification, Film Fabrication and Band Gap Tuning”. *Scientific Reports* 5 (2015), p. 10978. DOI: 10.1038/srep10978.
- [29] T. Lutz, A. MacLachlan, A. Sudlow, J. Nelson, M. S. Hill, K. C. Molloy, and S. A. Haque. “Thermal Decomposition of Solution Processable Metal Xanthates on Mesoporous Titanium Dioxide Films: A New Route to Quantum-Dot Sensitised Heterojunctions”. *Physical Chemistry Chemical Physics* 14.47 (2012), pp. 16192–16196. DOI: 10.1039/C2CP43534A.
- [30] Y. C. Choi and S. I. Seok. “Efficient Sb₂S₃-Sensitized Solar Cells Via Single-Step Deposition of Sb₂S₃ Using S/Sb-Ratio-Controlled SbCl₃-Thiourea Complex Solution”. *Advanced Functional Materials* 25.19 (2015), pp. 2892–2898. DOI: 10.1002/adfm.201500296.
- [31] N. S. Yesugade, C. D. Lokhande, and C. H. Bhosale. “Structural and Optical Properties of Electrodeposited Bi₂S₃, Sb₂S₃ and As₂S₃ Thin Films”. *Thin Solid Films* 263.2 (1995), pp. 145–149. DOI: 10.1016/0040-6090(95)06577-6.
- [32] K. Y. Rajpure and C. H. Bhosale. “Effect of Composition on the Structural, Optical and Electrical Properties of Sprayed Sb₂S₃ Thin Films Prepared from Non-Aqueous Medium”. *Journal of Physics and Chemistry of Solids* 61.4 (2000), pp. 561–568. DOI: 10.1016/S0022-3697(99)00240-1.

-
- [33] H. Wedemeyer, J. Michels, R. Chmielowski, S. Bourdais, T. Muto, M. Sugiura, G. Dennler, and J. Bachmann. "Nanocrystalline solar cells with an antimony sulfide solid absorber by atomic layer deposition". *Energy & Environmental Science* 6.1 (2013), p. 67. DOI: 10.1039/c2ee23205g.
- [34] O. Savadogo and K. Mandal. "Improved Schottky Barrier on N-Sb₂S₃ Films Chemically Deposited with Silicotungstic Acid". *Electronics Letters* 28.18 (1992), p. 1682. DOI: 10.1049/el:19921069.
- [35] O. Savadogo and K. C. Mandal. "Low-cost Technique for Preparing n-Sb₂S₃/p-Si Heterojunction Solar Cells". *Applied Physics Letters* 63.2 (1993), pp. 228–230. DOI: 10.1063/1.110349.
- [36] O. Savadogo and K. C. Mandal. "Fabrication of Low-Cost N-Sb₂S₃/P-Ge Heterojunction Solar Cells". *Journal of Physics D: Applied Physics* 27.5 (1994), pp. 1070–1075. DOI: 10.1088/0022-3727/27/5/028.
- [37] O. Savadogo. "Low Cost Schottky Barrier Solar Cells Fabricated on CdSe and Sb₂S₃ Films Chemically Deposited with Silicotungstic Acid". *Journal of The Electrochemical Society* 141.10 (1994), p. 2871. DOI: 10.1149/1.2059248.
- [38] L. P. Deshmukh, S. G. Holikatti, B. P. Rane, B. M. More, and P. P. Hankare. "Preparation and Properties of Sb₂S₃ Thin Films for Photoelectrochemical Applications". *Journal of The Electrochemical Society* 141.7 (1994), pp. 1779–1783. DOI: 10.1149/1.2055004.
- [39] V. Killedar, C. Lokhande, and C. Bhosale. "Preparation and Characterization of Spray Deposited Sb₂S₃ Thin Films from Non-Aqueous Medium". *Materials chemistry and physics* 47 (1997), pp. 104–107.
- [40] R. Vogel, P. Hoyer, and H. Weller. "Quantum-Sized PbS, CdS, Ag₂S, Sb₂S₃, and Bi₂S₃ Particles as Sensitizers for Various Nanoporous Wide-Bandgap Semiconductors". *The Journal of Physical Chemistry* 98.12 (1994), pp. 3183–3188. DOI: 10.1021/j100063a022.
- [41] Y. Itzhaik, O. Niitsoo, M. Page, and G. Hodes. "Sb₂S₃ -Sensitized Nanoporous TiO₂ Solar Cells". *The Journal of Physical Chemistry C Letters* 113 (2009), pp. 4254–4256.

Bibliography

- [42] J. A. Chang, J. H. Rhee, S. H. Im, Y. H. Lee, H.-J. Kim, S. I. Seok, M. K. Nazeeruddin, and M. Graetzel. "High-Performance Nanostructured Inorganic-Organic Heterojunction Solar Cells." *Nano Letters* 10.7 (2010), pp. 2609–12. DOI: 10.1021/nl101322h.
- [43] S.-J. Moon, Y. Itzhaik, J.-H. Yum, S. M. Zakeeruddin, G. Hodes, and M. Grätzel. "Sb₂S₃-Based Mesoscopic Solar Cell using an Organic Hole Conductor". *The Journal of Physical Chemistry Letters* 1.10 (2010), pp. 1524–1527. DOI: 10.1021/jz100308q.
- [44] S. H. Im, C.-S. Lim, J. A. Chang, Y. H. Lee, N. Maiti, H.-J. Kim, M. K. Nazeeruddin, M. Grätzel, and S. I. Seok. "Toward Interaction of Sensitizer and Functional Moieties in Hole-Transporting Materials for Efficient Semiconductor-Sensitized Solar Cells." *Nano Letters* 11.11 (2011), pp. 4789–93. DOI: 10.1021/nl2026184.
- [45] J. C. Cardoso, C. A. Grimes, X. Feng, X. Zhang, S. Komarneni, M. V. B. Zanoni, and N. Bao. "Fabrication of Coaxial TiO₂/Sb₂S₃ Nanowire Hybrids for Efficient Nanostructured Organic–Inorganic Thin Film Photovoltaics". *Chemical Communications* 48.22 (2012), p. 2818. DOI: 10.1039/c2cc17573h.
- [46] J. A. Chang, S. H. Im, Y. H. Lee, H.-J. Kim, C.-S. Lim, J. H. Heo, and S. I. Seok. "Panchromatic photon-harvesting by hole-conducting materials in inorganic-organic heterojunction sensitized-solar cell through the formation of nanostructured electron channels." *Nano letters* 12.4 (2012), pp. 1863–7. DOI: 10.1021/nl204224v.
- [47] K. Tsujimoto, D.-C. Nguyen, S. Ito, H. Nishino, H. Matsuyoshi, A. Konno, G. R. A. Kumara, and K. Tennakone. "TiO₂ Surface Treatment Effects by Mg²⁺, Ba²⁺, and Al³⁺ on Sb₂S₃ Extremely Thin Absorber Solar Cells". *The Journal of Physical Chemistry C* 116.25 (2012), pp. 13465–13471. DOI: 10.1021/jp208937j.
- [48] S. Ito, K. Tsujimoto, D.-C. Nguyen, K. Manabe, and H. Nishino. "Doping Effects in Sb₂S₃ Absorber for Full-Inorganic Printed Solar Cells with 5.7% Conversion Efficiency". *International Journal of Hydrogen Energy* 38.36 (2013), pp. 16749–16754. DOI: 10.1016/j.ijhydene.2013.02.069.

-
- [49] S. A. Manolache and A. Dut. "The Development of Crystalline Sb₂S₃ Thin Films as A Component of The Three-Dimensional (3D) Solar Cells". 11.2 (2008), pp. 109–121.
- [50] S. Nezu, G. Larramona, C. Chone', A. Jacob, B. Delatouche, D. Pe're', and C. Moisan. "Light Soaking and Gas Effect on Nanocrystalline TiO₂/Sb₂S₃/CuSCN Photovoltaic Cells Following Extremely Thin Absorber Concept". *The Journal of Physical Chemistry C* 114.14 (2010), pp. 6854–6859.
- [51] Y. Rodriguez-Lazcano, M. T. S. Nair, and P. K. Nair. "Photovoltaic P-I-N Structure of Sb₂S₃ and CuSbS₂ Absorber Films Obtained via Chemical Bath Deposition". *Journal of The Electrochemical Society* 152.8 (2005), G635–G638. DOI: 10.1149/1.1945387.
- [52] S. Messina, M. Nair, and P. Nair. "Antimony sulfide thin films in chemically deposited thin film photovoltaic cells". *Thin Solid Films* 515.15 (2007), pp. 5777–5782. DOI: 10.1016/j.tsf.2006.12.155.
- [53] S. Messina, M. Nair, and P. Nair. "Solar cells with Sb₂S₃ absorber films". *Thin Solid Films* 517.7 (2009), pp. 2503–2507. DOI: 10.1016/j.tsf.2008.11.060.
- [54] D.-H. Kim, S.-J. Lee, M. S. Park, J.-K. Kang, J. H. Heo, S. H. Im, and S.-J. Sung. "Highly Reproducible Planar Sb₂S₃-Sensitized Solar Cells Based on Atomic Layer Deposition". *Nanoscale* 6.23 (2014), pp. 14549–14554. DOI: 10.1039/C4NR04148H.
- [55] E. Zimmermann, T. Pfadler, J. Kalb, J. A. Dorman, D. Sommer, G. Hahn, J. Weickert, and L. Schmidt-Mende. "Toward High-Efficiency Solution-Processed Planar Heterojunction Sb₂S₃ Solar Cells". *Advanced Science* (2015), p. 1500059. DOI: 10.1002/advs.201500059.
- [56] S. Yuan, H. Deng, D. Dong, X. Yang, K. Qiao, C. Hu, H. Song, H. Song, Z. He, and J. Tang. "Efficient Planar Antimony Sulfide Thin Film Photovoltaics with Large Grain and Preferential Growth". *Solar Energy Materials and Solar Cells* 157 (2016), pp. 887–893. DOI: 10.1016/j.solmat.2016.07.050.

Bibliography

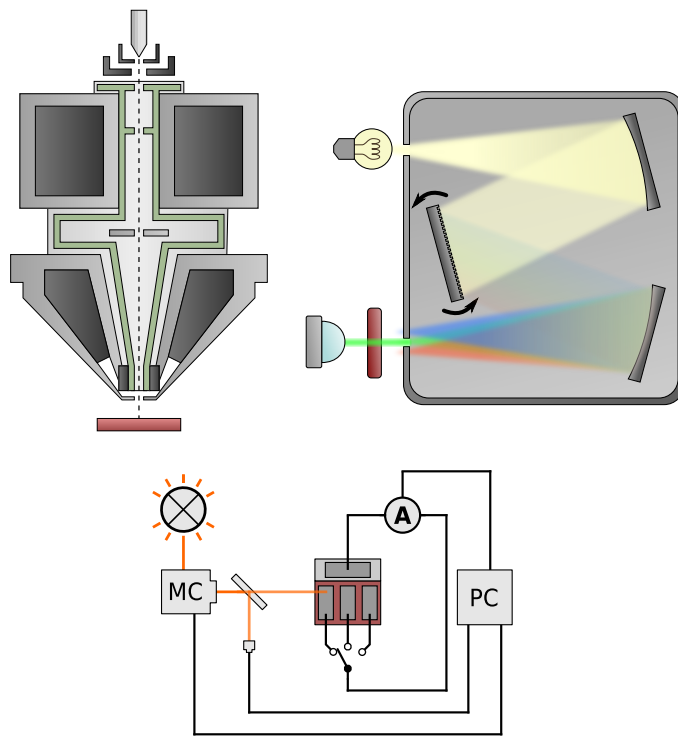
- [57] H. Lei et al. “Efficient Planar Sb₂S₃ Solar Cells Using a Low-Temperature Solution-Processed Tin Oxide Electron Conductor”. *Physical Chemistry Chemical Physics* (2016). DOI: 10.1039/C6CP02072K.
- [58] T. Muto, G. Larramona, and G. Dennler. “Unexpected Performances of Flat Sb₂S₃-Based Hybrid Extremely Thin Absorber Solar Cells”. *Applied Physics Express* 6.7 (2013), p. 072301. DOI: 10.7567/APEX.6.072301.
- [59] G. Chen, W. Li, Y. Yu, and Q. Yang. “Fast and low-temperature synthesis of one-dimensional (1D) single-crystalline SbSI microrod for high performance photodetector”. *RSC Advances* 5.28 (2015), pp. 21859–21864. DOI: 10.1039/C5RA01180A.
- [60] P. Szperlich, B. Toroń, M. Nowak, M. Jesionek, M. Kepinska, and W. Bogdanowicz. “Growth of large SbSI crystals”. *Materials Science-Poland* 32.4 (2014). DOI: 10.2478/s13536-014-0247-4.
- [61] E. Dönges. “Über Chalkogenohalogenide Des Dreiwertigen Antimons Und Wismuts. I. Über Thiohalogenide Des Dreiwertigen Antimons Und Wismuts”. *Zeitschrift für anorganische und allgemeine Chemie* 263.1-3 (1950), pp. 112–132. DOI: 10.1002/zaac.19502630113.
- [62] A. Kikuchi, Y. Oka, and E. Sawaguchi. “Crystal Structure Determination of SbSI”. *Journal of the Physical Society of Japan* 23.2 (1967), pp. 337–354. DOI: 10.1143/JPSJ.23.337.
- [63] E. Fatuzzo, G. Harbeke, W. J. Merz, R. Nitsche, H. Roetschi, and W. Ruppel. “Ferroelectricity in SbSI”. *Physical Review* 127.6 (1962), pp. 2036–2037. DOI: 10.1103/PhysRev.127.2036.
- [64] V. Keppens. “Structural transitions: ‘Ferroelectricity’ in a Metal”. *Nature Materials* 12.11 (2013), pp. 952–953. DOI: 10.1038/nmat3774.
- [65] P. Kwolek, K. Pilarczyk, T. Tokarski, J. Mech, J. Irzmański, and K. Szaciłowski. “Photoelectrochemistry of n-type antimony sulfoiodide nanowires”. *Nanotechnology* 26.10 (2015), p. 105710. DOI: 10.1088/0957-4484/26/10/105710.
- [66] K. Irie. “Excitation of Trapped Electrons in SbSI”. *Journal of the Physical Society of Japan* 34.6 (1973), pp. 1530–1535. DOI: 10.1143/JPSJ.34.1530.

-
- [67] M. Nowak, E. Talik, P. Szperlich, and D. Stroz. “XPS Analysis of Sonochemically Prepared SbSI Ethanogel”. *Applied Surface Science* 255.17 (2009), pp. 7689–7694. DOI: 10.1016/j.apsusc.2009.04.138.
- [68] M. Yoshida, K. Yamanaka, and Y. Hamakawa. “Semiconducting and Dielectric Properties of C-Axis Oriented SbSI Thin Film”. *Japanese Journal of Applied Physics* 12.11 (1973), pp. 1699–1705. DOI: 10.1143/JJAP.12.1699.
- [69] M. Nowak, P. Szperlich, A. Kidawa, M. Kepinska, P. Gorczycki, and B. Kauch. “Optical and Photoelectrical Properties of SbSI”. *Proceedings of SPIE*. Ed. by J. Rutkowski and A. Rogalski. Vol. 5136. 2003, pp. 172–177. DOI: 10.1117/12.518846.
- [70] K. T. Butler, J. M. Frost, and A. Walsh. “Ferroelectric materials for solar energy conversion: photoferroics revisited”. *Energy & Environmental Science* 8.3 (2015), pp. 838–848. DOI: 10.1039/C4EE03523B.
- [71] K. Ohi and O. Arizumi. “Refractive Indices of SbSI”. *Journal of the Physical Society of Japan* 22.5 (1967), 1307A–1307A. DOI: 10.1143/JPSJ.22.1307A.
- [72] R. Nitsche and W. J. Merz. “Photoconduction in Ternary V-VI-VII Compounds”. *Journal of Physics and Chemistry of Solids* 13.1 (1960), pp. 154–155. DOI: 10.1016/0022-3697(60)90136-0.
- [73] A. Mansingh and T. S. Rao. “Growth and Characterization of Flash-evaporated Ferroelectric Antimony Sulphoiodide Thin Films”. *Journal of Applied Physics* 58.9 (1985), pp. 3530–3535. DOI: 10.1063/1.335779.
- [74] Z. Dziuba. “Crystallization of SbSI Crystal from the Vapour Phase”. *Journal of Crystal Growth* 35.3 (1976), pp. 340–342. DOI: 10.1016/0022-0248(76)90200-1.
- [75] H. Rau and A. Rabenau. “Crystal Syntheses and Growth in Strong Acid Solutions under Hydrothermal Conditions”. *Solid State Communications* 5.5 (1967), pp. 331–332. DOI: 10.1016/0038-1098(67)90767-3.
- [76] C. Wang, K. Tang, Q. Yang, B. Hai, G. Shen, C. An, W. Yu, and Y. Qian. “Synthesis of Novel SbSI Nanorods by a Hydrothermal Method”. *Inorganic Chemistry Communications* 4.7 (2001), pp. 339–341. DOI: 10.1016/S1387-7003(01)00208-8.

Bibliography

- [77] I. Cho, B.-K. Min, S. W. Joo, and Y. Sohn. “One-Dimensional Single Crystalline Antimony Sulfur Iodide, SbSI”. *Materials Letters* 86 (2012), pp. 132–135. DOI: 10.1016/j.matlet.2012.07.050.
- [78] M. Nowak, P. Szperlich, L. Bober, J. Szala, G. Moskal, and D. Stroz. “Sonochemical Preparation of SbSI Gel”. *Ultrasonics Sonochemistry* 15.5 (2008), pp. 709–716. DOI: 10.1016/j.ultsonch.2007.09.003.
- [79] M. Nowak et al. “Fabrication and characterization of SbSI gel for humidity sensors”. *Sensors and Actuators A: Physical* 210 (2014), pp. 119–130. DOI: 10.1016/j.sna.2014.02.012.
- [80] K. C. Gödel and U. Steiner. “Thin Film Synthesis of SbSI Micro-Crystals for Self-Powered Photodetectors with Rapid Time Response”. *Nanoscale* 8.35 (2016), pp. 15920–15925. DOI: 10.1039/C6NR04759A.
- [81] M. Nowak, K. Mistewicz, A. Nowrot, P. Szperlich, M. Jesionek, and A. Starczewska. “Transient characteristics and negative photoconductivity of SbSI humidity sensor”. *Sensors and Actuators A: Physical* 210 (2014), pp. 32–40. DOI: 10.1016/j.sna.2014.02.004.
- [82] M. Nowak, L. Bober, B. Borkowski, M. Kepinska, P. Szperlich, D. Stróż, and M. Sozańska. “Quantum efficiency coefficient for photogeneration of carriers in SbSI nanowires”. *Optical Materials* 35.12 (2013), pp. 2208–2216. DOI: 10.1016/j.optmat.2013.06.003.

Experimental techniques



This chapter describes the key experimental techniques which were used for this thesis. Further, a brief overview of the methods for material characterisation is given, followed by a short description of the recurring processing steps for fabricating solar cells and photodetectors. Finally, the measurement principles for obtaining optoelectronic properties of these devices are explained.

4.1 Material characterisation techniques

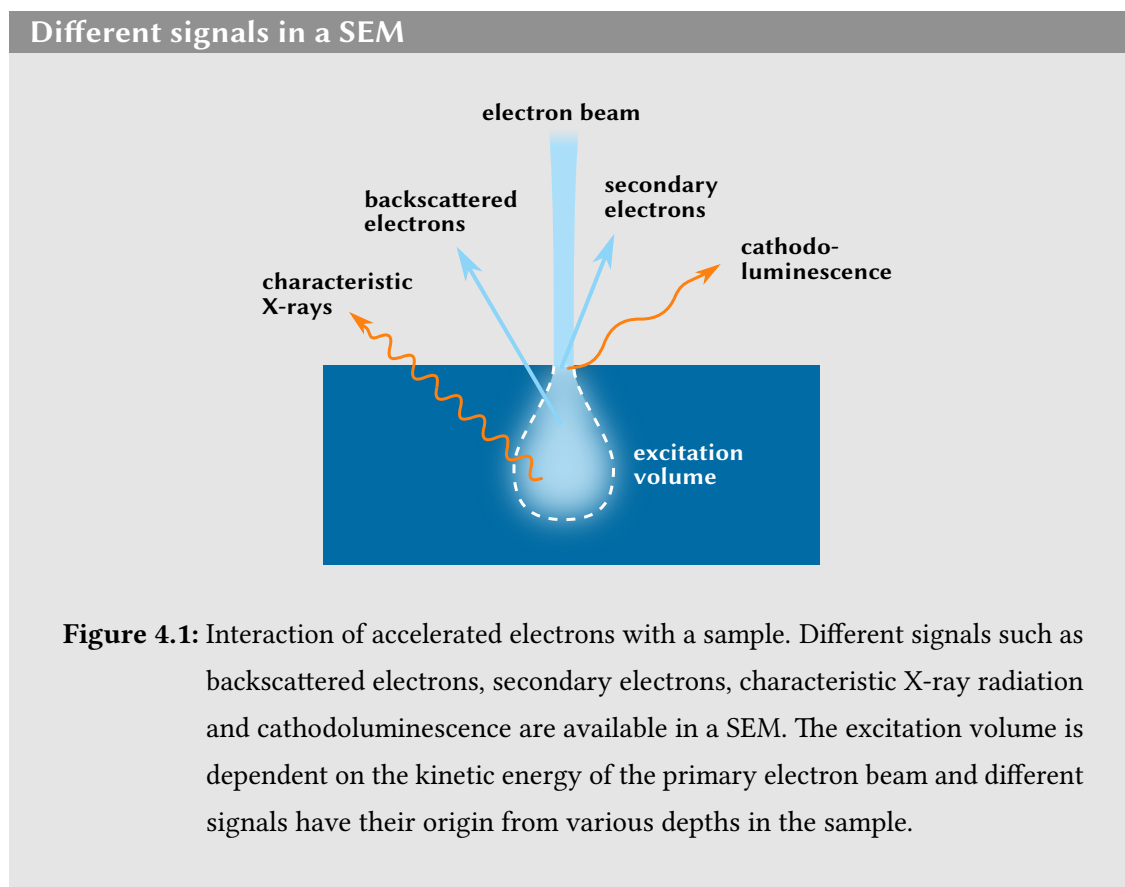
A large part of this thesis consists of new synthesis routes for sulfide semiconductors. The characterisation of the material properties is thus essential for a deep understanding of the materials and their use as components in optoelectronic devices. The material characterisation should incorporate the investigation of all, structural, chemical and physical properties of the synthesised substance.

4.1.1 Electron microscopy

Scanning electron microscopy

In this thesis, scanning electron microscopy (SEM) was primarily used for the micro- and nano-structural analysis of films, deposits or parts of devices. As the length scale of many relevant structures (e.g. film thickness or porosity of the components) is on the order of nanometres to micrometres, optical microscopy is not suitable due to its diffraction limited resolution. SEM, however, uses a beam of accelerated electrons with much shorter wavelengths compared to visible light, which can be deflected in the field of electromagnetic coils in high vacuum. Thus, it can scan the surface of the specimen under investigation and a localised signal of the interaction between the electron beam and the sample can be recorded. This signal can be of various forms, as there are several physical mechanisms describing the interaction of electrons with matter. Most notably one can detect backscattered electrons, secondary electrons, characteristic X-ray radiation and

cathodoluminescence. An overview of the different signals generated, when electrons in a SEM interact with the sample is schematically shown in Figure 4.1.



If not stated otherwise, the detector for secondary electrons was used for the structural analysis of the samples. Secondary electrons originate from inelastic scattering from weakly bound states with a relatively low kinetic energy on the order of a few eV. Because of the low energy, only secondary electrons can escape from the volume near the surface of the substrate and the signal therefore mainly contains information about the topology of the specimen. Nonetheless, the topographical information of a SEM image is always rather of qualitative nature, as charging effects and other artefacts can alter the appearance and scale of the image [1].

Images were recorded using a Leo Gemini 1530 VP SEM with a Schottky-emitter consisting of a zirconium oxide coated tungsten cathode and an in-lens secondary

electron detector. For imaging, acceleration voltages between $V = 3 - 5$ kV were used and the working distance (distance between the objective lens and the sample) was adjusted to roughly 3 mm. Non-conductive samples or materials with high resistivity were sputter-coated with a thin (< 1 nm) layer of a gold-palladium alloy to prevent charging of the sample and with that the occurrence of artefacts. The resolution limit for the used SEM lies at approximately 2 nm.

4.1.2 X-ray photoelectron spectroscopy

To examine the chemical composition of a material X-ray photoelectron spectroscopy (XPS) is a useful tool. XPS takes advantage of the photoelectric effect. The sample is irradiated with X-ray radiation of a well known energy, which leads to the emission of photoelectrons. The initial binding energy E_b of the photoelectron can be calculated from its kinetic energy E_{kin} after the emission process from the equation

$$E_b = \frac{hc}{\lambda} - E_{kin} - W . \quad (4.1)$$

where $\frac{hc}{\lambda}$ is the energy of the X-ray photon and W the (constant) work function of the detector material [2]. The binding energy is characteristic for the orbital from where the electron was released. The full photoelectron spectrum then provides a good map of the electronic structure of the investigated elements [2]. An illustration of the relationship of the XPS spectrum to the electronic structure of an element (lead is used as an example) is shown in Figure 4.2. Another signal, which can be probed by XPS, are Auger electrons. When a photoelectron is ejected, it leaves behind a hole which is then filled with an electron from a higher shell. The energy either results in the emission of characteristic X-ray radiation or in the release of Auger electrons.

XPS only accounts for electrons, which are actually released from the sample. The depth of signal received by the XPS detector is only on the order of a few nanometres (< 10 nm). XPS is therefore considered a surface sensitive characterisation technique [2].

The electron detectors need to be installed far away (on the order of metres) from the

Origin of a XPS spectrum

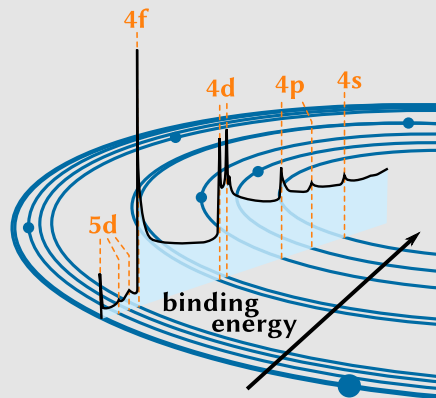


Figure 4.2: Illustration of how a XPS spectrum relates to the electronic structure of an atom. As an example lead (Pb) is used. The peaks correspond to the different orbitals. The background of the spectrum is caused by electrons which undergo elastic scattering and thus lose kinetic energy. The figure was redrawn from [2].

X-ray source, which leads to the necessity of ultra high vacuums for XPS instruments for an accurate detection of the kinetic energy of the photoelectrons.

4.1.3 X-ray diffraction

For many optoelectronic materials, the crystalline properties are of crucial interest. Crystals have distinct atomic layers, the lattice planes of the crystal. These can be probed by electromagnetic radiation in the X-ray spectrum ($\lambda = 0.01 - 10 \text{ nm}$), because the planes have spacings on similar length scales as the X-ray wavelength, on the order of 0.1 nm .

X-ray diffraction (XRD) measurements use the interference of X-ray radiation, which is reflected on parallel lattice planes.

The reflected modes interfere constructively, when Bragg's law is fulfilled

$$n\lambda = 2d \sin(\theta), \quad (4.2)$$

where λ is the wavelength of the X-ray radiation, θ the angle of incidence, d the lattice spacing of the crystal planes and n is the diffraction order. The diffraction from a crystal lattice is schematically illustrated in Figure 4.3.

X-ray diffraction on a crystal

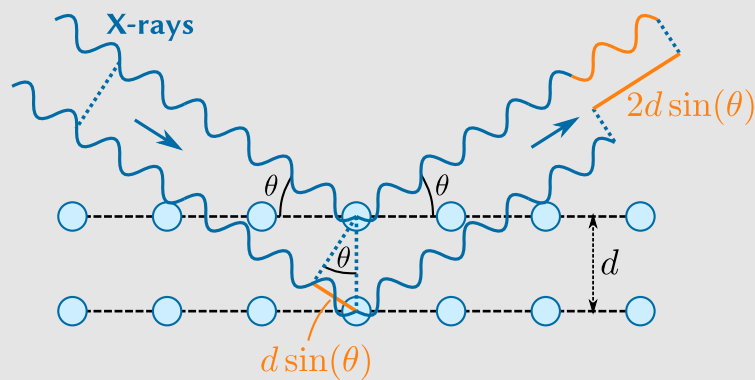


Figure 4.3: X-ray diffraction from a crystal lattice with lattice spacing d . The schematic illustrates constructive interference of X-rays for the second order ($n = 2$), because the phase shift of the two beams is exactly twice the wavelength λ .

Measuring the interference intensity at different angles θ yields a pattern, which is characteristic for a specific crystal. For a powder of crystalline material or randomly oriented polycrystalline samples, all different planes of the crystal lattice are probed and peaks in the pattern can be attributed accordingly.

XRD can be used to identify crystalline phases by comparing measured data to reported standards. From the pattern, it is also possible to determine the crystallinity of the sample and to calculate the average crystal size. Amorphous (i.e. non-crystalline) parts lead to very broad peaks and to an overall offset of the intensity. The smaller the width of the peaks, the larger are the crystallites in the sample.

The mean crystal size D can be calculated using the so-called Scherrer equation

$$D = \frac{K\lambda}{\Delta_{2\theta} \cos(\theta)}, \quad (4.3)$$

where $\Delta_{2\theta}$ is the peak broadening and K a dimensionless factor with a value around one, depending on the shape of the crystals [3, 4]. The peak broadening can be determined using the FWHM of the peaks, or better the integral breadth, which is the width of a rectangle with same height and area as the peak [5]. When using the integral breadth, one can assume $K = 1$ [5]. The analysis of crystallite sizes using the Scherrer equation is only valid for mean crystal sizes up to $D = 100 - 200$ nm. For larger crystals other factors such as the instrument broadening become more dominant [6].

XRD patterns were measured in the so called Bragg-Brentano geometry, where source and detector move simultaneously on a circle around the fixed sample, so that both of the apparatus (source and detector) confine an angle θ with the sample. With this setup, the pattern is typically described by a 2θ -intensity diagram. All XRD measurements were performed in the Department of Materials Science & Metallurgy of the University of Cambridge on a Bruker D8 theta/theta with a LynxEye position sensitive detector and a standard SC detector with an auto-absorber, graphite 2nd beam monochromator and sample rotation. The limit of the instrumental resolution was approximately 0.08° for the 2θ angle [7].

4.1.4 Absorption measurements

One of the most simple but also fundamental characterisation techniques for optoelectronic materials is the measurement of absorption spectra.

UV-vis spectroscopy

Ultraviolet-visible (UV-vis) spectrometry provides an estimate for the band gap of a semiconducting material and the amount of absorption can be quantified. The UV-vis

spectra shown in this thesis are transmittance measurements through material films. If reflection losses and scattering is neglected, the absorbance A can be calculated,

$$A(\lambda) = -\log_{10} T(\lambda), \quad (4.4)$$

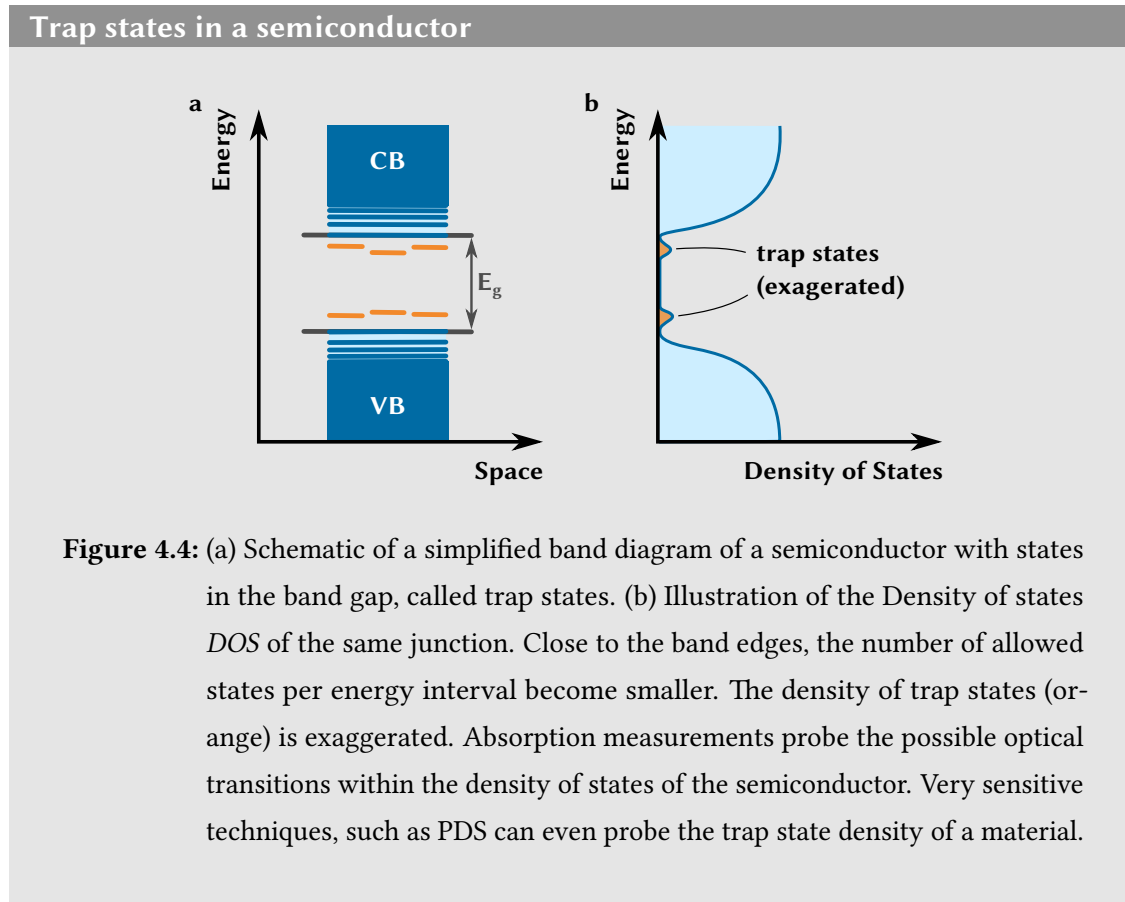
where the transmittance $T(\lambda) = \frac{\Phi_{e,t}(\lambda)}{\Phi_{e,i}(\lambda)}$ is the ratio of radiant flux with and without the sample. For scattering samples, an integrating sphere has to be used additionally. The inside of this sphere is coated with a highly diffuse reflective paint, enabling to measure spectra of scattering samples.

Two different spectrometers were used in course of this thesis. The first was an Agilent 8453 UV-vis spectroscopy system from Agilent Technologies which operates in a wavelength range from 190 nm to 1100 nm with an interval length of 1.0 nm. It uses two built-in light sources, a tungsten lamp and a deuterium lamp. The integration time of the photodiode detector array was set to 0.5 s. The second apparatus was an Ocean Optics USB 2000 spectrometer which has to be connected to glass fibres for light guiding and to an external tungsten light source.

Photothermal deflection spectroscopy

A very sensitive absorption measurement is possible using photothermal deflection spectroscopy (PDS). It probes sub band gap states (also called trap states) in semiconductors. Figure 4.4 illustrates the trap states of a semiconductor and its density of states. The density of sub band gap states is exaggerated for clarity. As the density of states below the band gap of a semiconductor is normally very low compared to above the band gap, absorption is several orders of magnitude lower when probing these states.

In transverse PDS, which was used for the studies in this thesis, a laser beam is sent along the surface of the sample where it is deflected due to a local change of refractive index. This change of refractive index is caused by a second perpendicular light beam, which is tunable in wavelength. It causes an increase in temperature when it is absorbed by the sample due to the non-radiative relaxation of the absorbed photons [8, 9]. The deflection is measured using a four quadrant photodiode. To increase the



deflection effect, samples are normally submerged into inert non-absorbing liquids, such as perfluorocarbons, which have a high change in refractive index per unit of temperature change. PDS is insensitive to reflection and scattering [9].

4.2 Device fabrication

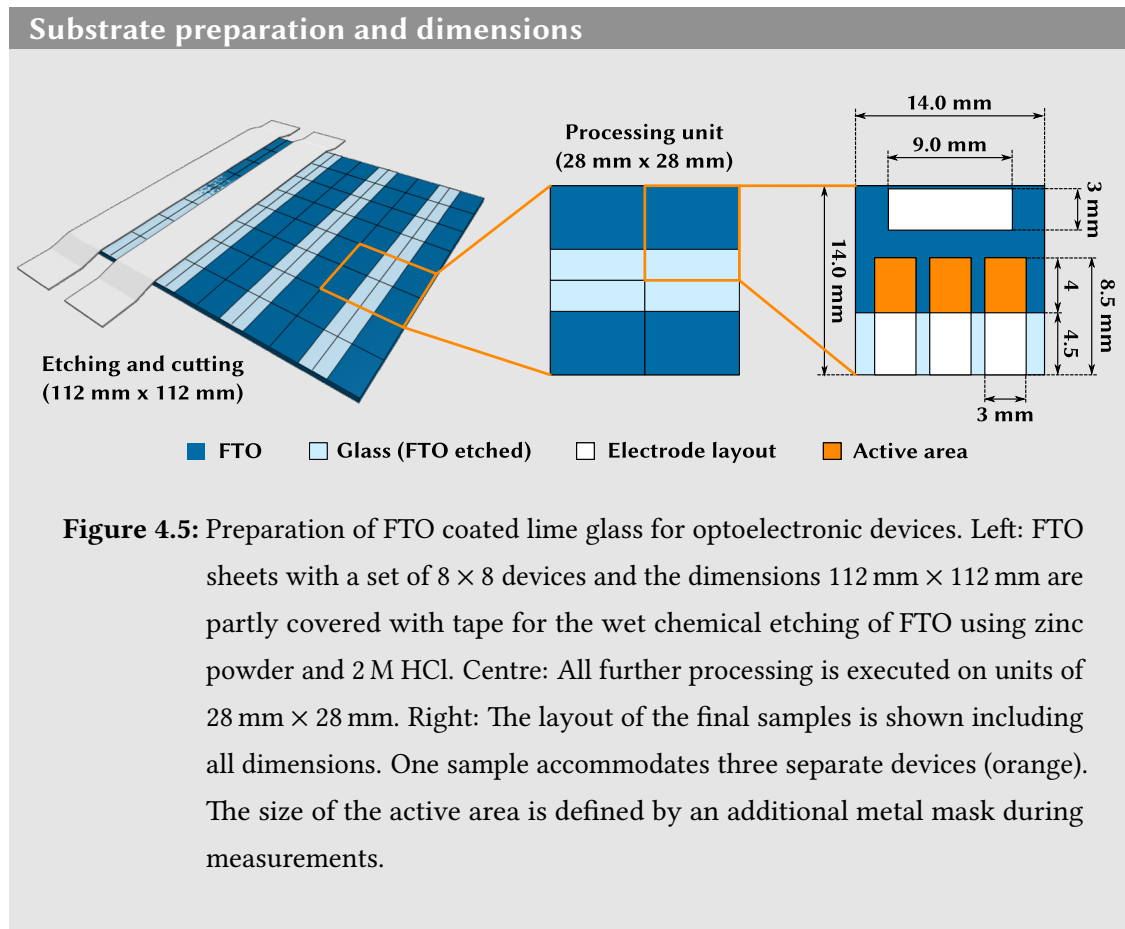
Many of the crucial steps for the device fabrication process are optimised, improved or part of the main subject of the individual studies presented in Chapters 5–7. Here, some reoccurring fabrication steps and experimental procedures are introduced and described. The focus is laid on the steps which were not the main focus of the studies in this thesis, but repeatedly used for the fabrication of different optoelectronic devices.

4.2.1 Substrate preparation

All devices and many specimen for material characterisation in this thesis were fabricated on conductive fluorine doped tin oxide (FTO) coated float glass. The glass sheets are 2.2 mm thick and are covered with a crystalline layer of FTO with a thickness on the order of 0.5 – 1 μm depending on the used conductivity. Normally, sheets from Solaronix or Sigma Aldrich with surface resistances of $R_s = 8 - 15 \Omega/\square$ were used.

The dimensions of the samples in this thesis, if not mentioned otherwise, were 14 mm \times 14 mm, accommodating three optoelectronic devices with an maximum active area of 3 mm \times 4 mm. The dimensions are illustrated in Figure 4.5 (right). The FTO glass comes in sheets of 300 mm \times 300 mm and was cut to size and labelled using a self-built automated glass cutting and labelling system, which was developed in collaboration with Raphael Dehmel. The glass is scored using a steel wheel cutter and labels are engraved with a diamond scribe.

To prevent shorting of the devices during electronic measurements, part of the conductive FTO layer has to be etched away. The etching procedure is normally done on a FTO sheet with a set of 8 \times 8 devices and the dimensions 112 mm \times 112 mm. The parts which are not supposed to be etched are protected using 3M Scotch Magic Tape which is available in a compatible width of 19 mm (see also Figure 4.5, left). The etching itself is done using zinc powder and hydrochloric acid (HCl) with a concentration of $c = 2 \text{ M}$ [10, 11]. The zinc powder is spread on the FTO between the protecting tape stripes and the 2 M HCl solution is added. After 1-2 min, both compounds are wiped off using paper towels and the substrate is rinsed with water to remove excess zinc and acid solution. The glass is further cleaned with a soap solution (2 % Hellmanex in DI water), cleaned in an ultrasonic bath subsequently with acetone and ethanol for 15 min each and then followed by an oxygen-plasma treatment for 10 min. For all further steps, the glass substrate is cut into processing units of 2 \times 2 devices and dimensions of 28 mm \times 28 mm (see Figure 4.5, centre), a convenient size for laboratory scale fabrication.



4.2.2 Porous metal-oxide anodes

For sensitised solar cells, a mesoporous electrode of metal oxide, most commonly titanium dioxide (TiO_2) has to be deposited. The following paragraphs describe the preparation of this TiO_2 electrodes, including a thin TiO_2 blocking layer, the mesoporous nanocrystalline film and a TiCl_4 treatment to improve charge injection from the absorber layer.

Compact titanium dioxide layer

Prior to the porous film, a very thin layer of compact TiO_2 is applied to prevent the direct contact of the absorbing material or the hole conductor with the FTO electrode. This layer is also sometimes referred to as the hole blocking layer. In course of this thesis, two different methods for the deposition of compact TiO_2 layers for photovoltaic devices were used, spray pyrolysis and sol-gel spin-coating.

The applied procedure follows in large parts the method described by Kavan et al. [12]. For the spray pyrolysis, the patterned FTO substrates were placed onto a hotplate at a temperature of $T = 450^\circ\text{C}$. Thin stripes of microscope slides were used to cover the part which later should be in direct contact with the metal counter-electrode. Titanium diisopropoxide bis(acetylacetonate) 75 wt. % in isopropanol (from Sigma Aldrich) was mixed with anhydrous ethanol at a volume ratio of 1:10. Approximately 1 ml per 25 cm^2 spray area of the mixture were then manually sprayed onto the substrates using a glass sprayer with air as the carriage gas. The samples were then heated at $T = 550^\circ\text{C}$ for one hour. This results in a compact TiO_2 layer with a thickness of approximately 50 nm – 100 nm.

Alternatively, the hole blocking layer can be deposited using a sol-gel method by spin-coating as described by Choi et al. [13]. To prepare the precursor solution, 50 ml absolute ethanol, 0.9 ml DI water and 0.12 ml HNO_3 are mixed. Then a solution of 50 ml absolute ethanol and 3.18 ml titanium isopropoxide is added. This solution is stable when stored in the fridge for several months, but should be filtered using a $0.45\text{ }\mu\text{m}$ PTFE filter before use. To form the compact TiO_2 film with a thickness of roughly 100 nm, five subsequent layers are spin-coated at 3000 RPM with an intermediate drying period of 2 min at a temperature of $T = 200^\circ\text{C}$.

Mesoporous titanium dioxide film

On top of the hole blocking layer, the porous electron conducting film provides the high surface area needed for sensitised solar cells. In this thesis, exclusively titanium

dioxide was used as mesoporous metal-oxide. However, different deposition methods and porosities were used.

In Chapter 5, a commercial paste (Dyesol, WER2-O) was used. It contains anatase TiO_2 nanoparticles with an average diameter of 200 nm. This paste is diluted with anhydrous ethanol (1 g per 2.5 ml ethanol) and the mixture is sonicated in an ultrasonic bath for 15 min. The solution is spin-coated at a spinning speed of 1500 RPM, which results in a film thickness of approximately 1 μm . To provide the porosity, the paste contains cellulose, which has to be removed using a heat treatment. Additionally, the nanoparticles need to be fused together for satisfying charge transport properties, which requires an annealing step at a temperature above $T = 500^\circ\text{C}$. The samples were thus heated at $T = 550^\circ\text{C}$ for two hours with a ramp time of 30 min on a high-temperature 2000 W titanium hotplate with programmable regulator (Harry Gestigkeit GmbH). The mesoporous TiO_2 films for the sensitised solar cells in Chapter 6, were screen-printed from a custom paste containing anatase nanoparticles with an average diameter of 50 nm. The paste was screen-printed with a mesh giving a thickness of 1 μm and sintered at $T = 550^\circ\text{C}$ for two hours, as described before.

Titanium chloride treatment

The deposition of the mesoporous titanium dioxide layer was followed by a titanium chloride treatment. The samples were immersed into an aqueous solution of 20 mM titanium chloride (TiCl_4). The bath was heated at $T = 70^\circ\text{C}$ in a box oven for one hour. After the titanium chloride treatment, the samples were rinsed in DI water and re-sintered at $T = 550^\circ\text{C}$ for two hours with a ramp time of 30 min.

This treatment improves the charge injection from the absorber to the titanium dioxide by forming a thin ($< 1 \text{ nm}$) ultra-pure anatase TiO_2 layer, which slightly shifts the conduction band edge of the metal oxide [14]. It further improves the electron lifetime, which leads to a higher electron diffusion length in the titanium dioxide [15].

4.2.3 Hole transport materials

After the deposition of the absorber layer in sensitised solar cells, which are discussed in more detail in Chapter 5 and Chapter 6, a hole transport material has to infiltrate the remaining pores. Both, inorganic and organic p-type semiconductors can be used, as long as solution-processing is possible.

For this thesis, organic polymers were utilised for hole conduction, because they are easier to handle during processing and in general higher efficiencies are possible [16]. Two different p-type polymers were used as hole conducting materials, poly(3-hexylthiophene-2,5-diyl) (P3HT) and poly[2,6-(4,4-bis-(2-ethylhexyl)-4H-cyclopenta [2,1-b;3,4-b']dithiophene)-alt-4,7(2,1,3-benzothiadiazole)] (PCPDTBT). P3HT is a well studied organic hole transport material and it was used for the antimony sulfide sensitised solar cells because of the appropriate band alignment. The HOMO of P3HT lies at $E = -5.2$ eV measured against vacuum and the valence band maximum of antimony sulfide at $E = -5.8$ eV [17]. This leads to a good injection of holes from the absorber without losing too much voltage. Figure 4.6 a shows the structural formula of P3HT.

The highest efficiencies of antimony sulfide sensitised solar cells, in literature and in the studies presented here, were achieved using PCPDTBT. The chemical structure of the p-type polymer is illustrated in Figure 4.6 b. The relative improvement when using PCPDTBT compared to P3HT can be attributed to the absorption loss in P3HT. P3HT has a band gap of $E_g = 1.9$ eV and hence absorbs in the visible spectrum itself. Electrons generated in the P3HT are inefficiently transported to the Sb_2S_3 layer [18]. PCPDTBT has a lower band gap of $E_g = 1.4$ eV, shifting its absorption into the red part of the optical spectrum, and thus this effect is reduced and higher currents can be achieved [17].

If not stated otherwise, the hole transport materials P3HT and PCPDTBT were dissolved in 1,2-dichlorobenzene at a concentration of $15 \frac{\text{mg}}{\text{ml}}$ and stirred for at least one hour before use. The solution was then spin-coated onto the samples at a spin speed of 1500-2000 RPM.

Hole transport polymers

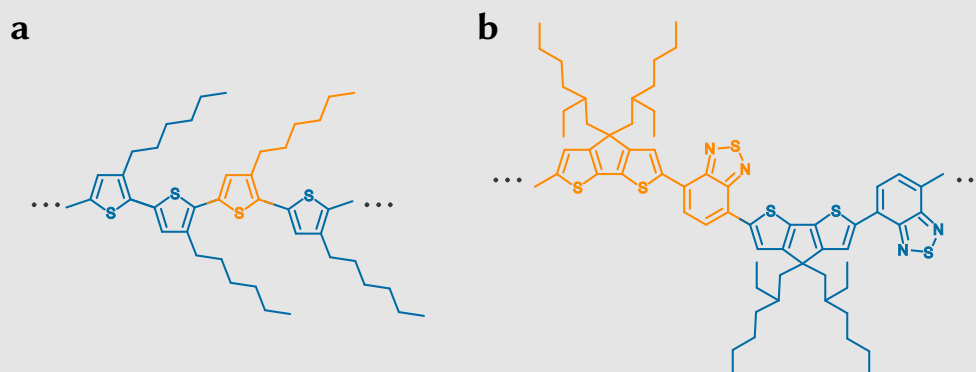


Figure 4.6: Chemical structures of polymers for hole transport in sensitised solar cells. (a) poly(3-hexylthiophene-2,5-diyl) (P3HT) (b) poly[2,6-(4,4-bis-(2-ethylhexyl)-4H-cyclopenta [2,1-b;3,4-b']dithiophene)-alt-4,7(2,1,3-benzothiadiazole)] (PCPDTBT). Both illustrations show a section of the polymer chain, the monomer is shown in orange.

4.2.4 Metal electrode deposition

For all solar cells and photodetectors, metal electrodes were evaporated onto the devices. Gold was chosen as electrode material, because of its high conductivity, easy processability and high robustness against oxidation.

The top and the bottom electrodes can be deposited via electron-beam evaporation in a single deposition step, due to the design of the device and the etching of the FTO layers as shown before. The size and layout of the electrodes was defined by a thin stainless steel metal shadow mask, to which the samples were taped prior to the evaporation of the gold layer. The dimensions of the electrodes were illustrated before, in Figure 4.5.

A Kurt J. Lesker e-beam evaporator operating at 10 kV and in high vacuum ($< 10^{-5}$ Torr) was used for the deposition of the gold electrodes. If not mentioned otherwise, 100 nm thick gold layers were evaporated at an evaporation rate of $0.15 \frac{\text{nm}}{\text{s}}$ for the electrodes of all optoelectronic devices.

4.3 Optoelectronic measurements

Here, the optoelectronic characterisation of the photodetectors and solar cells fabricated in the course of this thesis is described. First, an overview is given on the measurement of the current-voltage characteristic, the spectral response and the external quantum efficiency of optoelectronic devices. Then, intensity modulated spectroscopy techniques (IMVS/IMPS) are introduced and the experimental setup for time response measurements for photodetectors is explained.

4.3.1 Current-voltage measurements

The measurement of the current-voltage curve belongs to one of the core characteristics for optoelectronic devices. For solar cells, the I - V curve is measured in the dark and under illumination, matching the solar spectrum as closely as possible.

For the measurement of a terrestrial solar cell, an international standard, IEC 60904, exists [19]. A main part of the therein described standard test conditions (STC) is the specification of the spectrum of the light source used to irradiate the solar cell. For flat photovoltaic devices, the AM1.5 Global spectrum is used, which has an integrated irradiance of $1000 \frac{\text{W}}{\text{m}^2}$ and is sometimes also described as 1 sun illumination. Further, solar cells should be measured at a temperature of 25°C . A solar simulator from ABET technologies (Sun 2000, Model 11016) to simulate the AM1.5 Global spectrum was used. It is a Class BAA solar simulator: The spatial irradiance uniformity is met by less than $\pm 5\%$ (Class B), the AM1.5G spectral match deviates no more than $\pm 25\%$ (Class A) and the temporal stability is less than $\pm 1\%$ (Class A) [20]. The solar simulator uses a Xenon arc lamp and has an illumination field of $152 \text{ mm} \times 152 \text{ mm}$. After a heating up period of approximately 15 min, the irradiance of the solar simulator was calibrated to match 1 sun ($1000 \frac{\text{W}}{\text{m}^2}$) using a silicon reference cell (Czibula & Grundmann FHG-ISE, RS-OD4).

The electric connection is provided by a sample holder which contacts the evaporated electrodes using golden spring-loaded pin probes. The three different devices on each

sample can be selected using an external switch box. The sample holder and the switch box are connected to a Keithley 2635 sourcemeter by triaxial cables.

If not mentioned otherwise, all solar cells were measured in a forward scan from $V = -1\text{ V}$ to $V = 1\text{ V}$ with a step size of $\Delta V = 25\text{ mV}$ and a delay time of 0.05 s between steps. The analysis of the key parameters were evaluated according to Section 2.2.2 using custom written Python scripts.

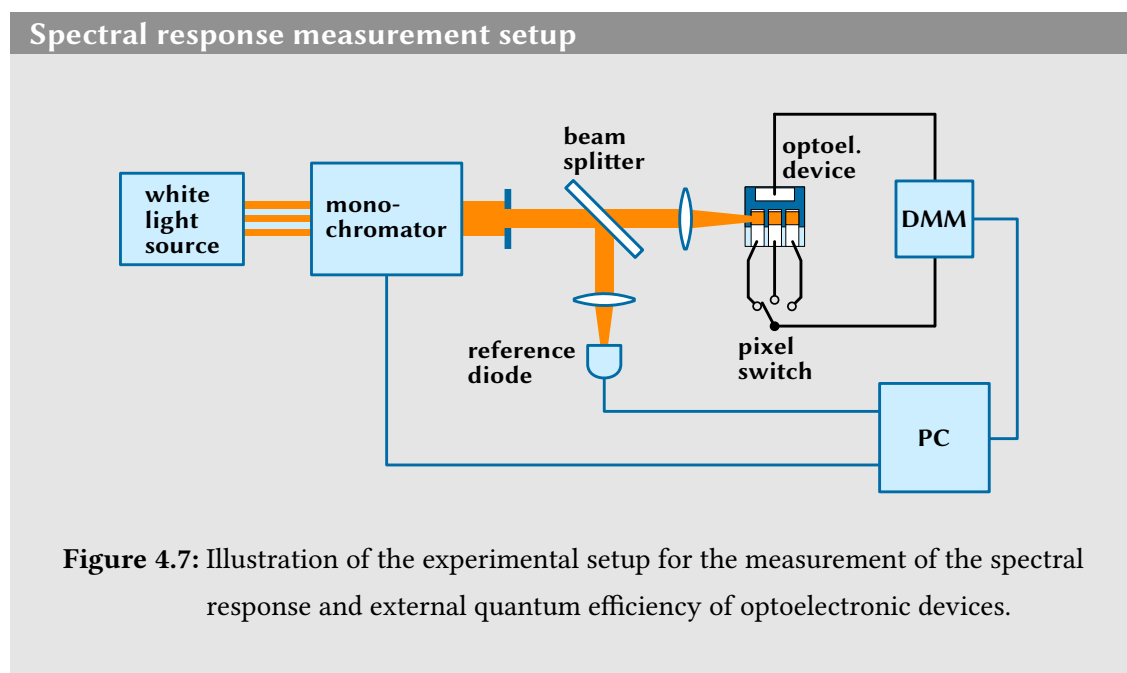
4.3.2 Spectral response

To measure the spectral response of the photodetectors and the solar cells, the setup as illustrated in Figure 4.7 was used. Monochromatic light is created from a 250 W tungsten halogen white light source (Newport, Model 66881) via an Oriel Cornerstone 130 monochromator. The light beam is then split into two paths using a semi-transparent mirror. One part is directed towards a reference photodiode (Thorlabs SM05PD1A), the second part is illuminating the optoelectronic device under investigation.

The electric connection was the same as described earlier for the I - V measurements using the Keithley 2635 sourcemeter to measure the wavelength dependent photocurrent. Prior to the actual measurement, the reference diode was calibrated using a second diode (Thorlabs SM05PD1A) with a known spectral responsivity. This and the measured current are then used to calculate the responsivity or external quantum efficiency of the optoelectronic device (see Section 2.1.2 and Section 2.2.2).

4.3.3 Time response measurements

The time response of the photodetectors was measured using an Autolab potentiostat (Autolab PGSTAT302N). As source of illumination, an array of six high power white light LEDs (LUMILEDS LL56.0171) were used, which were focused onto the detector area. The LED current source (Cavendish Laboratory J969) was triggered using a Hewlett Packard 33120 function generator with a square waveform. The photocurrent response



was recorded in fast chronoamperometry mode with and without voltage bias, controlled by the software package NOVA (version 1.11).

Due to long and poorly shielded cables from the Autolab setup and the low photocurrent levels on the order of 100 nA, the final signal has signatures of the 50 Hz mains frequency and is filtered by subtracting a sinusoidal least square fit with a 50 Hz frequency.

4.3.4 Intensity modulated spectroscopy

Charge transport and recombination processes in solar cells can be probed using intensity modulated photocurrent spectroscopy (IMPS) and intensity modulated photovoltage spectroscopy (IMVS) [21]. In Chapter 5, this technique is used to investigate the electron recombination lifetime in antimony sulfide sensitised solar cells.

IMPS probes the photocurrent signal at short-circuit conditions on an intensity modulated illumination. IMVS is the equivalent technique, probing the photovoltage at

open-circuit. A light source (normally a LED) illuminates the sample under investigation. The base irradiance E_e is then modulated by a sinusoidal variation ΔE_e with an amplitude of up to 10 % of the base value. Then, the response of the photocurrent (for IMPS) or of the photovoltage (for IMVS) is measured [22, 23]. The measurement is performed as a function of frequency f of the light modulation and for different base levels of the illumination irradiance. The phase-shift of the signal is dependent on the electron transport (for IMPS measurements) [22] and the electron recombination rate (for IMVS measurements) [23] within the device. IMPS yields a characteristic frequency f_c , where the imaginary part of the measured response is minimal. The transport lifetime τ_{tr} of electrons can then be determined by [24]

$$\tau_{tr} = \frac{1}{2\pi f_c} . \quad (4.5)$$

Analogously, the recombination lifetime $\tau_{rec} = \frac{1}{2\pi f_c}$ can be extracted from IMVS measurements [24].

The light source is an array of three LEDs (625 nm) driven by an Autolab LED Driver. The DC output of the Autolab LED Driver is controlled using the Autolab DAC164 and the AC output for the light modulation by the Autolab FRA32M module [25]. The AC current amplitude is set to 10 % of the DC current. The system is monitored and controlled via the software package NOVA (version 1.11). The Autolab system measures the transfer function H , which is defined as $H_{IMPS} = \frac{\Delta I_{sc}(t)}{\Delta I_{LED}(t)}$ and $H_{IMVS} = \frac{\Delta V_{oc}(t)}{\Delta I_{LED}(t)}$. Here, $\Delta I_{sc}(t)$ is the modulation of the short-circuit current, $\Delta V_{oc}(t)$ is the modulation of the open-circuit voltage and $\Delta I_{LED}(t)$ is the modulation current driving the LED, which illuminates the sample [25].

Bibliography

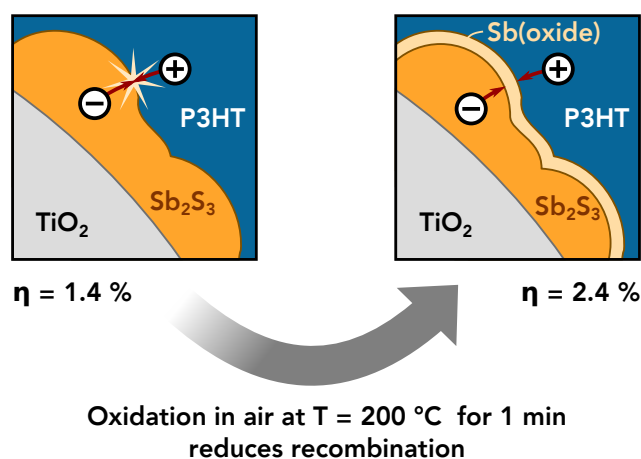
- [1] P. F. Kane and G. B. Larrabee. *Characterization of Solid Surfaces*. Springer Science & Business Media, **2013**.
- [2] J. F. Watts and J. Wolstenholme. *An Introduction to Surface Analysis by XPS and AES*. John Wiley & Sons, Ltd, **2003**.
- [3] P. Scherrer. “Bestimmung der inneren Struktur und der Größe von Kolloidteilchen mittels Röntgenstrahlen”. *Kolloidchemie Ein Lehrbuch*. Chemische Technologie in Einzeldarstellungen. Springer Berlin Heidelberg, **1912**, pp. 387–409. DOI: 10.1007/978-3-662-33915-2_7.
- [4] A. L. Patterson. “The Scherrer Formula for X-Ray Particle Size Determination”. *Physical Review* 56.10 (**1939**), pp. 978–982. DOI: 10.1103/PhysRev.56.978.
- [5] B. E. Warren. *X-Ray Diffraction*. Dover Publications, Inc., New York, **1990**.
- [6] U. Holzwarth and N. Gibson. “The Scherrer Equation versus the 'Debye-Scherrer Equation'”. *Nature Nanotechnology* 6.9 (**2011**), pp. 534–534. DOI: 10.1038/nnano.2011.145.
- [7] *DMSM: X-Ray Facility - Equipment*. <http://www.msm.cam.ac.uk/xray/equip.php>. **2016**.
- [8] A. C. Boccara, W. Jackson, N. M. Amer, and D. Fournier. “Sensitive Photothermal Deflection Technique for Measuring Absorption in Optically Thin Media”. *Optics Letters* 5.9 (**1980**), p. 377. DOI: 10.1364/OL.5.000377.
- [9] W. B. Jackson, N. M. Amer, A. C. Boccara, and D. Fournier. “Photothermal Deflection Spectroscopy and Detection”. *Applied Optics* 20.8 (**1981**), p. 1333. DOI: 10.1364/AO.20.001333.
- [10] H. Tolner, B. Feldman, D. McLean, and C. Cording. *Transparent Conductive Oxides for Display Applications*. **2008**.

-
- [11] P. Docampo, S. Guldin, M. Stefik, P. Tiwana, M. C. Orilall, S. Hüttner, H. Sai, U. Wiesner, U. Steiner, and H. J. Snaith. “Control of Solid-State Dye-Sensitized Solar Cell Performance by Block-Copolymer-Directed TiO₂ Synthesis”. *Advanced Functional Materials* 20.11 (2010), pp. 1787–1796. DOI: 10.1002/adfm.200902089.
- [12] L. Kavan and M. Grätzel. “Highly Efficient Semiconducting TiO₂ Photoelectrodes Prepared by Aerosol Pyrolysis”. *Electrochimica Acta* 40.5 (1995), pp. 643–652. DOI: 10.1016/0013-4686(95)90400-W.
- [13] Y. C. Choi and S. I. Seok. “Efficient Sb₂S₃-Sensitized Solar Cells Via Single-Step Deposition of Sb₂S₃ Using S/Sb-Ratio-Controlled SbCl₃-Thiourea Complex Solution”. *Advanced Functional Materials* (2015), pp. 2892–2898. DOI: 10.1002/adfm.201500296.
- [14] P. Sommeling and B. O'Regan. “Influence of a TiCl₄ Post-Treatment on Nanocrystalline TiO₂ Films in Dye-Sensitized Solar Cells”. *The Journal of Physical Chemistry B* (2006), pp. 19191–19197. DOI: 10.1021/jp061346k.
- [15] A. Hagfeldt, G. Boschloo, L. Sun, L. Kloo, and H. Pettersson. “Dye-Sensitized Solar Cells.” *Chemical Reviews* 110.11 (2010), pp. 6595–663. DOI: 10.1021/cr900356p.
- [16] J. A. Chang, J. H. Rhee, S. H. Im, Y. H. Lee, H.-J. Kim, S. I. Seok, M. K. Nazeeruddin, and M. Graetzel. “High-Performance Nanostructured Inorganic-Organic Heterojunction Solar Cells.” *Nano Letters* 10.7 (2010), pp. 2609–12. DOI: 10.1021/nl101322h.
- [17] S. H. Im, C.-S. Lim, J. A. Chang, Y. H. Lee, N. Maiti, H.-J. Kim, M. K. Nazeeruddin, M. Grätzel, and S. I. Seok. “Toward Interaction of Sensitizer and Functional Moieties in Hole-Transporting Materials for Efficient Semiconductor-Sensitized Solar Cells.” *Nano Letters* 11.11 (2011), pp. 4789–93. DOI: 10.1021/nl2026184.
- [18] J. A. Chang, S. H. Im, Y. H. Lee, H.-J. Kim, C.-S. Lim, J. H. Heo, and S. I. Seok. “Panchromatic photon-harvesting by hole-conducting materials in inorganic-organic heterojunction sensitized-solar cell through the formation of nanostructured electron channels.” *Nano letters* 12.4 (2012), pp. 1863–7. DOI: 10.1021/nl204224v.
- [19] IEC. *IEC 60904-1 - Photovoltaic Devices*. 2006.

Bibliography

- [20] ABET Technologies. *Sun 2000 Solar Simulators*. <http://www.abet-technologies.com/literature/SSBrochure81106.pdf>. **2010**.
- [21] P. R. F. Barnes, K. Miettunen, X. Li, A. Y. Anderson, T. Bessho, M. Grätzel, and B. C. O'Regan. "Interpretation of Optoelectronic Transient and Charge Extraction Measurements in Dye-Sensitized Solar Cells". *Advanced Materials* 25.13 (**2013**), pp. 1881–1922. DOI: 10.1002/adma.201201372.
- [22] L. Dloczik, O. Ileperuma, I. Lauermann, L. M. Peter, E. A. Ponomarev, G. Redmond, N. J. Shaw, and I. Uhlenhof. "Dynamic Response of Dye-Sensitized Nanocrystalline Solar Cells: Characterization by Intensity-Modulated Photocurrent Spectroscopy". *The Journal of Physical Chemistry B* 101.49 (**1997**), pp. 10281–10289. DOI: 10.1021/jp972466i.
- [23] G. Schlichthörl, S. Y. Huang, J. Sprague, and A. J. Frank. "Band Edge Movement and Recombination Kinetics in Dye-Sensitized Nanocrystalline TiO₂ Solar Cells: A Study by Intensity Modulated Photovoltage Spectroscopy". *The Journal of Physical Chemistry B* 101.41 (**1997**), pp. 8141–8155. DOI: 10.1021/jp9714126.
- [24] Gamry Instruments. *Dye Solar Cells - IMPS/IMVS Measurements*. <http://www.gamry.com/application-notes/physechem/dye-solar-cells-imps-imvs/>. **2016**.
- [25] Metrohm Autolab B.V. *LED Driver User Manual*. http://www.ecochemie.nl/download/Manuals/LEDDRIVER_-_Installation_description_Autolab_LED_DRIVER_combination_NOVA.pdf. **2012**.

Improving solar cells by the partial oxidation of Sb_2S_3



Parts of this chapter are published in:

K. C. Gödel, B. Roose, A. Sadhanala, Y. Vaynzof, S. K. Pathak, U. Steiner. "Partial oxidation of the absorber layer reduces charge carrier recombination in antimony sulfide solar cells". *Physical Chemistry Chemical Physics*, (2016). doi: 10.1039/c6cp07559b.

Abstract In this chapter, the effect of a post heat treatment of the absorber layer in antimony sulfide (Sb_2S_3) sensitised solar cells is investigated. Controlling the oxidation process by an annealing step in air leads to improved photovoltaic parameters for oxidised Sb_2S_3 sensitised solar cells. A very short heat treatment resulted in an increase in power conversion efficiency from $\eta = 1.4\%$ to $\eta = 2.4\%$, while longer annealing decreased device performance. On a merely phenomenological level, previous reports indicated that it is beneficial for the photovoltaic performance to let Sb_2S_3 films cool in air after annealing at elevated temperatures in an inert atmosphere. Here, the detailed origins of this improvement are investigated. To this end, samples were annealed in air for differing time periods and the build-up of an antimony oxide layer was monitored by XPS. This improvement was linked to a reduction in charge carrier recombination at the interface of Sb_2S_3 with the organic hole conductor, arising from the oxide barrier layer, as demonstrated by intensity modulated photovoltage spectroscopy (IMVS).

5.1 Introduction

Dye-sensitised solar cells (DSSCs) were proposed as a cheap and easily processable alternative to conventional photovoltaic cells [1]. However, the possible leakage of liquid electrolytes and the degradation of the organic light absorber in DSSCs reduce the stability of these devices [2]. Solid-state sensitised solar cells with inorganic absorbing materials can overcome these problems. Crystalline Sb_2S_3 is a promising light absorber for solid-state sensitised solar cells, due to its high absorption coefficient ($\alpha \approx 1.8 \cdot 10^5 \text{ cm}^{-1}$ at $\lambda = 450 \text{ nm}$), its long-term stability and its suitable direct band gap of $E_g \approx 1.7 \text{ eV}$ [3–5]. Power-conversion efficiencies of up to $\eta = 7.5\%$ have been achieved using this material [6]. The architecture of these devices normally consists of a n-type mesoporous TiO_2 layer with a thin layer of antimony sulfide as the absorber material. For the hole transport, different inorganic and organic hole conducting materials, such as CuSCN , the small molecule spiro-OMeTAD and the conducting polymers PCPDTBT and P3HT were investigated in Sb_2S_3 sensitised solar cells [4, 5, 7, 8]. Antimony sulfide can be deposited in aqueous and non-aqueous chemical baths at low temperatures ($< 10^\circ\text{C}$)

[9–11]. Both methods yield amorphous Sb_2S_3 films, which have to be annealed at around $250^\circ\text{C} - 300^\circ\text{C}$ in an oxygen-free atmosphere.

In several publications it has been reported phenomenologically that the samples with the freshly annealed antimony sulfide film should cool down in air to improve the device efficiency [4, 7, 8, 12, 13]. It has been speculated that a thin film of antimony oxide forms, which possibly reduces recombination [7, 12]. To harness this effect to its full potential, one has to understand the underlying physical principles and find optimal conditions. In this study, physical insights into the origin of the improved device performance and a more detailed quantitative analysis of the oxidation effect on the Sb_2S_3 absorber layer is given. The change of the material properties as a function of oxidation time was studied using XPS, XRD and UV-vis spectroscopy. The efficiency improvement is shown by photovoltaic measurements. The electron transport and recombination behaviour is studied by IMPS and IMVS, respectively.

5.2 Materials and methods

5.2.1 Preparation of photovoltaic cells

Fluorine doped tin oxide (FTO) coated glass slides (Solaronix, $15 \Omega/\square$) were coated with a thin ($\approx 50 \text{ nm}$) compact TiO_2 hole-blocking layer by spin-coating, as described elsewhere [6]. Dyesol paste (WER2-O) containing TiO_2 nanoparticles with an average size of 200 nm was diluted with anhydrous ethanol ($2.5 \text{ ml EtOH per } 1 \text{ g paste}$) and spin-cast onto the substrate at 1500 RPM for 45 s , resulting in an approximately $1.5 \mu\text{m}$ thick mesoporous TiO_2 scaffold. The substrates were sintered at $T = 550^\circ\text{C}$ for 2 h . After sintering, the mesoporous electrodes were soaked in an aqueous TiCl_4 bath ($2 \cdot 10^{-2} \text{ M}$) for 1 h at 70°C . After rinsing with deionised water, the films were heated at 550°C in air for 30 min and then left to cool to room temperature. Antimony sulfide was deposited using the chemical bath technique described by Messina *et al.* [10]. The samples were submerged facing downwards into 100 ml of an aqueous solution containing $3.95 \text{ g Na}_2\text{S}_2\text{O}_3$ and

650 mg SbCl_3 . The solution was kept at 10°C for 1 h and then slowly cooled down to 6°C in 1 h. After the deposition, the orange samples were rinsed in deionised water and dried with air. To turn Sb_2S_3 into its brown crystalline form, the films were heated at 250°C for 45 min in a N_2 atmosphere. After this annealing step in a nitrogen-filled glove box, the samples were left to cool in the inert atmosphere.

For the experiments, the crystalline Sb_2S_3 samples were reheated to 200°C in air for times varying from 0 to 20 min. P3HT (Merck lisicon) in chlorobenzene was deposited as hole conducting material. In two subsequent steps P3HT was spin-coated onto the sample at 1500 RPM for 45 s, first, from a solution with a P3HT concentration of $5 \frac{\text{mg}}{\text{ml}}$, followed by spin coating a solution with a $15 \frac{\text{mg}}{\text{ml}}$ P3HT concentration. Prior to spinning, the solution was spread across the substrate with the tip of a pipette and allowed to infiltrate the porous scaffold for 10 s. 100 nm thick gold electrodes were evaporated onto the samples using a Kurt J. Lesker e-beam evaporator. The active area of the solar cells in this study was 0.12 cm^2 .

5.2.2 Material characterisation

SEM was performed using a Zeiss LEO 1550 FE-SEM with a field emission source operating at 3 kV acceleration voltage. XRD measurements were carried out using a Bruker D8 θ/θ (fixed sample) spectrometer with a position sensitive detector (LynxEye) and a standard detector (SC) with auto-absorber and graphite 2nd beam monochromator. The setup uses a Bragg Brentano para-focusing geometry and measures in reflection mode. A single sample was used for the XRD measurements. It was split into six parts prior to the annealing step. XPS samples were prepared on silicon wafers and were transferred into the ultra-high vacuum (UHV) chamber of an ESCALAB 250Xi. The measurements were carried out using a XR6 monochromated $\text{AlK}\alpha$ source (1486.6 eV) and a pass energy of 20 eV.

5.2.3 Optoelectronic characterisation

A solar simulator from ABET Technologies (Model 11016 Sun 2000) with a xenon arc lamp was used to illuminate the solar cells for J - V -measurements which were recorded by a Keithley 2635 sourcemeter. The intensity of the solar simulator is calibrated to $100 \frac{\text{mW}}{\text{cm}^2}$ using a silicon reference cell (Czibula & Grundmann FHG-ISE, RS-OD4). Prior to the measurement of the photovoltaic characteristics, the solar cells were light-soaked under the solar simulator for 15 min at open-circuit conditions [14]. The monochromatic light for the EQE -measurements came from a 250 W tungsten halogen lamp and an Oriel Cornerstone 130 monochromator. For IMPS and IMVS, three LEDs (625 nm) driven by an Autolab LED Driver were used as a light source. The DC output of the Autolab LED Driver was controlled using the Autolab DAC164 and the AC output for the light modulation by the Autolab FRA32M module. The AC current amplitude was set to 10 % of the DC current. The system was monitored and controlled by the software package NOVA (version 1.11).

5.3 Results and discussion

5.3.1 Characterisation of oxidised Sb_2S_3

Solar cells and plain antimony sulfide samples were prepared as described above in Section 5.2.1. After the annealing in a nitrogen glove box, the samples were left to cool in the inert atmosphere, to enable a more controlled oxidation procedure. The oxidation step was performed in air on a hotplate set to $T = 200^\circ\text{C}$ for different periods of time (0, 1, 2, 5, 10 and 20 min).

Absorption measurements

To probe whether the band-gap of the material changes upon heating in air, annealed samples were characterised by absorption spectroscopy.

Figure 5.1 shows the absorption spectrum of an amorphous Sb_2S_3 layer before annealing (dashed, grey line) and for different oxidation times after annealing. The absorption onset is in good agreement for the reported band gap values of amorphous Sb_2S_3 ($E_g = 2.2 \text{ eV}$, $\lambda_g = 564 \text{ nm}$) and crystalline antimony sulfide ($E_g = 1.7 \text{ eV}$, $\lambda_g = 729 \text{ nm}$) [3]. Slight variations between the samples are visible, but no clear trend with increasing oxidation times was observed. The shallow broad peak around 800-900 nm is an artefact caused by the relatively strong scattering of the underlying mesoporous TiO_2 film.

UV-vis spectroscopy of oxidised antimony sulfide

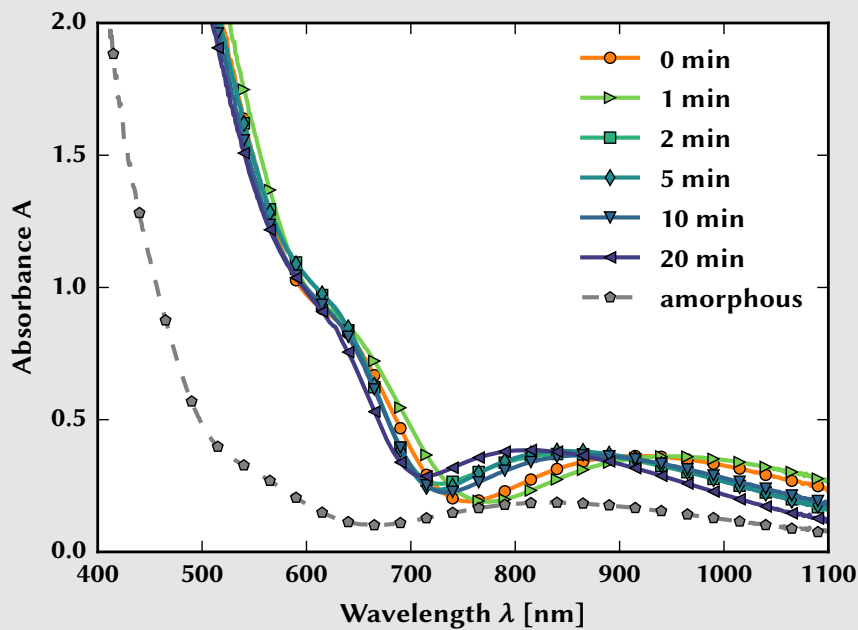
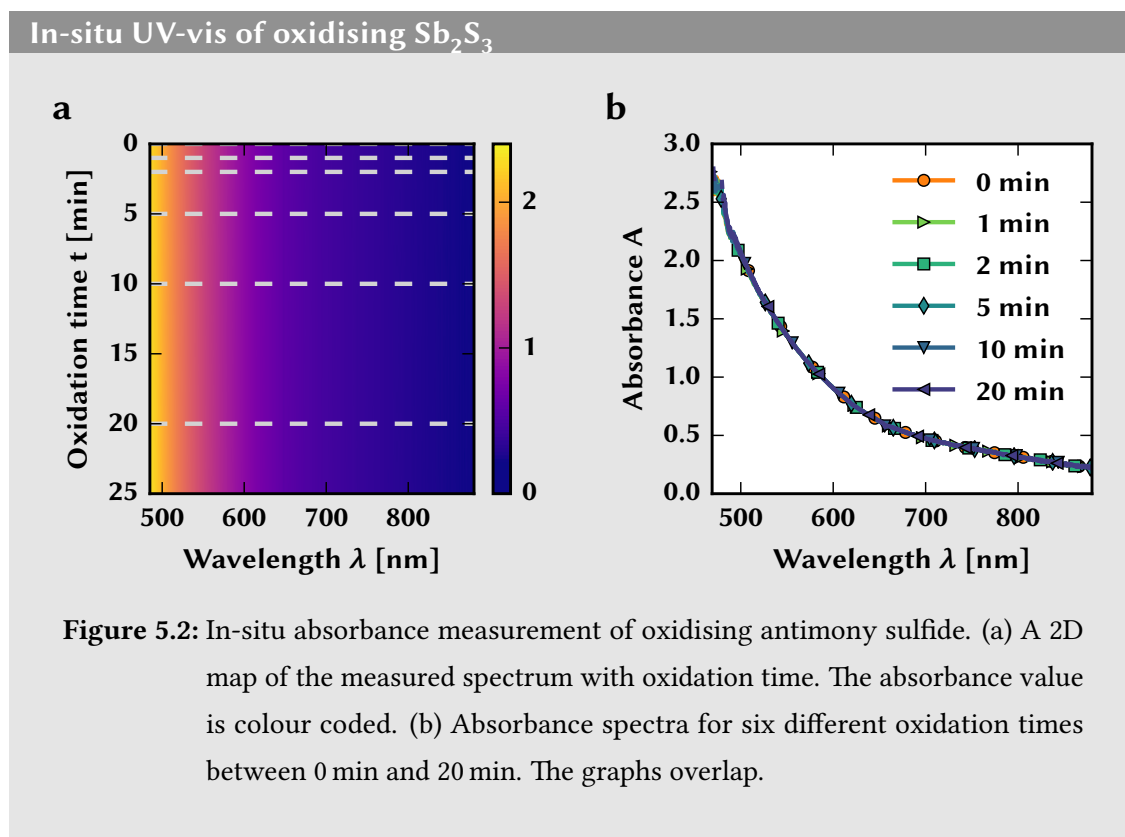


Figure 5.1: Absorption spectra of crystalline antimony sulfide measured after different oxidation times at 200°C , in air (solid lines). No clear trend can be observed for increasing oxidation periods. The dashed grey line shows the spectrum of amorphous antimony sulfide.

To get a more reliable result without sample to sample variation, UV-vis measurements were repeated on a single flat antimony sulfide sample using a heating stage with a transmittance path (Linkam HFS91 stage and TMS93 controller). The change of the

absorption spectrum was monitored in situ for 25 min in steps of 30 seconds during the annealing process at 200°C in air. Figure 5.2 a shows the recorded spectra as a 2D map. Figure 5.2 b shows spectra of the same oxidation times as in Figure 5.1. The measurement traces are nearly identical for oxidation times up to 25 min.



In order to demonstrate that the temperature of 200°C is high enough to have an impact on the antimony sulfide layer, one sample was kept at 200°C for 15 h. Figure 5.3 shows the absorption spectrum of this sample. The clear onset corresponding to the band gap of crystalline antimony sulfide disappeared and the overall absorption decreased. The oxidation of the sample is also observable by eye as a colour change from dark brown (typical for crystalline Sb_2S_3) to pale, transparent white.

To probe the inter band gap states, also called trap states, photothermal deflection spectroscopy (PDS) was used, an extremely sensitive absorption technique (see Chapter 2). One hypothesis is that the reduction in the trap state density could lead to the described

Absorption of extremely oxidised of antimony sulfide

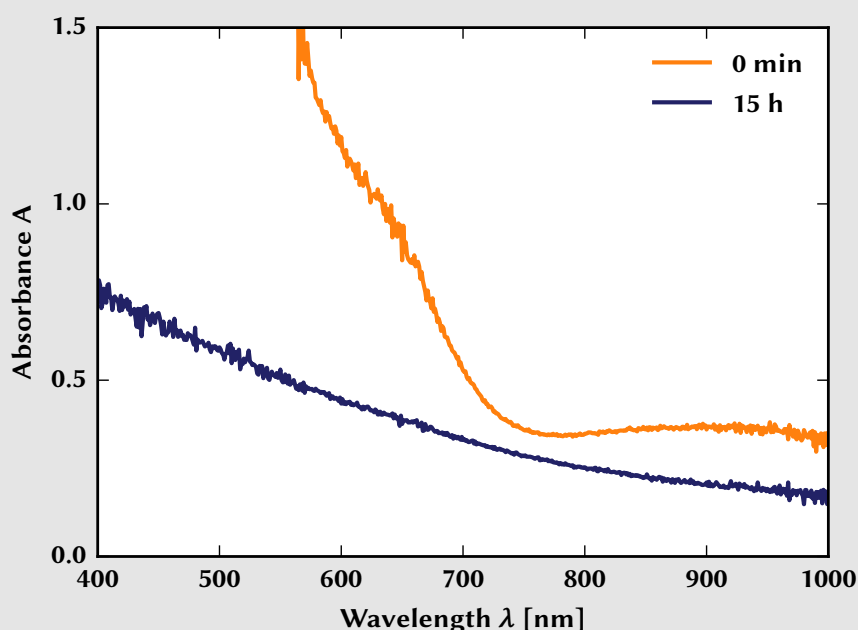


Figure 5.3: Absorbance spectra of Sb_2S_3 heated at 200°C measured after 0 min (orange) and 15 h (blue). The long oxidation period leads to the deterioration of the spectrum. The sample changes colour from dark brown to pale white.

efficiency improvement of oxidised Sb_2S_3 solar cells. Figure 5.4 shows the normalised absorbance in a semi-logarithmic plot, measured by PDS on oxidised antimony sulfide films (on mesoporous TiO_2).

The relevant region for the evaluation of trap states is below the band gap of antimony sulfide ($E_g = 1.7 \text{ eV}$). The absorbance in the region of $1 - 1.5 \text{ eV}$ does not show significant differences between long and short oxidation times, it is stable at values of approximately 10^{-2} . Thus a reduction in the density of deep trap states was not observed. Hence, the improvement of solar cells upon oxidation must have a different origin.

PDS of oxidised antimony sulfide films

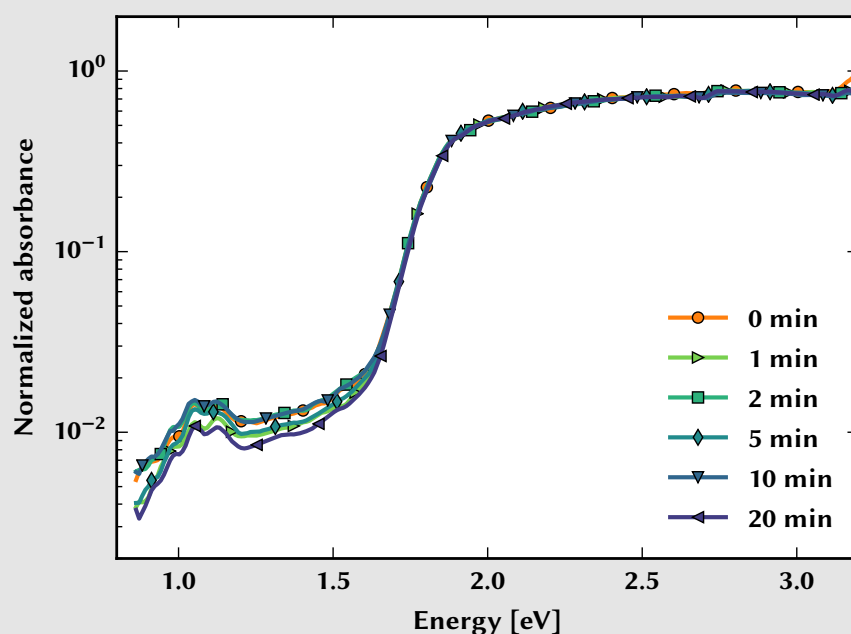


Figure 5.4: Photothermal deflection spectroscopy of antimony sulfide films, oxidised for different time periods from 0 min to 20 min. The deep trap states in the region of $E = 1 - 1.5$ eV show no significant difference for long oxidation times. The spectra were recorded by Dr. Aditya Sadhanala.

X-ray diffraction

The oxidised antimony sulfide samples were further characterised using XRD measurements. Pure Sb_2S_3 films on glass were prepared to avoid additional peaks from TiO_2 or SnO_2 (from the FTO layer). The crystalline samples were again oxidised for different time periods as described earlier. The measured XRD patterns are shown in Figure 5.5.

Additional peaks indicating a phase of crystalline antimony oxide are absent in the pattern. However, the relative height of the peaks corresponding to crystalline antimony sulfide decreases for longer oxidation times, indicating a decrease of crystallinity of the antimony sulfide film. It is worth noting that the crystallinity does not decrease

XRD of oxidised antimony sulfide

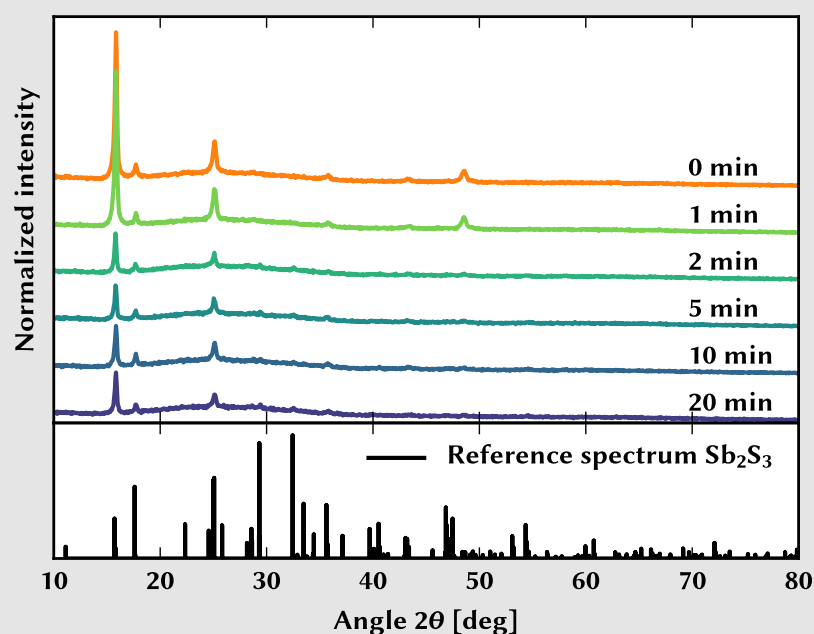
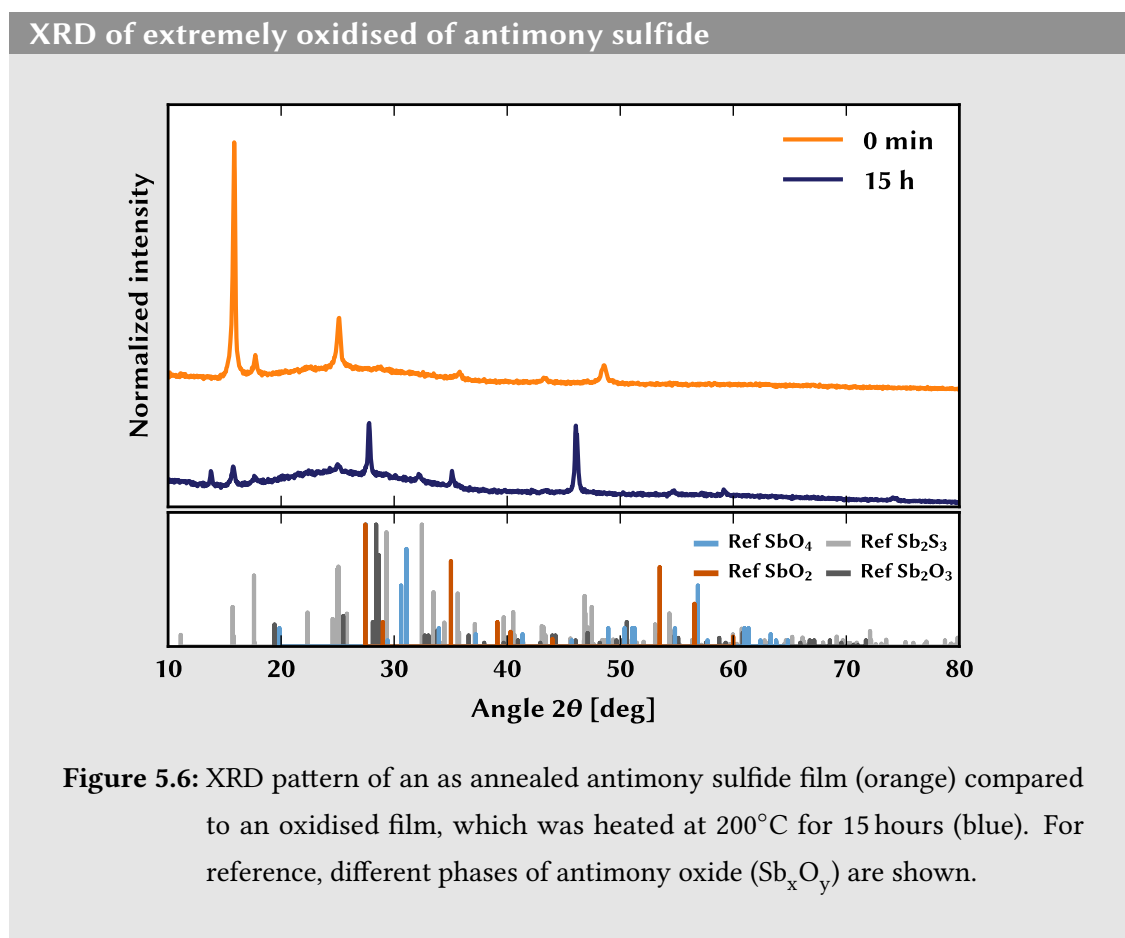


Figure 5.5: XRD pattern for antimony sulfide which was oxidised at 200°C for different time periods. Below the measured data, a reference spectrum of crystalline Sb_2S_3 is shown [15], where vertical bars indicate the relative intensities.

continuously, but that one can observe an abrupt reduction in peak size at oxidation times between 1 min and 2 min.

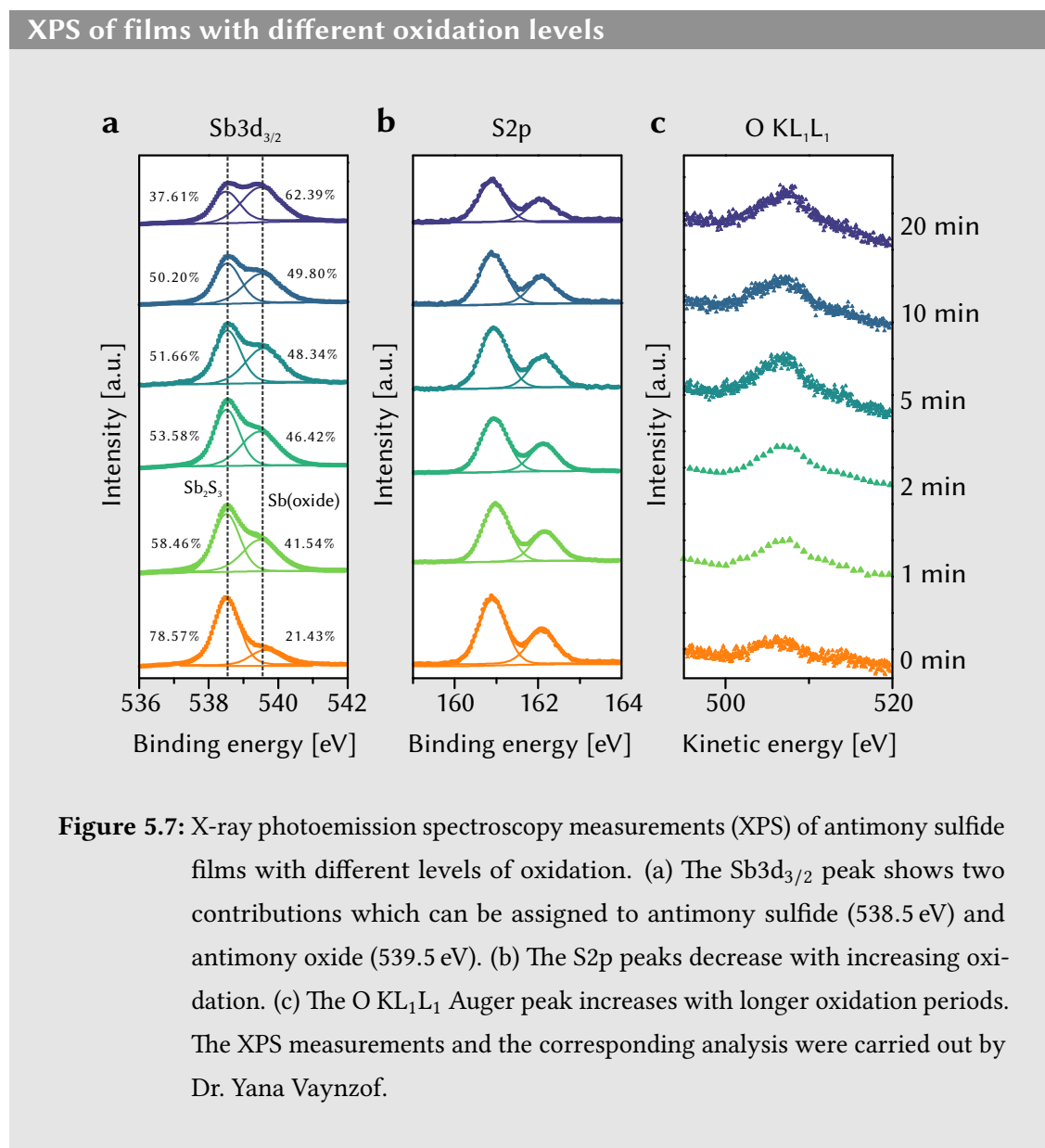
Again, the sample was oxidised for 15 h to probe which crystalline antimony oxide phases arise upon long oxidation. Figure 5.6 shows the XRD pattern of the extremely oxidised sample. The Sb_2S_3 peaks are barely detectable in this sample, but new peaks appear. They cannot be assigned to a single phase of antimony oxide, thus it is likely that different phases appear, such as SbO_2 , SbO_4 and Sb_2O_3 . The broad background, which results from amorphous material is also increased in the extremely oxidised sample compared to the reference. Hence, non-stoichiometric and amorphous antimony oxide seems to have formed.



X-ray photoemission spectroscopy

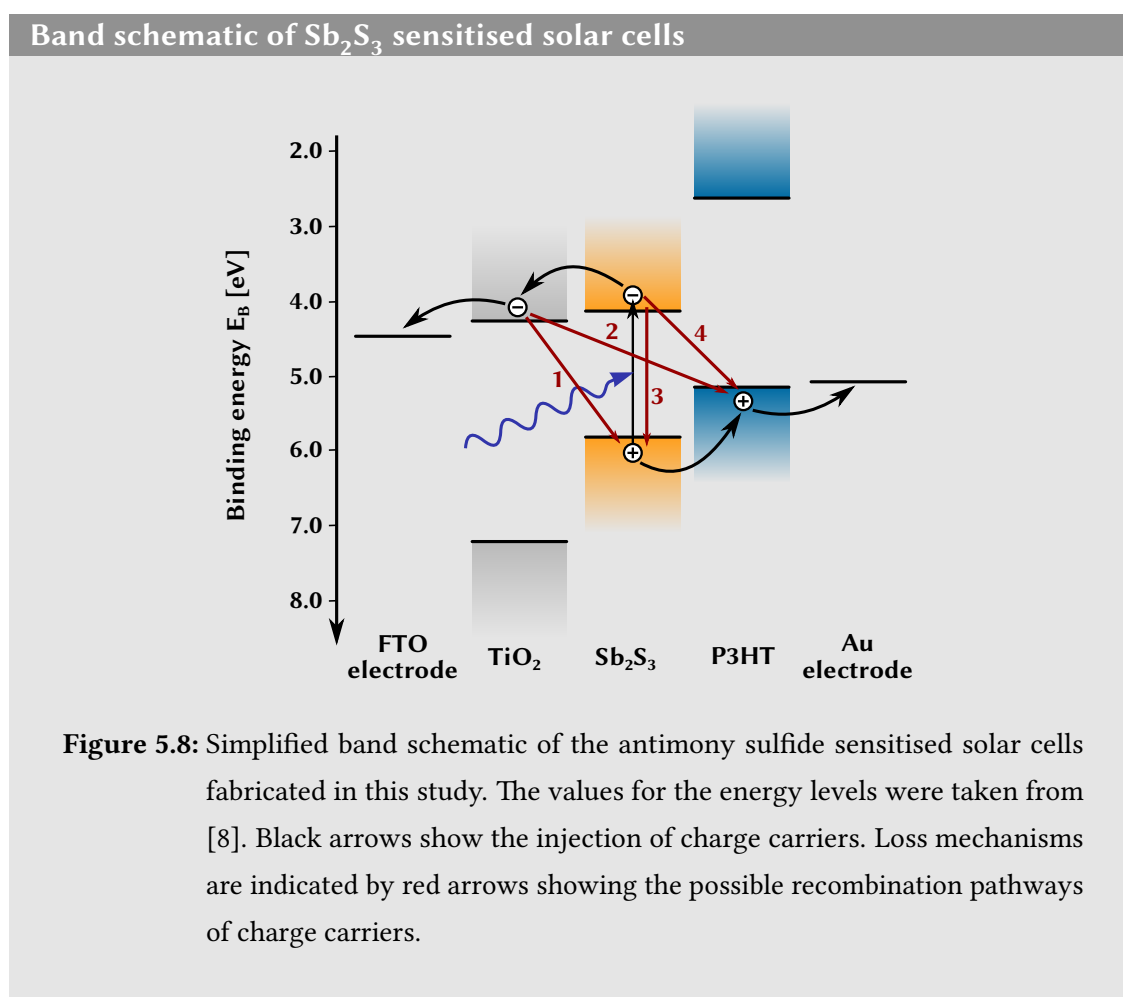
Subsequently, XPS measurements were performed on the different films to estimate the degree of surface oxidation of the Sb_2S_3 layer. The analysis of the O1s orbitals is complicated by the position of the $\text{Sb}3d_{5/2}$ peak at 529.5 eV, closely overlapping with the O1s peak at 530.5 eV. For this reason, the $\text{Sb}3d_{3/2}$ peak was analysed, which appears at a much higher binding energy due to the relatively large spin orbit splitting of Sb (9.35 eV) [16]. As shown in Figure 5.7 a, this peak has two overlapping contributions: a peak at 538.5 eV assigned to Sb_2S_3 and a peak at 539.5 eV corresponding to antimony oxides (Sb_xO_y). The relative contributions are displayed in the figure. Figure 5.7 b shows the corresponding S2p spectra appearing at 160.9 eV and 162.05 eV which does not vary

with the oxidising time. Finally, the increase of the oxygen content with the oxidation time was confirmed by measuring the Auger peak for the O KL_1L_1 transition, which is shown in Figure 5.7 c.



5.3.2 Improved photovoltaic devices with oxidised Sb_2S_3

To investigate the effect of the oxidation treatment on the solar cell performance, photovoltaic devices were fabricated. In all solar cells of this study, TiO_2 nano-crystals with an average diameter of 200 nm acted as the mesoporous n-type material and P3HT as a hole transport material. Electrons which are generated in the antimony sulfide sensitizer can be injected into the TiO_2 anode and conducted towards the electrode by diffusion [17]. A schematic band diagram of the entire solar cell is shown in Figure 5.8. The highest occupied molecular orbital of the hole conductor P3HT lies above the valence band of Sb_2S_3 and thus allows holes to be injected from the absorber into P3HT [8].



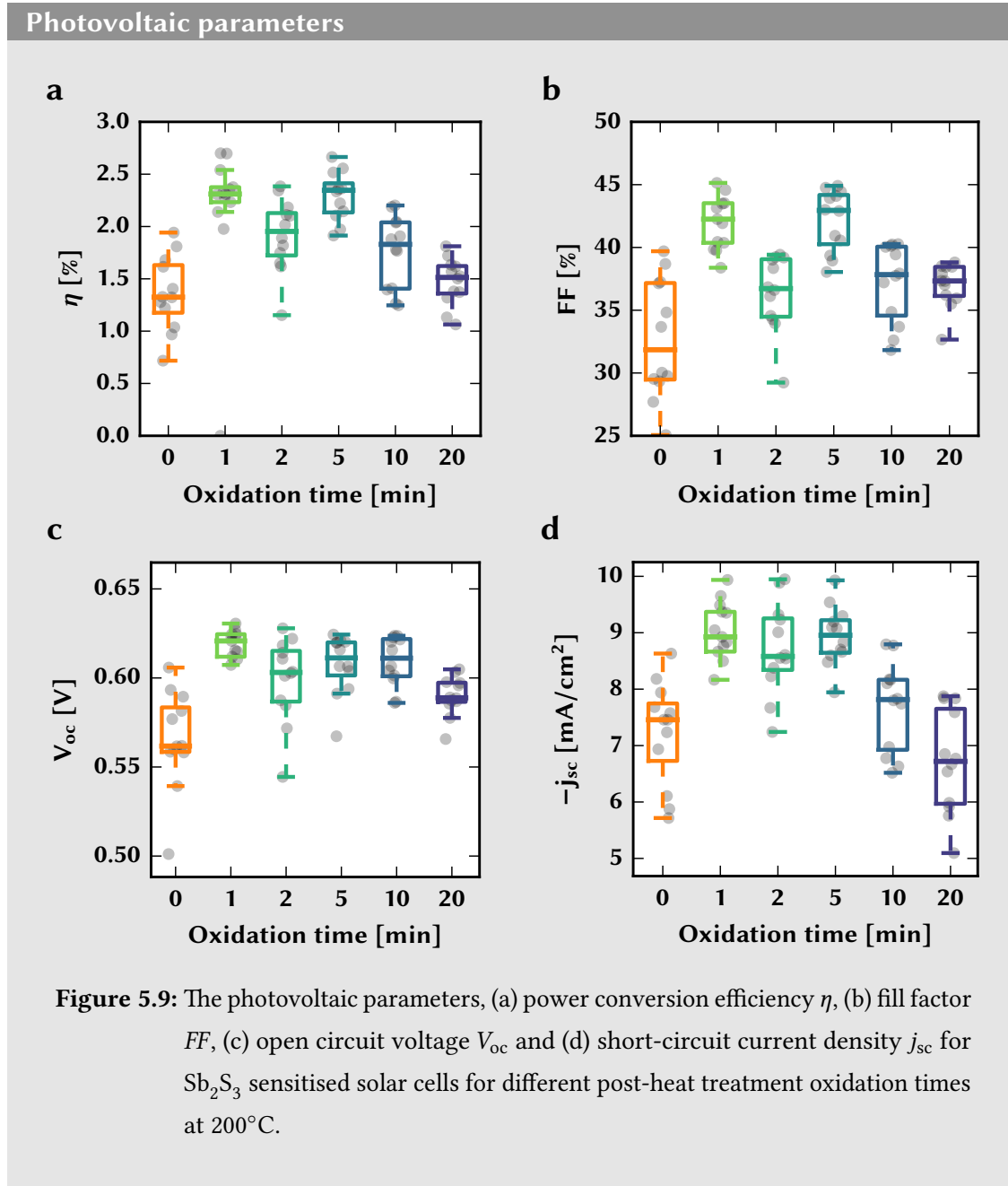
Different recombination pathways in the photovoltaic devices are shown in Figure 5.8, indicated by red arrows. Electrons in the titanium dioxide anode can recombine with holes from the P3HT hole transport material (1) or holes in the antimony sulfide film (2). Recombination can also take place in the absorber itself by direct recombination (3) and holes in P3HT can recombine with negative charge carriers in the Sb_2S_3 layer (4).

Before the deposition of the hole transport material, the solar cell samples were oxidised at 200°C for different time periods. Then, the devices were completed and optoelectronically characterised. For each oxidation time (0, 1, 2, 5, 10 and 20 minutes), twelve solar cells were built and I - V curves were recorded. The photovoltaic parameters, including the short-circuit current density j_{sc} , open circuit voltage V_{oc} , fill factor FF and power conversion efficiency η , are presented in Figure 5.9. The values, including the standard deviation, of the twelve devices each are summarised in Table 5.1.

For short oxidation times, the power conversion efficiency is greatly enhanced from an average of $\eta = 1.4\%$ for 0 min to $\eta = 2.4\%$ for 1 min heat treatment in air. For longer oxidation periods, the efficiency decreases again. The open-circuit voltage increases upon oxidation and then stays more or less constant at values of approximately 0.62 V. The fill factor and the short-circuit current first increase for short oxidation times and then deteriorate for longer periods of more than 5 min.

Figure 5.10 a shows the I - V characteristic of an oxidised (for 1 min) and a non-oxidised solar cell in comparison. Both, current and voltage are increased for the sample which was heat treated in air at 200°C for 1 min. The open-circuit voltage V_{oc} as well as the short-circuit current density j_{sc} of the latter is increased. The increase in j_{sc} can also be appreciated from Figure 5.10 b, which shows the EQE of the two solar cells. The oxidised sample shows higher EQE values throughout the entire visible spectrum. The dip at around $\lambda = 600\text{ nm}$ is a well known feature resulting from the optical band gap of the hole transporting material P3HT [18]. Charges which are generated in the P3HT are inefficiently transported to the Sb_2S_3 layer [18].

To ensure that the increase of the photovoltaic parameters is indeed due to the oxygen and not caused by a different effect during the heat treatment, control measurements



were carried out, where samples were heated at 200°C for 1 min in air and at the same temperature and for the same time in a nitrogen atmosphere. As shown in Figure 5.11, post heat treatment in a nitrogen atmosphere did not improve the device efficiency and the photovoltaic performance was still inferior compared to a solar cell heated in air.

Table 5.1: Photovoltaic parameters, including the power conversion efficiency η , short-circuit current density j_{sc} , open circuit voltage V_{oc} and fill factor FF , for five annealing times and unannealed samples. The listed values are averages from twelve solar cells each.

[min]	η [%]	$-j_{\text{sc}}$ [$\frac{\text{mA}}{\text{cm}^2}$]	V_{oc} [mV]	FF [%]
0 min	1.4 ± 0.3	7.2 ± 0.9	566 ± 26	32.7 ± 4.5
1 min	2.4 ± 0.2	9.1 ± 0.5	619 ± 7	41.9 ± 2.0
2 min	1.9 ± 0.3	8.7 ± 0.8	599 ± 23	36.4 ± 2.9
5 min	2.3 ± 0.2	8.9 ± 0.5	608 ± 16	42.3 ± 2.4
10 min	1.8 ± 0.3	7.7 ± 0.8	609 ± 13	37.2 ± 3.0
20 min	1.5 ± 0.2	6.7 ± 0.9	590 ± 11	37.0 ± 1.7

Comparison of I-V and EQE before and after oxidation

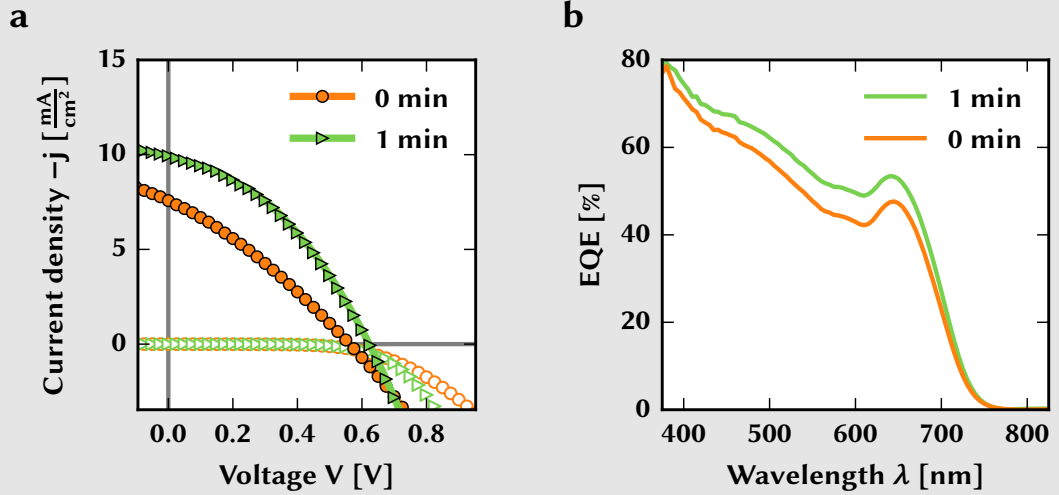
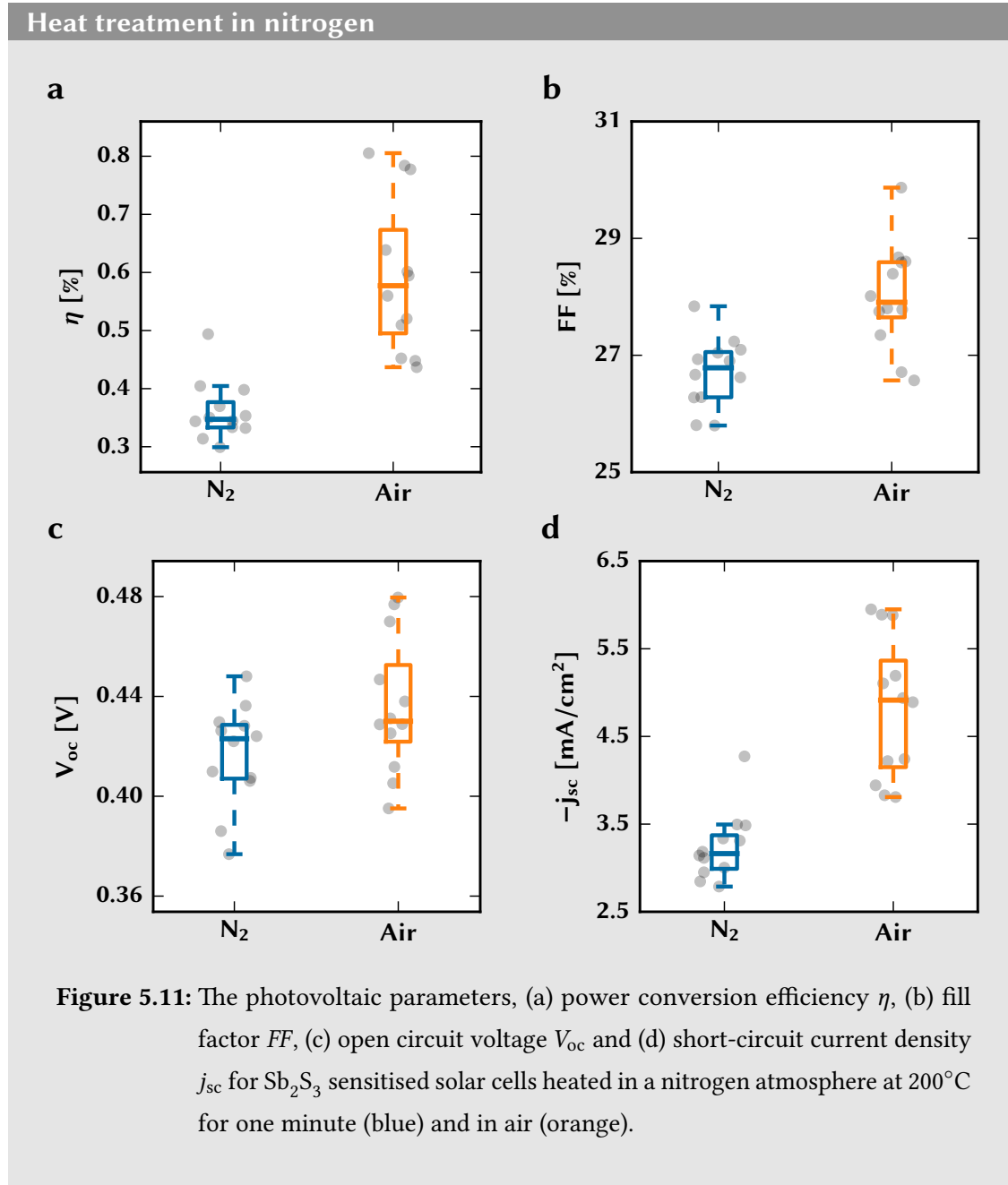


Figure 5.10: (a) Current-voltage characteristic of a non-oxidised (orange circles) and an oxidised solar cell (oxidation time: 1 min, green triangles) under 1 sun illumination and in the dark (curves with non-filled markers). (b) External quantum efficiency of the same devices.

This confirms the hypothesis that the oxidation process is the reason for the efficiency enhancement.



5.3.3 Reduced recombination in oxidised Sb_2S_3 solar cells

The origin of the improvement of in air heat-treated Sb_2S_3 sensitised solar cells was further examined.

High recombination rates lead to a decrease in the built-in potential [19]. A reduction of recombination should thus lead to a visible improvement of the open-circuit voltage V_{oc} . Further, high charge recombination also causes low fill factors [20, 21]. Lower recombination rates should hence result in a clear enhancement of the fill factor. The effect of increased open-circuit voltage and fill factor is indeed observed for the samples annealed in air, as shown in Figure 5.10 b and 5.10 c and in Table 5.1.

The reduced recombination is also beneficial for the short-circuit current, as it leads to a higher charge collection probability [22]. This explains the initial increase in j_{sc} for short oxidation periods shown in Figure 5.9 d. On the other hand, very high oxidation levels complicate the hole injection from the antimony sulfide absorber into the hole transport material (here P3HT), which can be observed in a reduction of the short-circuit current density and the fill factor (see Figure 5.9 b,d). The low FF values of the sample with 2 min oxidation period do not seem to follow the trend.

To further probe the hypothesis that the oxidisation process from the heat-treatment in air leads to a reduction in the recombination rate, intensity modulated photocurrent spectroscopy (IMPS) and intensity modulated photovoltage spectroscopy (IMVS) measurements are conducted. The raw data was recorded by Bart Roose at the Adolphe Merkle Institute in Fribourg, Switzerland.

As introduced in Chapter 4, IMPS probes the photocurrent response of the solar cell at short-circuit conditions under intensity modulated illumination. Equivalently, IMVS probes the photovoltage at open-circuit conditions [17, 23, 24]. An array of three LEDs ($\lambda = 625 \text{ nm}$) illuminates the device with different base irradiances and an additional sinusoidal variation with an amplitude of 10 % of the base value. The measurement is undertaken as a function of the modulation frequency f of the light source at different base level irradiances. The phase-shift of the response signal depends on the electron

transport (in case of IMPS measurements) [17] and on the electron recombination rate (in case of IMVS measurements) [23]. The characteristic frequency f_c is the minimum of the imaginary part of the measured response. In IMPS measurements, the transport lifetime τ_{tr} of electrons can be calculated, [25]

$$\tau_{tr} = \frac{1}{2\pi f_c} . \quad (5.1)$$

The recombination lifetime τ_{rec} can likewise be determined from IMVS measurements according to [25]

$$\tau_{rec} = \frac{1}{2\pi f_c} . \quad (5.2)$$

Figure 5.12 shows Nyquist- (a and b) and Bode-type (c and d) plots for a device without oxidation (orange tones, a and c) and one with a 1 min heat-treatment in air (green tones, b and d). Each plot shows the frequency dependent imaginary part of the transfer function H_{IMPS} , which is defined by the used Autolab LED driver system as

$$H_{IMPS} = \frac{\Delta I_{sc}(t)}{\Delta I_{LED}(t)} , \quad (5.3)$$

where $\Delta I_{sc}(t)$ is the modulated short-circuit current response of the solar cell and $\Delta I_{LED}(t)$ is the driving current of the intensity modulated LED illumination. For each device, the transfer function was measured for five different illumination base levels ($I_{LED} = 38 \text{ mA}, 75 \text{ mA}, 150 \text{ mA}, 300 \text{ mA}, 600 \text{ mA}$). The corresponding curves are shaded from dark orange/green (lowest illumination level) to bright orange/green (highest illumination level). The grey arrows also indicate the increase in base illumination irradiance.

Equivalently, for IMVS the transfer function H_{IMVS} is defined as

$$H_{IMVS} = \frac{\Delta V_{oc}(t)}{\Delta I_{LED}(t)} , \quad (5.4)$$

where $\Delta V_{oc}(t)$ is the modulated open-circuit voltage response of the photovoltaic device. Nyquist and Bode graphs for the IMVS measurements are shown in Figure 5.13. The characteristic frequency can be easily determined from the Bode plots (Figure 5.13 c and d) for the five different illumination irradiance levels by finding the frequency at which the imaginary part of the transfer function becomes minimal. Note that all plots show the negative imaginary part $-\text{Im}(H_{IMPS/IMVS})$.

Intensity modulated photocurrent spectroscopy (IMPS)

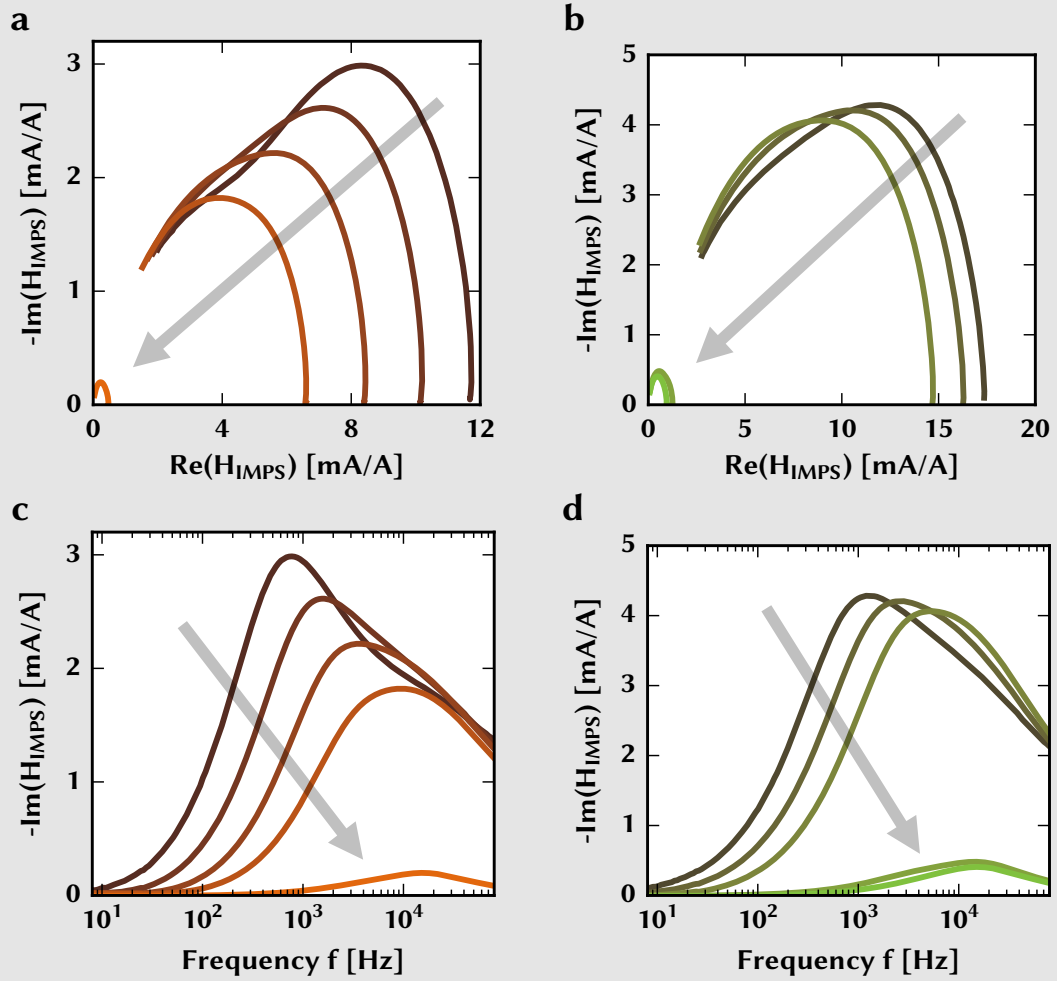
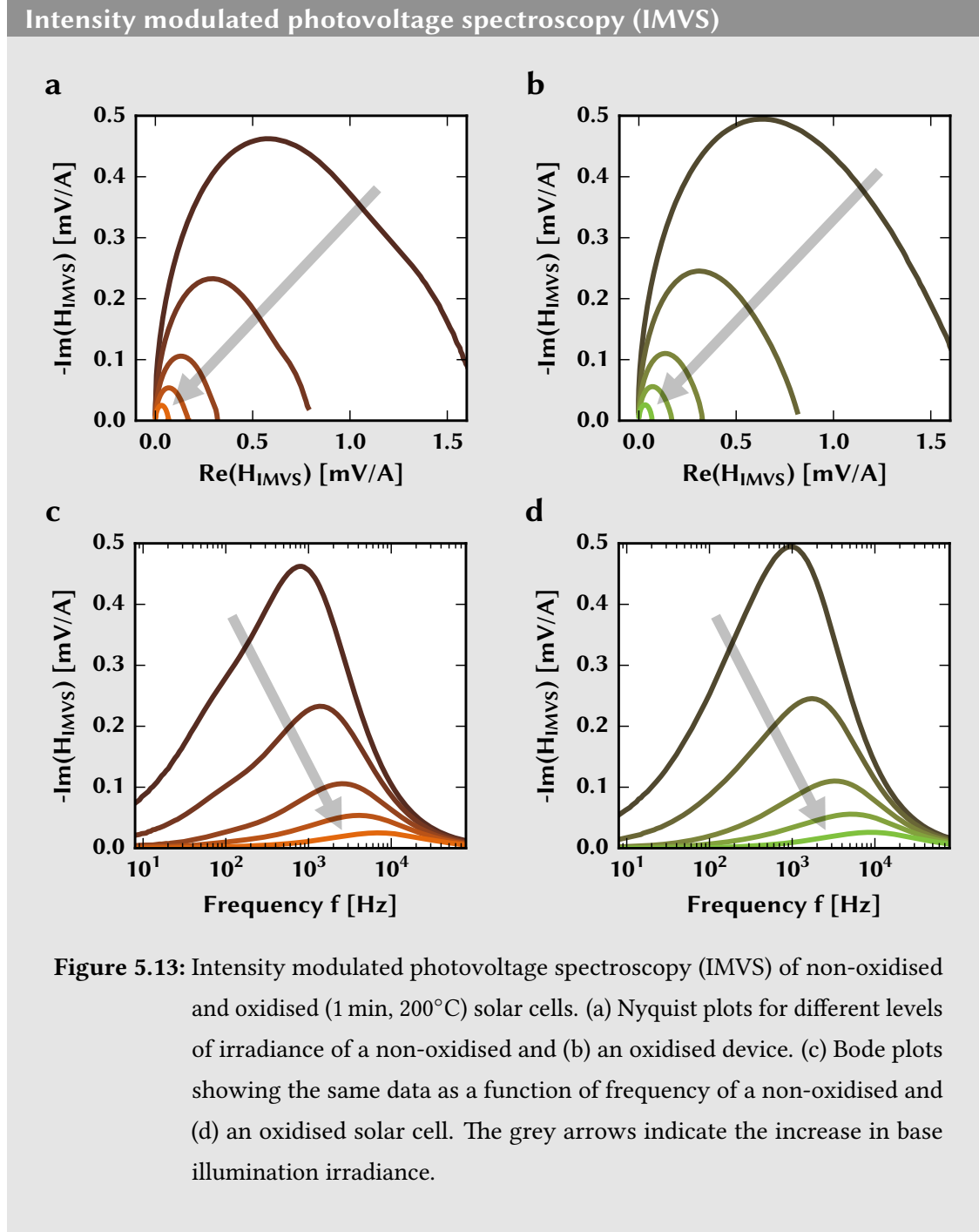


Figure 5.12: Intensity modulated photocurrent spectroscopy (IMPS) of non-oxidised and oxidised (1 min, 200°C) solar cells. (a) Nyquist plots for different levels of irradiance of a non-oxidised and (b) an oxidised device. (c) Bode plots showing the same data as a function of frequency of a non-oxidised and (d) an oxidised solar cell. The grey arrows indicate the increase in base illumination irradiance.

In Figure 5.14, the transport lifetimes (a) and recombination lifetimes (b) are shown as a function of the short-circuit current and the open-circuit voltage. The lifetimes were



calculated according to Equation 5.1 and Equation 5.2. The solid lines in the figure are least-square fits of single exponential functions of the form $\tau_{tr} = A_1 \exp(-B_1 \cdot I_{sc}) + C_1$

and $\ln(\tau_{\text{rec}}) = -A_2 \cdot V_{\text{oc}} + B_2$. The fitting parameters and the complementary standard deviations are shown in Table 5.2.

The transport lifetime τ_{tr} is unaffected by the oxidation process. As the electron transport is dominated by diffusion in the mesoporous TiO_2 layer [17], it is expected that the short heat treatment in air and the oxidation of the antimony sulfide layer does not alter the transport lifetime.

However, the short oxidation of the absorber film (1 min at 200°C) does indeed increase the recombination lifetime in the solar cell. Thus, recombination at the antimony sulfide - P3HT interface is decreased and the charge collection efficiency $\eta_{\text{cc}} = 1 - \frac{\tau_{\text{tr}}}{\tau_{\text{rec}}}$ is improved. In Figure 5.14 b, the recombination lifetime τ_{rec} is increased by a factor of approximately 3.5, when comparing the non-oxidised with the oxidised sample.

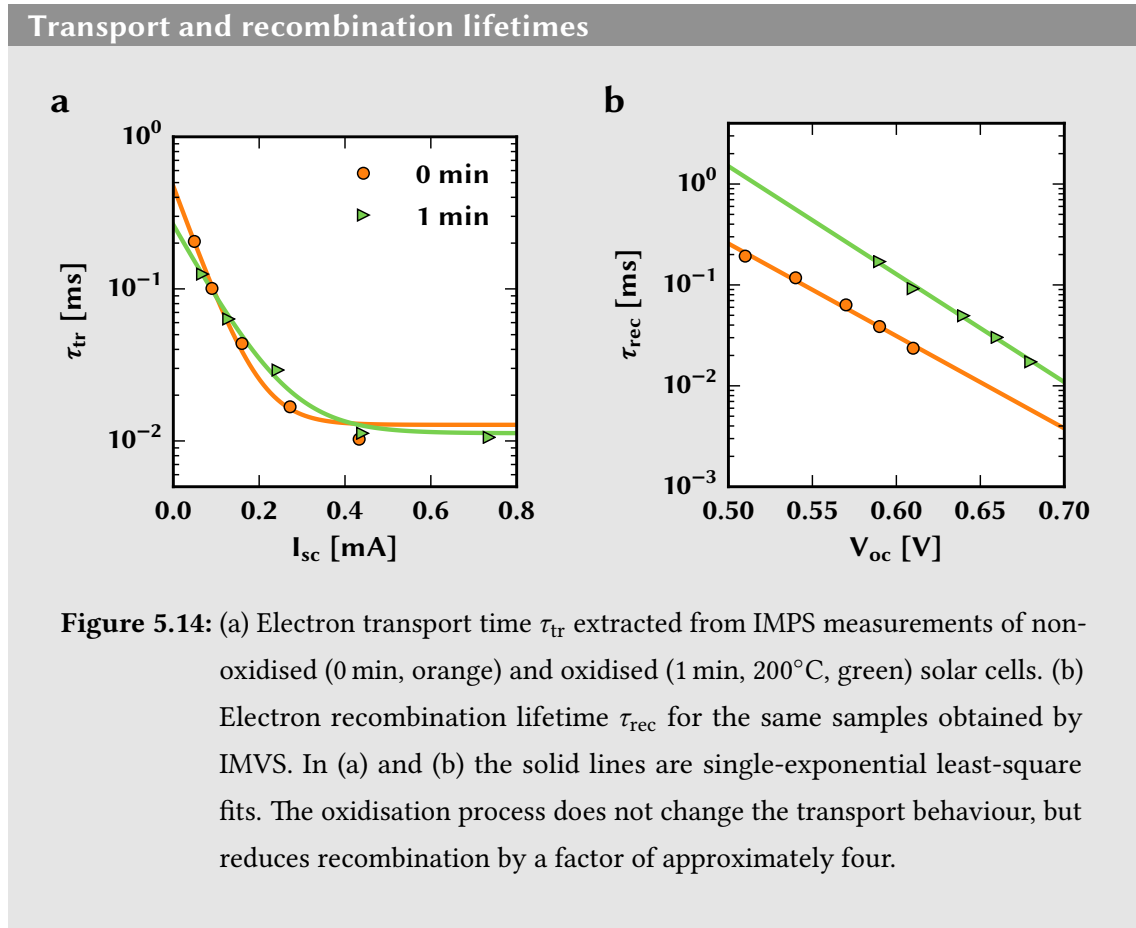


Table 5.2: Least-square fit parameters of a simple exponential function of the form $\tau_{tr} = A_1 \exp(-B_1 \cdot I_{sc}) + C_1$ and a logarithmic straight line $\ln(\tau_{rec}) = -A_2 \cdot V_{oc} + B_2$ to the data from IMPS and IMVS measurements.

	IMPS			IMVS	
	A_1 [ms]	$B_1 \left[\frac{1}{\text{mA}} \right]$	C_1 [ms]	$A_2 \left[\frac{\ln(\text{ms})}{\text{V}} \right]$	B_2 [ln(ms)]
0 min	0.46 ± 0.03	17.9 ± 1.4	0.013 ± 0.004	21.1 ± 1.8	9.2 ± 1.0
1 min	0.25 ± 0.02	11.8 ± 1.2	0.011 ± 0.003	24.6 ± 1.5	12.7 ± 1.0

Therefore, the hypothesis can be confirmed that cooling antimony sulfide solar cells in air after the annealing step or a better controlled post heat-treatment in air reduces recombination and is hence beneficial for the device performance.

5.4 Conclusion

In this study, the effect of oxidation of the crystalline antimony sulfide films for solid state sensitised solar cells has been investigated. A heat treatment in air at a temperature of $T = 200^\circ\text{C}$ leads to a partial oxidation of the antimony sulfide absorber film. The level of oxidation can be controlled accurately by changing the duration of the heat treatment, which was confirmed by XPS studies. XRD and UV-vis spectroscopy showed that the crystallographic and optical properties of the film are only marginally altered for short oxidation periods on the order of a few minutes. Sb_2S_3 sensitised solar cells were fabricated showing a device performance increase by more than 60 % for short oxidation times, but deterioration for longer oxidation. Finally, intensity modulated spectroscopy (IMPS and IMVS) confirmed the hypothesis that the thin antimony oxide layer reduces recombination at the interface of the absorber and the hole transport material. For very short oxidation times (1 min), the electron recombination lifetime is improved nearly fourfold compared to non-oxidised solar cells.

Bibliography

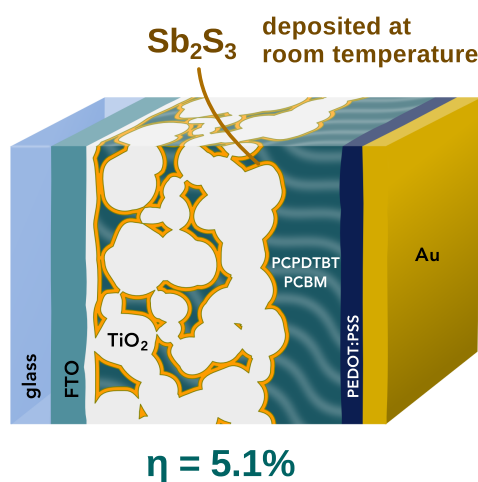
- [1] B. O'Regan and M. Grätzel. "A Low-Cost, High-Efficiency Solar Cell Based on Dye-Sensitized Colloidal TiO₂ Films". *Nature* 353.6346 (1991), pp. 737–740. DOI: 10.1038/353737a0.
- [2] B. Li, L. Wang, B. Kang, P. Wang, and Y. Qiu. "Review of Recent Progress in Solid-State Dye-Sensitized Solar Cells". *Solar Energy Materials and Solar Cells* 90.5 (2006), pp. 549–573. DOI: 10.1016/j.solmat.2005.04.039.
- [3] M. Y. Versavel and J. A. Haber. "Structural and optical properties of amorphous and crystalline antimony sulfide thin-films". *Thin Solid Films* 515.18 (2007), pp. 7171–7176. DOI: 10.1016/j.tsf.2007.03.043.
- [4] S.-J. Moon, Y. Itzhaik, J.-H. Yum, S. M. Zakeeruddin, G. Hodes, and M. Grätzel. "Sb₂S₃-Based Mesoscopic Solar Cell using an Organic Hole Conductor". *The Journal of Physical Chemistry Letters* 1.10 (2010), pp. 1524–1527. DOI: 10.1021/jz100308q.
- [5] S. H. Im, C.-S. Lim, J. A. Chang, Y. H. Lee, N. Maiti, H.-J. Kim, M. K. Nazeeruddin, M. Grätzel, and S. I. Seok. "Toward Interaction of Sensitizer and Functional Moieties in Hole-Transporting Materials for Efficient Semiconductor-Sensitized Solar Cells." *Nano Letters* 11.11 (2011), pp. 4789–93. DOI: 10.1021/nl2026184.
- [6] Y. C. Choi, D. U. Lee, J. H. Noh, E. K. Kim, and S. I. Seok. "Highly Improved Sb₂S₃ Sensitized-Inorganic–Organic Heterojunction Solar Cells and Quantification of Traps by Deep-Level Transient Spectroscopy". *Advanced Functional Materials* 24.23 (2014), pp. 3587–3592. DOI: 10.1002/adfm.201304238.
- [7] Y. Itzhaik, O. Niitsoo, M. Page, and G. Hodes. "Sb₂S₃-Sensitized Nanoporous TiO₂ Solar Cells". *The Journal of Physical Chemistry C Letters* 113 (2009), pp. 4254–4256.
- [8] J. A. Chang, J. H. Rhee, S. H. Im, Y. H. Lee, H.-j. Kim, S. I. Seok, M. K. Nazeeruddin, and M. Gratzel. "High-performance nanostructured inorganic-organic heterojunction solar cells." *Nano Letters* 10.7 (2010), pp. 2609–12. DOI: 10.1021/nl101322h.

-
- [9] M. T. S. Nair, Y. Pena, J. Campos, V. M. Garcia, and P. K. Nair. "Chemically Deposited Sb₂S₃ and Sb₂S₃-CuS Thin Films". *Journal of The Electrochemical Society* 145.6 (1998), 2113–2120.
- [10] S. Messina, M. Nair, and P. Nair. "Antimony sulfide thin films in chemically deposited thin film photovoltaic cells". *Thin Solid Films* 515.15 (2007), pp. 5777–5782. DOI: 10.1016/j.tsf.2006.12.155.
- [11] N. Maiti, S. H. Im, C.-S. Lim, and S. I. Seok. "A chemical precursor for depositing Sb₂S₃ onto mesoporous TiO₂ layers in nonaqueous media and its application to solar cells." *Dalton Transactions* 41.38 (2012), pp. 11569–72. DOI: 10.1039/c2dt31348k.
- [12] J. C. Cardoso, C. A. Grimes, X. Feng, X. Zhang, S. Komarneni, M. V. B. Zanoni, and N. Bao. "Fabrication of Coaxial TiO₂/Sb₂S₃ Nanowire Hybrids for Efficient Nanostructured Organic–Inorganic Thin Film Photovoltaics". *Chemical Communications* 48.22 (2012), p. 2818. DOI: 10.1039/c2cc17573h.
- [13] S. Ito, K. Tsujimoto, D.-C. Nguyen, K. Manabe, and H. Nishino. "Doping effects in Sb₂S₃ absorber for full-inorganic printed solar cells with 5.7% conversion efficiency". *International Journal of Hydrogen Energy* 38.36 (2013), pp. 16749–16754. DOI: 10.1016/j.ijhydene.2013.02.069.
- [14] S. Nezu, G. Larramona, C. Chone', A. Jacob, B. Delatouche, D. Pe're', and C. Moisan. "Light Soaking and Gas Effect on Nanocrystalline TiO₂/Sb₂S₃/CuSCN Photovoltaic Cells Following Extremely Thin Absorber Concept". *The Journal of Physical Chemistry C* 114.14 (2010), pp. 6854–6859.
- [15] A. Kyono and M. Kimata. "Structural variations induced by difference of the inert pair effect in the stibnite-bismuthinite solid solution series (Sb,Bi)₂S₃". *American Mineralogist* 89 (2004), pp. 932–940.
- [16] T. Birchall, J. Connor, and L. Hillier. "High-Energy Photoelectron Spectroscopy of Some Antimony Compounds". *Journal of the Chemical Society, Dalton Transactions* 2003 (1975), pp. 2003–2006. DOI: 10.1039/DT9750002003.

- [17] L. Dloczik, O. Ileperuma, I. Lauermann, L. M. Peter, E. A. Ponomarev, G. Redmond, N. J. Shaw, and I. Uhlenndorf. “Dynamic Response of Dye-Sensitized Nanocrystalline Solar Cells: Characterization by Intensity-Modulated Photocurrent Spectroscopy”. *The Journal of Physical Chemistry B* 101.49 (1997), pp. 10281–10289. DOI: 10.1021/jp972466i.
- [18] J. A. Chang, S. H. Im, Y. H. Lee, H.-J. Kim, C.-S. Lim, J. H. Heo, and S. I. Seok. “Panchromatic photon-harvesting by hole-conducting materials in inorganic-organic heterojunction sensitized-solar cell through the formation of nanostructured electron channels.” *Nano letters* 12.4 (2012), pp. 1863–7. DOI: 10.1021/nl204224v.
- [19] P. P. Boix, G. Larramona, A. Jacob, B. Delatouche, I. Mora-Seró, and J. Bisquert. “Hole Transport and Recombination in All-Solid Sb₂S₃-Sensitized TiO₂ Solar Cells Using CuSCN As Hole Transporter”. *The Journal of Physical Chemistry C* 116 (2012), pp. 1579–1587. DOI: 10.1021/jp210002c.
- [20] E. Palomares, J. N. Clifford, S. A. Haque, T. Lutz, and J. R. Durrant. “Slow charge recombination in dye-sensitised solar cells (DSSC) using Al₂O₃ coated nanoporous TiO₂ films”. *Chemical Communications* 14 (2002), pp. 1464–1465.
- [21] D. Bartesaghi, I. del Carmen Pérez, J. Kniepert, S. Roland, M. Turbiez, D. Neher, and L. J. A. Koster. “Competition between recombination and extraction of free charges determines the fill factor of organic solar cells”. *Nature communications* 6 (2015), p. 7083.
- [22] G. Schlichthörl, N. G. Park, and A. J. Frank. “Evaluation of the Charge-Collection Efficiency of Dye-Sensitized Nanocrystalline TiO₂ Solar Cells”. *The Journal of Physical Chemistry B* 103.5 (1999), pp. 782–791. DOI: 10.1021/jp9831177. eprint: <http://dx.doi.org/10.1021/jp9831177>.
- [23] G. Schlichthörl, S. Y. Huang, J. Sprague, and A. J. Frank. “Band Edge Movement and Recombination Kinetics in Dye-Sensitized Nanocrystalline TiO₂ Solar Cells: A Study by Intensity Modulated Photovoltage Spectroscopy”. *The Journal of Physical Chemistry B* 101.41 (1997), pp. 8141–8155. DOI: 10.1021/jp9714126.

- [24] P. R. F. Barnes, K. Miettunen, X. Li, A. Y. Anderson, T. Bessho, M. Grätzel, and B. C. O'Regan. "Interpretation of Optoelectronic Transient and Charge Extraction Measurements in Dye-Sensitized Solar Cells". *Advanced Materials* 25.13 (2013), pp. 1881–1922. doi: 10.1002/adma.201201372.
- [25] Gamry Instruments. *Dye Solar Cells - IMPS/IMVS Measurements*. <http://www.gamry.com/application-notes/physechem/dye-solar-cells-imps-imvs/>. 2016.

Room temperature deposition of antimony sulfide



Parts of this chapter are published in:

K. C. Gödel, Y. C. Choi, B. Roose, A. Sadhanala, H. Snaith, S. I. Seok, U. Steiner, S. K. Pathak. "Efficient room temperature aqueous Sb₂S₃ synthesis for inorganic-organic sensitised solar cells with 5.1% efficiencies". *Chemical Communication*, 51, 8640-8643 (2015). doi:10.1039/C5CC01966D.

Abstract Sb_2S_3 sensitised solar cells are a promising alternative to devices employing organic dyes. The manufacture of Sb_2S_3 absorber layers using the conventional chemical bath deposition technique is however cumbersome, as cooling equipment is required. In this chapter, a modified aqueous chemical bath synthesis of Sb_2S_3 absorber layers for sensitised solar cells is reported. The method is based on the hydrolysis of SbCl_3 to complex antimony ions which decelerates the reaction at ambient conditions, in contrast to the usual low temperature deposition protocol. Photothermal deflection spectroscopy shows that the sub band gap trap-state density is lower in Sb_2S_3 films deposited with our method, compared to standard deposition protocols. It yields devices with an improved performance. Optimising the room temperature deposition parameters and the device architecture allows to manufacture sensitised mesoporous TiO_2 solar cells with power conversion efficiencies of up to $\eta = 5.1 \%$.

6.1 Introduction

Antimony sulfide is a promising material for several optoelectronic applications. Due to its high absorption coefficient ($\alpha \approx 1.8 \cdot 10^5 \text{ cm}^{-1}$ at $\lambda = 450 \text{ nm}$) and a suitable direct band gap of $E_g \approx 1.7 \text{ eV}$, crystalline Sb_2S_3 (stibnite) is interesting as light absorber for solid-state sensitised solar cells [1, 2]. In particular, Sb_2S_3 -based solar cells excel in their stability of operation when compared to other organic-inorganic hybrid devices. Recently, power-conversion efficiencies of $\eta = 6.2 \%$ [3] and $\eta = 7.5 \%$ [4] were achieved using Sb_2S_3 as the absorber material obtained from chemical bath deposition. Further, the material has been used to improve the stability of methyl-ammonium lead iodide perovskite solar cells [5].

Antimony sulfide is typically deposited in aqueous or non-aqueous chemical baths at low temperatures (low-T deposition) [6–9]. The standard method is the aqueous CBD using antimony chloride (SbCl_3) and sodium thiosulfate ($\text{Na}_2\text{S}_2\text{O}_3$). This technique is however cumbersome since it requires a precise temperature control of the solution when cooling below 10°C and maintaining the sample at low temperatures. For large-scale

applications such a cooling protocol is inconvenient, costly and energy-intensive.

Here, an aqueous room temperature (RT) deposition route of Sb_2S_3 using the same precursor materials as the standard CBD method is presented. Optimised Sb_2S_3 sensitised solar cells using this RT deposition method demonstrate excellent device performance with efficiencies of up to $\eta = 5.1\%$.

6.2 Materials and methods

6.2.1 Solar cell preparation

Glass substrates with a conductive fluorine doped tin-oxide layer (FTO, $8\ \Omega/\square$, Sigma-Aldrich) were coated with a hole-blocking compact TiO_2 layer by a sol-gel spin-coating process as described in Chapter 4. A mesoporous TiO_2 layer was applied by spin-coating a Dyesol paste (WER2-O) containing 200 nm TiO_2 nanoparticles at 1500 RPM for 45 s. The dyesol paste was diluted using anhydrous ethanol (2.5 ml EtOH per 1 g paste) to give a mesoporous layer of approximately 1 – 1.5 μm in thickness. For optimised devices, mesoporous titania anodes with a thickness of 1 μm were fabricated by screen-printing a paste consisting of TiO_2 with 50 nm average particle size followed by sintering at 550°C for 2 h. To reduce surface traps in TiO_2 , the anode was immersed in a 40 mM aqueous TiCl_4 solution at 65°C for 1 h and resintered at 500°C for 1 h.

For the reference low-T samples, the standard aqueous deposition route of Sb_2S_3 was used in a chemical bath of SbCl_3 (Sigma-Aldrich, $\geq 99.0\%$) and $\text{Na}_2\text{S}_2\text{O}_3$ ($\geq 98.0\%$, Sigma-Aldrich) with a deposition temperature below 10°C , as described in Chapter 5. For the RT deposition, SbCl_3 was dissolved in 2.5 ml acetone followed by the addition of 72.5 ml deionised water. Antimony chloride hydrolysed, which lead to a cloudy solution with white precipitate. 3.95 g $\text{Na}_2\text{S}_2\text{O}_3$ in 25 ml H_2O was added while stirring. The substrates were immediately immersed into the solution. The deposition of Sb_2S_3 was indicated by an orange colour change of the bath. After the deposition, the orange substrates were rinsed in DI water and dried with nitrogen. To form brown crystalline Sb_2S_3 , the

samples were annealed in an argon atmosphere at 300°C for 5 min. P3HT (Merck lisicon) in chlorobenzene was used as a hole transport material. In two subsequent steps P3HT was spin-coated at 1500 RPM for 45 s. At first a concentration of $5 \frac{\text{mg}}{\text{ml}}$ was deposited, then a concentration of $15 \frac{\text{mg}}{\text{ml}}$. Prior to spinning, the solution was spread with the tip of a pipette and allowed to infiltrate the porous film for approximately 10 s. For the optimised solar cells, mesoporous TiO_2 films were screen-printed from a custom paste containing anatase nanoparticles with an average diameter of 50 nm. The paste was prepared by the group of Prof. Dr. Sang Il Seok at the KRICT institute, Daejeon, South Korea. It was screen-printed with a mesh giving a thickness of 1 μm and sintered at $T = 550^\circ\text{C}$ for two hours. Further, PCPDTBT was used as a hole conducting material. It was dissolved in 1,2-dichlorobenzene (15 mg/ml) and 5 mg/ml PC₇₀BM ([6,6]-Phenyl C71 butyric acid methyl ester) was added and spin-coated at 2000 RPM for 60 s onto the substrates. Gold electrodes (100 nm) were evaporated using a thermal or e-beam evaporator. The active area (9 mm² or 9.6 mm² for the optimised devices) of the solar cells was defined using a metal mask.

6.2.2 Material characterisation

X-ray diffraction was carried out using a Bruker D8 θ/θ (fixed sample) set-up with a LynxEye position sensitive detector and a standard SC detector with auto-absorber and graphite 2nd beam monochromator. The set-up uses a Bragg Brentano parafocusing geometry and operates in reflection mode. XPS spectra were measured in an ultra-high vacuum chamber of an ESCALAB 250Xi. The measurements were carried out using a XR6 monochromated $\text{AlK}\alpha$ source (1486.6 eV) and a pass energy of 20 eV. PDS spectra were measured with a Light Support MKII 100 W Xenon arc source coupled with a CVI DK240 monochromator. A Qioptiq 670 nm fiber-coupled diode laser was used for the probe beam.

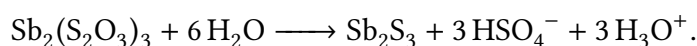
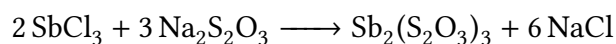
6.2.3 Optoelectronic measurements

An ABET Technologies (Model 11016 Sun 2000) solar simulator with a xenon arc lamp was used and the solar cell response was recorded with a Keithley 2635 sourcemeter. The intensity of the solar simulator was calibrated to $100 \frac{\text{mW}}{\text{cm}^2}$ using a silicon reference cell from Czibula & Grundmann (FHG-ISE, RS-OD4). The *EQE*-measurements were carried out using a 250 W tungsten halogen lamp and an Oriel Cornerstone 130 monochromator.

6.3 Results and discussion

6.3.1 Synthesis of Sb_2S_3 at room-temperature

The low-temperature synthesis of Sb_2S_3 for photovoltaic applications involves the following chemical reaction equations [7]:



These reactions have to be slowed down by cooling below 10°C to avoid immediate precipitation [7] and to enable strong adhesion of Sb_2S_3 to the substrate. Thus, the standard CBD method, termed low-T deposition throughout this chapter, requires cooling of the reaction solution, whereas the modified method that was developed here, RT deposition, can be performed without cooling at ambient conditions. The immediate precipitation of the low-T deposition without cooling is shown in a series of photographs in Figure 6.1 (top). By changing the order of reactant addition at RT, Sb_2S_3 formation is slowed down and well-adhering films are obtained. The reaction speed of the RT method is illustrated in Figure 6.1 (bottom). In the conventional method, sodium thiosulfate is first added to an antimony chloride solution in acetone before the addition of water. For the RT method, this order was reversed, i.e. water is added before the sulfur source.

Reaction time of different deposition methods at RT

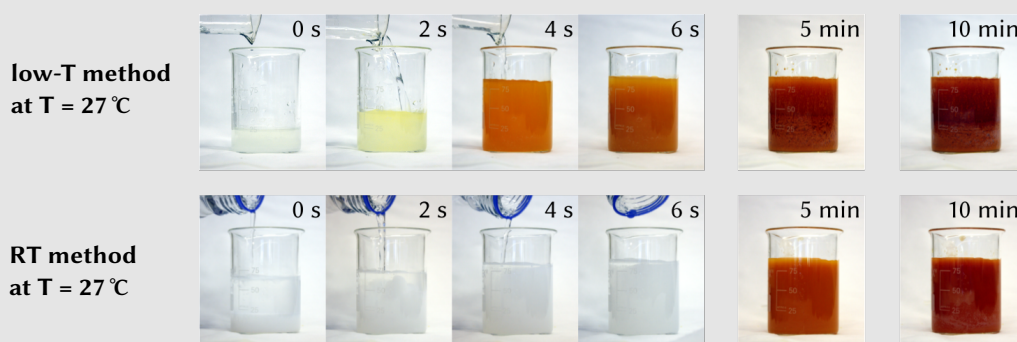


Figure 6.1: Photographic time series of the low-T method carried out at 27°C (top row) in comparison with the RT method at 27°C (bottom row). The pictures qualitatively show the reaction at different time periods after the addition of the sulfur source. If the conventional low-T method is carried out at RT, the reaction speed is too fast, which can be observed by the immediate colour change of the bath on the addition of the sulfur source, which indicates the fast formation of amorphous Sb_2S_3 . The high reaction speed leads to poor adhesion of the antimony sulfide to the substrate. The RT method complexes antimony ions by hydrolysing SbCl_3 and thus slows down the reaction.

In more detail, a 1.4 M SbCl_3 solution in acetone was prepared as the starting point for the RT deposition. SbCl_3 can be used without dissolution in acetone, changing the reaction behaviour very little. The addition of acetone, however, facilitates the handling of the highly hygroscopic SbCl_3 . Then, DI water is added under vigorous stirring to reduce the total concentration of SbCl_3 to 46 mM. The addition of water hydrolyses SbCl_3 , which leads to a solid white precipitate. The product of this hydrolysis reaction is not very well defined. It depends on many parameters such as the dilution of the reaction medium, the pH value of the solution and solvent composition [10, 11]. The aqueous solution containing hydrolysed SbCl_3 has a pH of 1.4.

To investigate the precipitate, it was filtered and dried and XRD measurements were performed on the white powder. The results are shown in Figure 6.2. The XRD pattern shows crystalline phases of $\text{Sb}_4\text{O}_5\text{Cl}_2$, $\text{Sb}_8(\text{OH})_6\text{O}_8\text{Cl}_2(\text{H}_2\text{O})$, $\text{Sb}_8\text{O}_{11}\text{Cl}_2(\text{H}_2\text{O})_6$ and $\text{Sb}_3\text{O}_6(\text{OH})$. This is in contrast to the reports by Li *et al.* and Yu *et al.* describing similar reactions [12, 13]. They also report upon the formation of a white precipitate on the hydrolysis of antimony chloride, but identify it as antimony oxychloride, SbOCl . The XRD pattern in Figure 6.2, however, shows no evidence of crystalline SbOCl formation. According to Chen *et al.* hydrolysis at pH 1–2 leads to the formation of $\text{Sb}_4\text{O}_5\text{Cl}_2$ for mixed solvents such as water and ethanol or water and ethylene glycol [11] supporting our findings.

Subsequently, a 1 M aqueous $\text{Na}_2\text{S}_2\text{O}_3$ solution was added at a final concentration of 0.25 M in the chemical bath. This causes the solution to turn clear as most of the precipitate dissolves, suggesting the formation of a water-soluble complex. After approximately 5 min at 20°C , the solution starts to turn orange, indicating the formation of amorphous Sb_2S_3 . This is accompanied by a pH change of the solution from $\text{pH} = 3.3$ immediately after the addition of sodium thiosulfate (with $\text{pH} = 7.3$) to $\text{pH} = 4.3$ after two hours, when the antimony sulfide deposition is complete. After deposition, the samples were rinsed in DI water and blow-dried with nitrogen.

6.3.2 Characterisation of room-temperature deposited Sb_2S_3

The material properties of both, low-T and RT antimony sulfide were measured and differences between the two methods were analysed. The films, fabricated using both deposition techniques, were annealed at 300°C for 10 min and characterised using various techniques, including XRD, XPS, conductivity, and absorption measurements.

The crystalline antimony sulfide was characterised by powder X-ray diffraction. Figure 6.3 compares the XRD pattern of the low-T and RT deposition methods. Both patterns are very similar and match the antimony sulfide reference pattern [14]. The nine most intense peaks in the region between $2\theta = 10^\circ - 30^\circ$ were fitted with Lorentz profiles and

XRD of the RT precursor

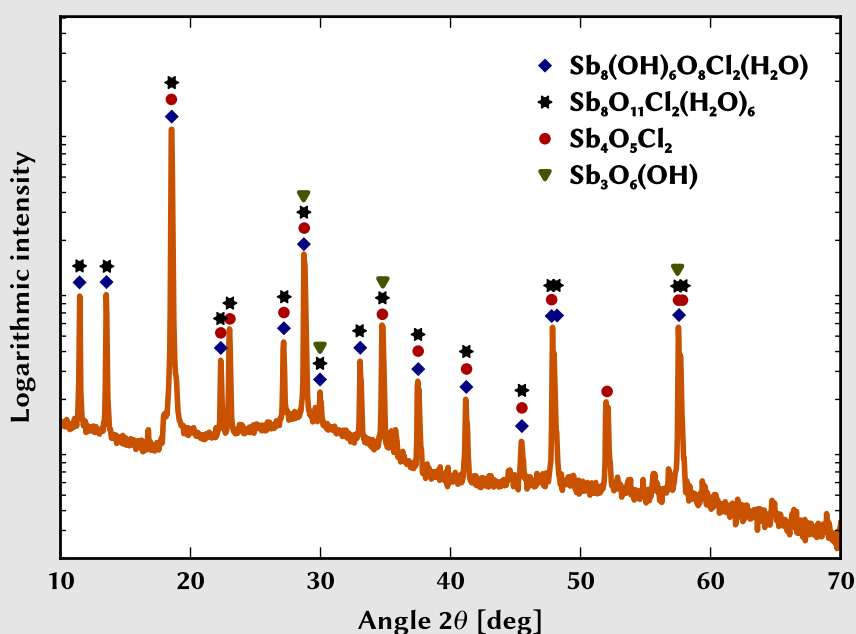


Figure 6.2: Semi-logarithmic XRD pattern of the intermediate precipitate which is the product of the hydrolysis of SbCl_3 . Possible peaks of compounds containing antimony, oxygen and chlorine were detected by the software HighScore (PANalytical). The peaks are marked with different symbols corresponding to various compounds, which are indicated in the figure legend. The SbOCl reference did not match any of the peaks in the measured pattern.

the crystallite size was analysed as described in Chapter 4. The mean crystallite sizes of the powders were 21 ± 1 nm for the low-T and 22 ± 5 nm for the RT deposition methods.

Sb_2S_3 films deposited by the RT method onto mesoporous TiO_2 substrates are shown in Figure 6.4. They also show the characteristic XRD peaks of crystalline Sb_2S_3 . The peak-widths are however broader and an average crystallite size of 14 ± 2 nm can be estimated from the three peaks between $2\theta = 15^\circ - 23^\circ$ by fitting Lorentzian functions to the data, as described in Chapter 4. The antimony sulfide in the configuration of a sensitised device is much thinner, explaining the smaller average crystallite diameter.

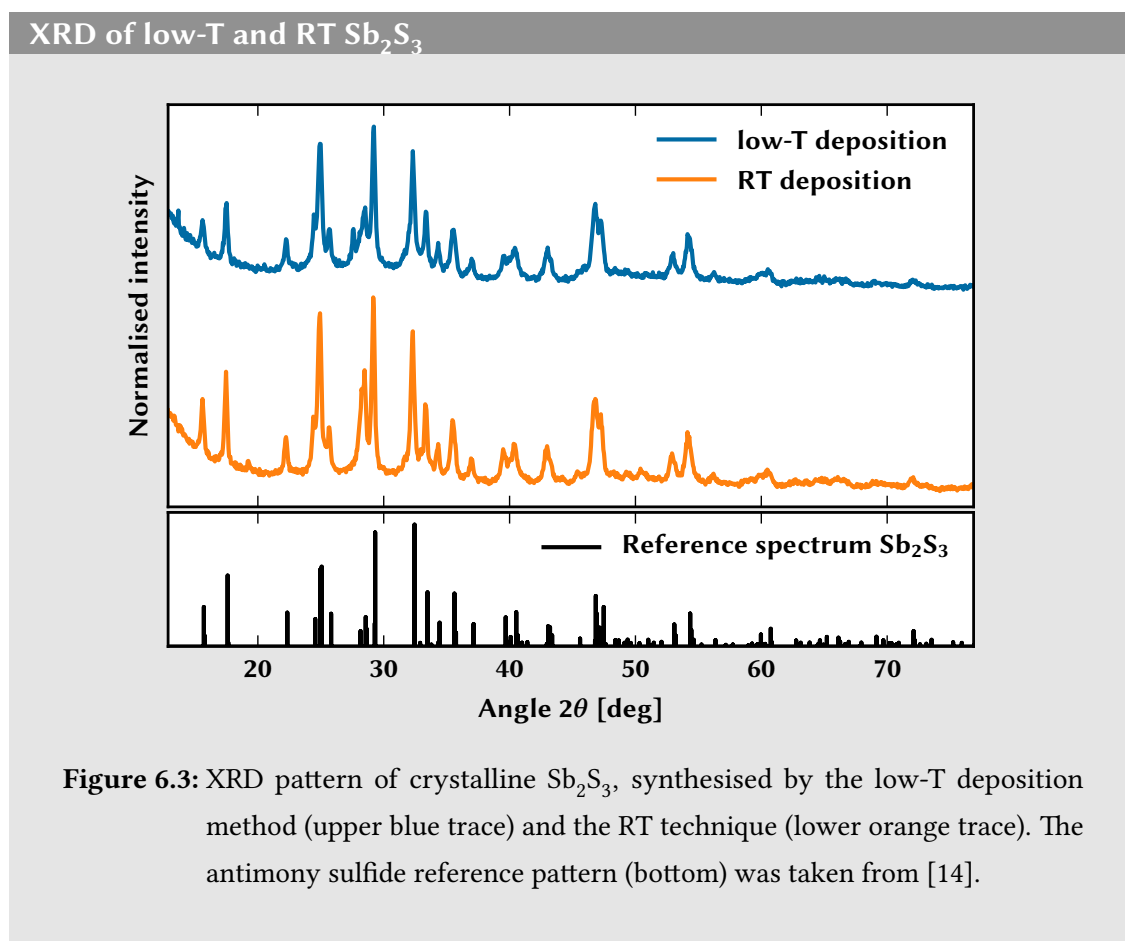
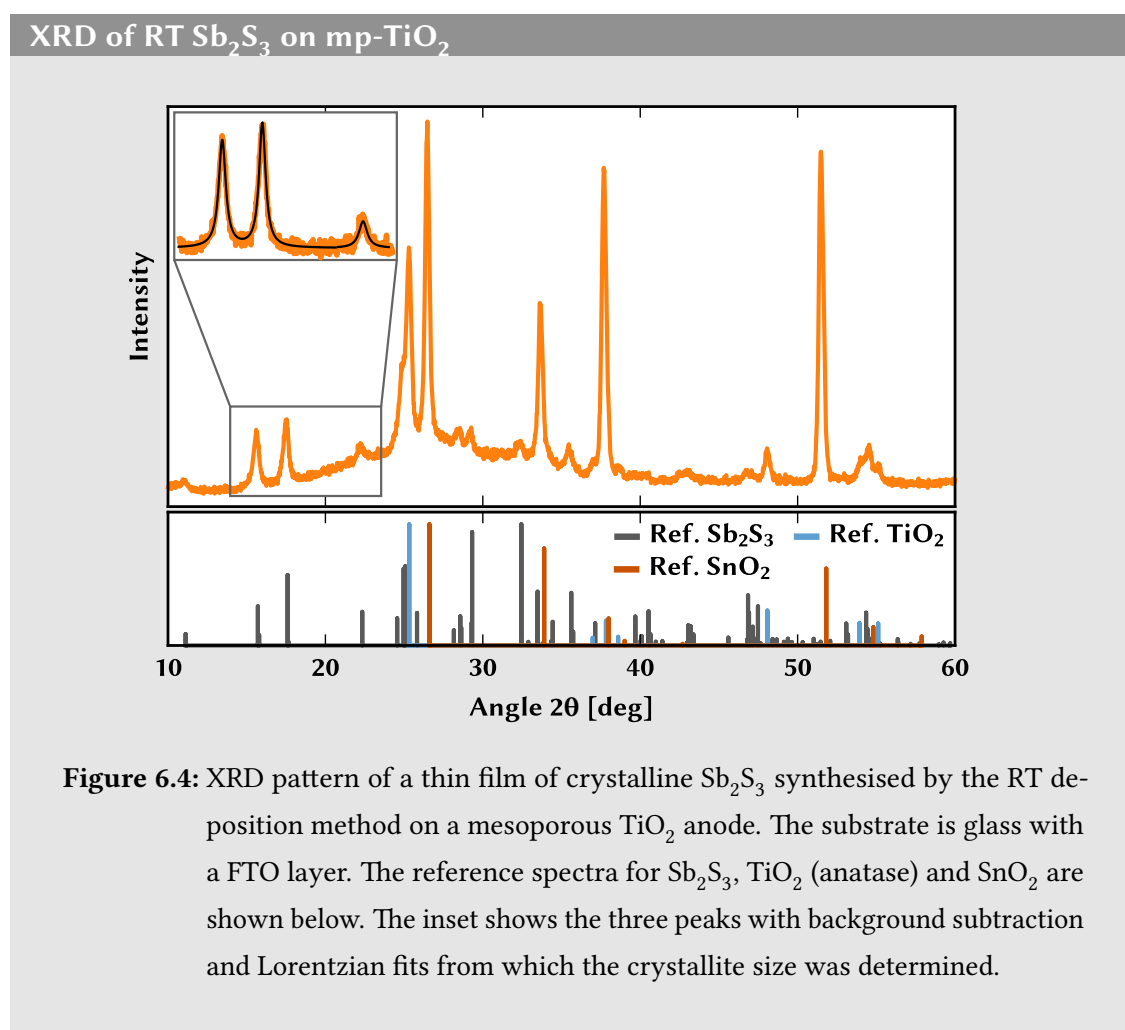


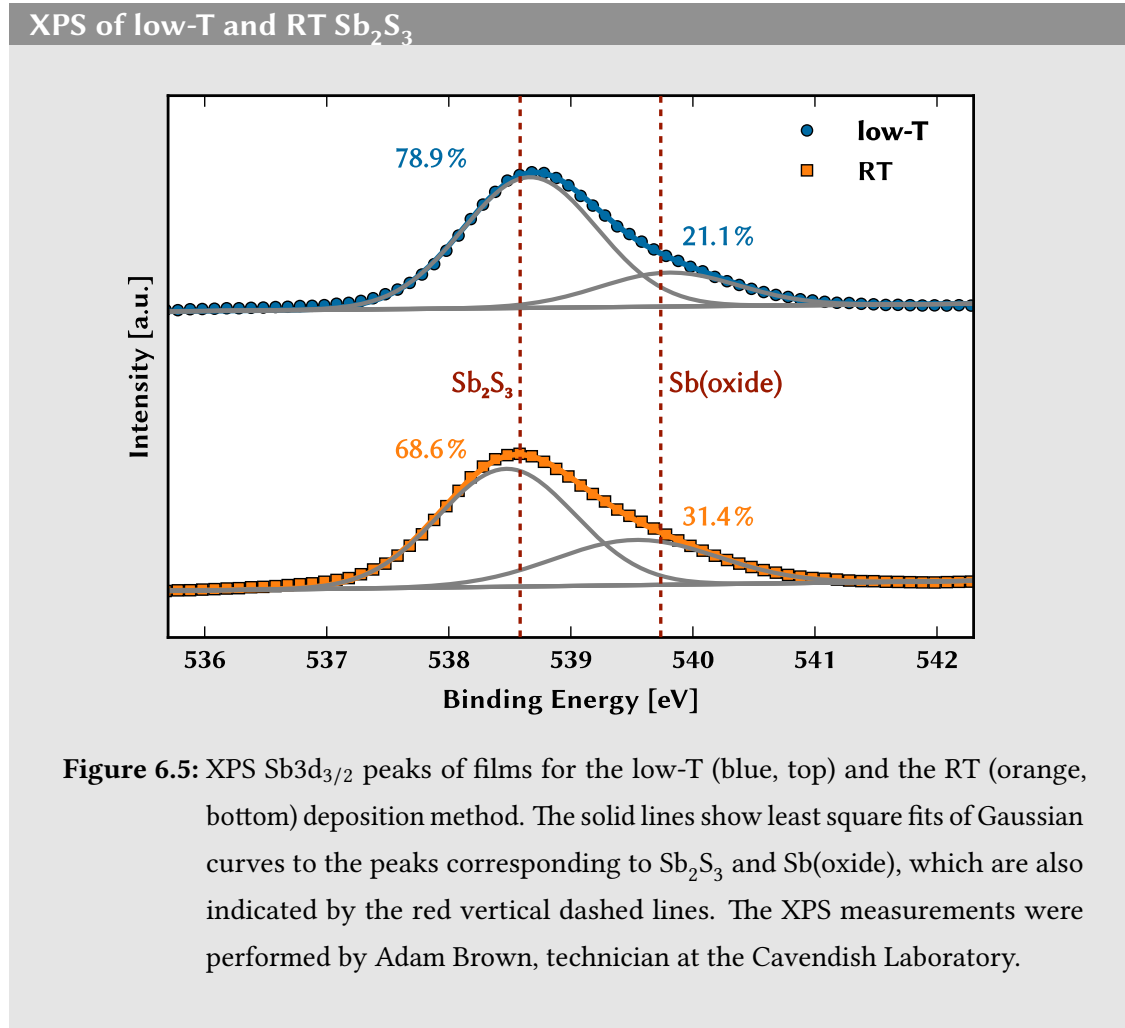
Figure 6.3: XRD pattern of crystalline Sb_2S_3 , synthesised by the low-T deposition method (upper blue trace) and the RT technique (lower orange trace). The antimony sulfide reference pattern (bottom) was taken from [14].

Further, XPS measurements were carried out on Sb_2S_3 films formed by both deposition techniques, shown in Figure 6.5. To compare the oxide content of the samples, the antimony $\text{Sb}3d_{3/2}$ peak was examined, because the oxygen $\text{O}1s$ peak directly overlaps with the antimony $\text{Sb}3d_{5/2}$ peak. The $\text{Sb}3d_{3/2}$ peak can be modelled using a superposition of two Gaussians, one at approximately 538.5 eV representing Sb_2S_3 and one at approximately 539.5 eV for Sb_xO_y [15]. The RT sample has a marginally higher oxide content compared to the low-T material. Unlike in Chapter 5, the increased oxide content is not caused by post oxidation and thus is not only a thin film at the surface but will be found throughout the Sb_2S_3 layer. Probably the formation of hydrolysed SbCl_3 in the RT method is causing this higher oxide content, as bonds between antimony and oxide are being formed. To study the influence of the oxide content on the conductivity,



low-T and RT deposited antimony sulfide films sandwiched between two gold electrodes were prepared. In Figure 6.6 the I - V curves of the low-T and RT films are shown in a semi-logarithmic plot. The curves show the average of the logarithmic current of four different antimony sulfide films for each deposition method. The conductivity of the RT film is reduced by more than two orders of magnitude compared to the low-T sample. However, as the film thickness of antimony sulfide in sensitised solar cells is thin (< 15 nm), the reduced conductivity is not too critical for device performance.

Subsequently, the absorption properties of the antimony sulfide films were measured in comparison. Figure 6.7 shows the absorbance spectra for amorphous (dashed lines)



and crystalline (solid lines) antimony sulfide films on mesoporous titanium dioxide for the low-T (blue) and the RT (orange) method. For both deposition methods, the absorption onset of the UV-vis measurements in Figure 6.7 corresponds well with the reported literature values of the band gap of amorphous ($E_g = 2.2$ eV, $\lambda_g = 564$ nm) and crystalline antimony sulfide ($E_g = 1.7$ eV, $\lambda_g = 729$ nm) [16]. For the crystalline sample, the RT deposition absorption is steeper compared to low-T sample. This is an indicator for a sharper band gap and could be a sign for a reduction in the trap-state density.

To further explore this, PDS was deployed to determine the trap-state density of Sb_2S_3 . It is known that the high density of electronic traps in this material, i.e. the number

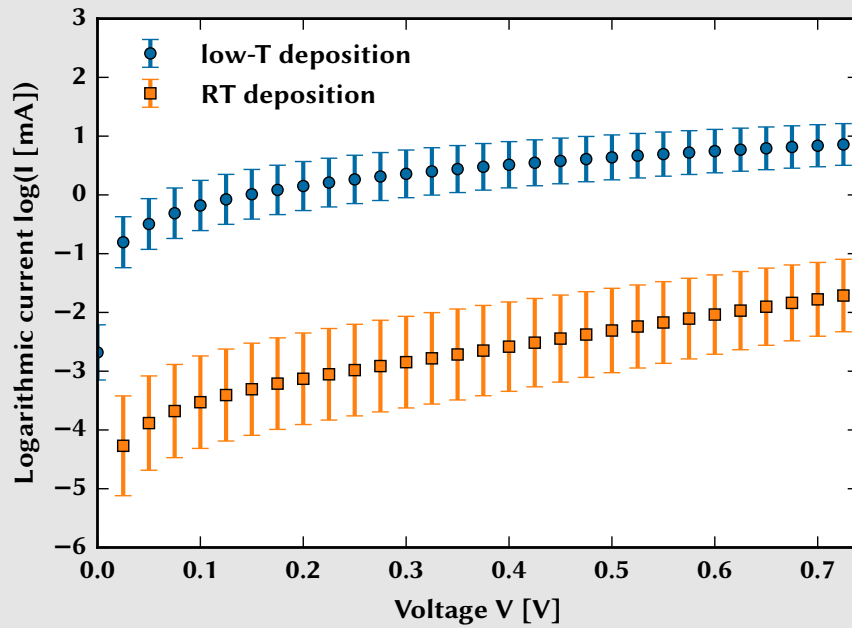
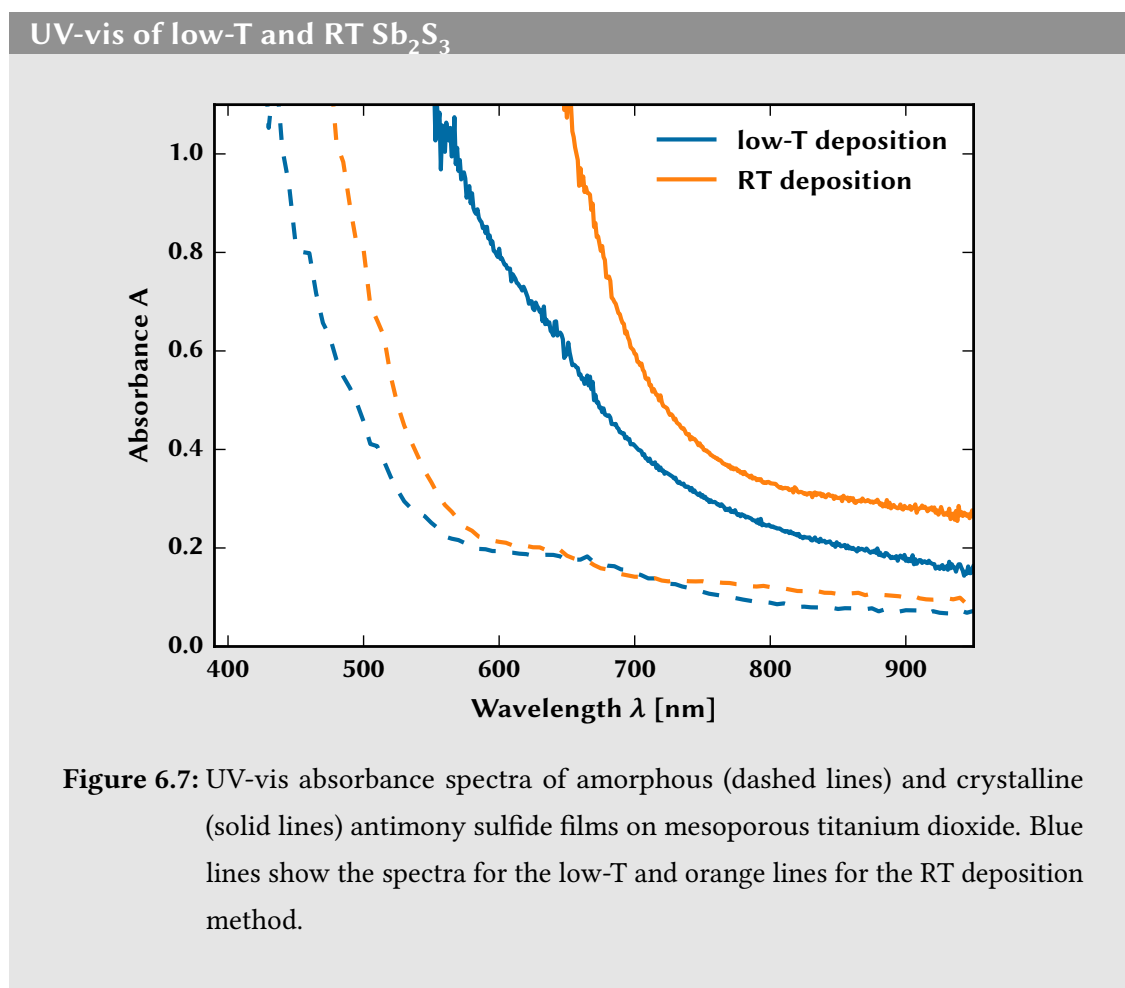
Conductivity of low-T and RT Sb_2S_3 films

Figure 6.6: I - V measurements of crystalline Sb_2S_3 films of the same thickness on a compact TiO_2 layer in the dark in a semi-logarithmic plot. The average of the logarithmic current of four different antimony sulfide films for each deposition method is shown. The RT method (orange squares) shows a much lower conductivity compared to the low-T method (blue circles).

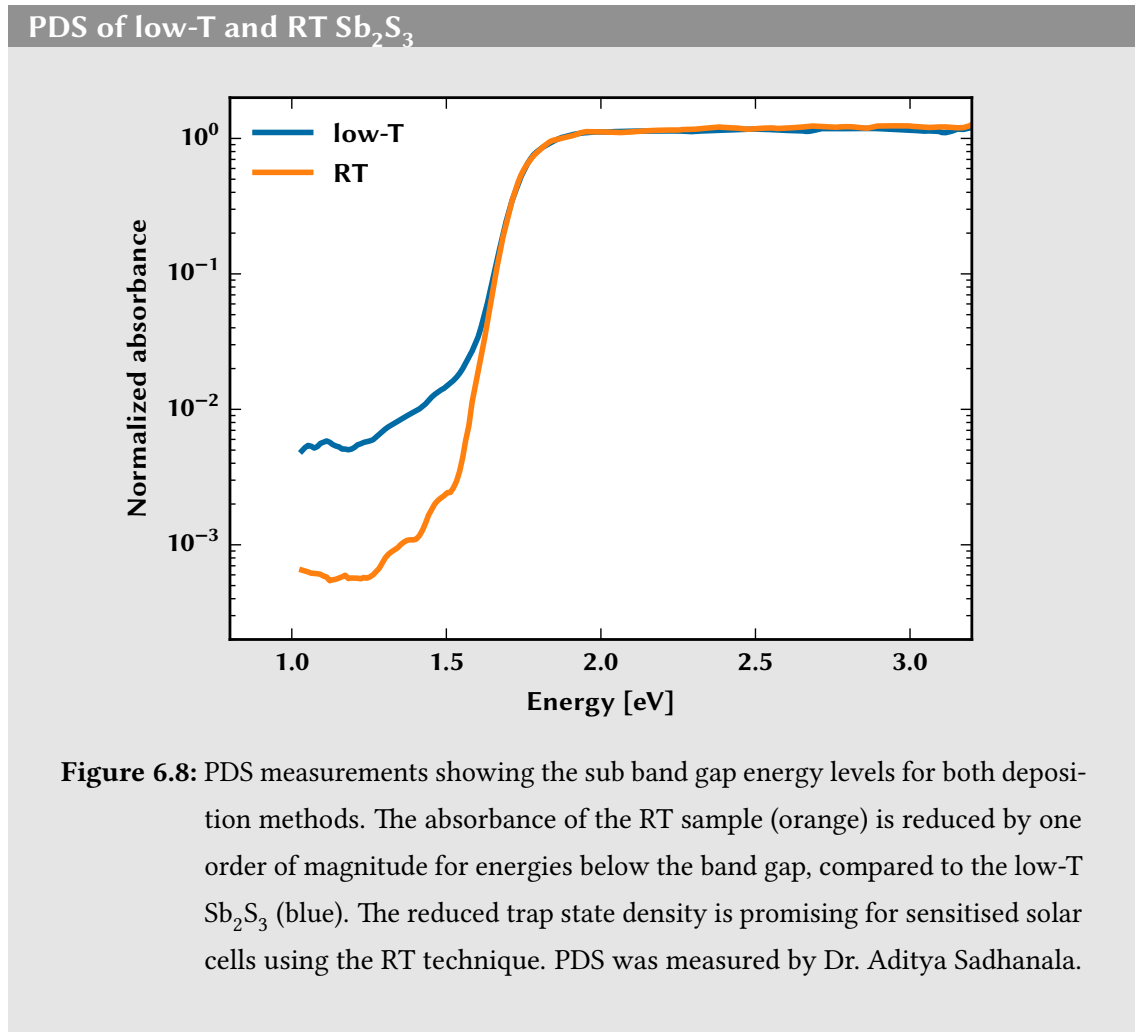
of energy states which lie in the band gap of Sb_2S_3 , is one of the biggest challenges of antimony sulfide sensitised solar cells [4, 17]. These trap-states lead to a significant loss in potential and to charge carrier recombination in the solar cell. Figure 6.8 shows the PDS spectra of Sb_2S_3 samples on mesoporous TiO_2 for both deposition methods. The absorption in the RT-deposited sample was significantly lower at energies below the band gap of Sb_2S_3 compared to the low-T sample. At energies below 1.6 eV the trap states are reduced by approximately one order of magnitude. This indicates a clear reduction in the density of deep-trap states for the RT deposited Sb_2S_3 and is a promising finding regarding the use of the material in sensitised solar cells.



6.3.3 Enhanced photovoltaics with room-temperature Sb_2S_3

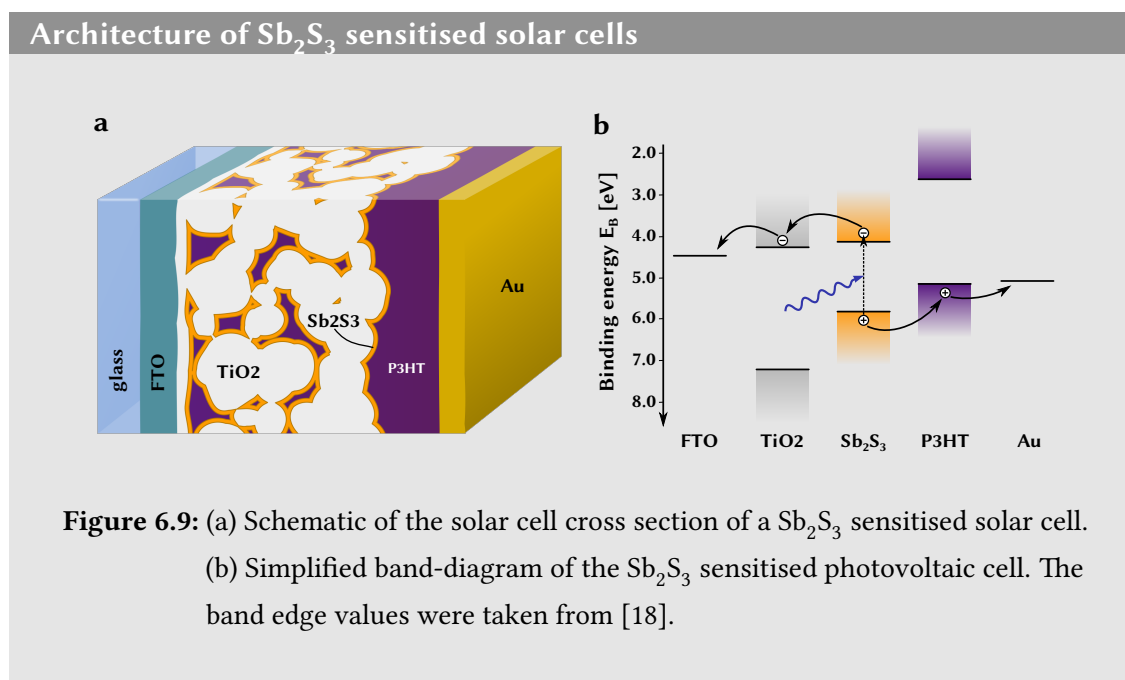
Sensitised solar cells using the RT deposition method and the conventional low-T synthesis were compared. The device architecture, schematically shown in Figure 6.9, is equivalent to the one introduced in Chapter 5. FTO was covered with a compact hole-blocking TiO_2 layer. Anatase TiO_2 nanocrystals with a diameter of 200 nm formed the mesoporous anode. P3HT was used as the hole transport material.

Twelve antimony sulfide sensitised solar cells for each of the two deposition methods (low-T and RT) were prepared and I - V curves were recorded. All precursor concentrations and processing steps were the same for the two different deposition methods, to ensure



comparable results. Only the synthesis step itself was changed as described earlier. The photovoltaic parameters, power conversion efficiency η , fill factor FF , open circuit voltage V_{oc} and short-circuit current density j_{sc} are presented in Figure 6.10. The results are also summarised in Table 6.1.

The average power conversion efficiency increased for the RT deposition method from $\eta = 1.0\%$ to $\eta = 1.2\%$ compared to the conventional low-T synthesis. Especially the open-circuit potential increased significantly from below $V_{oc} = 500$ mV to more than $V_{oc} = 580$ mV. Also the short-current density was improved for the RT sample. The only parameter which decreased, was the fill factor, due to the higher oxide content of the

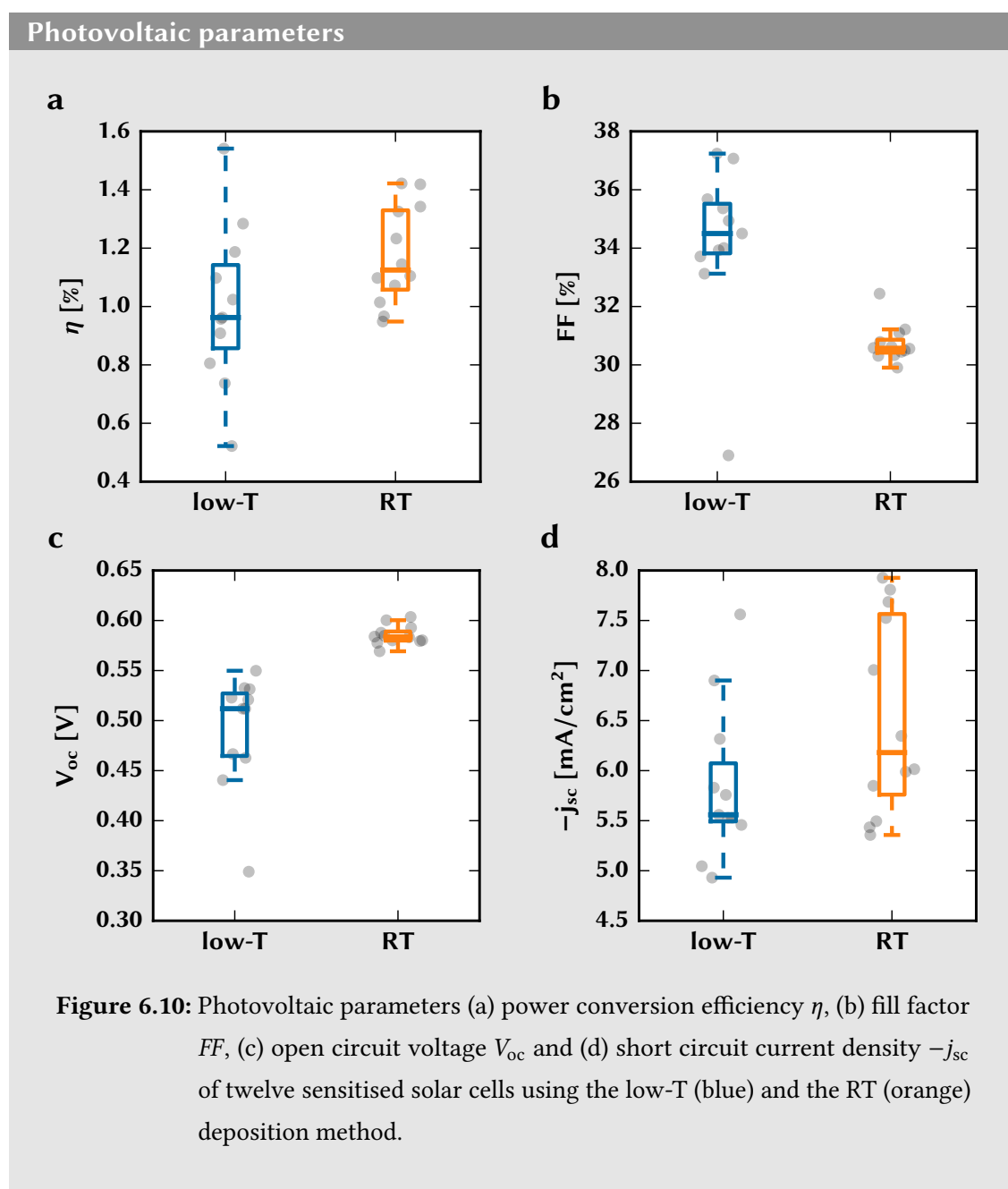


RT antimony sulfide and the thus lower conductivity (see Figure 6.5 and Figure 6.6). The improvement in voltage and current is very likely caused by the reduction of the trap-state density, as previously shown by the PDS measurements in Figure 6.8.

The I - V curves of representative devices for both deposition methods are shown in Figure 6.11 a, confirming again that the fill factor is decreased for the RT synthesis, but current and voltage are improved. The increase in short-circuit current can also be seen in Figure 6.11 b, which shows the EQE for the same representative solar cells and the integrated short circuit current density (dashed lines). As discussed earlier in Chapter 5, the drop in EQE at approximately $\lambda = 600$ nm arises from light absorption in the P3HT layer [19].

6.3.4 Optimising devices with room-temperature Sb_2S_3

With power conversion efficiencies of only 1 – 2 %, the solar cells for both, low-T and RT synthesis, lag far behind the efficiency record ($\eta_{\text{rec}} = 7.5$ % by Choi *et al.* [4]).



It was thus beneficial to collaborate with the Korean research group around Dr. Yong Chang Choi and Prof. Sang Il Seok to optimise the efficiency of the RT Sb_2S_3 sensitised solar cells. The results in this section are the outcome of a one month research stay at the Korean Research Institute of Chemical Technology (KRICT, Daejeon, South Korea) and

the collaboration with Dr. Yong Chang Choi. All presented experiments were done by the author of this thesis under supervision and with advice from Dr. Yong Chang Choi.

The main difference of the optimised solar cells is the use of the p-type polymer PCPDTBT as hole transport material. PCPDTBT has a band gap of $E_g = 1.4$ eV [3], thus absorbs in the far red and near infra-red spectrum. By the addition of PCBM,

Table 6.1: Average and standard deviation of the photovoltaic parameters of twelve solar cells each for low-T and RT deposition, as shown in Figure 6.10.

	η [%]	FF [%]	$-j_{sc}$ [$\frac{mA}{cm^2}$]	V_{oc} [mV]
low-T	1.0 ± 0.3	34.2 ± 2.6	5.86 ± 0.75	491 ± 55
RT	1.2 ± 0.2	30.7 ± 0.6	6.54 ± 0.95	585 ± 9

Solar cell characterisation

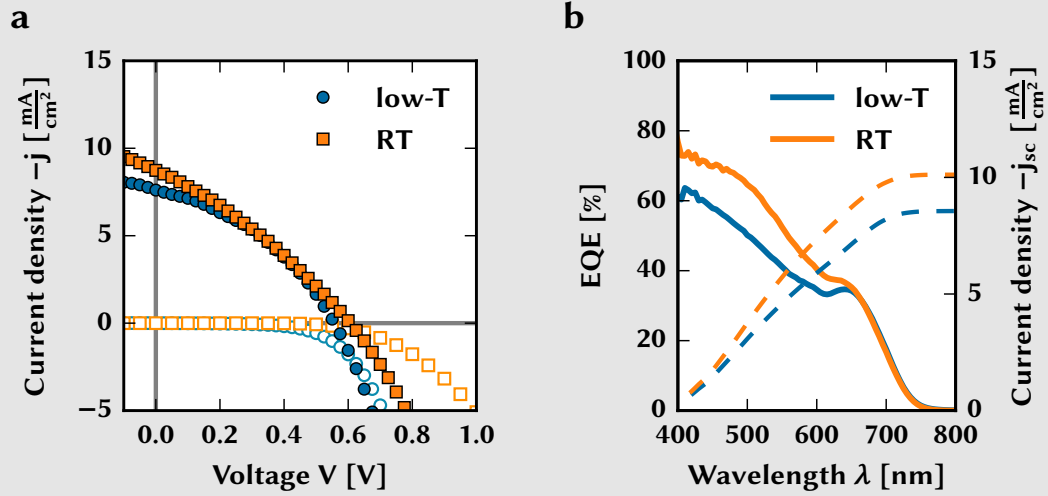
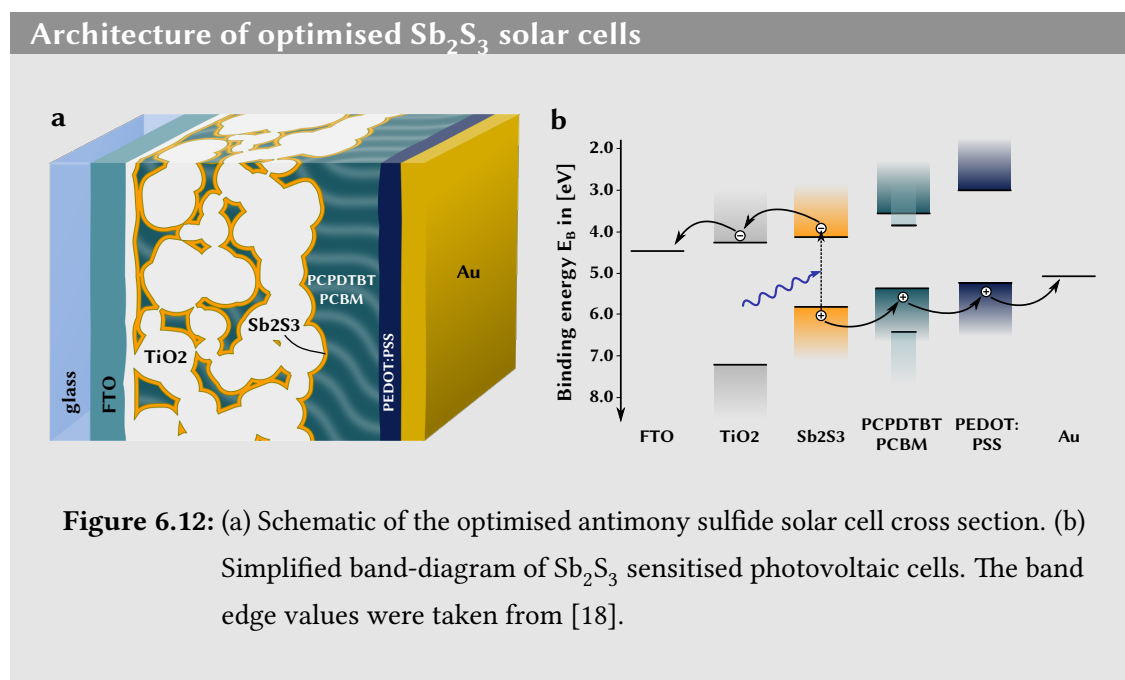


Figure 6.11: (a) Typical I - V curves for a solar cell with low-T (blue circles) and RT (orange squares) Sb_2S_3 at 1 sun illumination. The open data points are I - V curves for the same devices measured without illumination in darkness. (b) EQE of the same devices (solid line, left axis). The dashed lines show the integrated current density (right axis).

which forms electron conducting channels within the hole transporting layer, charges generated in this spectral region can be additionally harvested [19]. Further, instead of the commercial Dyesol TiO_2 paste used in Chapter 5, a custom made TiO_2 paste was used for the formation of the mesoporous n-type film. The exact composition was not revealed, but the paste contains anatase nanoparticles with an average diameter of 50 nm and was deposited to form a 1 μm thick layer using a screen printing technique. The paste was provided by the KRICT group. The RT and the conventional low-T antimony sulfide synthesis and all other preparation steps were performed in exactly the same way as described earlier in this chapter. Figure 6.12 a shows the architecture of the optimised antimony sulfide sensitised solar cell. The values of the band-edge position in Figure 6.12 b, which shows a simplified band schematic of the device, were taken from [18].



To optimise the solar cell and to increase the device performance, both, the deposition time and the concentration of the antimony sulfide precursor, were optimised.

In Figure 6.13, power-conversion efficiency, fill factor, open-circuit voltage and short-circuit current density are shown for three different deposition times (60 min, 90 min

and 120 min). For each time period in the chemical bath, six solar cells were prepared. After 60 min, the device performance drops significantly from on average $\eta = 4.9\%$ to $\eta = 4.1\%$. Especially the fill factor and the short circuit current decrease for longer deposition times. After the annealing, the surfaces of the 90 min and 120 min samples appeared shiny, whereas the 60 min sample looked matte. Probably, the antimony sulfide at least partly overgrows the mesoporous layer and clogs the pores. The hole transport material can no longer infiltrate the mesoporous network and thus fill factor and current decrease.

The deposition time was kept at 60 min and chemical baths using different antimony chloride precursor concentrations were prepared. The amount of SbCl_3 per total volume of the chemical bath $V = 100$ ml was varied from 350 mg to 1100 mg in steps of 150 mg and devices from the different RT bath compositions were fabricated. Figure 6.14 shows the photovoltaic parameters for the different antimony chloride concentrations. Up to 800 mg, the open-circuit voltage and short-circuit current increase, whereas the fill factor stays relatively constant. This leads to an initial increase in power conversion efficiency from $\eta \approx 3\%$ to $\eta \approx 5\%$ from 350 mg to 800 mg SbCl_3 in the 100 ml chemical bath. For higher concentrations, the efficiency deteriorates rapidly, due to a loss in the fill factor and in the short-circuit current. Again, one can assume that at higher concentrations pore clogging of the mesoporous layer occurs and holes from deeper areas in the mesoporous film cannot be extracted by the hole transport material.

Figure 6.15 a shows the I - V characteristic and Figure 6.15 b the EQE of the best performing solar cell employing RT deposited Sb_2S_3 . The EQE spectrum is integrated as described in Chapter 2 to show the short-circuit current as dashed line in Figure 6.15 b. All photovoltaic parameters are summarised in Table 6.2. The shunt and series resistances were obtained by a least square fit of the diode function (see Equation 2.11 in Chapter 2). The shoulder in the EQE spectrum at around 700 – 850 nm is caused by the additional charges originating from the PCPDTBT/PCBM blend, which was used in these devices (see also [19]).

Optimising the deposition time

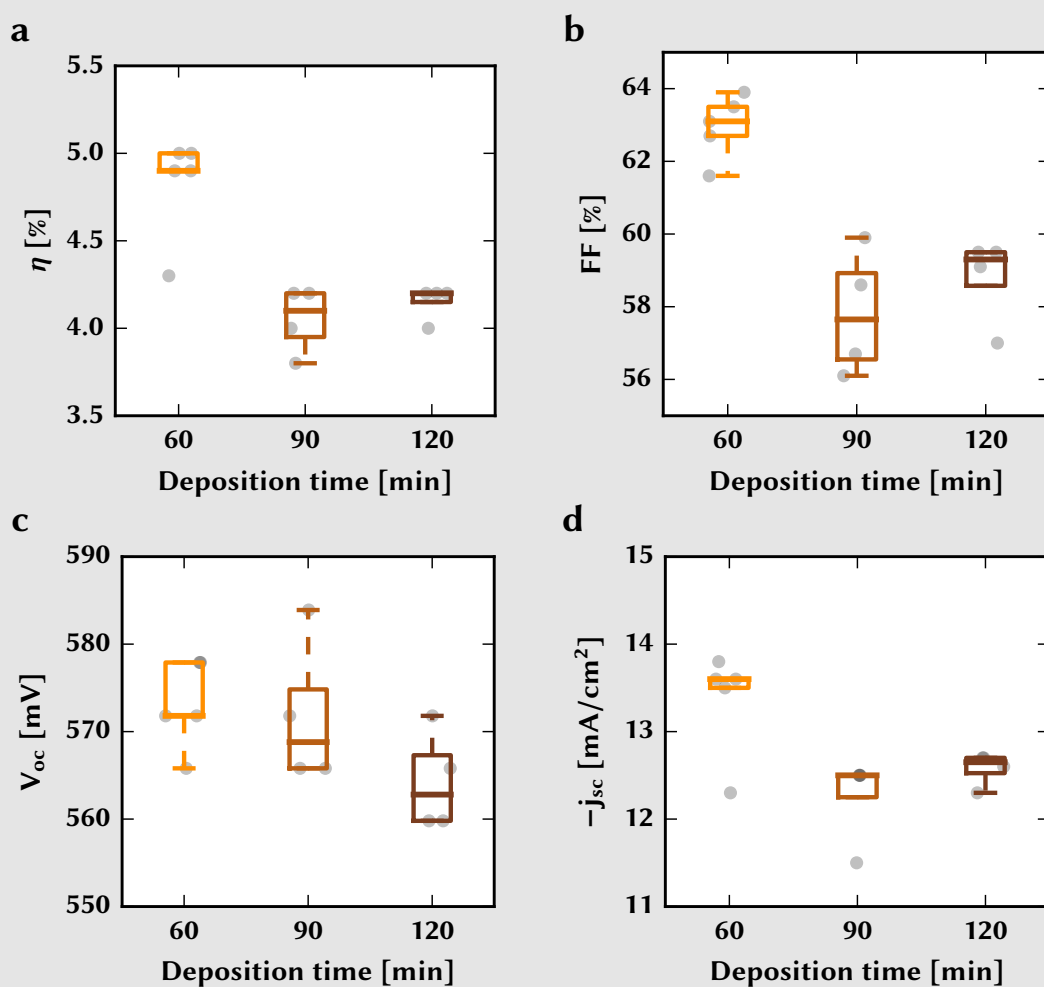


Figure 6.13: Photovoltaic parameters, (a) power-conversion efficiency, (b) fill factor, (c) open-circuit voltage and (d) short-circuit current density, of Sb_2S_3 sensitised solar cells as a function of the deposition time of the chemical bath at RT.

Optimising the precursor concentration

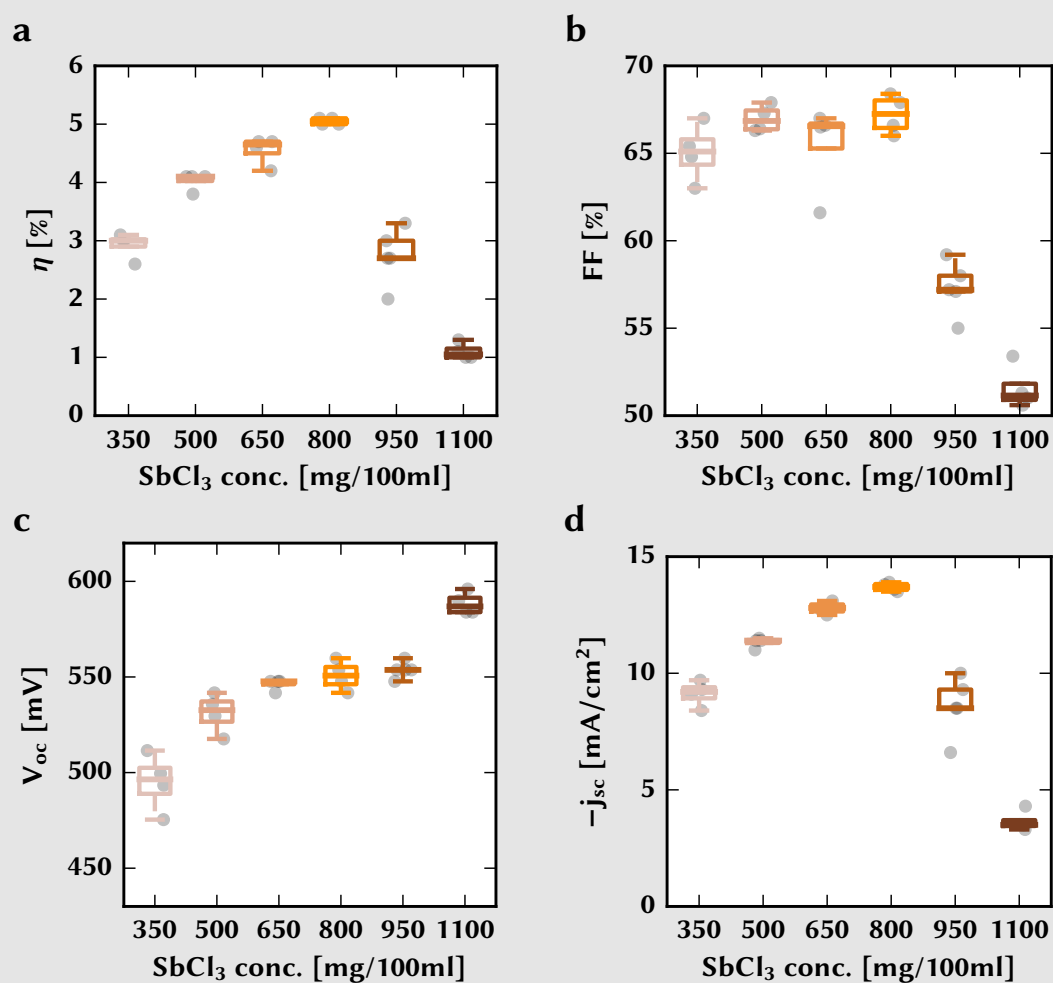


Figure 6.14: Photovoltaic parameters, (a) power-conversion efficiency, (b) fill factor, (c) open-circuit voltage and (d) short-circuit current density, of Sb_2S_3 sensitised solar cells as a function of the SbCl_3 concentration. The labels of the x-axis refer to the mass of SbCl_3 per 100 ml total volume of the chemical bath. The deposition time was kept constant at 1 h.

6.4 Conclusion

An aqueous deposition technique of antimony sulfide for sensitised solar cells was demonstrated, which can be carried out at room temperature. The chemical bath deposi-

Best performing solar cell

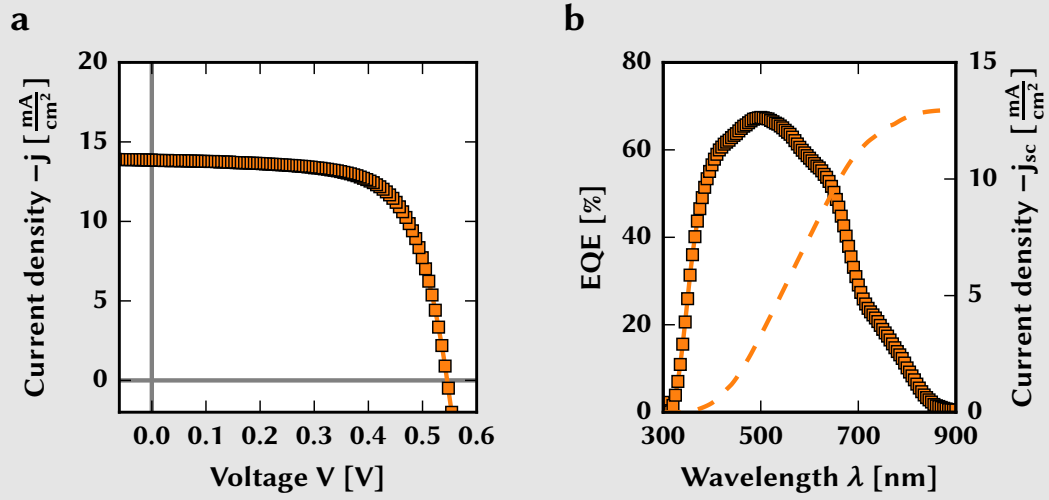


Figure 6.15: (a) I - V curve of the best performing solar cell device employing Sb_2S_3 synthesised using the RT method, achieving a power conversion efficiency of $\eta = 5.1\%$. (b) EQE of the device (orange squares, left axis). The integrated EQE yields the short circuit current density (dashed line, right axis).

tion method is based on the same precursor materials but uses the hydrolysis of SbCl_3 to complex antimony ions. This slows down the reaction speed and allows the reaction to take place at ambient conditions. The resulting Sb_2S_3 films were investigated using UV-vis spectroscopy, XRD, PDS and XPS. The RT methods yields antimony sulfide films with higher oxide content, which leads to a decrease in conductivity and a reduction in the fill factor in sensitised solar cells using this method. However, PDS shows a clear reduction in sub-band gap trap states in RT-deposited Sb_2S_3 , which improves all other

Table 6.2: Photovoltaic parameters of the best optimised device shown in Figure 6.15.

η [%]	V_{oc} [mV]	$-j_{sc}$ [$\frac{\text{mA}}{\text{cm}^2}$]	FF [%]	R_{sh} [$\text{k}\Omega$]	R_s [Ω]
5.1	548	13.9	67.7	16.78	41.45

photovoltaic parameters. All in all, comparisons of sensitised solar cells using the two different deposition methods show that the RT technique overall improves the device efficiency by a relative factor of approximately 20 % from $\eta = 1.0\%$ to $\eta = 1.2\%$. Optimised devices using PCPDTBT as hole transport material and a custom made TiO_2 film achieved a maximum power conversion efficiency of $\eta = 5.1\%$ for Sb_2S_3 sensitised solar cells using the RT deposition method. A more detailed optimisation of the deposition step, interfacial surface treatments [20, 21] or doping of the Sb_2S_3 [22] could lead to a further improvement in solar cell performance. This work is therefore an important step in the development of low-cost, stable and highly efficient solar cells.

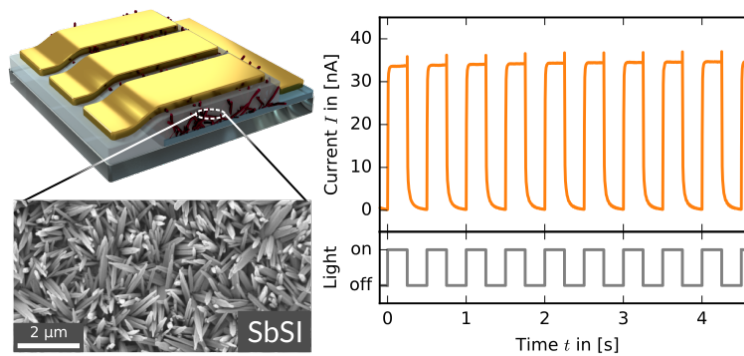
Bibliography

- [1] M. Y. Versavel and J. A. Haber. "Structural and optical properties of amorphous and crystalline antimony sulfide thin-films". *Thin Solid Films* 515.18 (2007), pp. 7171–7176. DOI: 10.1016/j.tsf.2007.03.043.
- [2] S.-J. Moon, Y. Itzhaik, J.-H. Yum, S. M. Zakeeruddin, G. Hodes, and M. Grätzel. "Sb₂S₃-Based Mesoscopic Solar Cell using an Organic Hole Conductor". *The Journal of Physical Chemistry Letters* 1.10 (2010), pp. 1524–1527. DOI: 10.1021/jz100308q.
- [3] S. H. Im, C.-S. Lim, J. A. Chang, Y. H. Lee, N. Maiti, H.-J. Kim, M. K. Nazeeruddin, M. Grätzel, and S. I. Seok. "Toward Interaction of Sensitizer and Functional Moieties in Hole-Transporting Materials for Efficient Semiconductor-Sensitized Solar Cells." *Nano Letters* 11.11 (2011), pp. 4789–93. DOI: 10.1021/nl2026184.
- [4] Y. C. Choi, D. U. Lee, J. H. Noh, E. K. Kim, and S. I. Seok. "Highly Improved Sb₂S₃ Sensitized-Inorganic–Organic Heterojunction Solar Cells and Quantification of Traps by Deep-Level Transient Spectroscopy". *Advanced Functional Materials* 24.23 (2014), pp. 3587–3592. DOI: 10.1002/adfm.201304238.
- [5] S. Ito, S. Tanaka, K. Manabe, and H. Nishino. "Effects of Surface Blocking Layer of Sb₂S₃ on Nanocrystalline TiO₂ for CH₃NH₃PbI₃ Perovskite Solar Cells". *The Journal of Physical Chemistry C* (2014). DOI: 10.1021/jp500449z.
- [6] I. Grozdanov. "A simple and low-cost technique for electroless deposition of chalcogenide thin films". *Semiconductor Science and Technology* 9.6 (1994), p. 1234. DOI: 10.1088/0268-1242/9/6/013.
- [7] M. T. S. Nair, Y. Pena, J. Campos, V. M. Garcia, and P. K. Nair. "Chemically Deposited Sb₂S₃ and Sb₂S₃-CuS Thin Films". *Journal of The Electrochemical Society* 145.6 (1998), 2113–2120.
- [8] S. Messina, M. Nair, and P. Nair. "Antimony sulfide thin films in chemically deposited thin film photovoltaic cells". *Thin Solid Films* 515.15 (2007), pp. 5777–5782. DOI: 10.1016/j.tsf.2006.12.155.

-
- [9] N. Maiti, S. H. Im, C.-S. Lim, and S. I. Seok. "A chemical precursor for depositing Sb₂S₃ onto mesoporous TiO₂ layers in nonaqueous media and its application to solar cells." *Dalton Transactions* 41.38 (2012), pp. 11569–72. DOI: 10.1039/c2dt31348k.
- [10] A. Koliadima, A. Henglein, and E. Matijević. "Colloidal hydrolysis products of SbCl₃ in acidic solutions". *Colloid and Polymer Science* 275.10 (1997), pp. 972–978. DOI: 10.1007/s003960050174.
- [11] X. Y. Chen, H. S. Huh, and S. W. Lee. "Hydrothermal synthesis of antimony oxy-chloride and oxide nanocrystals: Sb₄O₅Cl₂, Sb₈O₁₁Cl₂, and Sb₂O₃". *Journal of Solid State Chemistry* 181.9 (2008), pp. 2127–2132. DOI: 10.1016/j.jssc.2008.04.043.
- [12] C. Li, X. Yang, Y. Liu, Z. Zhao, and Y. Qian. "Growth of crystalline Sb₂S₃ nanorods by hydrothermal method". *Journal of Crystal Growth* 255.3–4 (2003), pp. 342–347. DOI: 10.1016/S0022-0248(03)01266-1.
- [13] Y. Yu, R. H. Wang, Q. Chen, and L.-M. Peng. "High-Quality Ultralong Sb₂S₃ Nanoribbons on Large Scale". *The Journal of Physical Chemistry B* 109.49 (2005), pp. 23312–23315. DOI: 10.1021/jp055132z.
- [14] A. Kyono and M. Kimata. "Structural variations induced by difference of the inert pair effect in the stibnite-bismuthinite solid solution series (Sb,Bi)₂S₃". *American Mineralogist* 89 (2004), pp. 932–940.
- [15] V. P. Zakaznova-Herzog, S. L. Harmer, H. W. Nesbitt, G. M. Bancroft, R. Flemming, and A. R. Pratt. "High resolution XPS study of the large-band-gap semiconductor stibnite (Sb₂S₃): Structural contributions and surface reconstruction". *Surface Science* 600.2 (2006), pp. 348–356. DOI: 10.1016/j.susc.2005.10.034.
- [16] M. Y. Versavel and J. A. Haber. "Structural and Optical Properties of Amorphous and Crystalline Antimony Sulfide Thin-Films". *Thin Solid Films* 515.18 (2007), pp. 7171–7176. DOI: 10.1016/j.tsf.2007.03.043.
- [17] A. Darga, D. Mencaraglia, C. Longeaud, T. J. Savenije, B. O'Regan, S. Bourdais, T. Muto, B. Delatouche, and G. Dennler. "On Charge Carrier Recombination in

- Sb₂S₃ and Its Implication for the Performance of Solar Cells”. *The Journal of Physical Chemistry C* 117.40 (2013), pp. 20525–20530. DOI: 10.1021/jp4072394.
- [18] J. A. Chang, J. H. Rhee, S. H. Im, Y. H. Lee, H.-j. Kim, S. I. Seok, M. K. Nazeeruddin, and M. Gratzel. “High-performance nanostructured inorganic-organic heterojunction solar cells.” *Nano Letters* 10.7 (2010), pp. 2609–12. DOI: 10.1021/nl101322h.
- [19] J. A. Chang, S. H. Im, Y. H. Lee, H.-J. Kim, C.-S. Lim, J. H. Heo, and S. I. Seok. “Panchromatic photon-harvesting by hole-conducting materials in inorganic-organic heterojunction sensitized-solar cell through the formation of nanostructured electron channels.” *Nano letters* 12.4 (2012), pp. 1863–7. DOI: 10.1021/nl204224v.
- [20] K. Tsujimoto, D.-C. Nguyen, S. Ito, H. Nishino, H. Matsuyoshi, A. Konno, G. R. A. Kumara, and K. Tennakone. “TiO₂ Surface Treatment Effects by Mg²⁺, Ba²⁺, and Al³⁺ on Sb₂S₃ Extremely Thin Absorber Solar Cells”. *The Journal of Physical Chemistry C* 116.25 (2012), pp. 13465–13471. DOI: 10.1021/jp208937j.
- [21] T. Fukumoto, T. Moehl, Y. Niwa, M. K. Nazeeruddin, M. Grätzel, and L. Etgar. “Effect of Interfacial Engineering in Solid-State Nanostructured Sb₂S₃ Heterojunction Solar Cells”. *Advanced Energy Materials* 3.1 (2013), pp. 29–33. DOI: 10.1002/aenm.201200540.
- [22] S. Ito, K. Tsujimoto, D.-C. Nguyen, K. Manabe, and H. Nishino. “Doping effects in Sb₂S₃ absorber for full-inorganic printed solar cells with 5.7% conversion efficiency”. *International Journal of Hydrogen Energy* 38.36 (2013), pp. 16749–16754. DOI: 10.1016/j.ijhydene.2013.02.069.

SbSI micro-crystals for fast response photodetectors



Parts of this chapter are published in:

K. C. Gödel and U. Steiner. “Thin film synthesis of SbSI micro-crystals for self-powered photodetectors with rapid time response”. *Nanoscale*, (2016).

doi:10.1039/C6NR04759A.

Abstract In this chapter, a new thin film deposition method for the growth of crystalline antimony sulfoiodide (SbSI) micro-needles is described. Sb_2S_3 films are converted to SbSI using SbI_3 vapour, in a facile process that takes less than 15 minutes. The SbSI films were used to construct photodetectors in a sandwich-type architecture, which are superior to previously reported SbSI photodetectors. The devices exhibited a detectivity of $D^* = 10^9$ Jones, a signal-to-noise ratio greater than $\text{SNR} = 10^3$ and a responsivity of $R = 10^{-5} \frac{\text{A}}{\text{W}}$. In time response measurements, raise and fall times of less than 8 ms and 34 ms were determined. This manufacturing method greatly simplifies the creation of fast photodetectors.

7.1 Introduction

Photodetectors are optoelectronic devices designed to convert light into electrical signals. They play an important role in a wide range of applications, from alarm systems and smoke detectors to consumer electronics and optocouplers for electronic circuits. Most commercial photodetectors use semiconducting materials such as Si, InGaAs, GaN or CdS. Recent research, however, focuses on new materials with facile deposition methods for inexpensive and scalable light sensing devices. In particular, quantum dots, polymer blends and organo-metal perovskites were investigated for their application in photodetectors [1, 2].

The photoconductive properties of antimony sulfoiodide are long known [3–6]. First photoconductivity measurements using antimony sulfoiodide nanowires were presented by Nowak *et al.* in 2013 [7], which were subsequently employed for humidity sensing applications [8]. In 2015, Chen *et al.* demonstrated an SbSI photodetector based on a macroscopic single crystal [9].

Antimony sulfoiodide exhibits a series of interesting properties. It is a ferroelectric material with a Curie temperature of $T_C = 20^\circ\text{C}$, a high piezoelectric constant and pyroelectric properties [10–12]. The n-type semiconductor has an indirect band gap of $E_g = 1.9 \text{ eV}$ [13, 14]. Theoretical calculations suggest a high charge mobility of

antimony sulfoiodide caused by the low effective masses of the charge carriers, making it a promising material for photovoltaic applications [14]. More detailed information on antimony sulfoiodide and its applications for sensing devices can be found in Section 3.2.

Here, a novel synthesis method for SbSI micro-crystals in a thin-film deposition route is presented. This method is used to fabricate an SbSI photodetector with a sandwich-type architecture. The device shows significantly improved figures-of-merit compared to earlier SbSI photodetectors [9].

7.2 Materials and methods

7.2.1 Photodetector fabrication

All chemicals were purchased from Sigma-Aldrich and used without further purification. The FTO substrate ($15 \Omega/\square$) was cleaned by sonicating in acetone and ethanol and then partly etched using a 2 M solution of HCl and zinc powder to prevent shorting during the measurements. Only for the symmetric devices, a 7.5 nm thin layer of gold was evaporated onto the FTO using a Kurt J. Lesker e-beam evaporator. Amorphous Sb_2S_3 was deposited in a low-temperature aqueous chemical bath as described elsewhere [15, 16]. Anhydrous SbI_3 crystals were dissolved in anhydrous ethanol at a concentration of 10 mg/ml. 2 ml of the solution was spread on a microscope slide at 100°C to evaporate the ethanol. This way, a thin, uniform layer of SbI_3 was formed, which was used as target for evaporation.

The target was placed onto a hotplate (Stuart CD162) in an inert atmosphere and covered by a 15 mm high Petri dish (see also Figure 7.1). The Sb_2S_3 -covered FTO sample was fixed to the bottom of this petri-dish, facing the SbI_3 target. The temperature of the hotplate was ramped to 250°C within 5 min and held at this temperature for 10 min. The evaporation of SbI_3 was observable by the condensation on the petri-dish. Within the first 5 min, the colour of the sample changed from orange to dark red, indicating the formation of SbSI crystals.

The samples were left to cool under the inert atmosphere. They were then rinsed in absolute ethanol to remove excess SbI_3 .

A barrier layer had to be applied to prevent shorting between the top and the bottom electrode. Here, a novel but simple procedure was used using PMMA as an insulating layer. This technique could also be useful for other micro- and nano-crystalline photodetectors with a sandwich type architecture.

The PMMA film was applied onto the SbSI-covered substrate by spin-coating a 100 mg/ml PMMA solution in chlorobenzene (Laurell Spin Coater Model WS-650MZ-23NPP). To increase the thickness of the polymer film, two layers were spin-coated subsequently at 4000 rpm.

The PMMA fills the gaps between the SbSI crystals and thus reduces the risk of short-circuits forming during the evaporation of the top electrode. Using the mentioned spin-coating technique, however, leads to a coverage of the crystals' surface which thus would lead to a poor electronic contact with the top electrode.

Hence, as a third step, pure chlorobenzene was dynamically spin-coated to remove the top layer of PMMA and to provide contact of the SbSI crystal needles with the counter-electrode. These electrodes were deposited by evaporating a 100 nm thick layer of gold using a Kurt J. Lesker e-beam evaporator.

It should be mentioned that the solvent spin-coating step is delicate and reduces the reproducibility of the method. If too much of the PMMA insulating layer is removed, electronic shorts are likely. Thus, it is hard to control how many of the SbSI needles are contacted and typically several devices had to be built to find one with optimum properties. In a typical batch, approximately four out of ten devices short-circuited.

7.2.2 Material characterisation

Optical transmission measurements were carried out using an Ocean Optics USB 2000 spectrometer and an integrating sphere. A Bruker D8 θ/θ (fixed sample) spectrometer

7.3 Conversion of Sb_2S_3 to SbSI in a SbI_3 vapour

with a LynxEye position sensitive detector and a standard SC detector with auto-absorber and graphite 2nd beam monochromator was used to measure X-ray diffraction patterns. The set-up operates in reflection mode and uses a Bragg Brentano parafocusing geometry. Scanning electron microscopy images were recorded with a Leo Gemini 1530 VP SEM.

7.2.3 Optoelectronic measurements

Current-voltage characteristics were measured under a solar simulator from ABET Technologies (Model 11016 Sun 2000) with a xenon arc lamp and recorded using a Keithley 2635 sourcemeter directly controlled by a custom Python program. The current was equilibrated for 10 s for each voltage step. The intensity of the solar simulator was calibrated to $100 \frac{\text{mW}}{\text{cm}^2}$ using a silicon reference cell from Czibula & Grundmann (FHG-ISE, RS-OD4). To alter the irradiance, neutral density filters from Thorlabs (NEK01S) were employed.

The spectral response measurements were carried out using a 250 W tungsten halogen lamp and an Oriel Cornerstone 130 monochromator. The photocurrent was measured by a Keithley 2000 Measurement Unit. For the time response measurements, light from an array of white LEDs was focused onto the sample. The light was modulated by a Hewlett Packard 33120A function generator and the response of the photodetector was measured with a Metrohm Autolab PGSTAT302N potentiostat and recorded using the Nova software (Version 1.11). The intensity of the LEDs was calibrated by measuring the photocurrent in a non-modulated mode.

7.3 Conversion of Sb_2S_3 to SbSI in a SbI_3 vapour

Several synthesis routes for antimony sulfoiodide (SbSI) have been proposed in the literature. Most common are a sonochemical method from elemental antimony, sulfur and iodine [8, 17], hydrothermal deposition in an auto-clave [18] or chemical vapour deposition at high temperatures [19]. These methods have long processing times of 4 h

and more [9, 19] and result in bulk SbSI crystals. A more detailed review on the synthesis and deposition of antimony sulfoiodide is presented in Section 3.2.

7.3.1 The conversion process

Here, a two-step synthesis method, where SbSI micro-crystals are formed in a thin film is reported. The first step entails the deposition of a thin film of antimony sulfide in a low temperature chemical bath as previously described [15, 16]. The conventional low-temperature method was chosen here, as on non-porous substrates, this method gives more uniform Sb_2S_3 films than the room-temperature technique introduced in Chapter 6. The second step is the conversion of the amorphous Sb_2S_3 to crystalline SbSI using antimony iodide vapour. This chemical reaction was described before e.g. as part of a hydrothermal deposition method [18]



To prevent oxidation of the antimony sulfide, the conversion reaction has to take place in an inert N_2 atmosphere. Therefore, the conversion step from antimony sulfide to antimony sulfoiodide was completed in a nitrogen-filled glove box.

Different methods were tried to convert the antimony sulfide film into crystalline SbSI using antimony iodide. Spin-coating SbI_3 directly onto the Sb_2S_3 layer lead to the evaporation of SbI_3 upon heating for the conversion of the layer stack into antimony sulfoiodide. Thus, a more promising method was the evaporation of the SbI_3 precursor onto the antimony sulfide film.

For the conversion procedure, first an SbI_3 evaporation target was prepared by the dissolution of SbI_3 crystals in ethanol. The solution was made in the glove box and has to be stirred extensively before use. The SbI_3 solution is then drop-cast onto a pre-heated microscope slide at roughly $T = 100^\circ\text{C}$. After the evaporation of the solvent, a thick and uniform film of antimony iodide is formed. In principle, the macroscopic crystals could be evaporated as delivered, but with the re-dissolution one obtains a much more

7.3 Conversion of Sb_2S_3 to SbSI in a SbI_3 vapour

controlled and uniform evaporation target. Then, the substrate with pre-deposited Sb_2S_3 was mounted onto the bottom of a Petri dish, facing the antimony iodide target as shown in Figure 7.1.

The setup of the conversion process

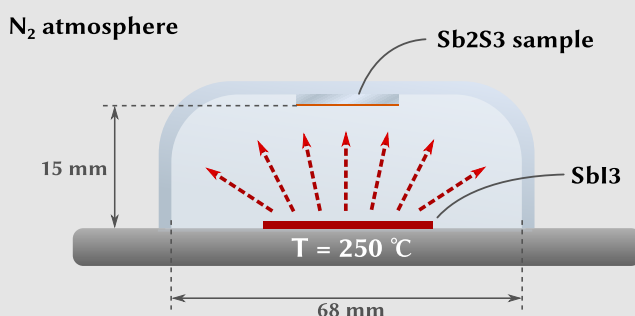
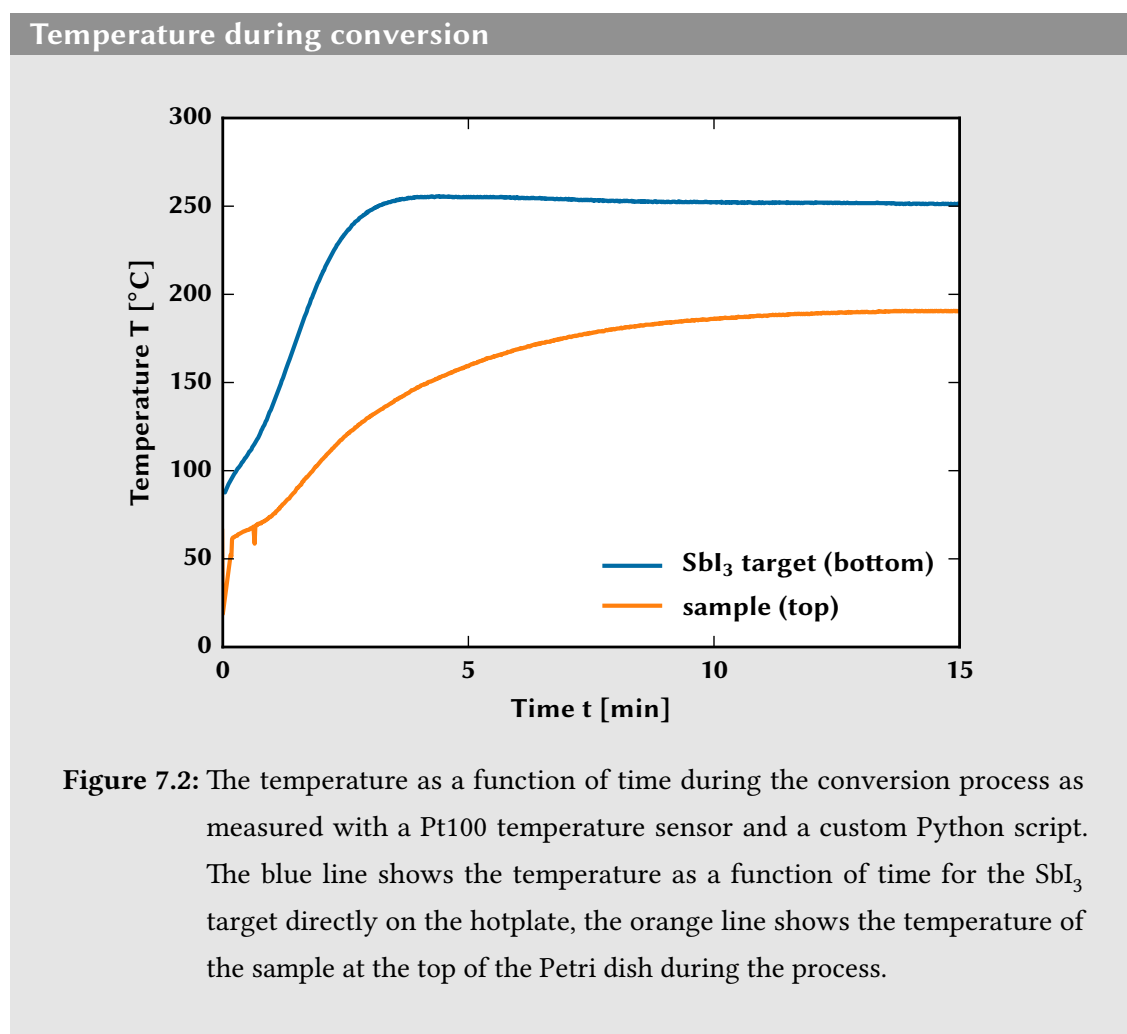


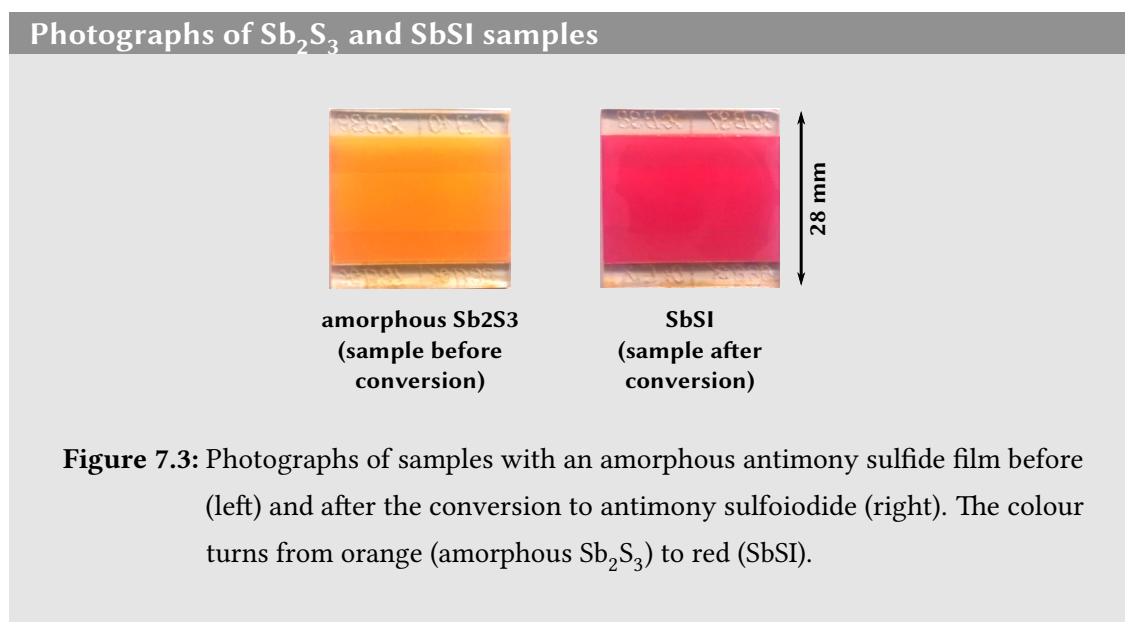
Figure 7.1: Schematic of the simple setup for the physical vapour conversion process from Sb_2S_3 to SbSI . The antimony iodide target is heated to $T = 250\text{ }^\circ\text{C}$ and evaporates. The vapour condenses on the surface of the Sb_2S_3 covered sample which is mounted facing downwards in a small Petri dish.

The SbI_3 target was heated to $T_t = 250\text{ }^\circ\text{C}$ within 5 min. The target temperature T_t and the temperature of the substrate T_s , were recorded using a Pt100 temperature sensor. The temperature curves are shown in Figure 7.2. Whereas the target reaches the set temperature of $T = 250\text{ }^\circ\text{C}$ within less than 3 min, the sample, which is not directly heated itself, increases its temperature much slower and does not reach more than $190\text{ }^\circ\text{C}$ during the whole process. This means that this process is possibly even suitable for flexible polymer substrates.

Within less than 5 min, an excess of antimony iodide sublimates and reacts with the Sb_2S_3 on the substrate to form SbSI . This reaction is indicated by a colour change of the sample from bright orange to dark red. To increase the crystallinity, the sample was heated indirectly for another 10 min. Upon cooling, the colour of the samples turns from dark to bright red. After cooling, the samples were rinsed in absolute ethanol to remove residual SbI_3 .

The conversion of the sample from a thin film of amorphous antimony sulfide to crystalline antimony sulfoiodide is accompanied by a change of colour of the substrate. The orange film, with its typical colour of amorphous Sb_2S_3 , changes to bright red. A photograph comparing the films before and after the conversion process is shown in Figure 7.3.





7.3.2 Characterisation of SbSI films

To confirm the formation of crystalline SbSI , the films were characterised by XRD and UV-vis spectroscopy. As explained in Chapter 3, antimony sulfoiodide has an orthorhombic crystal lattice, consisting of long chains along the (001)-axis. This anisotropy leads to the preferential growth of SbSI into needle like crystals. Figure 7.4 shows the XRD pattern of SbSI films as deposited on a FTO covered glass substrate. The peaks are in good agreement with the reference pattern for antimony sulfoiodide. Additional peaks can be attributed to tin oxide originating from the FTO layer of the substrate. The absence of other peaks indicates the formation of pure crystalline SbSI .

The band gap of SbSI was reported to lie at $E_g = 1.9 \text{ eV}$ [14]. The onset of absorption should therefore lie at a wavelength of $\lambda_g = \frac{hc}{E_g} \approx 650 \text{ nm}$. The transmittance onset of the UV-vis spectrum in Figure 7.5 is in good agreement with this value. At wavelengths between 600 – 650 nm, the transmittance decreases steeply. Due to the micro-structure of the SbSI film, the samples exhibit strong light scattering and the diffuse transmittance spectrum therefore had to be recorded using an integrating sphere. Olimpia Onelli granted access to the integrating sphere at the Chemistry Department of the University

X-ray diffraction of SbSI micro crystals

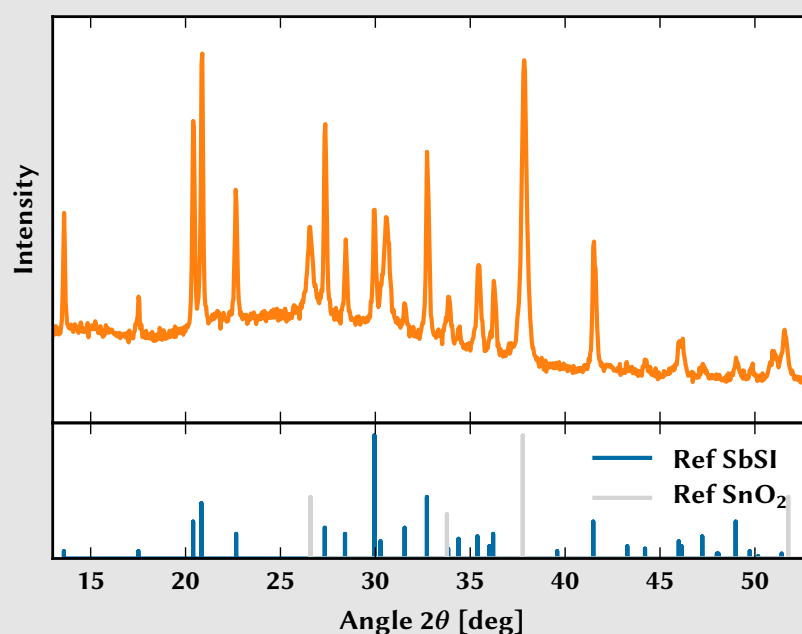


Figure 7.4: X-ray diffraction patterns of SbSI films as-deposited on a FTO covered glass substrate. Below the graph, the reference patterns for SbSI (JCPDS-ICCD PDF 00-021-0050) and tin oxide (JCPDS-ICCD PDF 00-046-1088) are shown.

of Cambridge and assisted during the measurements.

The microscopic structure was further investigated using SEM. To show that the final film geometry is not induced or dependent by the morphology of the initial Sb_2S_3 film, SEM images of the amorphous antimony sulfide layers before the conversion were recorded, as well. Figure 7.6 a shows the top view and Figure 7.6 b the cross-section of the Sb_2S_3 as deposited. It is a solid flat film with no needle-like or otherwise distinct morphology. Figures 7.6 c-d confirm the needle-like morphology of the SbSI crystals after the conversion process. The length of the individual crystals can be estimated from the SEM images. It lies between 1 – 5 μm , the width of the needles is on the order of 10 – 100 nm. The cross-sectional SEM image in Figure 7.6 d suggests a preferred orientation: The needles grow preferentially perpendicular to the substrate. This is

UV-vis spectroscopy of SbSI films

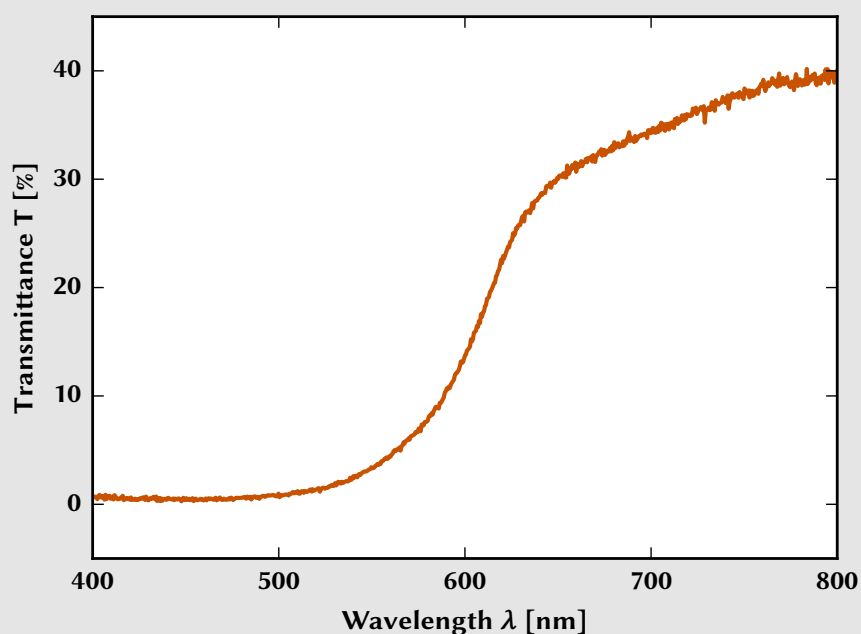


Figure 7.5: UV-vis transmittance spectrum of an SbSI film. Due to strong light scattering, the diffuse transmittance spectrum was recorded using an integrating sphere. The onset for the absorption at a wavelength of $\lambda_g \approx 650$ nm is in good agreement with the literature values of the band gap of SbSI ($E_g = 1.9$ eV) [14].

beneficial for the construction of photodetectors, since a large number of crystals will span across both electrodes. The reason for this preferential orientation is not clear. A possible explanation could be the surface roughness of the FTO substrate. Varghese *et al.* reported perpendicularly c-axis oriented SbSI crystals on anodic aluminum oxide, where the surface roughness of the substrate was the critical parameter for the orientation of the SbSI crystals [20].

SEM of Sb_2S_3 and SbSI films

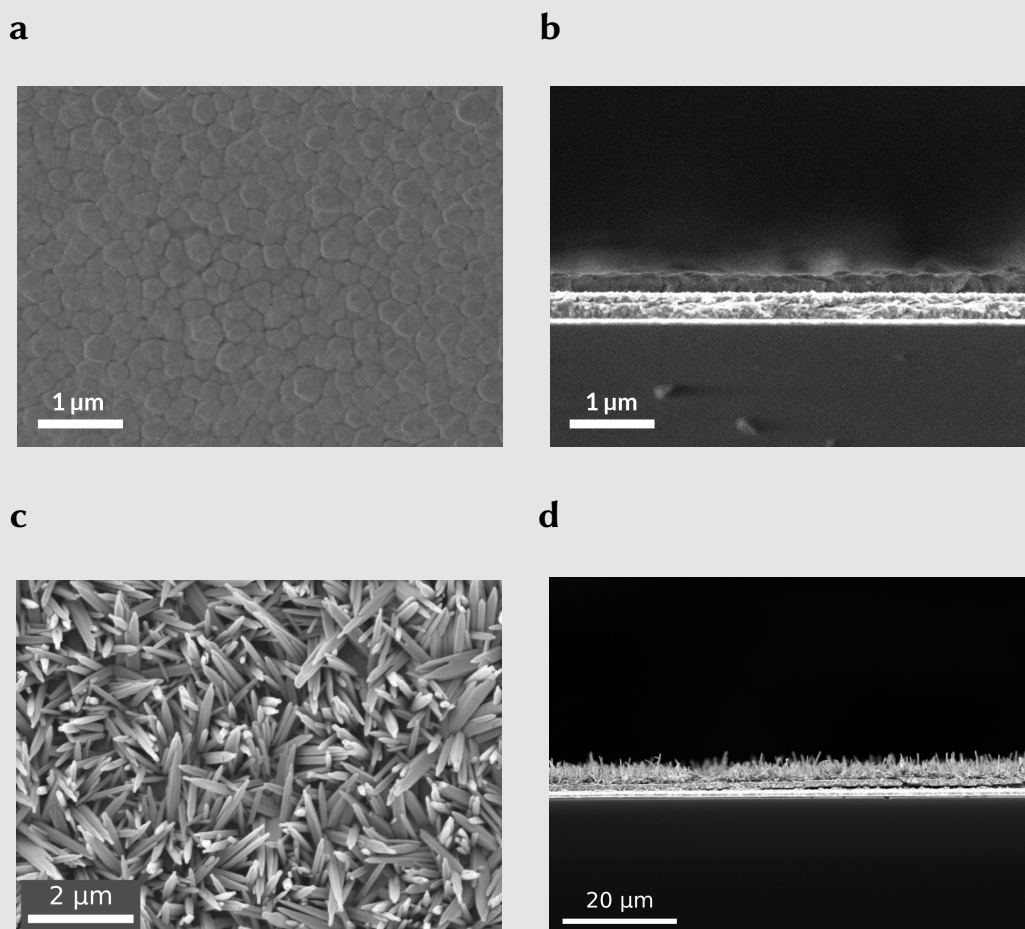


Figure 7.6: SEM images of antimony sulfide and antimony sulfoiodide films. (a) Top view and (b) cross sectional view of the as deposited amorphous Sb_2S_3 layer. (c) Top-view of the SbSI crystal needles after the conversion procedure. (d) Cross sectional image suggesting a slightly preferred orientation of crystal needles perpendicular to the substrate.

7.4 Fabrication process of SbSI photodetectors

The SbSI micro-crystal deposition method was used to fabricate functional optoelectronic devices. Earlier approaches to exploit the photoconductive properties of SbSI in humidity-

7.4 Fabrication process of SbSI photodetectors

sensors and photodetectors [7–9] were based on devices with macroscopic electrode spacings (0.1 – 1 mm). These large spacings limit both, the maximum photocurrent signal and the time response of the detector. Instead, photodetectors with a sandwich-type architecture were fabricated. This architecture allows the SbSI crystals to be contacted with electrode spacings of less than 2 μm .

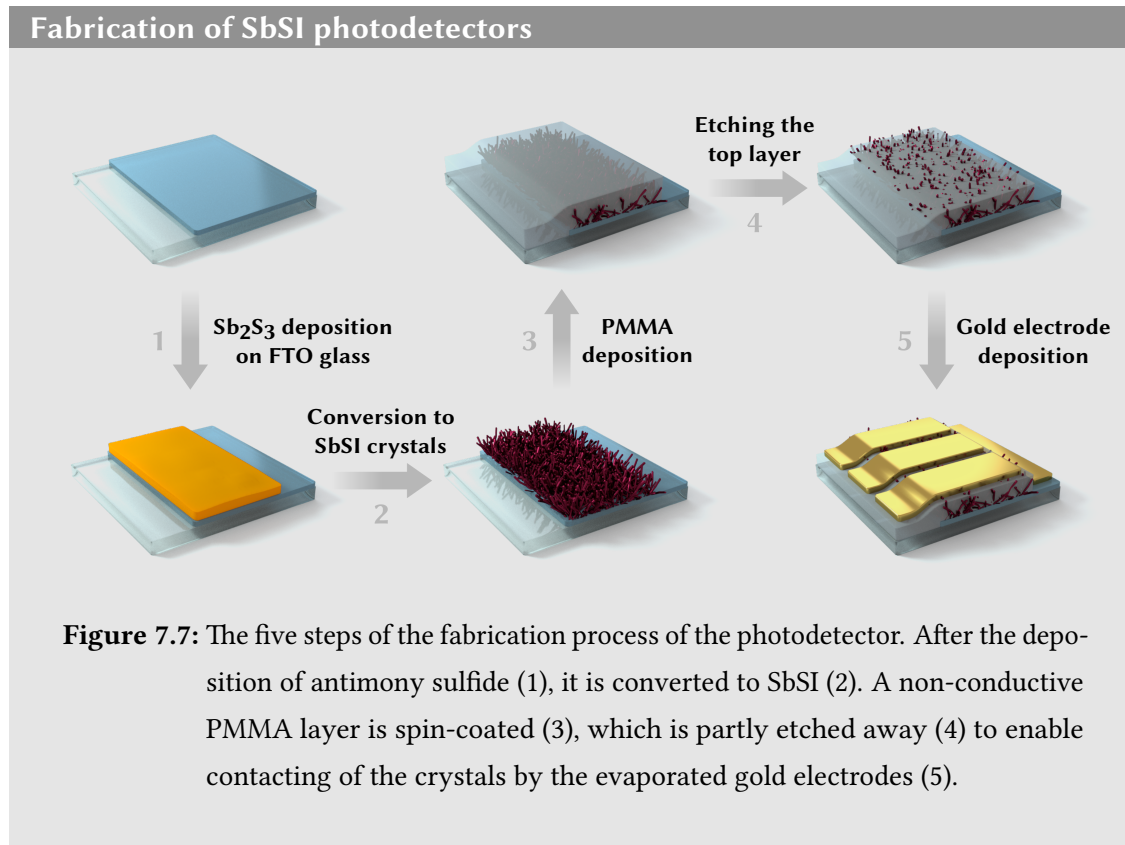
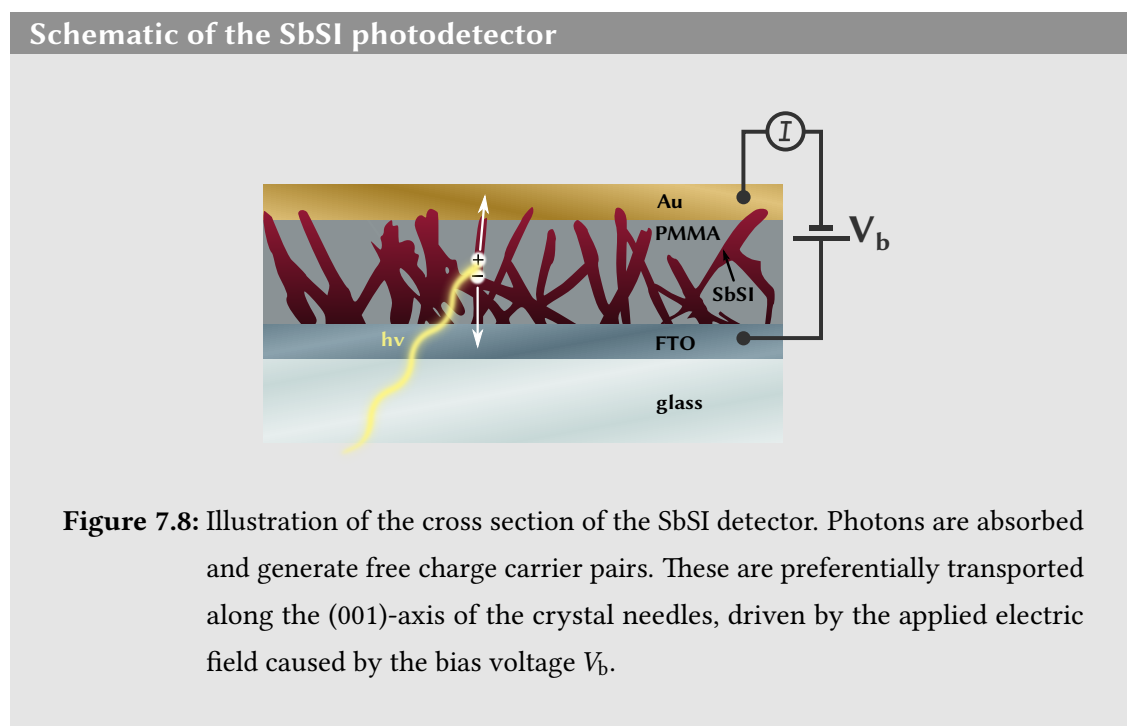


Figure 7.7: The five steps of the fabrication process of the photodetector. After the deposition of antimony sulfide (1), it is converted to SbSI (2). A non-conductive PMMA layer is spin-coated (3), which is partly etched away (4) to enable contacting of the crystals by the evaporated gold electrodes (5).

The fabrication process of the device is schematically shown in Figure 7.7. The first two steps (Step 1 and 2) show the deposition of antimony sulfide and the conversion to SbSI micro-crystals by SbI_3 , as described above. Then, an insulating buffer layer was deposited by spin-coating of PMMA from chlorobenzene at a concentration of $100 \frac{\text{mg}}{\text{ml}}$ (Step 3). Process optimisation revealed that one layer of PMMA is often not sufficient to prevent shorting between the top and the bottom electrodes, thus two layers were spun on subsequently. The PMMA layer entirely covered the SbSI crystals, preventing electrical contact with the top electrode. To partly etch the PMMA layer to reveal the

tips of the crystals, pure chlorobenzene was dynamically spin-coated (Step 4). Finally, a gold metal electrode was deposited by electron beam evaporation (Step 5).



A sketch of the cross-section of the device is shown in Figure 7.8. The schematic also illustrates the working principle of the photodetector relying on the intrinsic photoelectric effect, as introduced in Chapter 1. Photons with energies higher than the band gap of SbSI are absorbed by the detector, generating charge carrier pairs. These are preferentially transported along the (001)-axis of the crystal needles, driven by an external electric field which is generated by a bias voltage V_b . The density of free charge carriers is dependent on the intensity of the incident light, resulting in a variable photocurrent as electrical output signal. A cross sectional SEM image of the final photodetector is shown in Figure 7.9. The PMMA layer between the SbSI crystal needles prevents the gold electrode (top) from shorting with the FTO layer (bright layer at the bottom). However, the gold electrode is still in direct contact with the crystals to allow an electric contact.

Cross sectional SEM of the SbSI photodetector

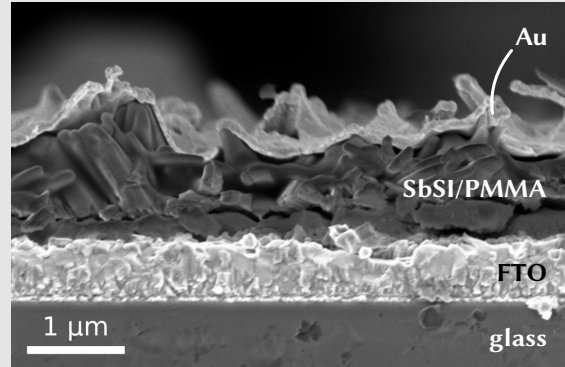


Figure 7.9: Cross sectional SEM image of a complete antimony sulfoiodide photodetector with sandwich architecture.

7.5 Optoelectronic characterisation of SbSI photodetectors

Figure 7.10 shows the current-voltage characteristics of the photodetector in the dark (blue squares) and under white light illumination of a solar simulator with an irradiance of $E_e = 100 \frac{\text{mW}}{\text{cm}^2}$ (orange circles). Each voltage step was followed by a 30 s equilibration period.

Note that even under zero bias $V_b = 0 \text{ V}$, the photodetector has a photocurrent of approximately $I = 40 \text{ nA}$. The device can hence be used in a self-powered mode without an externally applied voltage. The properties of the self-powered mode are described in Section 7.5.2. The photocurrent at zero bias arises from the use of two different electrode materials, namely FTO on the bottom and gold on the top, probably giving rise to a built-in potential. This effect is further investigated in Section 7.5.3.

Figure 7.11 shows the same measurements as in Figure 7.10 on a logarithmic current scale with absolute current values between -1 V to 1 V . The voltage-dependent signal to

I-V curve of the SbSI photodetector

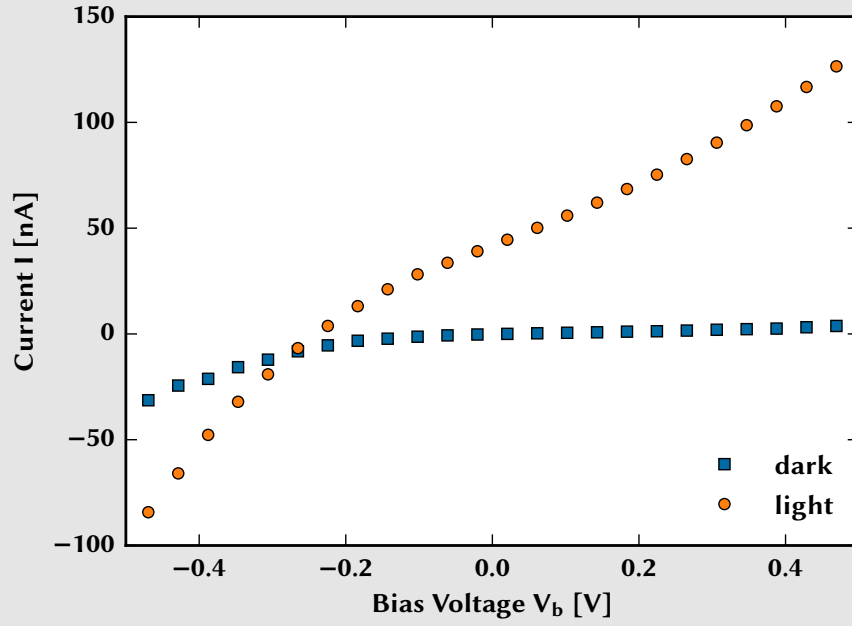
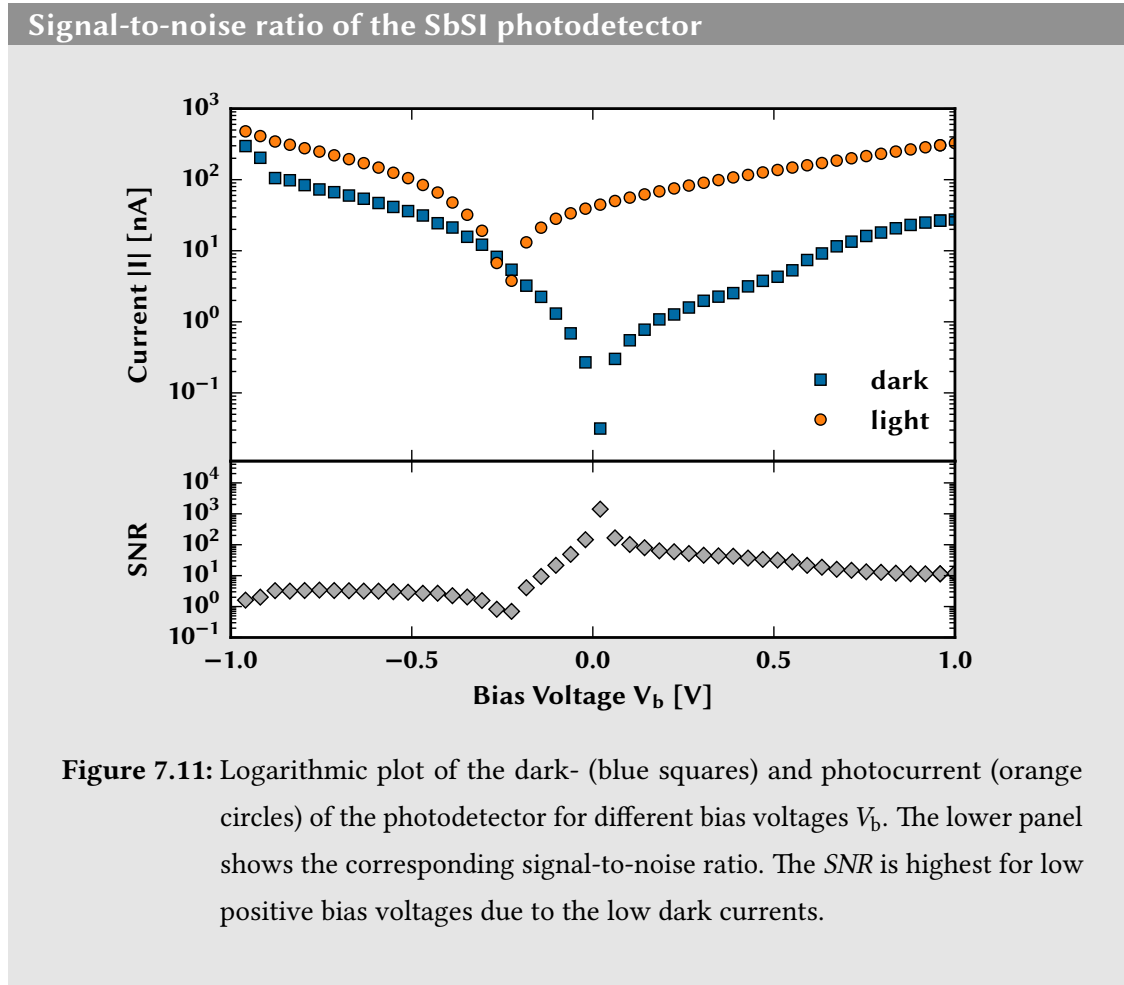


Figure 7.10: I - V characteristics of an SbSI photodetector. Blue squares show the current-voltage curve in the dark, orange circles under white light with an irradiance of $E_e = 100 \frac{\text{mW}}{\text{cm}^2}$. Even under zero bias $V_b = 0 \text{ V}$, the photodetector has a photocurrent of approximately $I = 40 \text{ nA}$.

noise ratio SNR (grey diamonds) is shown, too. The SNR is defined as

$$SNR = \frac{I_{\text{light}} - I_{\text{dark}}}{I_{\text{dark}}} . \quad (7.2)$$

Due to the low dark current, the SNR is highest for low voltages in the range between 0 V and 0.5 V . For this reason and because low operating voltages are preferable for most applications, a voltage of $V_b = 100 \text{ mV}$ was used for the following characterisation measurements under voltage bias.



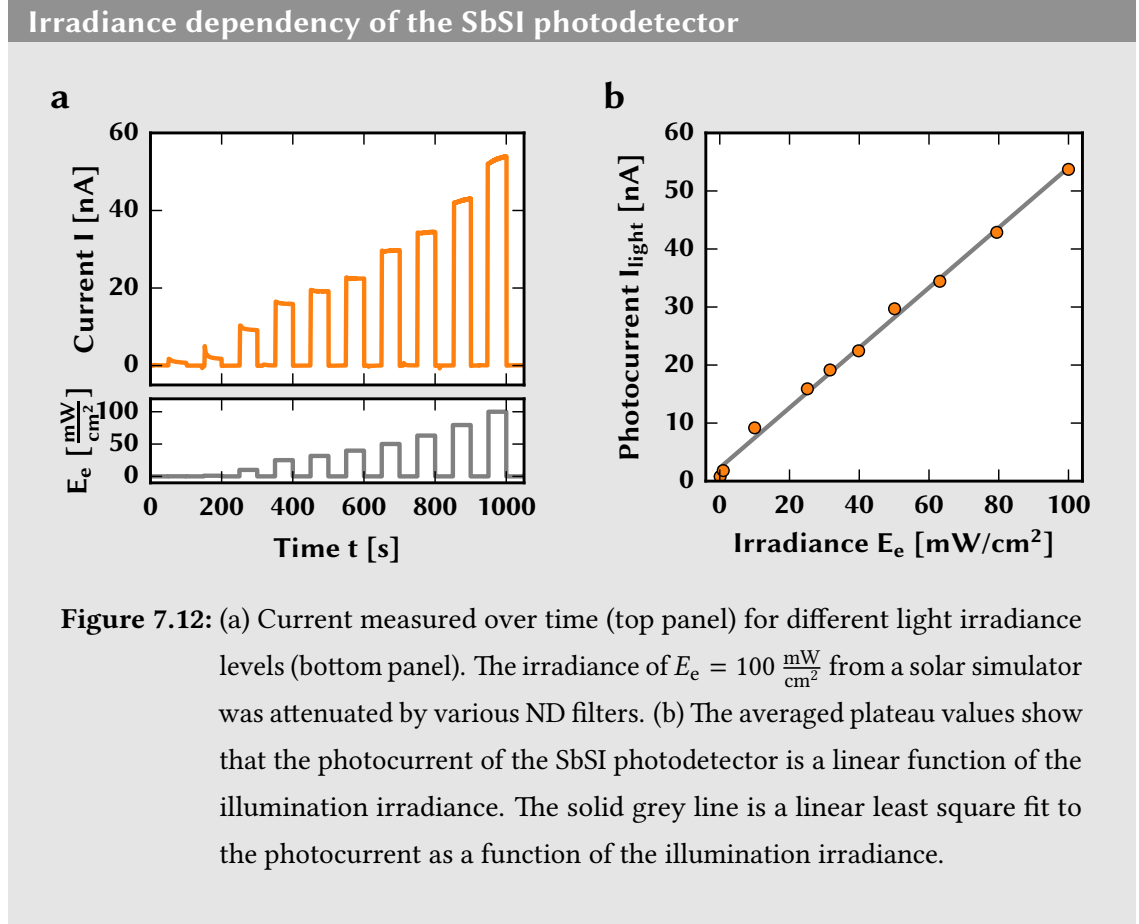
7.5.1 Photodetectors under voltage bias

The photodetector was kept at a bias voltage of $V_b = 100$ mV and its optoelectronic properties were characterised.

Irradiance dependence

The photocurrent was measured for different light intensities. White light of the solar simulator was set to an incident flux of $E_e = 100 \frac{\text{mW}}{\text{cm}^2}$ and the irradiance was attenuated using different neutral density (ND) filters. The ND filters were switched in the dark

period, when the light was off. During the change of the irradiance, the current was measured continuously, as shown in Figure 7.12 a. The plateau values were averaged and the linear response of the SbSI photodetector under different illumination intensities E_e is shown in Figure 7.12 b. The solid grey line is a linear least square fit, indicating the linearity of the output signal as a function of the illumination irradiance.



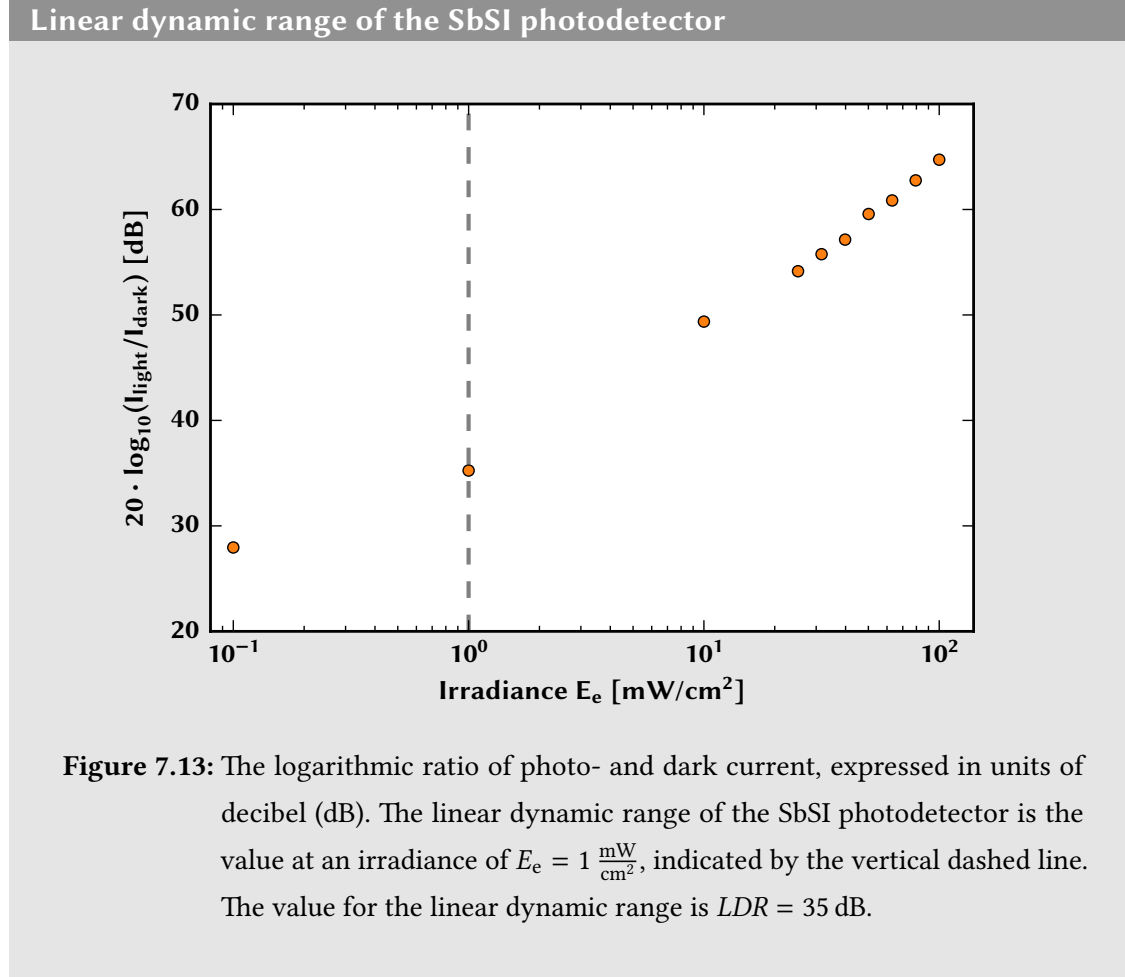
Linear dynamic range

The ratio of photocurrent to dark current at an irradiance of $E_e = 1 \frac{\text{mW}}{\text{cm}^2}$ is defined as the linear dynamic range LDR , typically given in units of decibel (dB),

$$LDR = 20 \text{ dB} \cdot \log_{10} \left(\frac{I_{\text{light}}(E_e = 1 \frac{\text{mW}}{\text{cm}^2})}{I_{\text{dark}}} \right). \quad (7.3)$$

7.5 Optoelectronic characterisation of SbSI photodetectors

Figure 7.13 shows the quantity $20 \cdot \log_{10} \left(\frac{I_{\text{light}}}{I_{\text{dark}}} \right)$ for the photodetector at different irradiance levels. The *LDR* at an irradiance of $E_e = 1 \frac{\text{mW}}{\text{cm}^2}$ is marked with the dashed grey vertical line. The here manufactured photodetector achieves a linear dynamic range of $LDR = 35 \text{ dB}$ at a bias voltage of $V_b = 100 \text{ mV}$.



Figures-of-merit

The performance of the photodetectors was further determined using the standard figures-of-merit introduced in Chapter 2. Figure 7.14 (top) shows the *SNR* as a function of E_e . The responsivity R is a measure for the electrical output per optical input.

It is defined as [21, 22]

$$R = \frac{I_{\text{light}} - I_{\text{dark}}}{E_e A}, \quad (7.4)$$

where A is the active area of the photodetector ($A = 0.12 \text{ cm}^2$). Figure 7.14 (middle) shows the responsivity R as a function of E_e for $V_b = 100 \text{ mV}$. The measured values are on the order of $R = 10^{-5} \frac{\text{A}}{\text{W}}$.

The ability of a photosensor to detect small signals is measured by the specific detectivity [23]

$$D^* = \frac{\sqrt{A} f R}{I_n}, \quad (7.5)$$

where f is the electrical frequency bandwidth of the detector. Assuming that the noise current I_n is dominated by shot noise of the dark current I_{dark} , the specific detectivity can be written as [1]

$$D^* = \frac{\sqrt{A} R}{\sqrt{2e I_{\text{dark}}}}, \quad (7.6)$$

where e is the elementary charge. The specific detectivity D^* is measured in Jones ($1 \text{ Jones} = 1 \frac{\text{cm}}{\text{W} \sqrt{\text{s}}}$). For the photodetector described here, the specific detectivity is on the order of $D^* = 10^9 \text{ Jones}$ for a bias voltage of $V_b = 100 \text{ mV}$, plotted as a function of E_e in Figure 7.14 (bottom).

Compared to previously published SbSI photodetectors, the figures-of-merit of the devices presented here are significantly improved. The maximum signal-to-noise ratio is nearly doubled and the specific detectivity is enhanced by a factor of three compared to the best previous device [9].

Spectral response

Figure 7.15 shows the spectral response of the photodetector at a bias voltage of $V_b = 100 \text{ mV}$, by plotting the measured photocurrent as a function of wavelength, normalised by the light intensity. A tungsten halogen lamp, a grating monochromator and a calibrated photodiode were used for this measurement. The output current has a clear onset at $\lambda = 650 \text{ nm}$, which matches well the reported band gap energy of antimony

Figures-of-merit of the SbSI photodetector

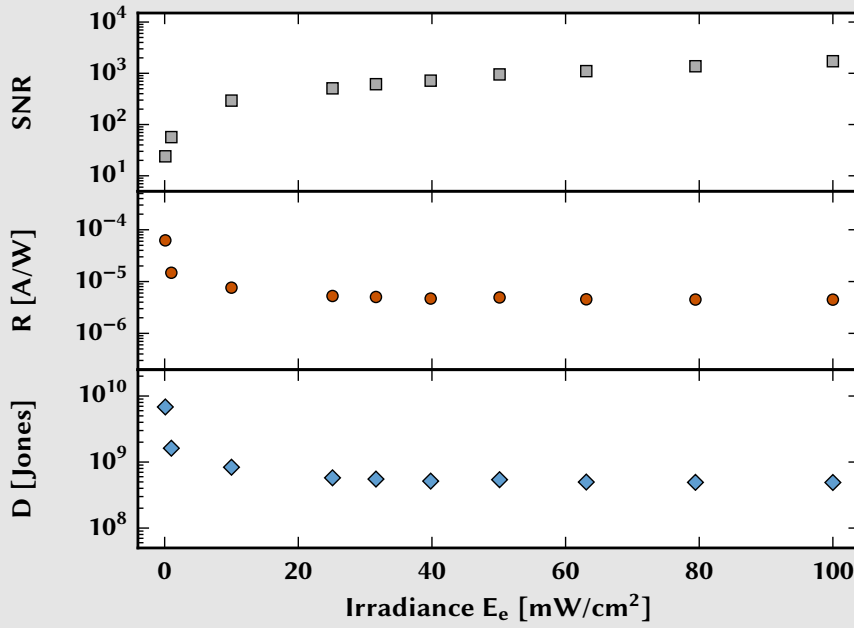


Figure 7.14: Signal-to-noise ratio SNR (top), responsivity R (middle) and specific detectivity D^* (bottom) as a function of illumination irradiance E_e for the best performing antimony sulfoiodide photodetector.

sulfoiodide of $E_g = 1.9$ eV [14]. It further agrees with the UV-vis spectrum in Figure 7.5, which shows that the detector is sensitive to most of the visible spectrum from red to blue.

Time response

For many optical sensing applications, short response times to changing light signals are essential. To determine the time response of the photodetector built here, an array of white light LEDs were pulsed by a function generator with a rectangular waveform and the current response of the SbSI devices was measured using an Autolab potentiostat in fast chronoamperometry mode with a bias voltage of $V_b = 100$ mV. Figure 7.16 a shows

Spectral response of the SbSI photodetector

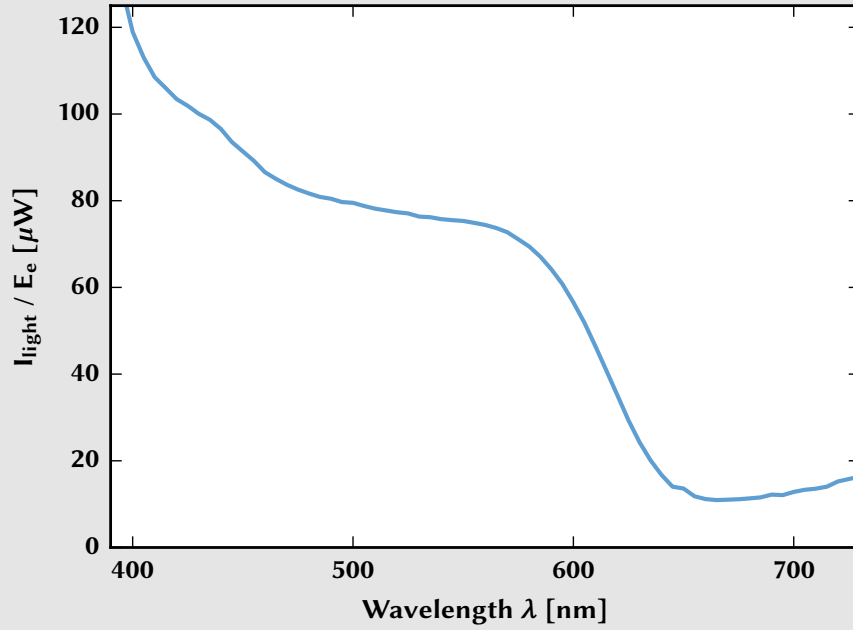


Figure 7.15: Photocurrent of an SbSI photodetector at a bias of $V_b = 100$ mV normalised by the irradiance as a function of wavelength. The onset of the spectrum at approximately 650 nm lies close to reported band gap values for SbSI ($E_g = 1.9$ eV, $\lambda_g = 653$ nm [14]).

the photocurrent response to a modulated light signal with a frequency of $f = 2$ Hz with a peak intensity of $E_e = 80 \frac{\text{mW}}{\text{cm}^2}$. A detailed view of one modulation cycle is shown in Figure 7.16 b. The rise time τ_r is the current increase from 10 % to 90 % of the maximum signal. Whereas the fall time, respectively, is defined by the current decrease from 90 % to 10 % [23]. Averaged over ten modulation cycles, values of $\tau_r = 7.4 \pm 0.4$ ms and $\tau_f = 33.8 \pm 1.5$ ms were determined, where the errors are the standard deviations. τ_r is two orders of magnitudes and τ_f one order of magnitude faster compared to the best previously reported SbSI photodetectors [9].

The time response of a photoconductive light sensor under bias is dominated by the drift time of the charge carriers and the RC constant of the device [24]. The significant

Time response of the SbSI photodetector

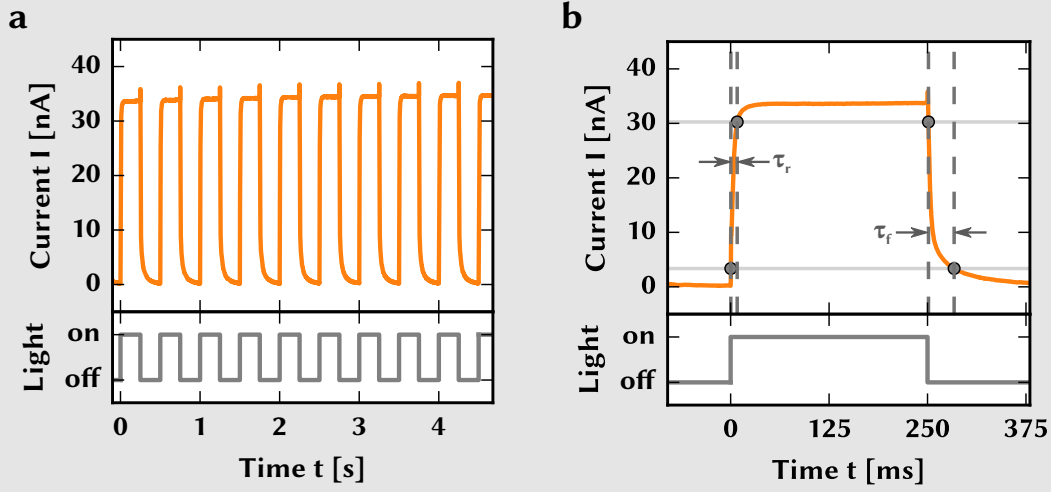


Figure 7.16: (a) Time response of the photocurrent, measured for a modulated light signal shown in the lower panel. The LED array was modulated with a frequency of $f = 2$ Hz and an irradiance of $E_e = 80 \frac{\text{mW}}{\text{cm}^2}$. (b) Detailed view of one modulation cycle. The rise-time τ_r and fall-time τ_f are indicated by arrows in the figure.

improvement in the time response of the photodetector can be explained by its sandwich-type architecture. The short electrode distance of $1 - 2 \mu\text{m}$ leads to a high electric field E at a given bias voltage. As the drift velocity v_d of charge carriers increases with the electric field ($v_d = -\mu E$, where μ is the charge carrier mobility) [25], the time response of the photodetector benefits from the small thickness of its active layer. As the active area $A = 0.12 \text{ cm}^2$ is relatively large for a light sensor, the time constants could be improved even further by reducing the area and hence the RC constant. This would however also lead to a decrease of the current output. Higher bias voltages V_b can also further improve rise- and fall-times, but at the cost of an increased noise current and hence a decreased signal-to-noise ratio.

7.5.2 Photodetectors in self-powered mode

Above, the current-voltage characteristic of the antimony sulfoiodide photodetector was investigated and it was found that even at zero bias $V_b = 0$ V a significant photocurrent of approximately $I = 40$ nA can be measured.

Thus, the photodetector can be used in a self-powered mode and does not have to rely on an external power supply. In this section, the properties for the SbSI photodetector at zero bias are examined.

Irradiance dependency at zero bias

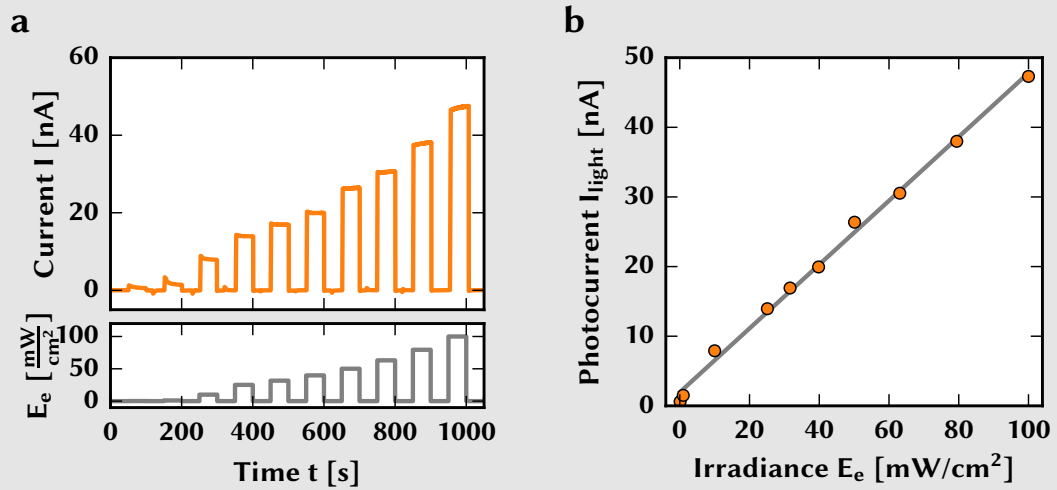
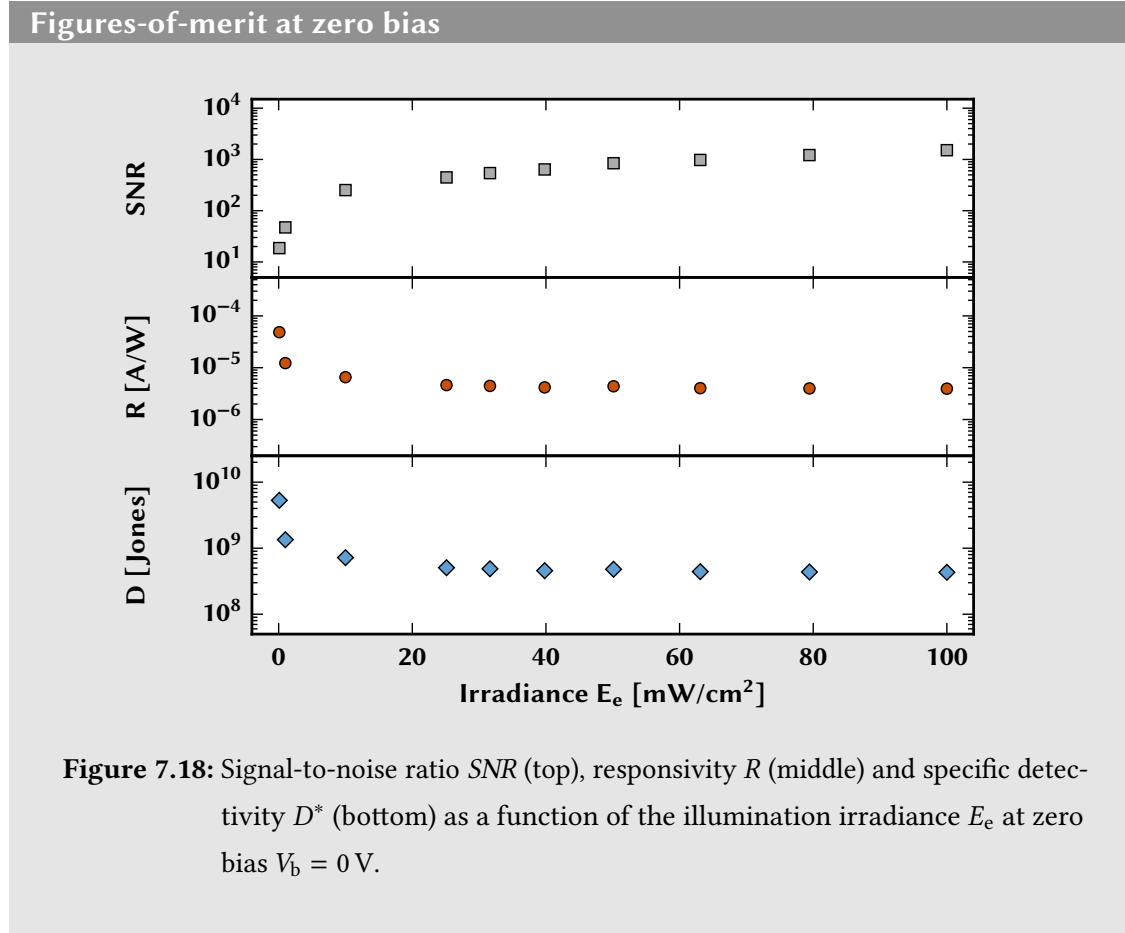


Figure 7.17: (a) Current as a function of time for different light irradiance levels at zero bias. The irradiance of $E_e = 100 \frac{\text{mW}}{\text{cm}^2}$ was attenuated using ND filters. (b) In self-powered mode, the photocurrent of the SbSI photodetector remains a linear function of the illumination irradiance. The grey line is a linear least square fit to the current as a function of the irradiance.

As before, the irradiance dependence of the photodetector response is investigated, this time in the self-powered mode ($V_b = 0$ V). The photocurrent was measured at zero bias for different light intensities. Again, the light of the solar simulator and ND filters were used to attenuate the irradiance. In Figure 7.17 a, the current was recorded while

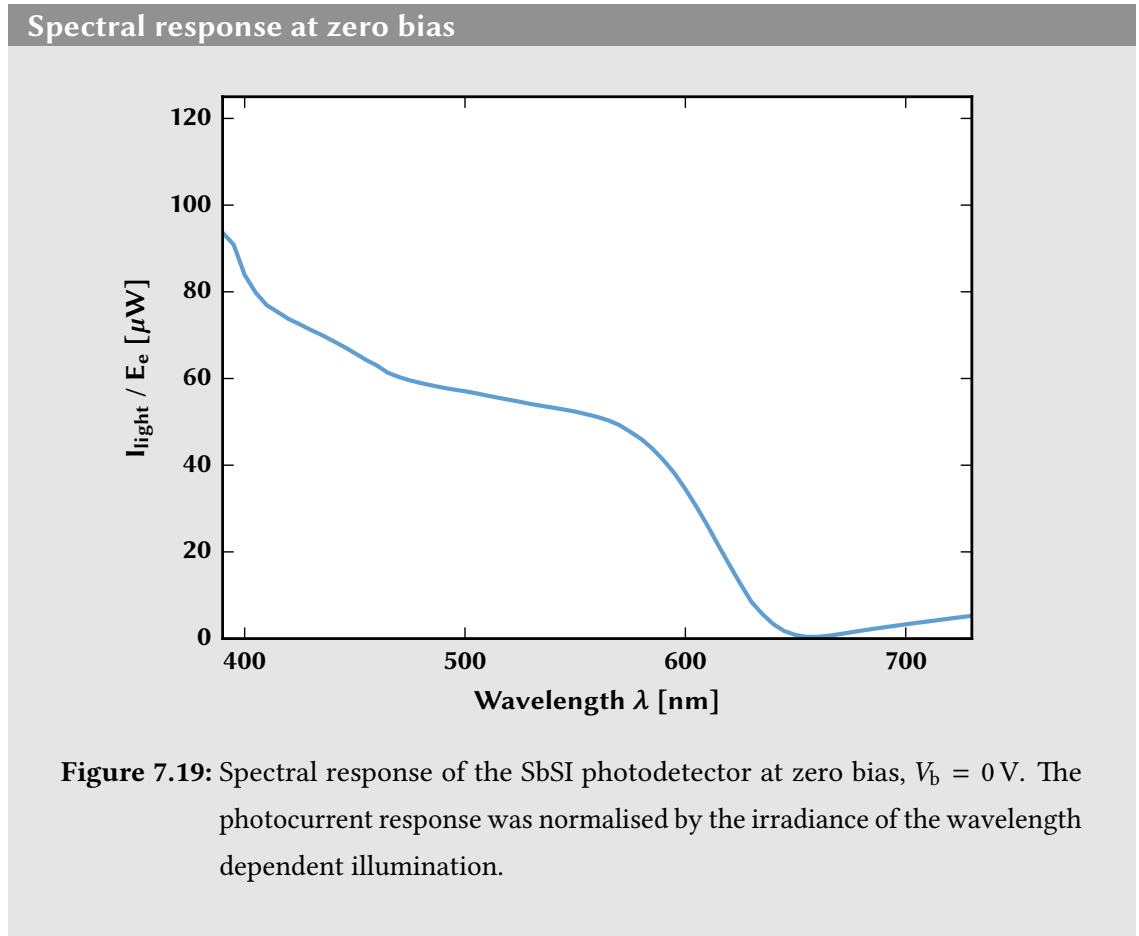
the filters were changed to reach different irradiance values. Figure 7.12 b shows the averaged photocurrent values and the linear response of the SbSI photodetector under different illumination intensities E_e . The solid grey line is a linear least square fit. Also for $V_b = 0$ V, the output signal is well presented by a linear function of the illumination irradiance.



It is worth to note that the absolute values of the photocurrent in self-powered mode are not much lower when compared to the values at $V_b = 100$ mV. At an irradiance of $E_e = 100 \frac{\text{mW}}{\text{cm}^2}$, the relative difference is only 12 %. This also means that the figures-of-merit for the SbSI photodetector in self-powered mode have values on the same order of magnitude as when operated at a bias. Signal-to-noise ratio SNR , responsivity R and the specific detectivity D^* are shown in Figure 7.18. Similar to the photodetector under bias,

the specific detectivity was still on the order of $D^* = 10^8 - 10^9$ Jones and responsivity values of $R = 10^{-6} - 10^{-5} \frac{\text{A}}{\text{W}}$ were achieved.

Figure 7.19 shows the spectral response of the antimony sulfoiodide photodetector at $V_b = 0$ V. The wavelength dependence is very similar to the detector under bias and the current output has again a clear onset at $\lambda = 650$ nm, which matches the literature value of the band gap of SbSI [14].



The origin of the non-zero photocurrent without bias voltage probably arises from the use of two different electrode materials. This effect is studied in more detail in the following section.

7.5.3 Symmetric photodetectors

The SbSI device in the previous sections, employed two different materials as electrodes, namely FTO on the bottom and gold on the top. The two electrodes have different work functions, causing a built-in potential. For FTO, the work function is 4.4 eV, for gold 5.2 eV [26].

To further investigate this, symmetric photodetectors with an additional 7.5 nm thick gold-layer on top of the FTO electrode were fabricated. The additional gold film has to be thin enough so that sufficient light can transmit through it, but thick enough to change the electrode's work function to the work function of gold. UV-vis spectroscopy found that the transmittance is reduced by approximately 40 % when the additional 7.5 nm gold layer was evaporated onto the FTO electrode. The architecture of the symmetric devices is shown in Figure 7.20. The gold film was evaporated prior to the deposition of antimony sulfide, all other steps were performed as described before.

The current-voltage characteristic of a symmetric SbSI photodetector is shown in Figure 7.21 a. With the additional gold layer, the I - V curve of the detector is rectified and voltage independent resistances can be assigned to the symmetric antimony sulfoiodide photodetector by determining the slope of the I - V curve. In the dark, the resistance of the photodetector was $R_{\text{dark}} = 173.5 \text{ M}\Omega$ and at a white light irradiance of $E_e = 100 \frac{\text{mW}}{\text{cm}^2}$ it was $R_{\text{light}} = 3.39 \text{ M}\Omega$. In these symmetric devices, the short circuit current under zero bias is considerably reduced, by approximately one order of magnitude, confirming that the asymmetric work functions caused the diode like behaviour and the photocurrent at zero bias.

However, the logarithmic plot of the two current-voltage curves in darkness and under illumination in Figure 7.21 b shows that the two graphs are still slightly shifted with regard to the $V_b = 0 \text{ V}$ axis. Possibly, the evaporated gold film was still too thin to completely level out the work functions of the two electrodes.

Symmetric photodetector

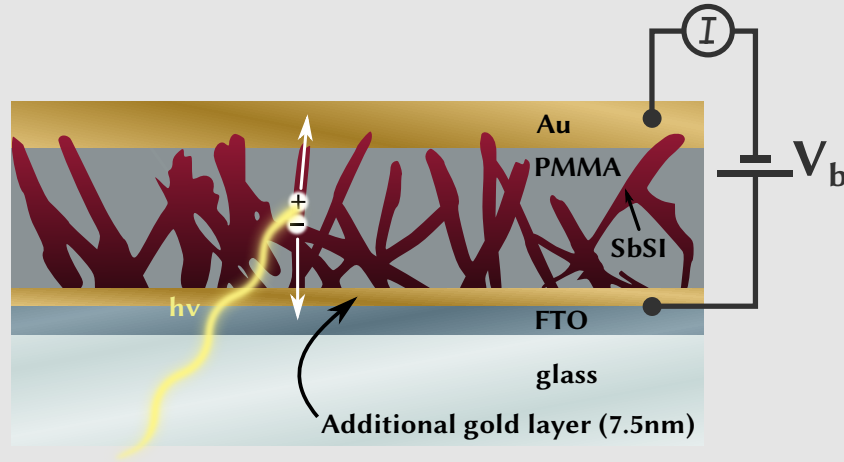


Figure 7.20: Schematic drawing of the photodetector with an additional layer of gold (thickness 7.5 nm) on top of the FTO electrode. This device was fabricated to demonstrate the effect of symmetrical electrode work functions, compared to asymmetric work functions of the previous devices.

7.6 Conclusion

In this chapter, a new method for the deposition of SbSI needle-shaped micro-crystals via the evaporation of SbI_3 onto amorphous Sb_2S_3 was introduced. The conversion process is facile and fast, with complete conversion in under 15 min compared to previous processes which took up to several hours. SbSI-covered substrates were employed for the fabrication of sandwich-type photodetectors. Optoelectronic investigations showed remarkable improvements compared to previously published SbSI light sensors [9]. In particular, the response and recovery time of these photodetectors is improved by one to two orders of magnitude. A promising specific detectivity of more than $D^* = 10^9$ Jones, a responsivity $R = 10^{-5} \frac{\text{A}}{\text{W}}$ and a high signal-to-noise ratio of more than $\text{SNR} = 10^3$ show that SbSI sandwich architectures are promising for the manufacture of efficient and low-cost light detectors. This is further substantiated in Table 7.1, where SbSI and

I-V curve of symmetric photodetectors

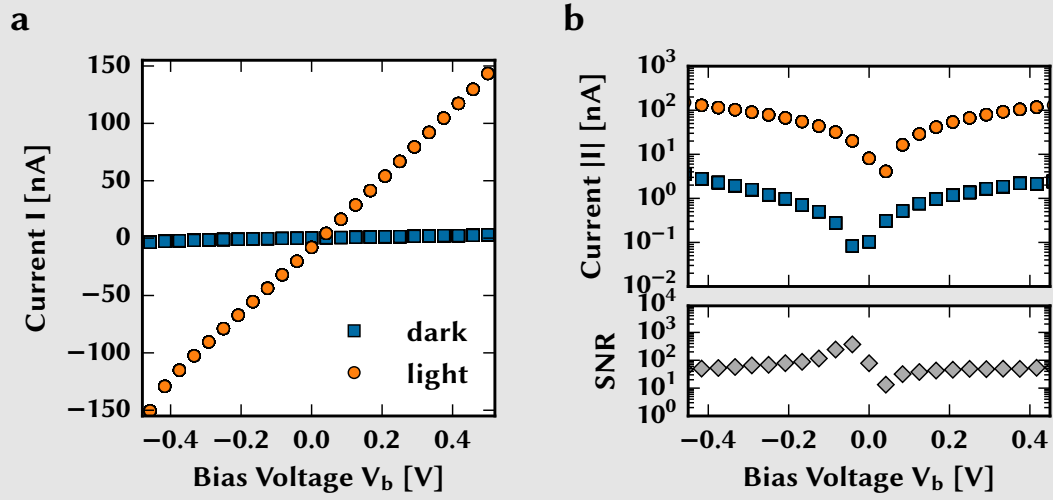


Figure 7.21: (a) Dark- (blue squares) and photocurrent (orange circles) of the photodetector with an additional gold layer as a function of bias voltages V_b . (b) Logarithmic plot of the same measurement. The lower panel shows the corresponding signal-to-noise ratio SNR .

perovskite photodetectors are compared. The SbSI photodetector presented here can also be used in a self-powered mode at zero voltage bias. The origin of this effect arises from the different work functions of the electrodes, namely gold and FTO. A thin additional gold layer on top of FTO rectifies the current-voltage curve and minimises the current at zero bias. For the asymmetric photodetector in self-powered mode, the figures-of-merit are on the same order of magnitude compared to the device under bias.

Table 7.1: Comparison of the figures-of-merit of different SbSI, perovskite-based and a high performance CdSe-nanowire photodetector.

Photodetector	I_{light} (0.1 V)	SNR	Detectivity D^*	Rise time τ_r	Fall time τ_f	Reference
“sandwich” SbSI	54 nA	1373	$6.8 \cdot 10^9$	8 ms	34 ms	This work
single-crystal SbSI	≈ 1.8 nA	700	$\approx 2.3 \cdot 10^9$	300 ms	300 ms	[9]
Perovskite ($\text{CH}_3\text{NH}_3\text{PbI}_3$)	≈ 10 nA	92	—	1200 ms	200 ms	[2]
CdSe- nanowire ^b	—	10^7	$4 \cdot 10^{13}$	350 ns	350 ns	[27]

Bibliography

- [1] L. Dou, Y. Yang, J. You, Z. Hong, W.-H. Chang, G. Li, and Y. Yang. “Solution-processed hybrid perovskite photodetectors with high detectivity”. *Nature Communications* 5 (2014), p. 5404. DOI: 10.1038/ncomms6404.
- [2] H. Lu, W. Tian, F. Cao, Y. Ma, B. Gu, and L. Li. “A Self-Powered and Stable All-Perovskite Photodetector–Solar Cell Nanosystem”. *Advanced Functional Materials* 26.8 (2016), pp. 1296–1302. DOI: 10.1002/adfm.201504477.
- [3] R. Nitsche and W.J. Merz. “Photoconduction in ternary V-VI-VII compounds”. *Journal of Physics and Chemistry of Solids* 13.1–2 (1960), pp. 154–155. DOI: 10.1016/0022-3697(60)90136-0.
- [4] A. Bhalla. *Ferroelectric Materials and Their Applications to Sensors*. CRC Press, 1988.
- [5] M. Nowak, P. Szperlich, A. Kidawa, M. Kepinska, P. Gorczycki, and B. Kauch. “Optical and photoelectrical properties of SbSI”. Ed. by J. Rutkowski and A. Rogalski. 2003, pp. 172–177. DOI: 10.1117/12.518846.
- [6] P. Kwolek, K. Pilarczyk, T. Tokarski, J. Mech, J. Irzmański, and K. Szaciłowski. “Photoelectrochemistry of n-type antimony sulfoiodide nanowires”. *Nanotechnology* 26.10 (2015), p. 105710. DOI: 10.1088/0957-4484/26/10/105710.
- [7] M. Nowak, L. Bober, B. Borkowski, M. Kepinska, P. Szperlich, D. Stróż, and M. Sozańska. “Quantum efficiency coefficient for photogeneration of carriers in SbSI nanowires”. *Optical Materials* 35.12 (2013), pp. 2208–2216. DOI: 10.1016/j.optmat.2013.06.003.
- [8] M. Nowak et al. “Fabrication and characterization of SbSI gel for humidity sensors”. *Sensors and Actuators A: Physical* 210 (2014), pp. 119–130. DOI: 10.1016/j.sna.2014.02.012.
- [9] G. Chen, W. Li, Y. Yu, and Q. Yang. “Fast and low-temperature synthesis of one-dimensional (1D) single-crystalline SbSI microrod for high performance photodetector”. *RSC Advances* 5.28 (2015), pp. 21859–21864. DOI: 10.1039/C5RA01180A.

Bibliography

- [10] E. Fatuzzo, G. Harbeke, W. J. Merz, R. Nitsche, H. Roetschi, and W. Ruppel. “Ferroelectricity in SbSI”. *Physical Review* 127.6 (1962), pp. 2036–2037. DOI: 10.1103/PhysRev.127.2036.
- [11] A. Kikuchi, Y. Oka, and E. Sawaguchi. “Crystal Structure Determination of SbSI”. *Journal of the Physical Society of Japan* 23.2 (1967), pp. 337–354. DOI: 10.1143/JPSJ.23.337.
- [12] A. S. Bhalla, R. E. Newnham, L. E. Cross, J. P. Dougherty, and W. A. Smith. “Pyroelectricity in SbSI”. *Ferroelectrics* 33.1 (1981), pp. 3–7. DOI: 10.1080/00150198108008060.
- [13] M. Nowak, B. Kauch, and P. Szperlich. “Determination of energy band gap of nanocrystalline SbSI using diffuse reflectance spectroscopy”. *Review of Scientific Instruments* 80.4 (2009), p. 046107. DOI: 10.1063/1.3103603.
- [14] K. T. Butler, J. M. Frost, and A. Walsh. “Ferroelectric materials for solar energy conversion: photoferroics revisited”. *Energy & Environmental Science* 8.3 (2015), pp. 838–848. DOI: 10.1039/C4EE03523B.
- [15] M. T. S. Nair, Y. Pena, J. Campos, V. M. Garcia, and P. K. Nair. “Chemically Deposited Sb₂S₃ and Sb₂S₃-CuS Thin Films”. *Journal of The Electrochemical Society* 145.6 (1998), pp. 2113–2120.
- [16] K. C. Gödel, Y. C. Choi, B. Roose, A. Sadhanala, H. J. Snaith, S. I. Seok, U. Steiner, and S. K. Pathak. “Efficient room temperature aqueous Sb₂S₃ synthesis for inorganic–organic sensitized solar cells with 5.1% efficiencies”. *Chemical Communications* 51.41 (2015), pp. 8640–8643. DOI: 10.1039/C5CC01966D.
- [17] M. Nowak, P. Szperlich, L. Bober, J. Szala, G. Moskal, and D. Stróż. “Sonochemical preparation of SbSI gel”. *Ultrasonics Sonochemistry* 15.5 (2008), pp. 709–716. DOI: 10.1016/j.ultsonch.2007.09.003.
- [18] Q. Yang, K. Tang, C. Wang, B. Hai, G. Shen, C. An, C. Zhang, and Y. Qian. “The synthesis of SbSI rodlike crystals with studded pyramids”. *Journal of Crystal Growth* 233.4 (2001), pp. 774–778. DOI: 10.1016/S0022-0248(01)01643-8.

-
- [19] H. K. Dubey, L. Deshmukh, D. Kshirsagar, M. Sharon, and M. Sharon. “A study of the electrical properties of SbSI synthesized using CVD techniques”. *QScience Connect* (2013), p. 40. DOI: 10.5339/connect.2013.40.
- [20] J. Varghese, C. O'Regan, N. Deepak, R. W. Whatmore, and J. D. Holmes. “Surface Roughness Assisted Growth of Vertically Oriented Ferroelectric SbSI Nanorods”. *Chemistry of Materials* 24.16 (2012), pp. 3279–3284. DOI: 10.1021/cm301928w.
- [21] M. Gong, A. Kirkeminde, Y. Xie, R. Lu, J. Liu, J. Z. Wu, and S. Ren. “Iron Pyrite (FeS_2) Broad Spectral and Magnetically Responsive Photodetectors”. *Advanced Optical Materials* 1.1 (2013), pp. 78–83. DOI: 10.1002/adom.201200003.
- [22] R. Huang, J. Zhang, F. Wei, L. Shi, T. Kong, and G. Cheng. “Ultrahigh Responsivity of Ternary Sb–Bi–Se Nanowire Photodetectors”. *Advanced Functional Materials* 24.23 (2014), pp. 3581–3586. DOI: 10.1002/adfm.201304176.
- [23] P. G. Datskos and N. V. Lavrik. “Detectors - Figures of merit”. *Encyclopedia of Optical Engineering* (2003), pp. 349–357.
- [24] M. Razeghi and A. Rogalski. “Semiconductor Ultraviolet Detectors”. *Journal of Applied Physics* 79.10 (1996), pp. 7433–7473. DOI: 10.1063/1.362677.
- [25] N. W. Ashcroft and N. D. Mermin. *Solid State Physics*. Harcourt College Publishers, 1976.
- [26] Q. Qiao and J. T. McLeskey. “Water-soluble polythiophene-nanocrystalline TiO_2 solar cells”. *Applied Physics Letters* 86.15 (2005), p. 153501. DOI: <http://dx.doi.org/10.1063/1.1900300>.
- [27] A. Littig, H. Lehmann, C. Klinke, T. Kipp, and A. Mews. “Solution-Grown Nanowire Devices for Sensitive and Fast Photodetection”. *ACS Applied Materials & Interfaces* 7.22 (2015), pp. 12184–12192. DOI: 10.1021/acsami.5b02547.

Conclusion and outlook

In this thesis, optoelectronic applications of antimony sulfide and antimony sulfoiodide were investigated. Using these materials, prototypes of solar cells and photodetectors were fabricated with a focus on the development of facile processing methods. In this final chapter, the results are summarised and put into a wider context. Where applicable, suggestions for future work are outlined.

In Chapter 5, the effect of a very thin antimony oxide layer as a recombination barrier in Sb_2S_3 sensitised solar cells was investigated. After the deposition of antimony sulfide onto a mesoporous anode, the Sb_2S_3 was partly oxidised by a post annealing step in air. The annealing parameters had to be balanced and only short heating times in air led to a barrier layer, which fulfils the two important conditions. On the one hand the barrier has to be thick enough to effectively reduce recombination of holes and electrons at the interface of the antimony sulfide absorber and the hole transport material. On the other hand, the layer should not be too thick to impede the injection of holes from the absorber film into the hole conductor. It was found that an annealing time in air of 1 min at 200°C leads to the desired effect. The efficiency of solar cells with a such oxidised absorber layer increases by more than 60 % (from $\eta = 1.4\%$ to $\eta = 2.4\%$) compared to non-oxidised photovoltaic devices. Phenomenologically, it was often speculated that the exposure of antimony sulfide to air at elevated temperatures leads to the reduction of recombination at the Sb_2S_3 -HTM interface. With the results presented in this chapter, this hypothesis could finally be confirmed. IMVS measurements proved the increase in the electron recombination lifetime and thus the decrease in the recombination rate for solar cells, where the absorber film was partly oxidised. The recombination lifetime

increased by a factor of 3.5, explaining the large improvement in device efficiency. In the last two years, research on antimony sulfide solar cells shifted towards non-sensitised, flat film devices. So the question arises whether a partial oxidation is also important in these flat Sb_2S_3 solar cells. For flat devices, the surface area of the interface between absorber and hole transport material is much smaller, thus recombination of charge carriers at this interface is less important. Hence, it is expected that annealing flat antimony sulfide photovoltaic layers in air will not be beneficial. In this case, reduction in charge transfer at the antimony sulfide interface probably outweighs the advantage of reduced recombination.

The need for cooling equipment complicated the deposition of antimony sulfide in the laboratory environment. When running reactions at low temperatures, the preparation of solutions and the chemical bath itself is time consuming. But also for industrial scale processes it is beneficial if deposition steps can be performed at room temperature. In Chapter 6 the CBD method was altered so that antimony sulfide can be deposited at ambient conditions, without the need for cooling during the preparation and the process itself. The novel method uses the same precursor materials as the established technique, antimony chloride, sodium thiosulfate and water. To be able to execute the deposition at higher temperatures, the reaction speed has to be reduced. This was achieved by changing the order of the precursor addition steps. For the new method, water was added to antimony chloride first, which led to its hydrolysis. The hydrolysed precipitate complexes antimony ions, slowing down the deposition of antimony sulfide after the addition of the sodium thiosulfate. Sb_2S_3 which was formed via the new room temperature method was analysed with regard to its material properties. There are two differences which stand out when comparing the room temperature deposited Sb_2S_3 to the conventionally prepared antimony sulfide: a higher residual antimony oxide content and a significantly lower trap state density. The former leads to a reduced conductivity of the films, which is disadvantageous for its application. However, the latter is beneficial and improves one of the major problems in sensitised antimony sulfide solar cells. A comparative study of Sb_2S_3 solar cells showed that the advantages outperform the disadvantages and that it is possible, and even favourable, to replace the low temperature

deposition routine with the new method. The power conversion efficiency was improved from on average $\eta_{\text{low-T}} = 1.0\%$ to $\eta_{\text{RT}} = 1.2\%$. These efficiencies were however not the state of the art for Sb_2S_3 sensitised photovoltaics and lagged far behind the efficiency record of $\eta_{\text{rec}} = 7.5\%$. The solar cells were further optimised to increase the performance in collaboration with Dr. Yong Chang Choi and Prof. Sang Il Seok from KRICT in Daejeon, South Korea, who are holding the mentioned record. During a research stay at KRICT, the power conversion efficiency of the room temperature synthesised Sb_2S_3 devices was increased to $\eta = 5.1\%$. The main difference to the previous devices was the use of a different mesoporous titanium dioxide film and a combination of PCPDTBT, PCBM and PEDOT:PSS as hole transport layer. Although 5.1% is a respectable efficiency for antimony sulfide solar cells, it will still need to be improved significantly in order to transition from research towards practical applications of these devices. Despite the prospects of low manufacturing costs, an efficiency of 10% and above is normally seen as the threshold for profitable market applications. The question whether antimony sulfide has a future as a material for solar cells remains unanswered, especially with the recent emergence of alternative materials, such as hybrid lead-halide perovskites. The comparably low toxicity and high stability makes antimony sulfide an interesting alternative which is worth exploring - in terms of scientific curiosity which may one day lead to a significant improvement in efficiency, or potentially alternative applications of the material.

Building on the experience with antimony sulfide, its use as a precursor for new materials was explored in Chapter 7. Films of amorphous Sb_2S_3 were converted into antimony sulfoiodide in a fast and facile process using a physical vapour of antimony iodide. The SbI_3 was simply evaporated onto the antimony sulfide film in less than 15 min. As the temperature of the substrate did not exceed 190°C , the process is probably also suitable for flexible substrates. The product of the conversion consisted of a thin film of dense needle-like SbSI micro-crystals with lengths between $1 - 5\ \mu\text{m}$. The SbSI films were then used to build photoconductive sensors in a sandwich-type architecture. PMMA was spin-coated as a protection layer to block voids between the crystals and to prevent shorting between the bottom FTO and the top gold electrode. The photodetector

was characterised optoelectronically. The maximum signal-to-noise ratio was doubled and the specific detectivity was enhanced by a factor of three compared to the best previously reported SbSI photosensor. The biggest improvement, however, was the decrease in response and recovery time, which was achieved by the small electrode spacing of the sandwich-type architecture. Time response measurements revealed rise times of less than 8 ms and fall times lower than 34 ms. Further, the photodetectors showed photocurrents at zero voltage bias, offering the possibility to operate the device in a self-powered mode without the need for an external power supply. The origin of this behaviour was found in the two distinct electrode materials, FTO and gold with its different work functions. Adding a very thin gold film onto the FTO electrode rectified the current-voltage characteristic, confirming this hypothesis. Despite having achieved the best SbSI photodetector published so far, the figures-of-merit have to be further improved before the devices will become competitive with established photodetecting technologies using materials such as cadmium selenide, gallium arsenide or crystalline silicon. However, the research of antimony sulfoiodide for optoelectronic applications is still in its early stages. Yet there are opportunities to improve the proposed SbSI photodetector design further. It might be possible to increase the degree of orientation of the SbSI crystal needles so that they are perfectly perpendicular to the surface of the substrate. This would ensure that more crystals are contacted by both electrodes thereby significantly increasing the current output of the sensor. The work presented here might also be seen as a first step towards SbSI solar cells. The self-powered mode of the photodetectors presented in this chapter, shows that photovoltaic devices using antimony sulfoiodide might be a viable and interesting field for future research.

With this thesis, a contribution to the development of solution processable antimony sulfide and antimony sulfoiodide optoelectronic applications was made and it will be interesting to witness the future progress of these devices.